Numerical study and optimization of photonic crystals

PAR

Momchil MINKOV

EPFL

ÉCOLE POLYTECHNIQUE
FÉDÉRALE DE LAUSANNE

Suisse
2016

'Don't stop me now!'
— Freddie Mercury

To my family.

Acknowledgements

The pages you are about to read (because you are not going to just read the Acknowledgments, right?) are a fairly comprehensive exposition of what most of my time in the last four years was spent on, professionally. I would like to take this chance and thank everybody who helped me on the way.

First and foremost, I would like to thank Prof. Vincenzo Savona, who contributed to the completion of this work in about a million different ways. I am grateful to him for starting me off with the photonic crystal project a long time ago when I first appeared as a clueless Master's student – it turned out to be a gold mine! I also want to thank him for trusting my skills and offering me the doctoral position that I am now finishing. And, of course, for the great guidance throughout it. Vincenzo could always keep my interest high, and insightfully direct me towards the exciting research in and out of the photonic crystal domain. Our daily discussions, as well as the thousands of exchanged emails, were an invaluable part of my work, pushing both my understanding and my curiosity. For all that, and everything I learned from him – I am most thankful.

I would also like to acknowledge the great environment at the ITP. The relaxed atmosphere, and the possibility to freely discuss matters in and out of the professional scope, made for a comfortable work experience. I'd like to thank the colleagues in my group: Eduardo, Hugo, Joseph and Pierre, for expanding the horizon of my understanding of Physics. Special thanks goes to Hugo for the help with the French abstract of this thesis. I am also grateful to them, and to all my other ITP-mates – Davide, Diego, Gabriel, Giacomo, Fernando, and Nauni – for the countless fun moments during coffee breaks, and also (and especially) in the after-work hours.

A big thank you goes to all the researchers with whom I collaborated, whose work is part of the results presented here. Thanks to Prof. Houdré and to Mario, Mohamed, and Peru, for fabricating and measuring some of my designs, showing that my simulations do in fact work. Thanks to Prof. Badolato for his strong enthusiasm about my designs, and to Yiming for the superb fabrication quality. Thanks for the great work also goes to all my other collaborators: Prof. Grandjean, Jean-François, Noelia, Raphael, Prof. Galli, Prof. Gerace, Giulia, and Stefano. Special thanks to Dario for many, many useful hints along the way.

A good work-life balance is one of my main priorities – in fact I am much less productive when I am feeling down. Fortunately, there were a lot of people who made sure I never did, and who made my stay in Lausanne very memorable. It's a great town in itself,

Acknowledgements

but it's my friends here who made it truly special. Unfortunately I cannot name them all, so I'm sorry if anyone feels left out. That said, thanks to Ana, Claudia, Ceco, Fanny, Francisco, Petar, Terry, Thierry, and Vil, for all the fun that was had on countless occasions, and for being there for me in times of need.

As the first page reads, this thesis is dedicated to my family. They know who they are. Thank you for your constant support – I would be nowhere near here if it weren't for it.

Lausanne, 12 January 2016   Momchil

Abstract

Photonic crystals (PhCs) are engineered nanostructures that enable an extraordinary control over the flow of light. These structures can be fabricated out of common semiconductors, are compatible with existing industrial fabrication technologies, and are expected to play a major role in future devices integrating photonic circuits – e.g. for telecommunications or in future quantum technologies. In this thesis, we explore a wide range of properties of the most common class of PhCs, formed by a lattice of circular holes in a semiconductor slab. To compute the electromagnetic eigenmodes of a given structure, we use fast mode-expansion methods, which are presented in detail here. The first application consists in a detailed analysis of the effects of fabrication disorder on the PhC structures. It is by now well-known that disorder is in many cases the limiting factor in device performance. Here, we shed more light on its effects, by statistically comparing various designs for PhC cavities with a high quality factor, and by analyzing the effect of irregular hole shapes on a PhC waveguide. The second application presented here stems from the fact that PhCs are in fact tremendously flexible, and their features are determined by a large number of controllable parameters. This is on one hand a great advantage, but on the other a great challenge when it comes to finding the optimal device for a given application. To face this challenge, we have developed an automated optimization procedure, using a global optimization algorithm for the exploration of an insightfully selected parameter space. This was applied to various devices of interest, and inevitably resulted in a vast improvement of their qualities. Specifically, we demonstrate various high-Q cavity designs, and a slow-light coupled-cavity waveguide with extraordinary features. We also present several experimental confirmations of the validity of our designs. Finally, we discuss two domains in which PhCs (and our optimization procedure) can be expected to play a major role. The first one is integrating quantum dots with the goal of long-range, photon-assisted dot-dot coupling, with implications for quantum information processing. We develop a semi-classical formalism, and analyze the magnitude and attenuation length of this coupling in large PhC cavities, as well as in a waveguide. The second outlook is in the field of topological photonics. We describe an array of resonators, in which an effective gauge field for photons can be induced through an appropriate time-periodic modulation of the resonant frequencies. This results in a Quantum Hall effect for light, and, in a finite system, one-directional edge states immune to fabrication disorder are predicted. We discuss the possibilities

Résumé

Les cristaux photoniques (CPh) sont des structures nano-fabriquées qui permettent un contrôle sans précédent du flux de lumière. Ces structures peuvent être fabriquées à partir de semi-conducteurs standards, sont compatibles avec les technologies de fabrication industrielles existantes et devraient jouer un rôle important pour le développement futur de circuits photoniques, par exemple pour les télécommunications ou les technologies quantiques. Au long de cette thèse, nous explorons les propriétés du type de CPh le plus populaire, formé d'un réseau d'orifices circulaires percés dans une plaque de matériau semi-conducteur. Afin de calculer les modes électromagnétiques issus d'une telle structure, nous utilisons des méthodes numériques rapides, faisant appel à une expansion sur une base optimale de modes électromagnétiques. Ces méthodes sont présentées en détail. La première application est une analyse fine de l'impact du désordre lié à la fabrication sur les CPh. Il est bien connu qu'un tel désordre est souvent un facteur limitant pour les performances des structures. Ici, nous élucidons l'impact de ces effets à l'aide d'une analyse statistique comparative de différents modèles des cavités CPh à facteur de qualité (Q) élevé et en analysant les conséquences de la présence de trous de formes irrégulières sur l'efficacité un guide d'onde. Une deuxième application de notre méthode est rendue possible par la grande flexibilité des CPh, dont les caractéristiques sont affectées par un grand nombre des paramètres qui peuvent être finement contrôlés. Si d'un côté cette variété constitue un avantage, d'autre part elle pose un grand défi pour l'optimisation de ces structures en vue d'applications ciblées. Dans ce cadre, nous avons développé une méthode d'optimisation automatisée, basée sur un algorithme d'optimisation global pour l'exploration d'un espace des paramètres judicieusement choisis. Cette méthode est appliquée à divers systèmes et conduit à une amélioration significative de leurs propriétés. Plus spécifiquement, nous avons achevé une maximisation très significative du facteur Q de plusieurs cavités optiques, ainsi qu'un guide d'onde à cavités couplées propageant efficacement un flux de lumière ralentie (slow light). Nous discutons également deux domaines d'applications pour lesquels les CPh (et notre procédure d'optimisation) peuvent jouer un rôle majeur. Le premier est l'intégration de boîtes quantiques, que peuvent être couplées à longue distance par l'intermédiaire de la lumière, avec des implications directes pour le traitement quantique de l'information. Nous développons un formalisme semi-classique, et analysons l'amplitude et la longueur d'atténuation de ce couplage dans des longues cavités CPh ainsi que

Contents

Contents

List of Figures

List of Acronyms

0..3D   0..3-dimensional.

AlN   Aluminum Nitride.

BME   Bloch-mode Expansion.

BZ   Brillouin Zone.

CCW   Coupled-cavity Waveguide.

CDF   Cumulative Distribution Function.

CMOS   Complementary Metal–oxide–semiconductor.

DBP   Delay-Bandwidth Product.

DOS   Density of States.

FDTD   Finite-difference Time-domain.

FEM   Finite-element Method.

FWHM   Full Width at Half Maximum.

GaAs   Gallium Arsenide.

GaN   Gallium Nitride.

GBP   Group Index-Bandwith Product.

GME   Guided-mode Expansion.

GVD   Group Velocity Dispersion.

InAs   Indium Arsenide.

InN   Indium Nitride.

IPN   Inverse Participation Number.

Acronyms

IR   Infra-red.

NIR   Near Infra-red.

PBC   Periodic Boundary Conditions.

PhC   Photonic Crystal.

PWE   Plane-wave Expansion.

Q   Quality Factor.

QD   Quantum Dot.

QED   Quantum Electrodynamics.

RS   Resonant Scattering.

SEM   Scanning Electron Microscope.

SHG   Second-harmonic Generation.

Si   Silicon.

SiO$_2$ Silicon Oxide.

SOI   Silicon-on-insulator.

TE   Transverse Electric.

TM   Transverse Magnetic.

TRS   Time-reversal Symmetry.

UV   Ultra-violet.

V   Mode Volume.

Introduction

In 1987, two researchers independently published results that have since avalanched into one of the most vigorously developing fields in optics and photonics. John [1] demonstrated that light in certain dielectric lattices can exhibit behaviour reminiscent of the localization of the electron wave-function in disordered crystals, first discussed by Anderson [2]. Yablonovitch [3] demonstrated that periodic dielectric structures modify the local density of states of optical modes, leading to, among other effects, inhibited spontaneous emission. It was then quickly realized that both effects are just scratching the surface of the vast possibilities for control of electromagnetic radiation with dielectric lattices, and the study of Photonic Crystals (PhCs) began.

The defining characteristic of a photonic crystal is a periodic modulation of the dielectric permittivity in at least one spatial dimension. The permittivity effectively acts in a way analogous to the external potential in the Schrödinger equation, and thus, in a PhC, the standard vocabulary of solid-state physics: Bloch momentum, Brillouin zone, energy bands and band gaps, etc., becomes applicable. The possibility for a full 3-dimensonal (3D) photonic band gap is a particularly striking feature of PhCs. A structure with such a property can be viewed as a perfect mirror for the spectrum of light with energy within the band gap. Furthermore, low-dimensional defects in the lattice open states within the band gap that can be used for confining or guiding light, which is widely explored for various applications.

As is often the case, nature is one step ahead of us. One way to create a colored surface is through the use of pigments – molecules whose particular absorption and/or reflection properties yield a given color. It turns out, however, that some of the most intricate color patterns that we can think of are produced not through pigmentation, but through photonic-crystal-like structures. Simply put, this means that a (quasi-) periodic arrangement of an otherwise transparent material produces an interplay between transmission and reflection (due to the band-gap effects) that results in sophisticated color patterns. This is illustrated in Fig. 1, where we show the beautiful coloration of an opal gemstone, a peacock feather, and a butterfly, as well as micro-graphs showing the underlying sub-micrometer structures, through which the coloring can, at least qualitatively, be understood. The spectrum of the reflected light is determined by,
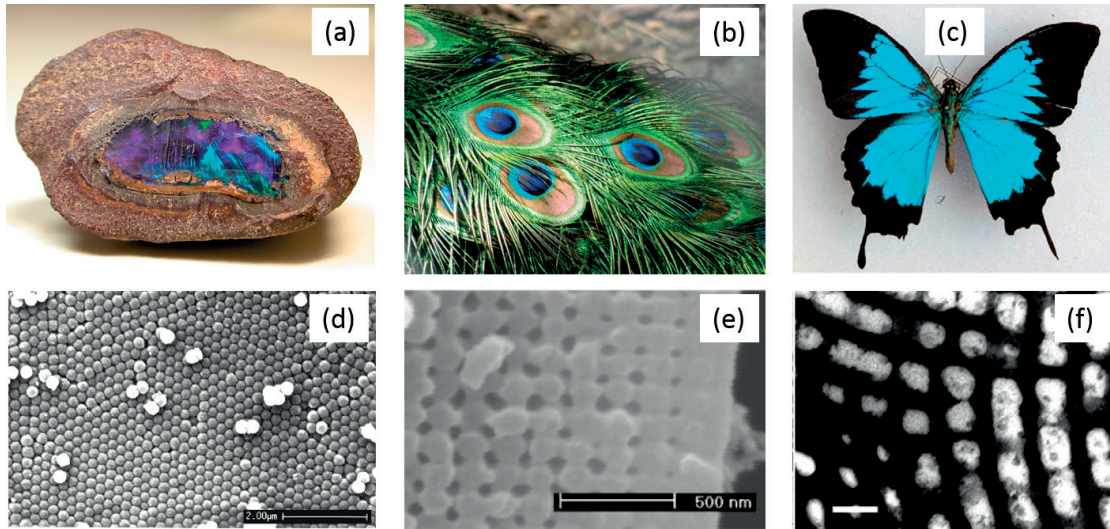
Figure 1: Gem-quality opal: photo in (a) and SEM micro-graph in (d); images from [4]. Peacock feather: photo in (b) and SEM image from [5] in (e). *Papilio ulysses* butterfly: photo in (c) and STM micro-graph in (f) (length of scale bar: 2μm); images from [6].

among other parameters, the lattice constant, i.e. the length-scale of the periodicity. Defects add an extra variation by trapping light of certain well-defined colors. The possible realizations of such structural coloration are thus practically unlimited, which is arguably not the case when using a restricted number of pigments.

The first proposals for experimental realizations of PhCs aimed at 3D structures with omni-directional band gaps [7–9], but such structures remain challenging to fabricate even today. In contrast, the availability of advanced silicon-chip fabrication technologies, perfected for the purposes of commercial electronics, served as an impetus for the class of PhCs now known as photonic crystal slabs (or slab-PhCs). These devices consist of a two-dimensional periodic pattern inscribed in a dielectric slab, with the confinement in the third dimension provided by total internal reflection. While there is no 3D band gap (the periodicity is in two dimensions only), a lot of fascinating – and useful – features are still exhibited by such structures. The modeling, optimization, and applications of slab-PhCs is thus the central topic of this thesis, which is organized in the following manner.

Chapter 1 outlines the theory of photonic crystals in general and photonic crystal slabs in particular, as well as their importance for applications. Cavities and waveguides, and their important figures of merit, are introduced.

Chapter 2 presents the numerical methods used in the simulations within the subsequent chapters of this thesis. These include the guided-mode expansion, the Bloch-mode expansion, and the finite-difference time-domain methods.

Chapter 3 presents an analysis of the effect of fabrication disorder on the properties of PhC cavities and waveguides. In many situations, this is the main limiting factor determining all experimentally measured quantities. Quantifying the impact of imperfections is thus the first and most important step to understanding the experimental limitations, and potentially overcoming them.

Chapter 4 demonstrates various device optimizations. A main focus is given to improving the quality factor of a number of cavities in several different materials. A global optimization algorithm is used to find the best configuration of a number of experimentally accessible parameters. This has led to record-high quality factor values both in theory and in practice. An optimization of a coupled-cavity waveguide is also demonstrated and yields a record-high group index-bandwidth product – the main figure of merit for slow-light applications.

Chapter 5 deals with an important potential application of PhCs: integrating quantum dots for a solid-state quantum computation architecture. A semi-classical formalism for treating a PhC-quantum dot system is outlined, and applied to the radiative coupling of two dots in various structures. The potential for coupling at-a-distance is analyzed, including fabrications imperfections which are once again the limiting factor.

Chapter 6 presents a proposal for implementing the Quantum Hall effect for light in an array of optical cavities using a dynamic modulation of the resonant frequencies. First, a generic system is presented and its topological properties are studied. This is followed by a discussion of possible experimental realizations, for which photonic crystal slabs could once again prove to be the best platform.

A final remark is due. This thesis comprises results obtained in the last four years, many of which have already been published in various scientific journals. Thus, in some cases, the presentation here is adapted from the corresponding publications. When this is the case, it is clearly stated in the introduction of the Sections, and our collaborators are properly acknowledged. To help the reader in recognizing Sections and Subsections with only minor changes from already published manuscripts, an asterisk (*) is placed at the end of their titles. We note that care was taken for the whole thesis to still be a coherent, well-organized read.

1 Introduction to Photonic Crystals

This Chapter presents both a theoretical and a practical introduction to photonic crystals. Light propagation in general and in a periodic medium in particular is discussed in Section 1.1. The early proposals for photonic crystals are summarized in Section 1.2.1. The specific class of photonic crystal slabs, which have gained significant popularity in the last decade and are the main object of study of this thesis, is presented in Section 1.2.2. Finally, the two most important functional elements – waveguides and cavities – are discussed in Section 1.3, and some important figures of merit like the group index, Quality Factor (Q), and Mode Volume (V) are defined.

1.1 Theoretical preliminaries

The mathematics needed to describe light propagation in periodic structures is a combination of Maxwell's equations and the theory of Bloch states borrowed from solid-state physics. An overview is presented below, while a detailed discussion and a derivation of some intermediate steps can be found in e.g. Refs. [10, 11].

1.1.1 From Maxwell to Helmholtz

Classical electromagnetism in a material is fully contained within the four Maxwell equations, which, in their most general formulation, read

$$\nabla \cdot \mathbf{D} = \rho, \qquad \nabla \cdot \mathbf{B} = 0, \tag{1.1}$$
$$\nabla \times \mathbf{E} = -\frac{\partial \mathbf{B}}{\partial t}, \qquad \nabla \times \mathbf{H} = \mathbf{J} + \frac{\partial \mathbf{D}}{\partial t},$$

where $\mathbf{E}$ is the electric field, $\mathbf{D}$ is the displacement field, $\mathbf{H}$ is the magnetic field, and $\mathbf{B}$ is the magnetic induction. For the study of photonic crystals, several simplifying assumptions can be made from the very start. First, we assume no free charges ($\rho = 0$)

and currents ($\mathbf{J} = 0$), i.e. we look at light propagation and neglect the sources. We also assume a non-magnetic medium in which $\mathbf{B} = \mu_0 \mathbf{H}$, with μ_0 the vacuum permeability, which is true for a wide range of semiconductors. For the displacement field (in a macroscopic material with no birefringence), we have

$$D_i = \varepsilon_0 \varepsilon(\mathbf{r}, \omega) E_i + \varepsilon_0 \sum_{j,k} \chi_{ijk}^{(2)}(\mathbf{r}, \omega) E_j E_k + \mathcal{O}(E^3), \tag{1.2}$$

with $\varepsilon(\mathbf{r}, \omega)$ the relative dielectric permittivity and $\chi^{(2)}$ the second-order susceptibility tensor (higher orders enter in the $\mathcal{O}(E^3)$ terms). The dependence of ε on the angular frequency ω, i.e. the material dispersion, can be neglected if we consider a narrow interval around some ω_0 and set $\varepsilon(\mathbf{r})$ appropriately for that frequency. The limit of small electric field magnitude and/or small susceptibility (as compared to ε), in which all but the first terms of eq. (1.2) can be neglected, is the linear-response limit. While this is usually fulfilled in the structures we study here, most applications rely on the presence of the non-linear second- and/or higher-order terms in eq. (1.2). In fact, enhancing these effects is one of the major goals of this thesis. Fortunately, they can typically be analyzed in a perturbative sense after the linear-response modes of a structure are found.

With the assumptions enumerated thus far, the Maxwell equations simplify to

$$\nabla \cdot [\varepsilon(\mathbf{r})\mathbf{E}] = 0, \qquad \nabla \cdot \mathbf{H} = 0, \tag{1.3}$$

$$\nabla \times \mathbf{E} + \mu_0 \frac{\partial \mathbf{H}}{\partial t} = 0, \qquad \nabla \times \mathbf{H} - \varepsilon_0 \varepsilon(\mathbf{r}) \frac{\partial \mathbf{E}}{\partial t} = 0,$$

where the $\mathbf{E}$ and $\mathbf{H}$ fields depend on $(\mathbf{r}, t)$. The spatial and temporal dependences are, however, separable, and, since there are no time-dependent terms, any solution is a superposition of harmonic modes that oscillate at a given frequency:

$$\mathbf{H}(\mathbf{r}, t) = \mathbf{H}(\mathbf{r})e^{-i\omega t}, \qquad \mathbf{E}(\mathbf{r}, t) = \mathbf{E}(\mathbf{r})e^{-i\omega t}. \tag{1.4}$$

With this final consideration, the original problem starting with the Maxwell equations is reduced to finding all solutions of the Helmholtz equation for the magnetic field:

$$\nabla \times \left(\frac{1}{\varepsilon(\mathbf{r})} \nabla \times \mathbf{H}(\mathbf{r}) \right) = \left(\frac{\omega}{c} \right)^2 \mathbf{H}(\mathbf{r}), \tag{1.5}$$

with c the speed of light in vacuum. This is the starting point for all simulations in the chapters to follow. The electric field corresponding to a solution of eq. (1.5) can be obtained through

$$\mathbf{E}(\mathbf{r}) = \frac{i}{\omega \varepsilon_0 \varepsilon(r)} \nabla \times \mathbf{H}(\mathbf{r}). \tag{1.6}$$

1.1.2 Eigenvalue problem

Equation (1.5) looks like an eigenvalue problem: some operator acting on the magnetic field yields a constant times this same magnetic field. As we will see, the eigendecomposition is a useful tool for finding allowed solutions of a system, and also reveals the similarities between electromagnetism and single-particle quantum mechanics. First, we define an inner product

$$(\mathbf{H}_\mu, \mathbf{H}_\nu) = \int \mathbf{H}_\mu^* \cdot \mathbf{H}_\nu \mathrm{d}r, \tag{1.7}$$

which turns the vector space of $\{\mathbf{H}(\mathbf{r})\}$ – i.e. the set of all functions from $\mathbb{R}^3$ to $\mathbb{C}^3$ – into a Hilbert space. In this space, eq. (1.5) is defined as finding the eigenmodes of the linear operator

$$\hat{\Theta} \bullet \equiv \nabla \times \left(\frac{1}{\varepsilon(\mathbf{r})} \nabla \times \bullet \right). \tag{1.8}$$

This the can be shown [11] to be Hermitian, i.e. $(\hat{\Theta}\mathbf{H}_\mu, \mathbf{H}_\nu) = (\mathbf{H}_\mu, \hat{\Theta}\mathbf{H}_\nu)$, as well as positive semi-definite, which means that all the eigenvalues $(\omega/c)^2$ are real and positive, as needed if ω is to be interpreted as the frequency of light. In addition, two modes $\mathbf{H}_\mu$ and $\mathbf{H}_\nu$ that correspond to frequencies $\omega_\mu \neq \omega_\nu$ are orthogonal, in the sense that $(\mathbf{H}_\mu, \mathbf{H}_\nu) = 0$. Furthermore, if there is a number of degenerate modes at a given frequency, a finite set of those can be chosen such that the elements are all orthogonal to each other, and span the sub-space of solutions at that frequency. Finally, we note that the equation $\hat{\Theta}\mathbf{H}(\mathbf{r}) = (\omega^2/c^2)\mathbf{H}(\mathbf{r})$ is strongly reminiscent of the Schrödinger equation of Quantum Mechanics, $\hat{H}\Psi(\mathbf{r}) = E\Psi(\mathbf{r})$, where the same considerations enumerated here hold and are commonly employed.

1.1.3 Bloch's theorem

For an exhaustive discussion of the theory outlined in this section, we refer the reader to chapters 1, 2, 9, and 10 of [12] and/or chapters 4, 5 and 7 of [13].

If the operator $\hat{\Theta}$ has spatial periodicity such that $\hat{\Theta}(\mathbf{r}) = \hat{\Theta}(\mathbf{r} + \mathbf{R})$ for any $\mathbf{r}$ and some $\mathbf{R}$, then the Bloch theorem can be applied. In particular, the translation operator $\hat{\mathcal{T}}_\mathbf{R}$, which acts as $\hat{\mathcal{T}}_\mathbf{R}\mathbf{H}(\mathbf{r}) = \mathbf{H}(\mathbf{r} + \mathbf{R})$, commutes with the operator $\hat{\Theta}$, and so the two can be diagonalized simultaneously:

$$\hat{\Theta}\mathbf{H} = (\omega^2/c^2)\mathbf{H}; \qquad \hat{\mathcal{T}}_\mathbf{R}\mathbf{H} = c(\mathbf{R})\mathbf{H}. \tag{1.9}$$

In addition, solutions to eq. (1.5) have an extra conserved quantum number, apart from the frequency ω. A short explanation is due: the term 'quantum number' here is used only due to the analogy with quantum mechanics; we are fully in the domain of

classical electromagnetism, but the resulting wave equation is conceptually similar to the single-particle Schrödinger equation. An important difference is that in the latter, only normalized solutions are physical, while in our case arbitrary amplitudes are allowed. However, all symmetry considerations that are standard in quantum mechanics also hold here, and in particular - Bloch's theorem, which is a consequence of the discrete translation symmetry. The theorem states that the eigenvalue of the translation operator in eq. (1.9) can be written as $c(\mathbf{R}) = \exp(i\mathbf{k}\mathbf{R})$, where the *Bloch momentum* $\mathbf{k}$ is a conserved quantity (the quantum number). Alternatively this means that a solution to eq. (1.5) can be written as

$$\mathbf{H}(\mathbf{r}) = \exp(i\mathbf{k}\mathbf{r})\mathbf{u}(\mathbf{r}), \tag{1.10}$$

with $\mathbf{u}(\mathbf{r})$ a function periodic with $\mathbf{R}$. In our discussion to follow, we will not always have periodicity of $\hat{\Theta}$ in all three spatial dimensions; it is thus convenient to re-state the theorem for a single spatial dimension in which periodicity is present. Assume that $\varepsilon(x, y, z) = \varepsilon(x + x_0, y, z)$ for all x and some x_0 (thus enforcing the same periodicity on $\hat{\Theta}$). Then, any solution to eq. (1.5) can be written as a *Bloch state*:

$$\mathbf{H}(x, y, z) = \exp(ik_x x)\mathbf{u}_{k_x}(x, y, z), \tag{1.11}$$

where $\mathbf{u}_{k_x}(x, y, z) = \mathbf{u}_{k_x}(x + x_0, y, z)$. Written in this form, it is easy to extract an important consequence of Bloch's theorem: the system is fully described by values of k_x within a finite region. In particular, assume $-\pi/x_0 < k_x < \pi/x_0$, and $G_x = n_x 2\pi/x_0$, with n_x an integer. Then, any Bloch state of momentum $k_x + G_x$ is given by

$$\mathbf{H}(\mathbf{r}) = \exp(ik_x x)[\exp(iG_x x)\mathbf{u}_{k_x}(\mathbf{r})] = \exp(ik_x x)\tilde{\mathbf{u}}(\mathbf{r}), \tag{1.12}$$

where we used the fact that $\exp(iG_x x)$ is x_0-periodic to absorb it into a new function $\tilde{\mathbf{u}}$ that has the required properties for a Bloch state. The interval $-\pi/x_0 < k_x < \pi/x_0$ is called the Brillouin Zone (BZ) of the crystal.

In dimensions higher than one, a Brillouin zone (a subspace of $\mathbf{k}$-values which is the minimum needed to fully describe the system) can also be defined through the notions of a Bravais lattice and a reciprocal lattice, and of a Wigner-Seitz cell. Any three-dimensional periodicity can be represented in terms of three *primitive vectors* $(\mathbf{a}_1, \mathbf{a}_2, \mathbf{a}_3)$, taken with the smallest possible norm in the three (not necessarily orthogonal) directions in which the structure is periodic. The latter clarification is needed since, if a function is periodic with $\mathbf{a}_i$, it is also periodic with any integer multiple of $\mathbf{a}_i$. In fact, starting from the set $(\mathbf{a}_1, \mathbf{a}_2, \mathbf{a}_3)$, the set of all points at positions $\mathbf{R}$ such that $\mathbf{R} = n_1\mathbf{a}_1 + n_2\mathbf{a}_2 + n_3\mathbf{a}_3$ for integer n_1, n_2, n_3, is called the *Bravais lattice* of the crystal. The importance of this is that the crystal can be fully described by a single, finite *primitive cell* that is repeated in all directions, always centred at a Bravais lattice site. The primitive cell, or the *Wigner-Seitz cell*, is constructed such that it contains
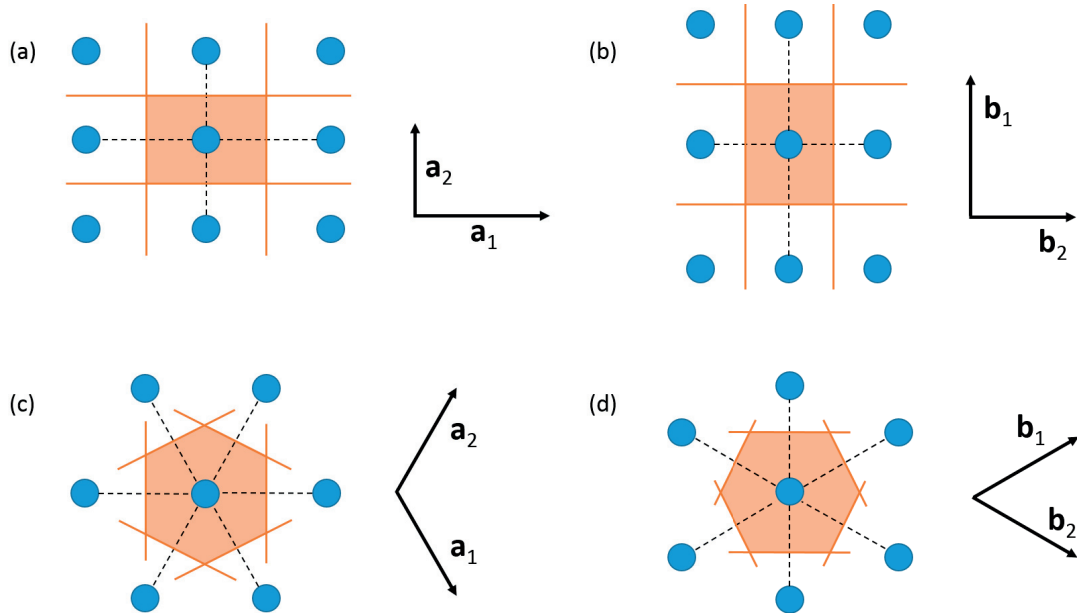
Figure 1.1: Wigner-Seitz cells in two dimensions. Rectangular lattice in (a) – real space, and (b) – reciprocal space. Triangular lattice in (c) – real space and (d) – reciprocal space. The primitive vectors are also shown, and the Wigner-Seitz (or 'primitive') cell is shaded in orange.

only one lattice site and has the smallest volume such that, when repeated, it spans all space. The construction is illustrated in Fig. 1.1(a) and (c), in two dimensions for clarity. Starting from a lattice site, a line is drawn to each of the neighbouring lattice sites; then, a plane orthogonal to each line and passing through its centre is drawn, and the volume enclosed within the crossing planes is the primitive cell. Due to its periodicity, the function $\mathbf{u}(\mathbf{r})$ appearing in eq. (1.10) only needs to be computed within this restricted domain.

The space of crystal momenta $\mathbf{k}$ – which has the same dimensionality as that of the real-space periodicity – is called the *reciprocal space*. We can also define a lattice in this space – the *reciprocal lattice* – with primitive vectors $\mathbf{b}_j$ such that $\mathbf{a}_i \mathbf{b}_j = 2\pi \delta_{ij}$. The Wigner-Seitz cell of the reciprocal lattice, shown in Fig. 1.1(b) and (d) for the 2D lattices of (a) and (d) respectively, is then the Brillouin zone of the crystal, which has the significance mentioned above: the Bloch momentum $\mathbf{k}$ can be restricted to within this region only.

We conclude this section with a few more definitions: the dependence of the frequency of a Bloch state on the momentum, i.e. the function $\omega(\mathbf{k})$, is called the *dispersion relation*. A plot of the dispersion (of all of the allowed states) for $\mathbf{k}$ within the Brillouin zone is called the *band diagram*. A sub-interval of the ω-axis for which no state is supported by the structure for any $\mathbf{k}$ is called a *band gap*. For easier visualization of the band diagram in 2D and 3D, a 1D path in $\mathbf{k}$-space traversing all high-symmetry points
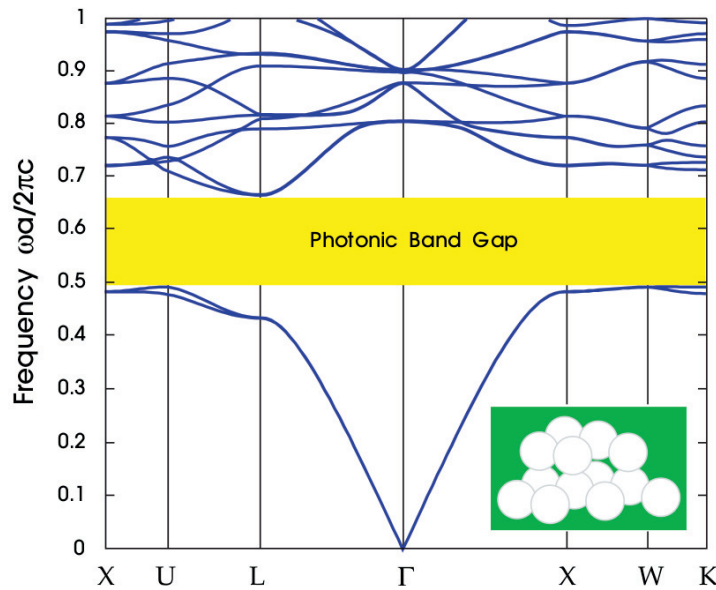
Figure 1.2: Photonic band structure of the diamond lattice of air spheres in a dielectric medium of permittivity $\varepsilon = 13$. Reprinted from [11].

can be chosen such that a band gap appearing in this representation is guaranteed to hold for any other momentum (see [12, 13], and also Fig. 1.2).

1.2 Photonic crystals

1.2.1 In 3 dimensions

Discovering a periodic dielectric medium with a complete, 3D band gap was the main goal of early photonic crystal research. The first theoretical proposal came from Ho and colleagues [14] in 1990, who simulated the band diagram of a structure composed of a diamond lattice of air spheres embedded in a dielectric material. As shown in Fig. 1.2, a wide band gap is opened for a relative permittivity $\varepsilon = 13$ of the dielectric, which is a value similar to the one of some commonly used semiconductors, like Silicon (Si) or Gallium Arsenide (GaAs). Unfortunately, despite 25 years of improvement of our nanofabrication techniques, such a structure with a band gap centred in the visible or the Near Infra-red (NIR) spectrum remains outside the domain of what is experimentally feasible.

To fit within the boundaries imposed by fabrication technologies, in 1991 Yablonovitch et al. [7] proposed a clever design that resulted in the first experimentally measured photonic band gap. The material, now dubbed 'Yablonovite', is made starting from a dielectric slab, in which cylindrical holes at three different angles are drilled in a
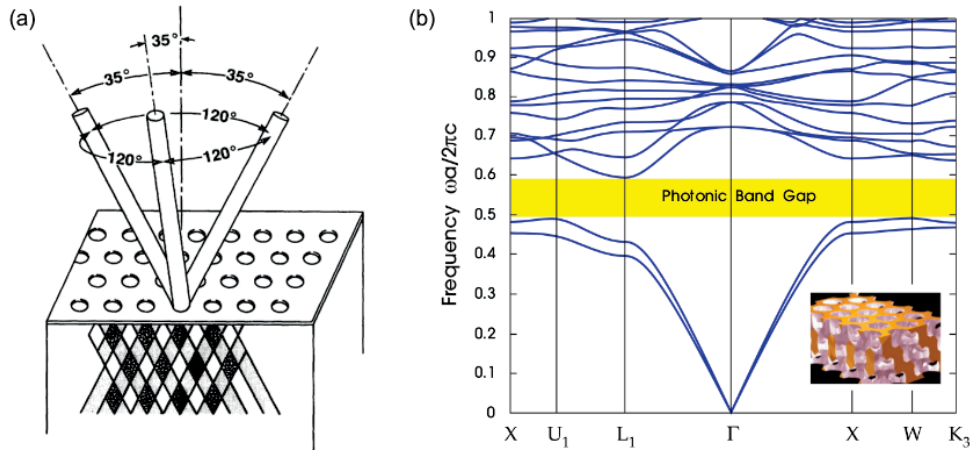
Figure 1.3: (a): The fabrication proposed by Yablonovitch and colleagues; image reprinted from the original paper [7]. (b): Photonic band structure of the material, reprinted from [11].

periodic manner as shown in Fig. 1.3(a). This results in a 3D structure that can be thought of as a face-centered cubic lattice of non-circular air 'atoms'. The structure presents an omni-dicrectional band gap (Fig. 1.3(b)), which was also observed in experiment [7].

A number of other 3D photonic crystal implementations have since been realized in practice. These include (but are not limited to) self-assembled colloidal or 'inverse opal' crystals [15–18], woodpile [8,9,19,20] and inverse woodpile [9,21,22] crystals, and stacked 2D crystals [23, 24]. These all represent important conceptual developments that have extremely high potential for applications due to their 3D band gaps. Thus far, however, they all share the same disadvantage of being challenging to fabricate, in particular in a manner that is scalable and easy to integrate in existing technologies. For this reason, the class of PhCs that is currently most widely investigated in view of applications is that of photonic crystal slabs, which we introduce in the subsequent Section (1.2.2).

1.2.2 In dielectric slabs

The idea of slab-PhCs is based on the fact that a planar layer (i.e. a 'slab') of a dielectric material can confine light due to total internal reflection, as illustrated in Fig. 1.4(a). In the Figure, we label by d the thickness of the slab, and by ε its dielectric permittivity, which is related to another commonly used material constant, the *refractive index* n, through $\varepsilon = n^2$. In this system, the solutions of eq. (1.5) can be characterized by their in-plane momentum $\mathbf{k}_{||}$, which is a conserved quantity due to the continuous 2D translation symmetry. The energy spectrum of modes supported by the slab versus this in-plane momentum is plotted in panel (b). For a given $k_{||}$ (notice we only consider

11
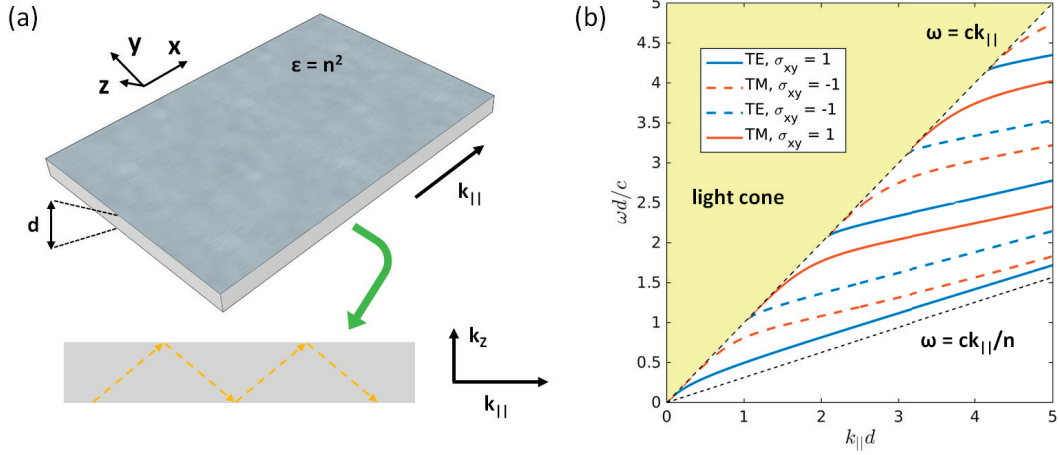
Figure 1.4: (a): A dielectric slab of thickness d and permittivity ε acts as a planar waveguide due to total internal reflection. (b): Dispersion with respect to the in-plane momentum $k_{||}$. Discrete, guided solutions exist in the region between $\omega = ck_{||}$ and $\omega = ck_{||}/n$, while a continuum of solutions exists in the 'light cone' above $\omega = ck_{||}$, where k_z is real and the modes are not confined inside the slab.

the magnitude of the vector $\mathbf{k}_{||}$ since the system is isotropic), there is a solution at any frequency ω larger than $ck_{||}$. This region of the dispersion diagram is called the *light cone*, because the corresponding modes are not truly confined inside the slab, but are instead propagating above or below it, with a momentum in the vertical direction given by $k_z = \sqrt{\omega^2/c^2 - k_{||}^2}$. In contrast, below the *light line* $\omega = ck_{||}$, only a discrete number of modes is allowed, and those are truly guided inside the slab, in the sense that they are exponentially decaying (evanescent) above and below it (the formula for k_z still holds, but it yields an imaginary value whose magnitude is the exponential decay length). In the asymptotic limit $k_{||} \to \infty$, all the discrete guided bands tend to $\omega = ck_{||}/n$. Below that line, no solutions are permitted.

The modes in 1.4(b) are classified based on their parity with respect to reflection in the xy-plane, as well as with their being Transverse Electric (TE) or Transverse Magnetic (TM) [25]. There is a bit of confusion that may arise here, so we discuss the underlying symmetries in more detail. In general, if the operator $\hat{\Theta}$ is invariant under a transformation $\hat{O}$, i.e. if $\hat{O}^{-1}\hat{\Theta}\hat{O} = \hat{\Theta}$, then $\hat{O}$ is called a symmetry of the system, and the eigenvectors of $\hat{\Theta}$ are also eigenvectors of $\hat{O}$, and can be classified by their corresponding eigenvalue. This argument was already used to introduce the momentum $\mathbf{k}$, which is a conserved quantity due to the translational symmetry. Now we look at the specific case where $\hat{O}$ represents mirror reflection with respect to a plane. This operation is unitary (reflecting twice brings back the initial state), and so the possible eigenvalues are ± 1. A small technicality worth noting is that under reflections, the electric field transforms as a vector, $\hat{O}(\mathbf{E}(\mathbf{r})) = (\hat{O}\mathbf{E})(\hat{O}^{-1}\mathbf{r})$, while the magnetic
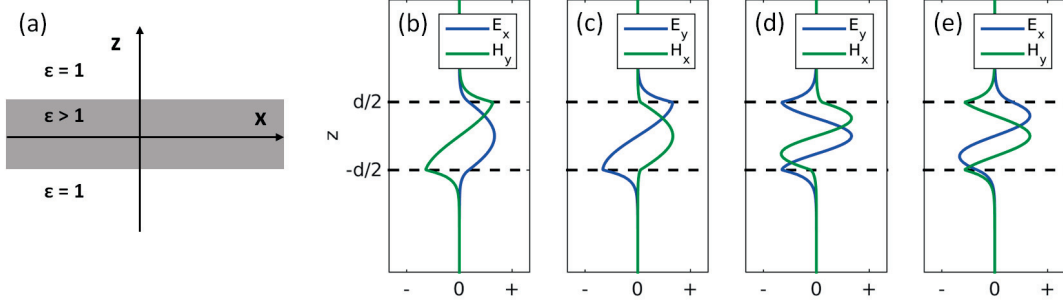
Figure 1.5: (a): Cross-section of a dielectric slab as in Fig. 1.4(a). (b)-(e): Spatial dependence in the z-direction of the in-plane electric and magnetic field components for the four possible guided band symmetries (Fig. 1.4(b)), assuming a wave-vector $\mathbf{k}_\parallel$ in the y-direction (orthogonal to x and z in panel (a)). (b): $\sigma_{xy} = 1$, TE ($\sigma_{yz} = -1$); (c): $\sigma_{xy} = -1$, TM ($\sigma_{yz} = 1$); (d): $\sigma_{xy} = 1$, TM ($\sigma_{yz} = 1$); (e): $\sigma_{xy} = -1$, TE ($\sigma_{yz} = -1$).

field transforms as a pseudo-vector: $\hat{O}(\mathbf{H}(\mathbf{r})) = -(\hat{O}\mathbf{H})(\hat{O}^{-1}\mathbf{r})$ (see e.g. Chapter 6 of [26]). Nevertheless, if $\sigma = \pm 1$ is the eigenvalue of a particular eigenstate, it has a global meaning in the sense that $\hat{O}(\mathbf{H}(\mathbf{r})) = \sigma\mathbf{H}(\mathbf{r})$, $\hat{O}(\mathbf{E}(\mathbf{r})) = \sigma\mathbf{E}(\mathbf{r})$. Now, let $E_\perp$ and $\mathbf{E}_\parallel$ denote the electric field components that are respectively perpendicular and parallel to the reflection plane, and same with $H_\perp$ and $\mathbf{H}_\parallel$ for the magnetic field. It is then straightforward to see that for $\sigma = 1$ modes, both $E_\perp$ and $\mathbf{H}_\parallel$ must vanish on the plane, and, similarly, for $\sigma = -1$ modes, both $H_\perp$ and $\mathbf{E}_\parallel$ must vanish on the plane.

In the case of a two-dimensional system (e.g. with no z-dependence of ε, $\mathbf{E}$, $\mathbf{H}$), there is a symmetry with respect to reflection in the xy-plane (we denote the reflection operator $\hat{\sigma}_{xy}$). Thus, the modes can be classified through their parity, and the ones with $\sigma_{xy} = 1$ have zero electric field in the z direction, while the ones with $\sigma_{xy} = -1$ have a vanishing H_z component. The former case corresponds to electric field *transverse* to the reflection plane and so the modes are often called TE, while in the latter case the magnetic field is transverse, hence the label TM. In the case of the slab geometry, however, the σ_{xy} and the TE/TM classifications no longer match. In particular, in this 3D system, the reflection in the xy-plane is only a symmetry for the plane at $z = 0$ (the one bisecting the slab, see Fig. 1.5(a)), and so it is only in that plane that E_z or H_z must vanish; they can be non-zero at any point which is not in the center of the slab. On the other hand, there is another reflection symmetry in the system – with respect to the $\mathbf{k}_\parallel z$ plane for a mode of in-plane momentum $\mathbf{k}_\parallel$. Assuming without loss of generality that this momentum is along y (Fig 1.5(a)), we see that modes with $\sigma_{yz} = 1$ have zero H_y and H_z **everywhere**. The only non-zero component is H_x, and such modes can thus be appropriately called TM. It must be kept in mind, however, that the **E**-field can **also** have an in-plane component (E_x vanishes, but not E_y). Similarly, modes with $\sigma_{yz} = -1$ can only have an electric field along x and are thus TE, even though, again, H_y is not necessarily zero. In Fig. 1.4(b), modes of eigenvalue $+1$ of the reflection operator $\hat{\sigma}_{xy}$

13
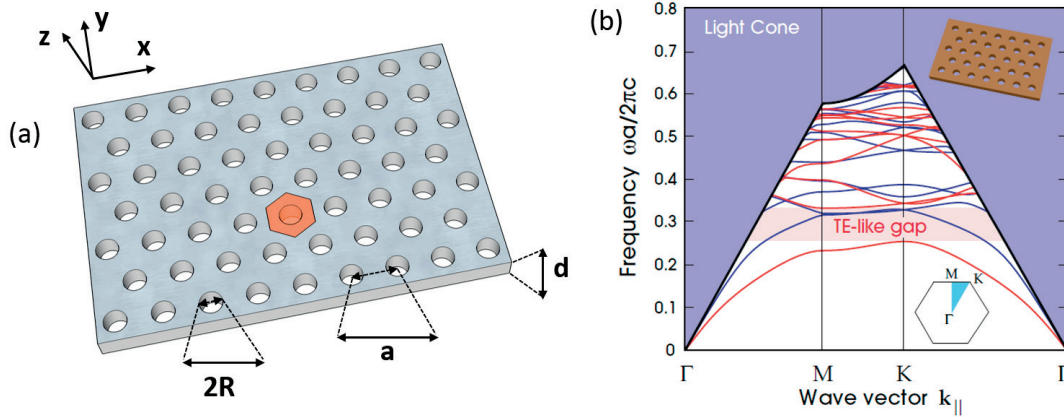
Figure 1.6: (a): Example of a photonic crystal slab consisting of a hexagonal lattice of pitch a of circular air-holes of radius R in a slab of some dielectric material of thickness d. The 2D primitive cell of the crystal is highlighted in orange. (b) (Reprinted from [11]): band diagram for in-plane propagating modes. Red lines show $\sigma_{xy} = +1$ modes, while blue lines: $\sigma_{xy} = -1$.

are plotted with solid lines, while modes of eigenvalue -1 are plotted with dashed lines. In addition, TE modes are plotted in blue, while TM modes are plotted in red.

To further illustrate the important distinction between the two classifications, in Fig. 1.5(b)-(e) we show the z-dependence of the magnetic and electric field components in the plane of the slab, for the four possible combinations of symmetry eigenvalues. The TE/TM classification now comes from the σ_{yz} symmetry (assuming $\mathbf{k}_\parallel$ along y), and not from the σ_{xy} one. Panels (d) and (e) are of particular interest, since they illustrate the two cases which are not possible in a 2D geometry: $\sigma_{xy} = 1$, TM, and $\sigma_{xy} = -1$, TE. Generally, TE modes have zero E_z everywhere, while $\sigma_{xy} = 1$ modes have zero E_z on the $z = 0$ plane; the analogous holds true for TM, $\sigma_{xy} = -1$, and H_z.

Based on the discrete, confined modes of the slab, we can introduce a 2D-periodic modulation of the permittivity $\varepsilon(\boldsymbol{\rho})$, where $\boldsymbol{\rho} = (x, y)$, with the aim of creating a band gap, in the spirit of our discussion of Bloch states in section 1.1.3. The presence of the light cone – the region where total internal reflection 'fails' – means that it is not possible to have a complete band gap, but as we will see throughout this thesis, even a partial one is sufficient for a wide variety of applications. An example of such a *photonic crystal slab* is shown in Fig. 1.6(a), where air-holes of radius R are made in the dielectric in a periodic fashion. In this example, the holes form a 2D triangular lattice, and we call the separation between nearest-neighbor holes the *lattice pitch* or *lattice constant*, labelled by a in the Figure. The in-plane band diagram for this structure is shown in panel (b), where Γ, M and K on the x-axis refer to the high-symmetry points of the 2D Brillouin zone shown as an inset to the Figure. Notice that the frequency is inversely proportional to a, which highlights an important feature of PhCs in general:

their properties are spectrally tunable through a re-scaling of all lengths. This is why, throughout this thesis, quantities will often be given in units of a and a/c, with c the speed of light in vacuum.

Another important clarification about the symmetry is due. In a slab-PhC, the $\hat{\sigma}_{xy}$ symmetry is preserved, while the TE/TM one is generally broken by the lattice of holes. Thus, in Fig. 1.6(b), the modes are classified only with respect to their σ_{xy} eigenvalue: modes in red have $\sigma_{xy} = 1$, while modes in blue have $\sigma_{xy} = -1$. However, the TE/TM analogy is often carried over especially for the low-energy modes, which are commonly called *quasi-TE* or *TE-like* for $\sigma_{xy} = 1$, and *quasi-TM* or *TM-like* for $\sigma_{xy} = -1$. This classification is not rigorous but still commonplace, as it is valid in the limit of very low frequencies. Indeed, in Fig. 1.4(b) we see that the two lowest bands of the slab are $\sigma_{xy} = 1$, TE, and $\sigma_{xy} = -1$, TM, respectively. It is however important to keep in mind that for higher energies – or for thicker slabs – the TE/TM notation becomes inappropriate in a slab-PhC, while the σ_{xy} classification still holds.

In a PhC slab as in Fig. 1.6(a), a partial band gap is opened for the positive-symmetry ($\sigma_{xy} = 1$) modes (Fig. 1.6(b)), which is sufficient for many applications. Because of that, the hexagonal lattice of circular holes has become ubiquitous in slab-PhCs, and is the basic structure underlying all of the devices presented in this thesis.

1.3 Building blocks for applications

The potential applications of slab-PhCs are multifold, beginning with improving the quality of telecommunication devices for example through novel laser technologies [27–33] and all-optical computational paradigms (both optical switching [34] and optical RAM memory [35, 36] have already been experimentally demonstrated). They can also be used for biochemical sensing in lab-on-chip devices [37–40]. In the quantum domain, PhC slabs can be employed for non-classical light generation [41–46], cavity quantum electrodynamics experiments [47–49] and, ultimately, quantum computation paradigms [50]. There are two functional elements that are ubiquitous for all these applications: *waveguides*, in which light propagates in a controlled manner, and *cavities*, in which light stays confined for a certain amount of time.

It is well-known that defects in the crystal structure of a band-gap material introduce states with energies inside the band gap, which are localized in the region of the defects (see e.g. Chapter 19 of [12] and Chapter 30 of [13]). In the case of photonic crystals, the underlying lattice is nano-fabricated, which yields a great amount of control, including the possibility to deliberately introduce lattice 'defects', which in fact become functional elements. Below we review how, based on that principle, waveguides and cavities can be fabricated in the PhC-slab platform.
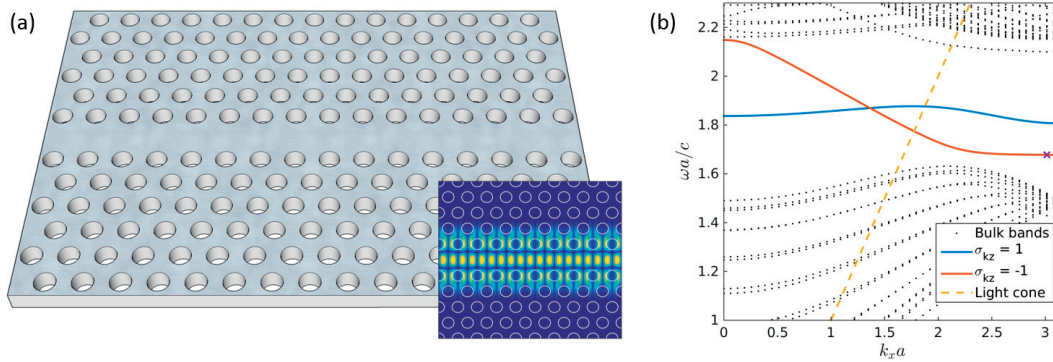
Figure 1.7: (a): Example of a photonic crystal waveguide consisting of a row of missing holes in a slab-PhC as the one illustrated in Fig. 1.6(a). (b): Dispersion of modes with a k–vector in the direction of the missing row of holes. The modes marked in black are delocalized along the entire PhC, while the two bands marked in red and blue consist of modes 'guided' within the missing-hole region. The electric field amplitude of the mode marked by a cross is shown in the inset to panel (a).

1.3.1 Waveguides

Starting from a PhC with a (partial) band gap as the one of Fig. 1.6(a), guiding of light can be achieved through a one-dimensional 'defect' in the lattice of holes. An example is illustrated in Fig. 1.7(a) in the form of a PhC with a row of 'missing' holes. The structure now has only 1D-periodicity – along the direction of the missing row. The band diagram for modes of momentum pointing in this direction (and with $\sigma_{xy} = 1$) is illustrated in Fig. 1.7(b); two 'guided' bands (marked blue and red) appear in the spectral region where the band gap of the underlying 2D-PhC lies. Modes in those bands are localized close to the defect region, as illustrated in the inset of panel (a). The two bands have opposite parity with respect to reflection in the kz-plane bisecting the defect; the symmetry eigenvalue is given in the legend of panel (b). In that panel, the boundary of the light cone of the structure is also shown. Importantly, modes above that line propagate within the defect region but also in the direction orthogonal to the slab and are thus *leaky* or *lossy*, while the modes below that line are fully confined within the slab, and thus truly guided.

Photonic crystal waveguides are of particular interest in terms of *slow-light* propagation. 'Slowing down' light is one of the possible ways to increase the optical non-linearities arising from the light-matter interaction. This is desirable for a variety of applications [51, 52]. Slow light can be used, for example, for non-linear frequency conversion for classical [53–55] and quantum [45, 46, 56] applications, in buffers for optical memories (both for classical and quantum bits) [57, 58], and for radiative coupling between distant quantum dots for solid-state quantum computation [50, 59, 60]. The speed of light can be modified through the material dispersion, since the group

velocity (the velocity of energy transport) is given by $v_g = \mathrm{d}\omega/\mathrm{d}k$, for a dispersion relation $\omega(k)$. Close to band-edge resonances in periodic photonic structures, this can then be made arbitrarily small in theory, since at the high-symmetry points, the derivative of the dispersion vanishes. Guided modes close to the $k_x a = \pi$ point in Fig. 1.7(b)) thus have exceptional qualities: on one hand, they are below the light line, thus *lossless*. On the other, the *group index* $n_g = c/v_g$, which is the most important figure of merit for slow light, is arbitrarily large.

In practice, these exceptional features of PhC waveguides are somewhat limited due to the inevitable imperfections resulting from the fabrication process. The phenomenology of light transport in (*disordered*) waveguides is very similar to the one of electron transport in a conducting medium, and analogous vocabulary is often used. For example, disorder can be thought of as introducing scattering events, with an associated mean scattering length L_s. For any given waveguide length L_w we can then distinguish the regime of *ballistic propagation*, when the magnitude of the imperfections is sufficiently low, so that $L_s > L_w$. In that regime it is meaningful to talk about transport, and the group index n_g is well-defined. With increasing disorder, the transmission at the end of the device drops as light is scattered more and more strongly in non-guided modes, or modes guided in the opposite direction. In this high-disorder limit, Anderson localization of light is predicted and observed [1, 61–65], meaning that the eigenmodes of the system become localized along a finite length of the device, given by a characteristic *decay length* L_l. Within this regime, the group index n_g is no longer meaningful, since the dispersion is degraded and in fact the Bloch momentum is no longer a conserved quantity. Instead, the eigenmodes have multiple $\mathbf{k}$-components that yield the spatial localization. The resulting sharp drop in transmission is sometimes referred to as *back-scattering*, but we note that the Anderson-localization analogy paints a more comprehensive picture of the effect.

The mean scattering length as well as the averaged decay length depend not only on the disorder magnitude, but also on n_g, and decrease with increasing group index. As mentioned above, n_g goes to infinity at the $k_x a = \pi$ point of the PhC waveguide dispersion, but, in a real device, disorder limits the maximum group index for which we can meaningfully talk about energy transport. In addition, the imperfections also introduce scattering to modes inside the light cone (radiating outside of the slab), which makes **all** modes lossy. These effects are often the determining factor for the quality of state-of-the-art PhC devices, and are discussed in detail in Chapters 3 and 5 of this thesis. To conclude our discussion here, it is anyway worth noting that in PhC waveguides similar to the one of Fig. 1.7, exceptionally high values of $n_g \approx 100$ have already been measured [66]. In other words, the propagation of light could be slowed down by a factor of 100 as compared to propagation in vacuum simply by using a properly designed piece of a dielectric, which is indeed a remarkable result.
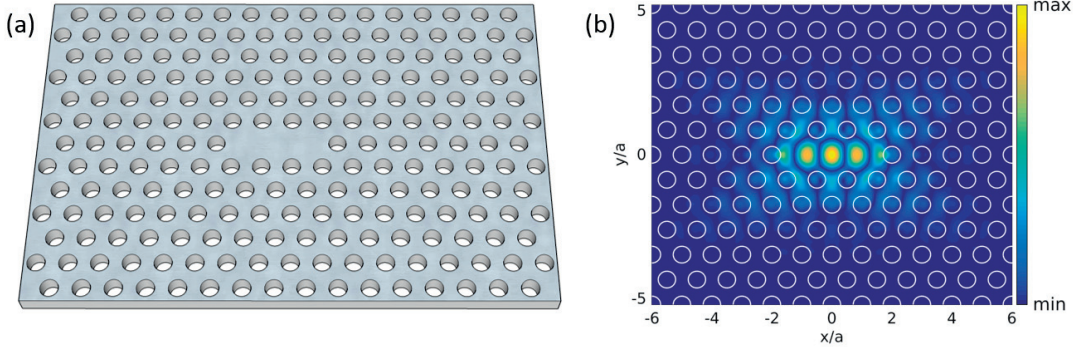
Figure 1.8: (a): Example of a photonic crystal cavity consisting of three missing holes in a PhC slab. (b): Magnitude of the y-component of the electric field $|E_y|$ of the fundamental mode of the cavity.

1.3.2 Cavities

By introducing a localized defect (aka a *point defect* or a *0D defect*), an optical cavity, also called an optical *resonator*, can be made in the slab-PhC. This is illustrated in Fig. 1.8, where the cavity is made by three missing holes in the lattice. In panel (b), we plot the electric field profile in the xy-plane bisecting the slab, for the mode with the lowest energy inside the photonic band gap (the *fundamental* mode). As can be seen, the electric field is fully confined within the defect region. This is analogous to placing two mirrors opposite each other: light in the intermediate region oscillates between the mirrors, but stays confined in a finite space. Here, the 'reflection' is due to the photonic band gap, and the light is confined in an impressively small region of space.

An optical cavity has no translational symmetry and thus the momentum k is not a conserved quantity. Unlike the structures we considered so far, where we always had continuous dispersion, the modes of a cavity are *discrete*, i.e. they have a certain well-defined *resonance frequency*. In addition, light confined in the cavity only stays there a finite amount of time (the cavity is inevitably lossy). Calling the resonant frequency ω_0 and the lifetime τ, the electric field of a cavity mode evolves in time as

$$\mathbf{E}_c(\mathbf{r}, t) = \mathbf{E}_0(\mathbf{r})e^{-i\omega_0 t - t/\tau}, \tag{1.13}$$

i.e. the phase of the electric field rotates with a frequency ω_0, while the field amplitude $|\mathbf{E}_c|$ decays with a half-life τ (it decreases by a factor of $1/e$ after time τ). One can also define the *loss rate* $\kappa = 2/\tau$, which has the units of frequency, as well as the complex frequency $\omega_c = \omega_0 - i\kappa/2$, so that the electric field evolution is simply given by

$$\mathbf{E}_c(\mathbf{r}, t) = \mathbf{E}_0(\mathbf{r})e^{-i\omega_c t}. \tag{1.14}$$

This particular definition of κ is commonly chosen, since the *intensity* of the electric

field $|\mathbf{E}_c|^2$ is what is actually measured in experiments, and this decays with a lifetime of $\tau/2$ – thus κ represents the physically observable loss rate. In some texts, however, the decay rate is defined as simply $1/\tau$, so caution is advised. With our definition of ω_c, the Fourier transform in time of the electric field has a square amplitude given by a *Lorentzian distribution*,

$$\mathcal{F}(\omega) \propto \frac{\kappa/2}{(\omega - \omega_0)^2 + (\kappa/2)^2}. \tag{1.15}$$

Experimentally, this is proportional to the measured spectrum of the light emitted from the cavity, thus κ also has the meaning of the Full Width at Half Maximum (FWHM) of a measured spectral peak.

We can also define the dimensionless quantity $Q = \omega_0/\kappa$ to describe the losses of the cavity. This widely used parameter is known as the *quality factor*. It has a straightforward physical interpretation as the number of oscillations of the electric field inside the cavity before its amplitude decays by a certain factor ($e^{-\pi}$). In addition, Q is related to the power P of the radiative losses and the energy U stored in the cavity through

$$Q = \frac{\omega_0 U}{P}. \tag{1.16}$$

As the name suggests, there is a fair amount of correlation between the Q of a cavity and its quality in terms of practical applications. This is why in Chapter 4 significant attention is directed towards maximizing the Q of various cavity designs.

Another important figure of merit of a cavity is the *effective mode volume*. This quantifies the degree of electric field confinement, and can in some cases differ significantly from the physical size of the cavity. There are actually several different definitions of the mode volume stemming from different practical considerations. One of the most common of those is derived with respect to the Purcell enhancement of the emission of a point emitter placed in the maximum of the electric field of the cavity mode [67, 68], and reads:

$$V_1 = \frac{\int \varepsilon(\boldsymbol{r})|\boldsymbol{E}(\boldsymbol{r})|^2 \mathrm{d}\mathbf{r}}{\max \left[\varepsilon(\boldsymbol{r})|\boldsymbol{E}(\boldsymbol{r})|^2\right]}, \tag{1.17}$$

where the integration is over all space. Other definitions are better suited for discussing effects stemming from the non-linear light-matter interaction in the dielectric (i.e. from the susceptibility χ, see eq. (1.2)) [69, 70]. The mode volume relevant to the Kerr effect or to two-photon absorption is

$$V_2 = \frac{(\int \varepsilon(\boldsymbol{r})|\boldsymbol{E}(\boldsymbol{r})|^2 \mathrm{d}\mathbf{r})^2}{\int (\varepsilon(\boldsymbol{r})|\boldsymbol{E}(\boldsymbol{r})|^2)^2 \mathrm{d}\mathbf{r}}. \tag{1.18}$$

This definition is reminiscent of the Inverse Participation Number (IPN) in Quantum

Mechanics, and is thus also useful when studying Anderson localization of light [1, 61–63]. For other non-linear effects, like free-carrier absorption and dispersion, yet another definition is appropriate:

$$V_3 = \frac{(\int \varepsilon(\boldsymbol{r})|\boldsymbol{E}(\boldsymbol{r})|^2 \mathrm{d}\mathbf{r})^3}{\int (\varepsilon(\boldsymbol{r})|\boldsymbol{E}(\boldsymbol{r})|^2)^3 \mathrm{d}\mathbf{r}}. \tag{1.19}$$

There are numerous possible applications of cavities in the field of non-linear optics, each with its own, sometimes complicated, dependence on the cavity quality factor and mode volume. The figures of merit, however, typically increase with Q and decrease with V. We give a few examples: the Purcell enhancement factor is proportional to Q/V_1, while the cavity-emitter coupling coefficient for cavity Quantum Electrodynamics (QED) is proportional to $Q/\sqrt{V_1}$ [68]. Furthermore, the refractive index change due to the accumulation of electromagnetic energy in the cavity is (roughly) proportional to Q/V_2 in the case of the Kerr effect, and to $(Q/V_3)^2$ in the case of free-carrier dispersion [69, 70]. This refractive index change (as well as the cavity-emitter coupling in cavity-QED) can be used for example for optical switching.

Photonic crystal cavities typically have the smallest mode volumes (regardless of the definition) when compared to any other cavities in a dielectric material. In fact, the values are often of the order of $(\lambda/n)^3$, with λ the resonant wavelength and n the refractive index, which is the *diffraction limit* imposed by the wave nature of light. This, together with the possibility for very high Q-values that we will demonstrate in this thesis makes them attractive as functional elements for a variety of applications.

2 Numerical Simulation of Photonic Crystals

In this Chapter we describe the numerical tools that were used in this thesis for the simulation of PhC structures. In Section 2.1, we give a general outline of the Finite-difference Time-domain (FDTD) method, which is a numerical integration of Maxwell's equations over a discretized mesh in space and time. This method is sometimes expensive in terms of computational time, but provides a *first-principle* solution that is useful for validating the results of the mode-expansion methods that are presented in the subsequent Sections and used throughout this thesis. The Plane-wave Expansion (PWE), which is very robust and can be applied to any periodic structure, is outlined in Section 2.2. Another method based on a similar idea – the Guided-mode Expansion (GME) – is presented in Section 2.3. The application of this method is restricted to PhC slabs only, but it has a significant advantage in the required computational time, and is thus the method of choice for most of the simulations in the subsequent Chapters. Because of that, we also discuss some practical aspects like convergence versus relevant computational parameters. In Section 2.4, we present yet another related method, the Bloch-mode Expansion (BME), which is particularly useful for analyzing disorder effects in 1D-periodic structures.

2.1 Finite-difference time-domain

The most conceptually straightforward way to solve any differential equation is by approximating space and time by a discrete uniform grid, and derivatives by e.g.

$$\frac{\partial f}{\partial x}(x_n) \approx \frac{f(x_{n+1}) - f(x_{n-1})}{2\Delta x}, \tag{2.1}$$

with $f(x)$ some function, x_n the discrete points in space and Δx the grid spacing. Time derivatives can be approximated in an analogous way. Computational methods employing this idea are generally called *finite-difference*, for obvious reasons. The finite-difference time-domain method for solving Maxwell's equations then simply

consists in evolving Maxwell's equations (1.1) in time, using a discrete mesh in both space and time, and starting with some (usually time-dependent) current source $\mathbf{J}(t)$. Both static and dynamic properties of a structure can then be inferred from the simulated electric and magnetic field evolution.

Of course, there are numerous technicalities when it comes to stability and convergence of the simulation [71]. The mesh in space has to be sufficiently fine to capture the features of the system. For stability, the step in time Δt has to decrease proportionally to the spatial step Δx, thus the computational time for a 3D structure typically scales with the fourth power of the linear resolution. Furthermore, for faster convergence it is better to compute the electric and magnetic fields at slightly different positions within a grid cell, using the so-called *Yee grid* [72]. The propagation in time can also benefit from a similar trick, and the electric and magnetic fields are usually computed at half-steps, e.g. the $\mathbf{E}$-field at time t is computed through the $\mathbf{E}$-field at time $t - \Delta t$ and the $\mathbf{H}$-field at time $t - \Delta t/2$. Eigenmodes of a system appear as resonances in the Fourier transform of the time-dependent fields taken after the current sources $\mathbf{J}(t)$ have decayed. The quality factor of localized modes can also be computed if an exponential decay of the fields with time can be extrapolated (cf. eq. (1.13)).

For a comprehensive presentation of the method and all the associated technicalities, the reader is referred to e.g. Ref. [71]. There are several sophisticated FDTD solvers which are publicly available for free (e.g. MEEP [73]) or commercially (e.g. Lumerical solutions [74]). Here, we use those as black-box solvers, mostly for verifying the results of the GME and BME methods presented below. While very powerful and usually robust, one major disadvantage of the FDTD method is that the computational time needed to obtain the quality factor of a cavity mode increases with increasing Q, since the simulation has to be evolved longer in time for the decay constant to be reliably extracted. This requires simulation times of the order of ten hours or more on a modern CPU for ultra-high-Q cavities ($Q > 10^6$), which hinders the possibility for exploration of new cavity designs. This challenge can be tackled using some of the methods presented below.

2.2 Plane-wave expansion

The PWE is essentially a Fourier series expansion. For a periodic structure with reciprocal lattice vectors $\mathbf{G}$, we can expand a solution of eq. (1.5) of Bloch momentum $\mathbf{k}$ as

$$\mathbf{H_k}(\mathbf{r}) = \sum_{\mathbf{G}} \mathbf{c_k}(\mathbf{G}) e^{i\mathbf{G}\mathbf{r}}. \tag{2.2}$$

The viability of this expansion is guaranteed by the fact that the *plane-wave* functions $e^{i\mathbf{G}\mathbf{r}}$ span the Hilbert space of complex-valued, periodic functions over $\mathbb{R}^3$ (i.e. they
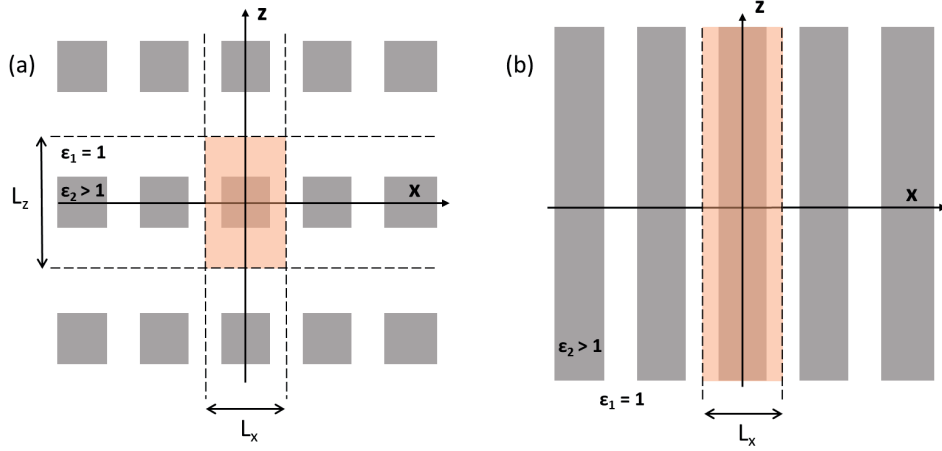
Figure 2.1: (a): The modes of a photonic crystal slab as in Fig. 1.6(a) can be simulated with 3D-PWE. The slab is in the plane orthogonal to the z-axis. The computational cell for a simulation is marked in orange. In the vertical, z-direction, a 'stack' of slabs is effectively simulated, with L_z increased until convergence is reached. (b): Cross-section for a 2D-PWE simulation; the geometry has no z-dependence. The computational cell is again highlighted in orange. The slab thickness has to be taken into account through a properly chosen effective permittivity ε_2.

form an orthonormal basis). Equation (1.5) then becomes an eigenvalue problem with the expansion coefficients as eigenvectors:

$$\sum_{\mathbf{G}} -\varepsilon^{-1}(\mathbf{G} - \mathbf{G}') \cdot \left((\mathbf{k} + \mathbf{G}) \times (\mathbf{k} + \mathbf{G}')\right) \times \mathbf{c_k}(\mathbf{G}) = \frac{\omega_{\mathbf{k}}^2}{c^2} \mathbf{c_k}(\mathbf{G}'), \qquad (2.3)$$

where $\varepsilon^{-1}(\mathbf{G})$ is the Fourier transform of $1/\varepsilon(\mathbf{r})$,

$$\varepsilon^{-1}(\mathbf{G} - \mathbf{G}') = \frac{1}{V} \int_V \frac{1}{\varepsilon(\mathbf{r})} e^{-i(\mathbf{G} - \mathbf{G}')\mathbf{r}} \mathrm{d}\mathbf{r}, \qquad (2.4)$$

with V the volume of the primitive cell. Eq. (2.3) is a system of an infinite number of linear equations. This can in practice be solved by restricting the $\mathbf{G}$-vectors to a finite number, usually the ones with the lowest magnitude up to a certain cut-off $G_{\max}$. This is analogous to discarding (very) high-frequency terms in a Fourier expansion. Solving eq. (2.3) then amounts to diagonalizing an $n_G \times n_G$ matrix, where n_G is the number of $\mathbf{G}$-vectors kept in the expansion.

The PWE is a very robust method and is an invaluable tool in particular for the simulation of 3D PhCs. By construction, the method assumes Periodic Boundary Conditions (PBC) and is thus best-suited for regular crystals, but it can equally well be applied to structures with no periodicity in one or more dimensions, as long as the modes of interest are localized in the non-periodic directions. The way 3D-PWE can be applied

to slab-PhCs, which are periodic in 2D only, is illustrated in Fig. 2.1(a). A computational cell (marked in orange in the Figure) of some finite length L_z in the orthogonal, z-direction can be defined, such that the effective structure consists of infinitely many slabs stacked at a distance L_z from one another. This then allows us to define the G_z component of the lattice vectors, which goes in integer steps of $2\pi/L_z$. The exact PhC modes confined in and close to the slab are obtained in the limit of L_z going to infinity; in practice, this parameter can be increased until convergence is reached. This method can be used to compute the PhC dispersion, but also has the extra feature that losses due to light emission in the direction orthogonal to the slab can be directly computed by summing over all components with a non-zero G_z.

There is a subtle trick associated with the PWE and in particular with the Fourier transform of eq. (2.4), related to the fact that the permittivity presents sharp discontinuities at the material boundaries. Namely, faster convergence with $G_{\max}$ is typically reached if the Fourier transform $\varepsilon(\mathbf{G} - \mathbf{G}')$ is computed first, and the inverse ε^{-1} is computed through matrix inversion of the ε-matrix constructed with $\mathbf{G}$ in the columns and $\mathbf{G}'$ in the rows [14, 75]. The computational complexity for this operation is the same as the one for the matrix diagonalization: $\mathcal{O}(n_G^3)$ (when no additional properties of the matrix can be exploited), which is then also the scaling of the PWE with the number of plane waves. For a cubic geometry with a unit cell of size L_x, L_y, and L_z in the three directions, and for a fixed $G_{\max}$, we have $n_G \propto L_x L_y L_z$. If a large L_z is needed for convergence, the computational time could thus become quite sizable.

One way to overcome this for slab-PhCs, which are periodic in 2D only, is to perform a two-dimensional PWE. This means assuming no z-dependence (see Fig. 2.1(b)), or, interpreted differently, an infinitely thick slab. The $\mathbf{G}$-vectors then have just two components, (G_x, G_y). The finite thickness of the slab can be effectively captured through a properly defined permittivity $\bar{\varepsilon}_2$ of the material. This greatly reduces the complexity (which is now just $\mathcal{O}(L_x^3 L_y^3)$), but also comes at a cost. First, the 3D-PWE is theoretically exact in the limit of infinite number of plane waves n_G and infinite L_z; here instead, the effective $\bar{\varepsilon}_2$ is an approximation that can lead to inaccuracies that are hard to predict and estimate. Additionally, there is no way to compute out-of-plane losses, as there is no out-of-plane G_z component.

In Section 2.3, we introduce a method which is particularly suited for the slab geometry and which has the same computational overhead as 2D-PWE, but overcomes its disadvantages.
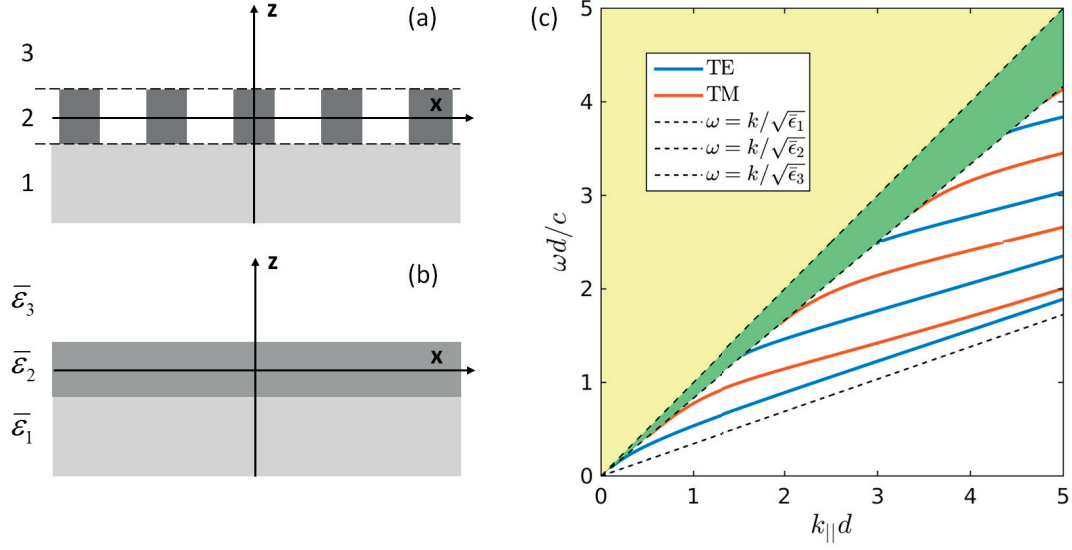
Figure 2.2: (a): Example of a slab-PhC consisting of three layers – 1): lower cladding; 2): the patterned slab; 3): upper cladding. Layers 1 and 3 are semi-infinite, while layer 2 has a thickness d. (b): Effective homogeneous layers for the guided-mode expansion; each has the average permittivity $\bar{\varepsilon}_i$ of the layers in (a). (c): Electromagnetic modes for the structure in (b), which can be classified as TE or TM due to the $\sigma_{k_\parallel z}$ symmetry. In the yellow region, there is a continuum of modes radiating both in the upper and in the lower cladding. In the green region there is again a continuum of modes, which are however radiating only in the lower cladding.

2.3 Guided-mode expansion

2.3.1 Definition of the method

The GME [25] bears a lot of similarity to the PWE: it is again a mode-expansion method, and the basis functions are similar to 2D plane waves, but they are much better suited to the slab geometry. Namely, we expand the PhC-slab modes on the basis of the guided modes of an effective homogeneous slab, i.e. on the basis of modes as the ones shown in Fig. 1.4, and, in a more general setting, in Fig. 2.2. Thus far in this thesis we have only considered slabs suspended in air, but below, following closely Ref. [25], we outline the details of the method for the more general case illustrated in Fig. 2.2(a).

We consider a PhC consisting of three layers, denote the z-direction to be orthogonal to the layers, and call $\boldsymbol{\rho}$ the in-plane vector (x, y) (Fig. 2.2(a)). The dielectric permittivity of the structure can thus be described by three functions $\varepsilon_1(\boldsymbol{\rho})$, $\varepsilon_2(\boldsymbol{\rho})$, $\varepsilon_3(\boldsymbol{\rho})$. We further define the averaged values

$$\bar{\varepsilon}_i = \frac{1}{S} \int_S \varepsilon_i(\boldsymbol{\rho}) \mathrm{d}\boldsymbol{\rho}, \qquad i = 1 \cdots 3, \tag{2.5}$$

where S is the area of the 2D unit cell, and assume $\bar{\varepsilon}_2 > \bar{\varepsilon}_1, \bar{\varepsilon}_3$, so that modes can be localized in the intermediate layer due to total internal reflection. The basis for the GME is then obtained by considering a structure composed of three effective, homogeneous slabs of permittivity $\bar{\varepsilon}_{1..3}$ (Fig. 2.2(b)), whose eigenmodes can be computed analytically and are given in Ref. [25] and shown in Fig. 2.2(c). Notice that in the case $\bar{\varepsilon}_1 \neq \bar{\varepsilon}_3$, the σ_{xy} symmetry is not present, while the TE/TM symmetry is still present for the homogeneous layers (Fig. 2.2(c)), but not for the PhC (see Section 1.2.2).

Next, we index the discrete guided modes, i.e. the modes below both light lines in Fig. 2.2(c), by $\mu = (\mathbf{g}, \alpha)$, with $\mathbf{g}$ the in-plane momentum, and α the band number. We can then expand the Bloch modes of momentum $\mathbf{k}$ of the 2D-periodic PhC on the basis of these guided modes of the effective homogeneous structure:

$$\mathbf{H}_{\mathbf{k}}(\mathbf{r}) = \sum_{\mu} \mathbf{c}_{\mu} \mathbf{H}_{\mu}(\boldsymbol{\rho}, z). \tag{2.6}$$

This basis is not complete, since it does not include the continuum of radiative modes. However, it is a very good starting point for the computation of modes confined in the PhC slab, which are the modes of interest. Coupling to the radiative components can be included in a perturbative fashion as will be shown below. Due to the Bloch theorem, only guided modes of momentum $\mathbf{k} + \mathbf{G}$, with $\mathbf{G}$ a reciprocal lattice vector, can contribute to the above summation. Thus, below we assume $\mu = (\mathbf{g}, \alpha) = (\mathbf{k} + \mathbf{G}, \alpha)$. We also note that the guided modes are orthogonal, i.e. $(\mathbf{H}_{\mu}, \mathbf{H}_{\nu}) = \delta_{\mu\nu}$, with the notation of eq. (1.7), and $\nu = (\mathbf{k} + \mathbf{G}', \alpha')$. Using this and the expansion of eq. (2.6), we obtain once more an eigenvalue problem, which can be written as

$$\sum_{\mathbf{G}', \alpha'} \mathcal{H}_{\mu\nu} c_{\nu} = \frac{\omega_{\mathbf{k}}^2}{c^2} c_{\mu}, \tag{2.7}$$

with the matrix for diagonalization $\mathcal{H}_{\mu\nu}$ given by

$$\mathcal{H}_{\mu\nu} = (\mathbf{H}_{\mu}, \Theta \mathbf{H}_{\nu}), \tag{2.8}$$

which can also be written as

$$\mathcal{H}_{\mu\nu} = \int \frac{1}{\varepsilon(\boldsymbol{\rho})} \left(\nabla \times \mathbf{H}_{\mu}^*(\boldsymbol{\rho}, z) \right) \cdot \left(\nabla \times \mathbf{H}_{\nu}(\boldsymbol{\rho}, z) \right) \mathrm{d}\boldsymbol{\rho} \mathrm{d}z. \tag{2.9}$$

The z-integration in the above expression can be carried out analytically, while the $\boldsymbol{\rho}$-integration introduces, just as in the case of the PWE, the Fourier transform of ε^{-1} as given in eq. (2.4). The final form of the matrix elements $\mathcal{H}_{\mu\nu}$ can be found in Ref. [25].

The GME outlined thus far has the same computational complexity as 2D-PWE, but uses a basis better-suited to the slab geometry. In particular, the slab thickness d enters analytically in the z-integration in eq. (2.9). Another advantage of the method
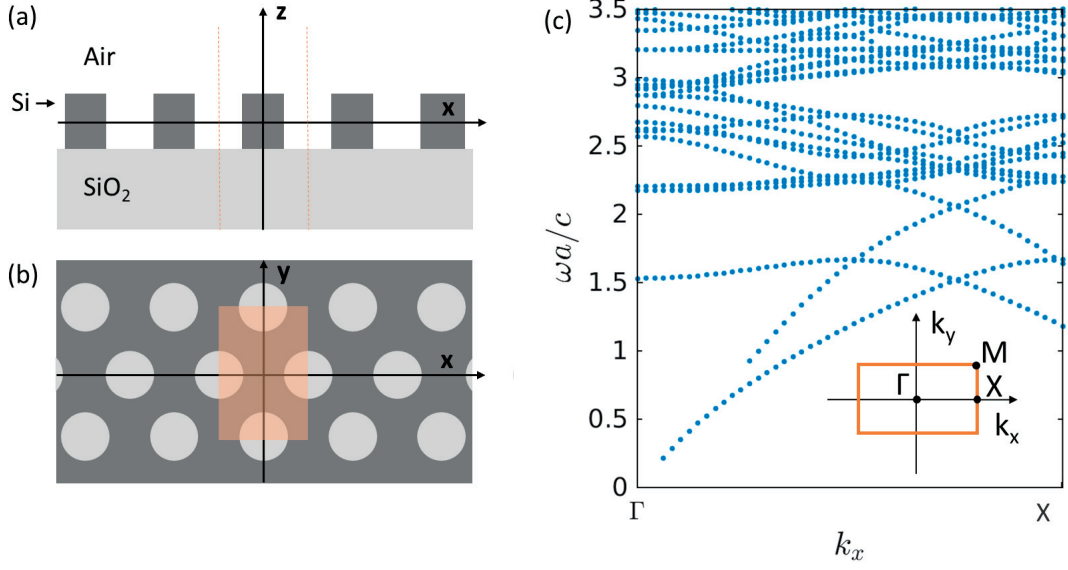
Figure 2.3: (a)-(b): Cross-section views for a photonic crystal consisting of a silicon slab with a hexagonal lattice of air holes, grown on silicon oxide. The 2D unit cell used for the GME computation is highlighted in orange. (c): The GME-computed PhC modes confined within the silicon slab (evanescent in both claddings), for $\mathbf{k}$ in the ΓX direction. The Brillouin zone of the crystal is shown as an inset.

is the fact that the coupling of the PhC modes to the continuum of radiative modes can be estimated in a Fermi-golden-rule fashion. Namely, the imaginary part of the eigenvalue $(\omega_{\mathbf{k}}^2/c^2)$ can be computed through

$$-\Im\left(\frac{\omega_{\mathbf{k}}^2}{c^2}\right) = \pi \sum_{\mathbf{G}'} \sum_{\lambda,j} |\mathcal{H}_{\mathbf{k}}^{\mathrm{rad}}|^2 \rho_j \left(\mathbf{k}+\mathbf{G}'; \frac{\omega_{\mathbf{k}}^2}{c^2}\right), \tag{2.10}$$

where λ labels polarization of the radiative guided modes (TE or TM), $j = 1, 3$ labels whether those modes are leaky in the upper or the lower cladding, and $\rho_j\left(\mathbf{k}+\mathbf{G}'; \frac{\omega_{\mathbf{k}}^2}{c^2}\right)$ is their 1D photonic density of states at fixed wave-vector. The matrix element $\mathcal{H}_{\mathbf{k}}^{\mathrm{rad}}$ is the overlap between a PhC mode and a leaky mode,

$$\mathcal{H}_{\mathbf{k}}^{\mathrm{rad}} = \int \frac{1}{\varepsilon(\mathbf{r})} \left(\nabla \times \mathbf{H}_{\mathbf{k}}^*(\mathbf{r})\right) \cdot \left(\nabla \times \mathbf{H}_{\mathbf{k}+\mathbf{G}',\lambda,j}^{\mathrm{rad}}(\mathbf{r})\right) \mathrm{d}\mathbf{r}, \tag{2.11}$$

and can be computed using the expansion of eq. (2.6) and the analytical matrix elements between guided and leaky modes of the slab (see [25]). The quality factor of a PhC mode can thus also be found through $Q = \omega_{\mathbf{k}}/\kappa$, where $\omega_{\mathbf{k}}$ is the real part of $\sqrt{\omega_{\mathbf{k}}^2 + i\Im(\omega_{\mathbf{k}}^2)}$, and κ is twice the imaginary part.

In Fig. 2.3, we show the modes of a photonic crystal computed using the GME method.

27

The structure we consider is a silicon slab grown on Silicon Oxide (SiO_2) (Fig. 2.3(a)-(b)), where the silicon slab is patterned by a hexagonal lattice of air holes. Even though the primitive cell of the structure is hexagonal (see Fig. 1.6), here we use a square cell (highlighted in orange in Fig. 2.3(b)), whose area is two times larger than that of the unit cell. This is recurrent in almost all GME simulations shown in this thesis: a square computational cell is used unless there is a very particular argument against it. There are several reasons for this. The main one is related to the fact that, as discussed in Section 2.2, the best way to avoid problems due to the discontinuity of $\varepsilon(\boldsymbol{\rho})$ is to compute the Fourier transform $\varepsilon^{-1}(\mathbf{G} - \mathbf{G}')$ through a matrix inversion of the matrix with elements $\varepsilon_{\mathbf{G}\mathbf{G}'} = \varepsilon(\mathbf{G} - \mathbf{G}')$. In the case of a square computational cell, and thus a square lattice of $\mathbf{G}$-points in reciprocal space, this matrix has a particular form, namely it is block-Toeplitz, where each block is itself a Toeplitz matrix [75]. This allowed us to implement an algorithm [76, 77] for an efficient inversion of the matrix, which decreases the complexity from $\mathcal{O}(n_{G_x}^3 n_{G_y}^3)$ to $\mathcal{O}(n_{G_x}^3 n_{G_y}^2)$, where n_{G_x} and n_{G_y} are the number of distinct G_x and G_y values, respectively. This left the diagonalization of the matrix of eq. (2.9) as the bottleneck of the computation. However, this can also be significantly improved by looking for a limited number of eigenvalues (e.g. the N_e lowest-energy ones) instead of for all of them, using e.g. a Lanczos method. These two improvements – one for the matrix inversion and one for the diagonalization – reduce the computational time in some cases by an order of magnitude. We also note that the quantities of interest – like a PhC band gap, a waveguide dispersion, or a cavity mode and Q-factor, can be computed with any computational cell that fits the underlying periodicity, i.e. we are not restricted to using the smallest-area, primitive cell.

The modes of the particular PhC of Fig. 2.3 are shown in panel (c) for $\mathbf{k}$ in the KX direction (i.e. $k_y = 0$). The structural parameters we used are $d = 0.5a$, $r = 0.3a$, $n_{Si} = 3.46$, $n_{SiO_2} = 1.44$. The guided modes in the expansion were truncated at $G_{\max} = 4 \times 2\pi/a$ and $\alpha_{\max} = 4$, although convergence within the y-axis scale of the plot was already reached around $G_{\max} = 3 \times 2\pi/a$ and $\alpha_{\max} = 3$. Obviously, these parameters need to be increased to compute the higher-frequency PhC modes, but those are rarely of interest. Importantly, the structure does **not** present a photonic band gap. This is due to the fact that the σ_{xy} symmetry is broken by the different claddings above and below the slab. In the case of the symmetric system, as we saw in Fig. 1.6(b), there is a band gap for the positive-symmetry modes, and no band gap for the negative-symmetry ones. Here, these modes are all mixed, which means no band gap overall. This shows that preserving the symmetry with respect to the $z = 0$ plane of a slab-PhC is of great importance (this is illustrated further below, see Fig. 2.6 and the related discussion).
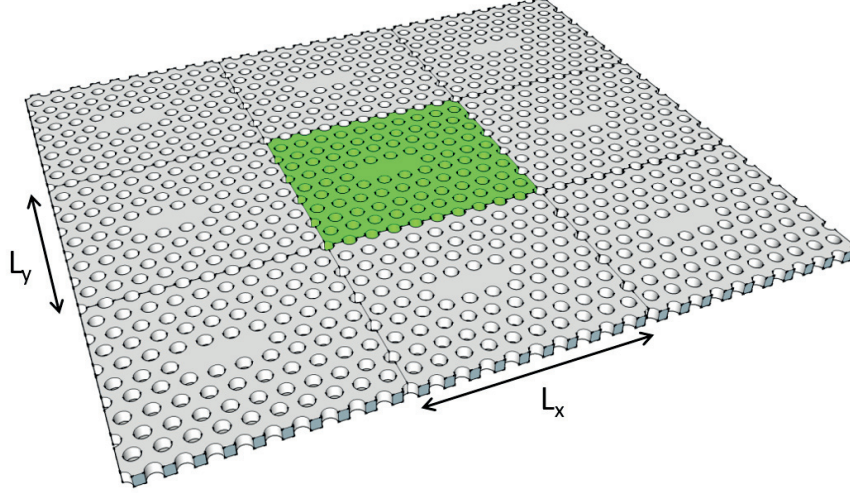
Figure 2.4: Highlighted in green: an example of a computational cell for a PhC cavity simulation using the GME. Effectively, due to the PBC, an array of cavities is simulated. With increasing L_x and L_y, the coupling between modes localized on different sites decreases exponentially.

2.3.2 Simulating localized modes

The GME assumes periodic boundary conditions and is thus ideal for simulating band structures of regular crystals, but it can also be used for defect-based functional elements like the ones introduced in Section 1.3. The simulation of PhC cavities in particular is in the backbone of this thesis, and is thus discussed in detail here. The idea is that, since the cavity mode is localized in a small region of space (cf. Fig. 1.8(b)), we can take a large enough computational cell such that the field becomes negligible at the boundaries. This approach is similar to the way the 3D-PWE can be applied to PhC slabs, as discussed in Section 2.2, and is further illustrated in Fig. 2.4 for an L3 cavity. We take a computational cell of size $L_x \times L_y$ around the defect that defines the cavity (in the L3 case, the three missing holes). Effectively, this results in simulating the Bloch modes of a periodic *lattice* of cavities, as shown in the Figure. In the limit of vanishing field overlap between modes localized at different lattice sites, the 'band' of cavity modes becomes **k**-independent (i.e. 'flat'), and has the resonant frequency $\omega_{\mathbf{k}} = \omega_0$ of an isolated cavity.

In Fig. 2.5, we illustrate a computation of an L3 cavity optimized for a high quality factor. The particular *five-shift* design used here is taken from Ref. [78] and is discussed in much more detail in Chapter 4. The underlying PhC is formed by a silicon slab of thickness $d = 220$nm suspended in air, with a hexagonal lattice of air holes with parameters $a = 400$nm and $r = 100$nm. In Fig. 2.5(a), we show the dispersion of this PhC-slab, computed as in Fig. 2.3. The σ_{xy} symmetry in this case is preserved, and we only show the positive-symmetry modes, for which there is a band gap. In panel (b), we
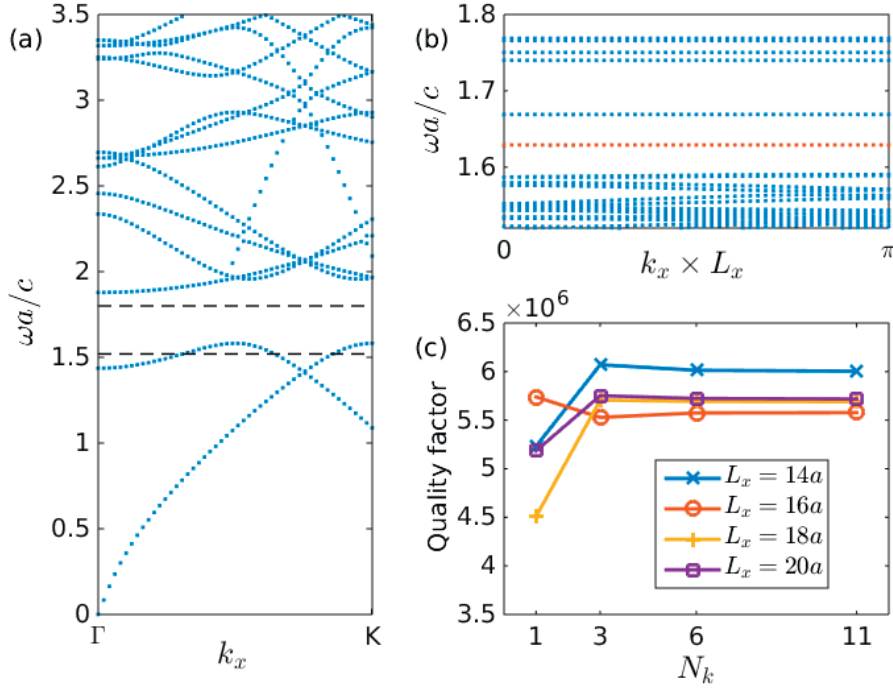
Figure 2.5: (a): $\sigma_{xy} = 1$ modes of a silicon PhC slab suspended in air, with $a = 400$nm, $d = 220$nm, $r = 100$nm. Dashed black lines show the range of the y-axis in (b). (b): GME-computed bands from an L3-cavity simulation as in Fig. 2.4, with $L_x = 16a$ and $L_y = 12\sqrt{3}a/2$. The band in red corresponds to the fundamental cavity mode. (c): Quality factors computed for $L_x = 14a, 16a, 18a, 20a$, and with increasing number of k-points in the Brillouin-zone averaging.

plot the GME-computed dispersion for a lattice of cavities as in Fig. 2.4, with $L_x = 16a$, $L_y = 12\sqrt{3}a/2$. The red band corresponds to the *fundamental* (i.e. lowest-frequency) cavity mode. Modes below that are not localized but instead come from the *folding* of the PhC valence bands. The bands above, which are also flat, are all in the band gap of the regular PhC, and constitute higher-order cavity modes.

The Bloch modes of the cavity array are periodic, i.e. they are not localized on a single site, regardless of the size of the computational cell. However, it **is** possible to construct a cavity mode which is localized on a single site. If $\mathbf{H_k}(\mathbf{r})$ are the modes belonging to the red band in Fig. 2.5, then the *Wannier function*

$$\mathbf{H}_W(\mathbf{r}) = \frac{1}{\sqrt{\Omega}} \int_{BZ} \mathbf{H_k}(\mathbf{r}) \mathrm{d}\mathbf{k}, \tag{2.12}$$

where the integration is over the whole Brillouin zone of area Ω, is localized on the site at $x = 0$, $y = 0$. In the limit of infinitely large L_x, L_y, when $\omega_\mathbf{k} = \omega_0$, this mode is also an eigenstate of frequency ω_0. This is already to a very good approximation true for the computation shown in Fig. 2.5(b), where the relative variation of ω is smaller

than 10^{-4}. Within this tolerance, the frequency also does not change with further increasing the supercell size. The GME-computed resonant frequency is thus quite stable in terms of convergence. The imaginary part of the frequency, however, has a non-trivial **k**-dependence (see also Fig. 2.6 below) that has to be taken into account. The coupling of the Wannier mode to radiative modes can be obtained in a way similar to eq. (2.10):

$$-\Im\left(\frac{\omega_0^2}{c^2}\right) = \pi \int d\mathbf{g} \sum_{\lambda,j} |\mathcal{H}_W^{\mathrm{rad}}|^2 \rho_j\left(\mathbf{g}; \frac{\omega_0^2}{c^2}\right), \tag{2.13}$$

where now the overlap integral $\mathcal{H}_W^{\mathrm{rad}}$ is defined as

$$\mathcal{H}_W^{\mathrm{rad}} = (\mathbf{H}_W, \Theta\mathbf{H}_{\mathbf{g},\lambda,j}^{\mathrm{rad}}) = \frac{1}{\sqrt{\Omega}} \int_{BZ} (\mathbf{H}_{\mathbf{k}}, \Theta\mathbf{H}_{\mathbf{g},\lambda,j}^{\mathrm{rad}}) d\mathbf{k} =$$
$$\frac{1}{\sqrt{\Omega}} \int_{BZ} \mathcal{H}_{\mathbf{k}}^{\mathrm{rad}} \delta_{\mathbf{g},\mathbf{k}+\mathbf{G}'} d\mathbf{k} = \frac{1}{\sqrt{\Omega}} \mathcal{H}_{\mathbf{k}}^{\mathrm{rad}}, \tag{2.14}$$

where $\mathcal{H}_{\mathbf{k}}^{\mathrm{rad}}$ is that of eq. (2.11) with **k** and $\mathbf{G}'$ such that $\mathbf{k} + \mathbf{G}' = \mathbf{g}$ (which determines them uniquely). Thus,

$$\Im\left(\frac{\omega_0^2}{c^2}\right) = -\frac{1}{\Omega} \int_{BZ} d\mathbf{k}\pi \sum_{\mathbf{G}'\lambda,j} |\mathcal{H}_{\mathbf{k}}^{\mathrm{rad}}|^2 \rho_j\left(\mathbf{k} + \mathbf{G}'; \frac{\omega_W^2}{c^2}\right) = \frac{1}{\Omega} \int_{BZ} d\mathbf{k}\Im\left(\frac{\omega_{\mathbf{k}}^2}{c^2}\right). \tag{2.15}$$

Thus, the loss rate of the localized Wannier mode is computed by averaging out the loss rates of the Bloch modes over the Brillouin zone. This now also allows us to compute the Q of the cavity. To do this, we compute the integral in eq. 2.15 numerically, by simulating N_k^2 points in **k**-space. More precisely, we take a uniformly distributed rectangular grid defined by N_k k_x-points in the interval $[0, \pi/L_x]$ and N_k k_y-points in the interval $[0, \pi/L_y]$. We remark that the loss rates for negative k_x and/or k_y values are identical to the ones for positive values, due to time-reversal symmetry. In Fig. 2.5(c), we plot the Q of the L3 cavity computed with $N_k = 1, 3, 6, 11$, and for four different L_x values. $N_k = 1$ means that the **k** $= 0$ value was taken only. As can be seen, in that case the supercell size has a significant effect on the computed quality factor. However, this size-dependence is suppressed by the **k**-averaging: the values for $L_x = 16a, 18a$, and $20a$ in particular become very close with increasing N_k. We also note that the Q converges fast with N_k – the results do not vary much already starting from $N_k = 3$.

In Fig. 2.6(a), we present a 2D map of the imaginary part $\Im(\omega_{\mathbf{k}}^2)$, in units of $(c/a)^2$. There are no sharp features present, which explains the fast convergence with N_k of the numerical integration of eq. (2.15). In the Figure, we also compare the losses of this cavity to the ones of the same design 'buried' in SiO_2 (panel (b)), as well as to the same design with a SiO_2 cladding on one side (panel (c)). In the buried case, the losses are stronger because of the lower refractive index contrast between the slab and the claddings, resulting in weaker mode confinement. The **k**-dependence of the
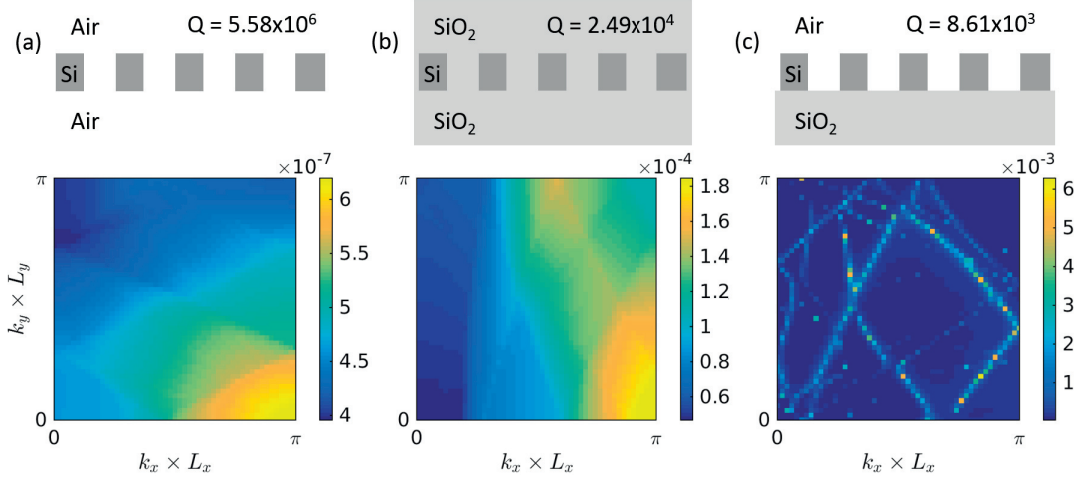
Figure 2.6: The **k**-dependent losses (i.e. $\Im(\omega_{\mathbf{k}}^2)$ in units of $(c/a)^2$) of the cavity Bloch modes. (a): Air-bridge cavity (like the one analyzed in Fig. 2.5); (b): Cavity 'buried' in SiO_2; (c): Cavity with just one SiO_2 cladding. The quality factors Q for the three cases are also noted.

losses is, however, still smooth. In contrast, when the σ_{xy} symmetry is broken as in panel (c), the underlying PhC no longer has a band gap (Fig. 2.3), and the cavity Bloch modes mix **resonantly** with bulk-PhC modes. This produces the very sharp features visible in the plot, which occur at values of **k** where the cavity and the bulk bands cross. This leads to a significant decrease of the quality factor, and illustrates once again the importance of preserving the σ_{xy} symmetry. Also, in the case of an asymmetric structure, the computational advantage of the GME is somewhat lost, since a very fine grid in **k**-space has to be used to properly capture all losses. We note that this can in principle be better handled through a numerical integration using an adaptive grid, and/or through analytically computing the band crossings where the losses present a sharp **k**-dependence.

In all the computations thus far, we truncated the guided modes at $G_{\max} = 3 \times 2\pi/a$ and $\alpha_{\max} = 4$. Notice that, when the σ_{xy}-symmetry is preserved, only two guided bands enter the computation, since bands 2 and 3 are negative-symmetry and so decoupled (cf. Fig. 1.4(b)). In Fig. 2.7, we study the convergence of the GME-computed quality factor with these basis-truncation parameters. The supercell size for all results shown in the Figure was kept at $L_x = 16a$, $L_y = 12\sqrt{3}a/2$. Each line represents the dependence of Q on one parameter while keeping the others fixed as follows: $G_{\max} = 3 \times 2\pi/a$ for the blue and the red line, $\alpha_{\max} = 4$ for the blue and the yellow line, and $N_k = 3$ for the red and the yellow line. The results are compared to the FDTD-computed $Q = 4.2 \times 10^6$, which was obtained using Lumerical solutions [74]. The GME-computed Q is somewhat higher than the FDTD result, a feature that is consistently observed for all the various simulations presented in Chapters 3 and 4.
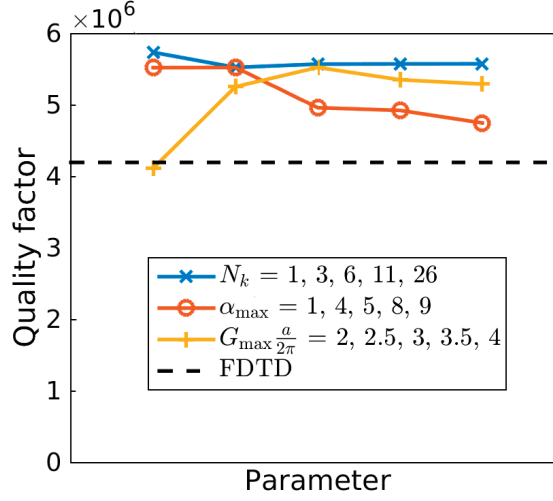
Figure 2.7: GME-computed quality factor of the optimized L3 cavity vs. several simulation parameters. We used $G_{max} = 3 \times 2\pi/a$ for the blue and the red line; $\alpha_{max} = 4$ for the blue and the yellow line; and $N_k = 3$ for the red and the yellow line. The FDTD result is also shown.

As discussed above, convergence with N_k is reached already at $N_k \approx 3$. With respect to G_{max}, there is little variation beyond $2.5 \times 2\pi/a$. The convergence with the number of bands is the slowest, but, importantly, it tends towards the FDTD result – the last point on the red line is at $Q = 4.7 \times 10^6$. This is also the fully converged GME value: we checked that it does not change further with increasing both α_{max} and G_{max}. This is a good illustration that GME and FDTD match very well when the convergence parameters are pushed. However, in the interest of computational time, we never use such a high α_{max} in the simulations of Chapters 3 and 4. This is because the main source of losses is already captured by the first guided band only – the Q of the first red point is 5.5×10^6, which is sufficiently close to the FDTD result, especially in terms of variations between this method and finite-element simulations that have been reported [79]. Furthermore, we note that this difference of about 30% between the FDTD-computed Q and the single-band GME result for this particular cavity is among the highest observed in all the simulations of various cavity designs that we have performed [78, 79]: very often, the difference is $\lesssim 10\%$ (cf. Table 4.1 in Chapter 4). This validates the use of the method for fast analysis and optimization of various PhC cavity designs using e.g. $G_{max} \approx 3$ and $\alpha_{max} = 1$, while for more precise results these parameters can be increased, at the cost of a longer computational time.

2.4 Bloch-mode expansion

In this Section we outline the Bloch-mode expansion [63, 80], which is particularly useful for simulating large PhC structures with random disorder. The idea is illustrated
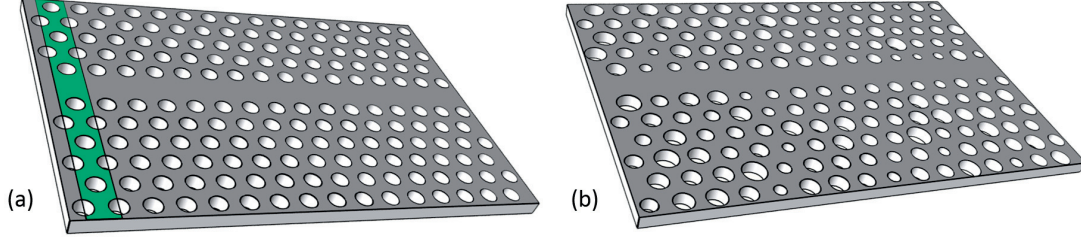
Figure 2.8: (a): A PhC waveguide; the modes guided inside the row of missing holes can be computed using the computational cell highlighted in green. (b): The same waveguide but with disorder in the positions and the radii of the holes. There is no longer any periodicity, and the full structure has to be included in the simulation. The disorder magnitude is largely exaggerated compared to state-of-the-art silicon devices.

in Fig. 2.8 for a PhC waveguide. The Bloch modes of the regular waveguide can be computed using a fairly small computational cell (panel (a)). Then, similarly to the PWE and GME methods, we can use these modes as a basis to compute the modes of a larger structure which is in some way related to the starting one – for example, the same waveguide in the presence of fabrication imperfections (panel (b)).

The starting point of the expansion are the Bloch modes $\mathbf{H}_{\mathbf{k}n}(\mathbf{r})$ of a periodic structure (here n is a number indexing different bands). These modes are solutions to eq. (1.5) with some starting periodic permittivity profile $\varepsilon(\mathbf{r})$ describing the PhC, and are normalized according to

$$\int d\mathbf{r}\,\mathbf{H}^*_{\mathbf{k}'n'}(\mathbf{r})\mathbf{H}_{\mathbf{k}n}(\mathbf{r}) = \delta_{\mathbf{k}'\mathbf{k}}\delta_{n'n}. \tag{2.16}$$

In presence of disorder, the dielectric permittivity $\varepsilon'(\mathbf{r})$ no longer has the lattice periodicity or symmetries, and so the momentum $\mathbf{k}$ is no longer a conserved quantity. We thus label the eigenmodes of the system by a global index β. These modes are solutions to eq. (1.5) with the $\varepsilon'(\mathbf{r})$ profile, and can be expanded on the basis of the Bloch modes of the regular structure:

$$\mathbf{H}_\beta(\mathbf{r}) = \sum_{\mathbf{k}n} U_\beta(\mathbf{k}, n)\mathbf{H}_{\mathbf{k}n}(\mathbf{r}). \tag{2.17}$$

Inserting this expansion in the Helmholtz equation (1.5) for the disordered structure, we obtain

$$\sum_{\mathbf{k}n} U_\beta(\mathbf{k}, n)\left[\frac{\omega_{\mathbf{k},n}^2 - \omega_\beta^2}{c^2} + \nabla \times \eta(\mathbf{r})\nabla\times\right]\mathbf{H}_{\mathbf{k}n}(\mathbf{r}) = 0, \tag{2.18}$$

where we defined $\eta(\mathbf{r}) = \frac{1}{\varepsilon'(\mathbf{r})} - \frac{1}{\varepsilon(\mathbf{r})}$, i.e. the difference of the inverse of the regular and irregular dielectric profiles. If we now multiply eq. (2.18) by $\mathbf{H}^*_{\mathbf{k}'n'}(\mathbf{r})$, integrate over $\mathbf{r}$,

and use the normalization in eq. (2.16), we obtain the eigenvalue problem

$$\sum_{\mathbf{k}'n'} \left[\frac{\omega_{\mathbf{k}n}^2 - \omega_\beta^2}{c^2} \delta_{\mathbf{k}\mathbf{k}'}\delta_{nn'} + V_{\mathbf{k}n\mathbf{k}'n'} \right] U_\beta(\mathbf{k}', n') = 0, \tag{2.19}$$

where the matrix $V_{\mathbf{k}n\mathbf{k}'n'}$ carries the information about disorder and is defined as

$$V_{\mathbf{k}n\mathbf{k}'n'} = \int \mathrm{d}\mathbf{r}\eta(\mathbf{r})(\nabla \times \mathbf{H}_{\mathbf{k}n}(\mathbf{r}))(\nabla \times \mathbf{H}_{\mathbf{k}'n'}^*(\mathbf{r})). \tag{2.20}$$

The starting Bloch modes $\mathbf{H}_{\mathbf{k}n}$ can in principle be computed using any method, e.g. FDTD or PWE, but in this thesis, we always use the GME. With the notation of the guided-mode expansion of eq. (2.6), the matrix elements read

$$V_{\mathbf{k}n\mathbf{k}'n'} = \sum_{\mu,\mu'} c_{n\mu}c_{n'\mu'}^* \int \mathrm{d}\mathbf{r}\eta(\mathbf{r})(\nabla \times \mathbf{H}_\mu(\mathbf{r}))(\nabla \times \mathbf{H}_{\mu'}^*(\mathbf{r})). \tag{2.21}$$

The integrals are analogous to the ones of eq. (2.9), and can be read out of Ref. [25], with the only difference that the Fourier transform of $\eta(\mathbf{r})$ enters in the place of that of $1/\varepsilon(\mathbf{r})$. The Fourier transform $\eta(\mathbf{g} - \mathbf{g}') = \varepsilon'^{-1}(\mathbf{g} - \mathbf{g}') - \varepsilon^{-1}(\mathbf{g} - \mathbf{g}')$ yields much better results when each of the two components is computed with the matrix-inversion method discussed above, and here the algorithm for inverting a Toeplitz-block Toeplitz matrix turns out particularly useful [75]. For large structures, the matrices $\varepsilon'(\mathbf{g} - \mathbf{g}')$ and $\varepsilon(\mathbf{g} - \mathbf{g}')$ which need be inverted become very big, causing problems from the perspective of both computational time and memory. The algorithm, however, solves both problems, first by reducing the complexity and second by removing the need to store the whole matrices at once. Apart from that, the size of the matrix for diagonalization in eq. (2.19) can be controlled by truncating the computation to a fixed number of bands (and checking convergence).

The radiative loss rates of the BME-computed modes can be computed perturbatively exactly as with GME. The overlap integrals between the modes $\mathbf{H}_\beta(\mathbf{r})$ and the leaky modes of the slab are

$$\mathcal{H}_{\beta,\mathbf{g}}^{\mathrm{rad}} = \int \mathrm{d}\mathbf{r}\frac{1}{\varepsilon'(\mathbf{r})}(\nabla \times \mathbf{H}_\beta^*(\mathbf{r})) \cdot (\nabla \times \mathbf{H}_{\mathbf{g}\lambda j}^{\mathrm{rad}}(\mathbf{r})) \tag{2.22}$$

$$= \sum_{\mathbf{k}'n'}\sum_{\mathbf{G}'\alpha} U_\beta^*(\mathbf{k}', n')c_{n'}^*(\mu') \int \mathrm{d}\mathbf{r}\frac{1}{\varepsilon'(\mathbf{r})} \left(\nabla \times \mathbf{H}_{\mu'}^*(\mathbf{r})\right) \cdot (\nabla \times \mathbf{H}_{\mathbf{g}\lambda j}^{\mathrm{rad}}(\mathbf{r})),$$

The amplitudes

$$\mathcal{H}_{\mu',\mathbf{g}}^{\mathrm{rad}} = \int \mathrm{d}\mathbf{r}\frac{1}{\varepsilon'(\mathbf{r})} \left(\nabla \times \mathbf{H}_{\mu'}^*(\mathbf{r})\right) \cdot (\nabla \times \mathbf{H}_{\mathbf{g}\lambda j}^{\mathrm{rad}}(\mathbf{r})) \tag{2.23}$$

are similar to the ones of eq. (2.11), but in this case the disorder is manifest in the inte-

gration measure $\frac{1}{\varepsilon'(\mathbf{r})}$, which breaks the translational invariance, and so the integrals are no longer proportional to $\delta_{\mathbf{k}\mathbf{k}'}$. For further details concerning the BME, the reader is directed to Refs. [63, 80], and to [75] for a convergence analysis.

3 Fabrication Disorder in Photonic Crystals

In this Chapter we study numerically some of the effects of fabrication imperfections on photonic crystal structures. Section 3.1 is adapted from Ref. [79] (M. Minkov et al., "Statistics of the disorder-induced losses of high-Q photonic crystal cavities," *Opt. Express* **21** (2013)), which was written in collaboration with Prof. Romuald Houdré and Dr. Perumal Dharanipathy from the LASPE here at EPFL. In this work, we analyze and compare the effect of disorder on the quality factor of six well-known photonic crystal cavity designs. These have vastly different intrinsic quality factors, but, nevertheless, we observe a similar behavior of the statistics of the disorder-induced light losses. In particular, we show that for high enough disorder, such that the quality factor is mainly determined by the disorder-induced losses, the measured quality factors differ marginally – not only on average as commonly acknowledged, but also in their full statistical distributions. This has implications for the optimization of cavity designs, which is the main subject of Chapter 4.

Section 3.2 is adapted from Ref. [81] (M. Minkov and V. Savona, "Effect of hole-shape irregularities on photonic crystal waveguides," *Opt. Lett.*, **37** (2012)), where we analyze the effect of irregular hole shapes on the spectrum and radiation losses of a photonic crystal waveguide. We find that the key parameter determining the magnitude of the effect of disorder is the standard deviation of the areas of the holes. One implication of this observation is that, for a fixed amplitude of the radius fluctuation around the hole, the disorder effects are strongly dependent on the correlation angle of the irregular shape.

3.1 Quality factor of PhC cavities

As discussed in Chapter 1, PhCs lie at the forefront of research in photonics. A variety of photonic crystal slab cavities with high quality factors and modal volumes of the order of the diffraction limit $(\lambda/n)^3$ have already been proposed [82–89]. Such devices

have found many applications, for example leading to one of the first observations of the strong coupling cavity quantum electrodynamics regime [90, 91] in a solid-state system [47]. Recently, there have been equally remarkable experimental breakthroughs in the all-optical domain, including the realization of low-power optical switching [34, 44, 92] and optical random-access memory [35]. The demonstration of strong coupling between two distant PhC cavities [93] is another remarkable result. The success of such experiments is due, on one hand, to the highly sophisticated fabrication technology, which allows for sub-nanometer precision in state-of-the-art silicon devices [94, 95], but on the other strongly relies on the introduction of cavity designs with a sufficiently high quality factor. However, a general feature of such designs is that the theoretically predicted Q is often much higher – sometimes by more than an order of magnitude – than the experimentally measured one. For some materials and wavelengths, this can be attributed to material absorption, but for silicon at $\approx 1.5\mu\mathrm{m}$ in particular, the effect is unanimously attributed to disorder residual in the fabrication process. For slab-PhCs, the most notable example is disorder in the size and positioning of air holes, though other contributions have also been identified [96–98].

Understanding the disorder effects has spurred some theoretical [98–100] and experimental [94, 95, 98] research, which has mostly focused on two specific designs – the L3 cavity shown in Fig. 1.8 and the *heterostructure* cavity introduced in Ref. [83]. In those, the most notable conclusion is that the disorder-averaged value of the disorder-induced cavity losses scales as σ^2, where σ is the magnitude of the random fluctuations in one spatial direction (e.g. in hole radius and/or position). Here, we will aim at a better understanding of the statistics of the disorder effects (through investigating the full probability distribution of Q values), and of how those compare among different cavity designs. To this end, we analyze and compare six very different, well-known PhC cavities with theoretical Q-s ranging from 5.4×10^4 to 7.5×10^7, i.e. spanning more than three orders of magnitude: the L3 [82], A3 and A1 [85, 86], heterostructure (HS) [83], H1 [101, 102] and H0 [89, 101]. We perform a detailed statistical analysis of the disorder effects, and conclude, most notably, that whenever the disorder-induced losses are clearly dominating over the intrinsic ones, their statistical distribution depends weakly on the particular cavity design, which validates and strengthens the common belief concerning the average value of Q.

3.1.1 Cavity designs and disorder model*

The designs of the six cavities studied here are presented in Fig. 3.1. All of the devices are based on a triangular lattice of circular air-holes of radius R in a silicon slab of thickness d (R and d differ among designs). We have already encountered the L3 cavity of Fig. 3.1(a) in Chapters 1 and 2; the design used here is the one also studied in Refs. [95, 99]. It has $R = 0.3a$ and $d = (220/420)a$, with a the lattice constant, and, for Q-optimization, the two holes (marked in red) on each side of the defect are shifted
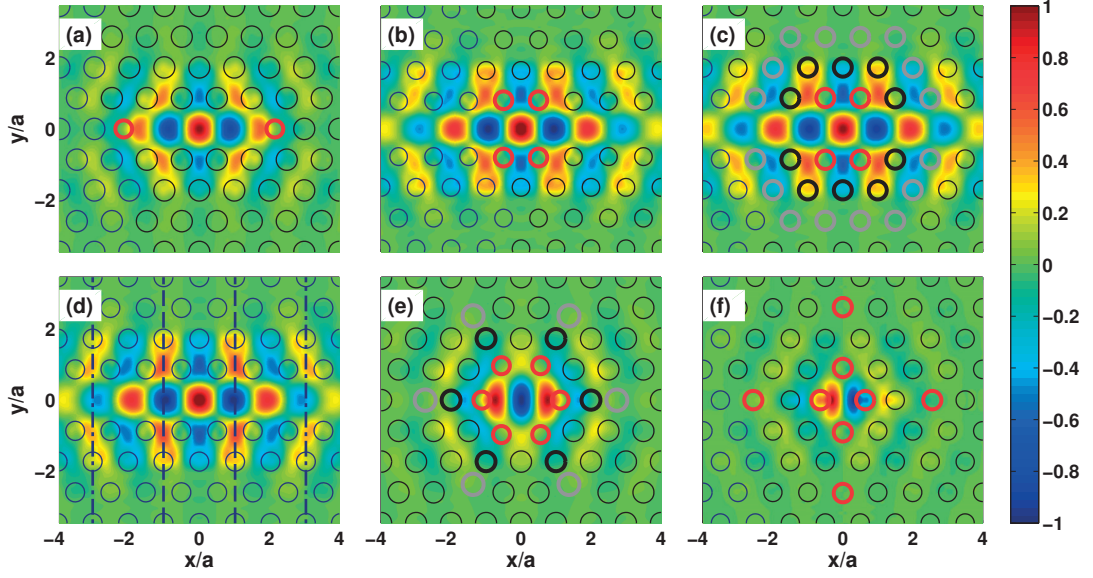
Figure 3.1: Designs and profiles (computed with the guided-mode expansion) of the y-component of the electric field, $E_y(\mathbf{r})$, for the different cavities studied here. (a): Improved L3 (see text); (b): A3, where the red holes are shifted outwards; (c): A1 with the red, black, and grey holes correspondingly shifted outwards by d_y, $2d_y/3$ and $d_y/3$; (d): Heterostructure, where the lattice constant is $(420/410)a$ in the region between the dashed lines and $(415/410)a$ in the two regions between a dashed and a dashed-dotted line; (e): Optimized H1: the holes marked in red are shifted outward by $0.12a$ and their radius is decreased by $0.06a$, the ones marked black have a radius decreased by $0.03a$, and the ones marked grey are shifted inward by $0.26a$. Only the y-polarized of the two degenerate modes is plotted; (f): Optimized H0, where the 8 holes marked in red are shifted symmetrically: the two shifts in the x-direction are $0.14a$, and $0.06a$, while the two shifts in the y-direction are $0.04a$ and $0.02a$ (cf. [89]).

outward by $0.16a$, while their radius is decreased by $0.06a$. The A3 and A1 cavities (Fig. 3.1(b) and Fig. 3.1(c)) are taken as originally defined in Ref. [85], with $R = 0.25a$, $d = 0.472a$ for the A3 and $R = 0.257a$, $d = 0.486a$ for the A1. The A3 cavity is formed by first introducing a one-dimensional waveguide defect of width $0.9a$, and then shifting two holes (marked with red contours in panel (b) of Fig. 3.1) on each side of the linear defect outward by $d_y = 0.0278a$. The A1 cavity is similar, but the width of the waveguide is $0.98a$, and three types of hole shifts are introduced: by $d_y = 0.0214a$ (red holes in Fig. 3.1(c)), by $2d_y/3$ (black holes) and by $d_y/3$ (grey holes). Next, we consider the heterostructure cavity first introduced in Ref. [83], with $R = (110/410)a$ and $d = (220/410)a$. It is again based on a linear waveguide (of width a), but the cavity defect is introduced by changing the lattice constant to $(420/410)a$ in the central region and to $(415/410)a$ in a region on each side (Fig. 3.1(d)). Fig. 3.1(e) shows an optimized [102] design for an H1 cavity formed by one missing hole, with $d = 0.5a$ and $R = 0.3a$ and nearby-hole shifts introduced as explained in the figure caption. This

cavity in fact has two degenerate modes, and in the figure only the y-polarized one is plotted. The last cavity is an optimized H0 as defined in Ref. [89], where $d = 0.6a$ and $R = 0.26a$, and the defining defect is outward shifts of neighboring holes.

In all simulations of disorder, random fluctuations in the positions and radii of the holes were considered, with an underlying Gaussian distribution with zero mean and standard deviation σ. The magnitude of the fluctuations was assumed to be spatially uniform, and no hole-hole correlations were considered. Spatial correlations between hole size and positions, as well as spatially non-uniform distribution of the disorder parameters could easily be included in our simulations. However, since there is to our knowledge no specific experimental characterization of the magnitude of such distribution properties and their influence on the PhC, such an analysis is beyond the scope of the work presented here. The disorder model can also be readily extended to include irregular hole shapes (see Section 3.2), but we expect the important disorder effects to be very well captured by the simpler model used here. We note that everywhere below, by 'disorder realization' we understand one particular set of $3n$ independent pseudo-random numbers drawn from a Gaussian distribution, giving the shifts in the x and y positions and in the radius R of each hole (for n holes included in the system). The magnitude of disorder included here ranges from $\sigma = 0.001a$ (relevant for state-of-the-art Si structures [94, 103]) to $\sigma = 0.015a$, i.e. also includes values relevant for different materials like GaAs, InGaAs or InP.

3.1.2   Statistics of the disorder-induced losses*

The measured Q of a cavity can be written as

$$\frac{1}{Q} = \frac{1}{Q_t} + \frac{1}{Q_d} + \frac{1}{Q_a}, \tag{3.1}$$

where Q_t is the theoretically predicted Q-factor for the particular cavity design in the absence of disorder (also called 'intrinsic'), Q_d is the quality factor associated to the disorder-induced losses, and Q_a accounts for any absorption (e.g. due to free carriers or water condensation). The absorption term Q_a could come from non-linear absorption and thus depend on e.g. the mode volume or field intensity in the cavity, but in any case it does not correspond to a stochastic effect, and for a particular cavity, it is expected to be constant for the different disorder realizations. Since the main interest of our analysis is the statistics of the disorder effects, this additional constant can then be incorporated into the constant Q_t. The same consideration applies to any other systematic effect that results in losses which are independent of the disorder realization, e.g. tilt of the hole walls. The expression of Eq. (3.1) is commonly employed [84, 94, 95, 98, 100] and stems from the definition of $Q \equiv \omega_0 U/P$, where U is the total electromagnetic energy of the cavity mode and P is the radiation power (see eq. (1.16) and discussion thereof). The physical assumption entering
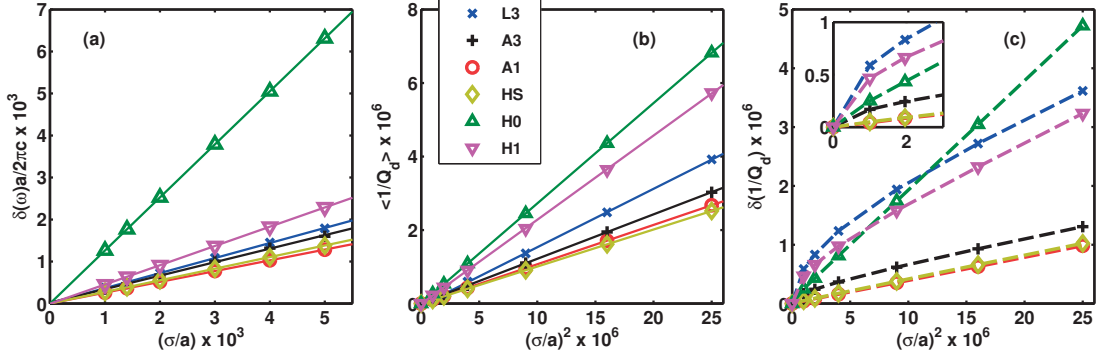
Figure 3.2: For the six different cavities, (a): Dependence of the standard deviation in the resonant mode frequency ω on the disorder magnitude σ; (b) and (c): Dependence of the mean and standard deviation of $1/Q_d$ on σ^2. In (a) and (b), the solid lines are determined from a linear interpolation, while in (c) the dashed lines only connect the individual points and serve as a guide for the eye. Inset in (c): zoom-in over the low-σ region.

eq. (3.1) (neglecting Q_a) is then that, upon small perturbations, the frequency and total energy of the cavity mode are approximately constant, while the total radiated power is obtained by summing the contributions of two radiation channels: one due to the intrinsically radiative components of a cavity mode and the other due to disorder-induced scattering into modes radiating outside of the slab (i.e. modes with frequency inside the light-cone). This summation is in fact not necessarily correct: the interference between the fields emitted through the two different channels has to be taken into account, which could potentially be **destructive**. This interference can be to a good approximation neglected when one of the channels is strongly dominating, but could be important when $Q_t \approx Q_d$. Nevertheless, in our analysis we use Eq. (3.1), bearing in mind that Q_d is, in general, a purely phenomenological quality factor that accounts for the difference between Q_t and the measured Q, and study the validity of interpreting Q_d as a quality factor associated to disorder-induced scattering losses which do **not** interfere with the intrinsic cavity losses. One example for which this interpretation is obviously not true can be found in the negative values of Q_d, which we show are possible for particular disorder realizations. Physically, this reflects the possibility for the disorder to cancel – due to destructive interference – some of the intrinsic radiative components, rather than introduce more losses. The possibility for negative Q_d-values is intuitive and by no means an artifact of our simulations: in the same way that small, controlled structural changes can dramatically increase the quality factor of a cavity (consider for example the difference between the A1 and the A3), particular configurations of the random disorder can do just the same.

In this Section, we use the guided-mode expansion (cf. [25] and Section 2.3) to compute the Q of a cavity with disorder, a method whose reliability was studied in Section 2.3 and which has already been utilized for a similar study [95]. The size of the computational

Table 3.1: Intrinsic quality factors of the disorder-less cavities. The FDTD results were taken from the corresponding references [83, 85, 89, 95, 102]. For the GME results, the computational cell length in the x-direction was $32a$ for the A1, A3 and HS cavities, $24a$ for the $L3$ cavity, and $16a$ for the H0 and H1. In the y-direction, the size was $16\sqrt{3}/2a$ for the A1, A3, HS, $20\sqrt{3}/2$ for the H1, and $14\sqrt{3}/2a$ for the L3 and H0.

Cavity	Q_t (FDTD)	Q_t (GME)
L3	8.9×10^4	1.1×10^5
A3	1×10^6	1.5×10^6
A1	70×10^6	75×10^6
HS	14×10^6	20×10^6
H0	2.8×10^5	3.3×10^5
H1	6.2×10^4	5.4×10^4

cell taken here is between $16a$ and $32a$ in the x-direction and between $14\sqrt{3}a/2$ and $20\sqrt{3}a/2$ in the y-direction, depending on the spread of the electric field of the different cavities, and the reciprocal space was truncated to $G_{max} = 2\frac{2\pi}{a}$ and $\alpha_{\max} = 1$ (see Section 2.3), resulting in 4080 to 9120 reciprocal lattice points, depending on the cell size. The intrinsic Q_t for the six different cavities computed with the GME using these parameters is compared to the corresponding FDTD results in Table 3.1.

Figure 3.2 shows the influence of random disorder on the resonant frequencies and quality factors for the six different designs, computed for $\sigma = 0.001a$, $0.0014a$, $0.002a$, $0.003a$, $0.004a$ and $0.005a$, and for 400 disorder realizations for each cavity and each σ. For all cavities and disorder magnitudes, the mean of the deviation from the ideal-cavity frequency ω_0, $\langle \omega - \omega_0 \rangle$, is at least one order of magnitude smaller than the standard deviation $\delta(\omega) = (\langle \omega^2 \rangle - \langle \omega \rangle^2)^{1/2}$, thus, to a good approximation, the frequency distribution can be considered centered around the ideal-cavity frequency. In contrast, the standard deviation increases linearly with increasing σ as shown in Fig. 3.2(a). This dependence matches previous results for the heterostructure [100], and is here observed for all six cavities (for the H1, where two modes with frequencies ω_1 and ω_2 exist, we define $\delta(\omega) = (\delta(\omega_1) + \delta(\omega_2))/2$). For some practical applications, having the smallest possible $\delta(\omega)$ is essential, but the main focus of this Section is the corresponding quality factors. For a given design, the statistics of the measured Q are determined by the statistics of Q_d, which is why in Fig. 3.2(b) and Fig. 3.2(c) we plot the mean $\langle 1/Q_d \rangle$ and standard deviation $\delta(1/Q_d) = \left(\langle (1/Q_d)^2 \rangle - \langle 1/Q_d \rangle^2 \right)^{1/2}$ vs. σ^2 for the different cavities, where $1/Q_d$ was computed from eq. (3.1). The scaling $\langle 1/Q_d \rangle \propto \sigma^2$ has already been numerically established for the L3 [99] and the HS [100], and is confirmed by our results (Fig. 3.2(b)), for those two as well as the other four cavities. The straight lines in the plot show linear interpolation based on the data. Additionally, we find that the standard deviation (Fig. 3.2(c)) also scales linearly with σ^2 for the A1 and HS in the range we consider, while for the other designs, the dependence is linear for all but the smallest values of σ.

An intuitive model for the disorder-induced scattering, which matches to some extent the computed results, is to assume that $1/Q_d = A_c\delta_d^2$, where δ_d is a random variable drawn from a Gaussian distribution of zero mean and standard deviation σ. Thus, $\langle 1/Q_d \rangle = A_c\sigma^2$ with A_c a design-specific constant, as observed in Fig. 3.2(b), while $\langle (1/Q_d)^2 \rangle = A_c^2 \langle \delta_d^4 \rangle = A_c^2 \times 3\sigma^4$, which means $\delta(1/Q_d) = \sqrt{2}A_c\sigma^2$, i.e. the standard deviation also scales linearly with σ^2, as observed in Fig. 3.2(c). However, there are two notable deviations from this simplified expectation. One is the fast increase of $\delta(1/Q_d)$ for the A3, L3, H0 and H1 for low σ. This, however, occurs in the σ range for which $\langle 1/Q_d \rangle^{-1} > \approx Q_t$; in this situation, as discussed earlier, Q_d is not determined in a straightforward way by the absolute value of the disorder-induced scattering losses, but instead also contains interference effects. Indeed, in this range we also observe $\delta(1/Q_d) > \langle 1/Q_d \rangle$, meaning that negative values for $1/Q_d$ are likely, thus the statistics lie beyond the simple, uncorrelated assumption. The second deviation is the fact that within the simple Gaussian-squared model, we obtain $\delta(1/Q_d)/\langle 1/Q_d \rangle = \sqrt{2}$ for all cavities. In our simulations, this value is much lower: 0.48, 0.43, 0.36, 0.40, 0.56 and 0.67 for the L3, A3, A1, HS, H1 and H0, respectively. This means that δ_d is actually not Gaussian-distributed, as $\langle \delta_d^4 \rangle < 3\langle \delta_d^2 \rangle^2$. A likely explanation is that while it is reasonable to expect that the statistics of the losses due to the fluctuation of a single hole follow a Gaussian model, the statistics of the total losses (due to the fluctuations of **all** holes) are **not** given by a direct sum over single-hole contributions. Our results show that this cooperative effect systematically results in a decrease of the variance of the $1/Q_d$ distribution.

The constant A_c (the slope of the lines in Fig. 3.2(b)) can in principle be interpreted as a measure of the robustness of a cavity to disorder effects. The values of A_c for the different cavities are 0.159, 0.121, 0.107, 0.101, 0.273 and 0.230 for the L3, A3, A1, HS, H1 and H0, respectively. With the exception of the HS, these decrease with increasing cavity mode volume; the HS has a volume slightly lower than the A3 and A1 combined with the lowest A_c. Additionally, a cavity with a lower A_c than the HS has been demonstrated [104], but at the cost of an even higher mode volume. However, by investigating the full probability distribution of $1/Q_d$, plotted for $\sigma = 0.0014a$, $\sigma = 0.005a$ and $\sigma = 0.015a$ in Fig. 3.3(a)-(c), we find that the difference is marginal whenever $\langle 1/Q_d \rangle^{-1} < Q_t$. The latter holds for all three values of σ for the A1 and HS, and indeed the distributions for those two cavities are almost identical in all the panels. Despite the fact that the slope of the A3 plot in Fig. 3.2(a) is visibly higher than of the A1 and HS, already for $\sigma = 0.005a$ (panel (b) of Fig. 3.3) it can be seen that the three distributions become very close, illustrating that the difference in $\langle 1/Q_d \rangle$ is actually minor. This reflects the fact that if disorder-induced losses are dominating, which is already the case for the A3 with $\sigma = 0.005a$, for which $Q_t = 1.5 \times 10^6$ and $\langle 1/Q_d \rangle^{-1} = 3.4 \times 10^5$, then the full statistical distribution of those losses – and not only the average Q – tends towards being **design-independent**. This conclusion is further supported by the data for the other cavities, despite the fact that their Q_t is more than
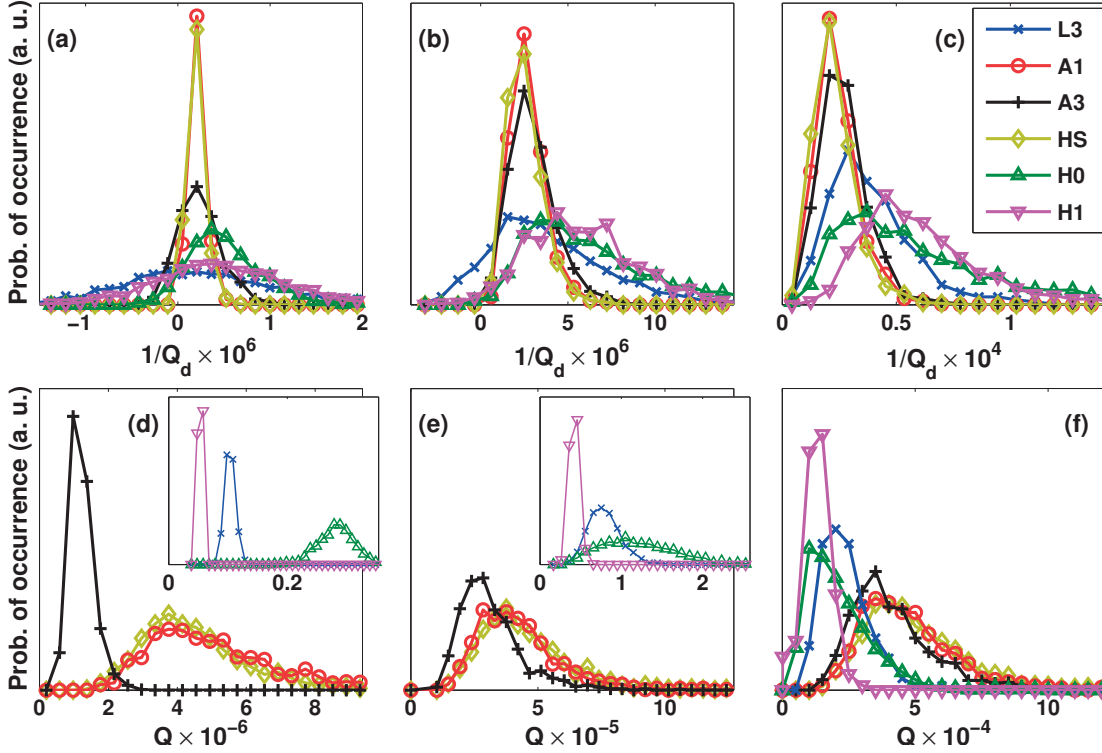
Figure 3.3: (a)-(c): Histograms showing the occurrence of $1/Q_d$ for the six different cavities, computed using the GME for 1000 disorder realizations with (a): $\sigma = 0.0014a$, (b): $\sigma = 0.005a$, and (c): $\sigma = 0.015a$. (d)-(f): Histograms showing the occurrence of Q with the same values of σ as in (a)-(c). The insets in (d) and (e) are a zoom-in over the low-Q range, where the L3, H0 and H1 values are sitting.

two orders of magnitude smaller than the A1 or HS values. Of course, the distributions of the quality factors (panels (d)-(f) in Fig. 3.3) differ vastly among the different designs for small σ, when Q_t is important. However, when Q_d is strongly dominant (Fig. 3.3(f)), the distributions come close together, and it can be expected that they will be even closer for yet higher disorder. However, this is a case which is, first of all, irrelevant to state-of-the-art devices, second, in which the scaling $\langle 1/Q_d \rangle \propto \sigma^2$ is expected to break down [99], and third, in which the disorder becomes comparable to the hole displacements defining the cavities.

The GME provides not only the resonant frequency and quality factor of a cavity, but also the full (near-field) mode profile, through eqs. (2.6) and (1.6). A parameter which is for example interesting for cavity-QED applications is the degree of polarization in the center of a cavity (where a quantum dot would be placed), which for the L3, A1, A3 and HS lies entirely along the y-direction in the ideal case. If we define the degree of polarization in the center of a cavity as $P = \frac{|E_y(0)|^2 - |E_x(0)|^2}{|E_y(0)|^2 + |E_x(0)|^2}$, so that $P = 1$ for fully y-polarized field (ideal-cavity case) and $P = -1$ for fully x-polarized field, we
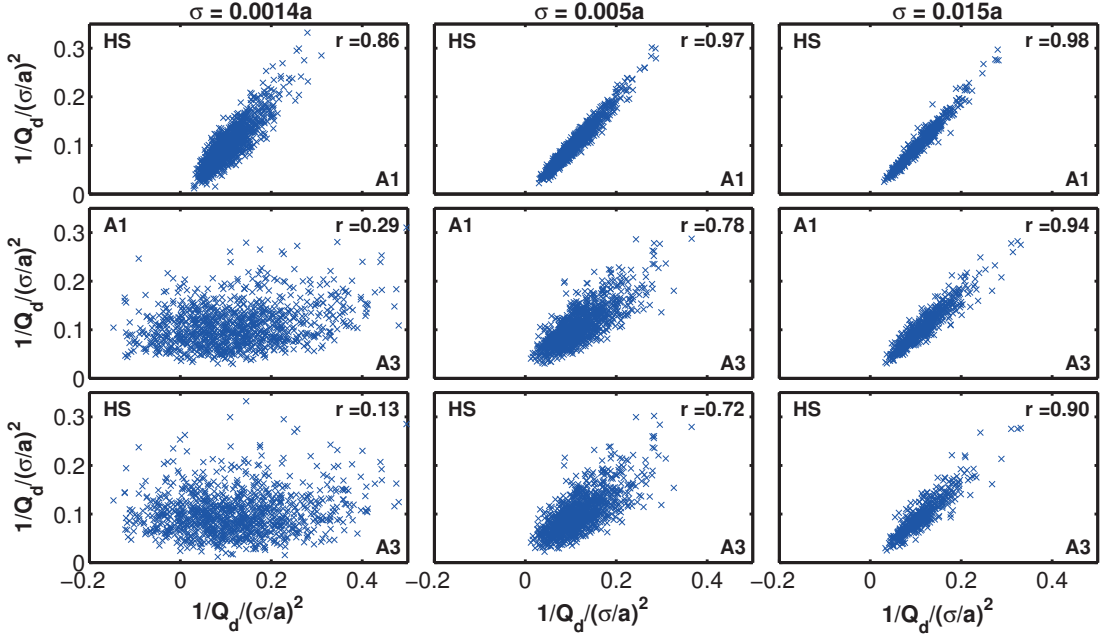
Figure 3.4: For the three waveguide-based cavities (A1, A3 and HS), each panel shows $1/Q_d$ in one cavity vs. $1/Q_d$ in another for the same underlying disorder configuration, with 1000 different configurations. First row: HS vs. A1; second row: A1 vs. A3; third row: HS vs. A3. Across columns, σ changes from $0.0014a$ to $0.005a$ to $0.015a$. The correlation coefficient r is indicated in the top right corner of each panel. Note that the range of the x-axis is twice larger than that of the y-axis due to the larger A3 spread.

obtain that the influence of disorder is not very profound: for the 1000 realizations with each of the three values of σ as in Fig. 3.3, the distribution of P is always peaked around 1, and all values are above 0.999 for $\sigma = 0.0014a$, 0.99 for $\sigma = 0.005a$, and 0.9 for $\sigma = 0.015a$. Note that the effect of disorder on the far-field is expected to be less trivial [100], but since our GME implementation is currently not suited for computing the far-field profile, this analysis is left for a future work.

The fact that the $1/Q_d$ distribution for the HS, A1 and A3 are almost identical, and that all three cavities are based on a local defect over a linear waveguide, suggests the question of whether the same disorder realization affects the cavities in a similar way. To investigate this, in Fig. 3.4 we plot, for the same three values of disorder as in Fig. 3.3, $1/Q_d$ in one cavity vs. $1/Q_d$ in another for the same random configuration of hole position and size shifts (taken separately from the defining cavity defect). Strong correlation (which gets stronger with increasing σ) is indeed found, with a correlation coefficient as high as 0.98 between the A1 and the HS for $\sigma = 0.015a$. To understand why correlation is expected, we note that the modes of these cavities can be expanded on the basis of Bloch modes of the waveguide (in the spirit of Section 2.4). In the ideal case, the main contribution comes from the modes close to the edge

of the main guided band, which are perfectly lossless, and the lossy contributions come from small components of modes above the light line [84, 88]. When disorder is introduced in the waveguide (without a cavity), the ideally-lossless modes acquire a finite quality factor [25, 63, 99]. We can thus further split the disorder losses of a cavity into $1/Q_d = 1/Q_{des} + 1/Q_{wm}$, where $1/Q_{des}$ is due to the way the disorder in the defining defect increases the coupling to modes above the light line (i.e. disorder makes the design sub-optimal), while $1/Q_{wm}$ reflects the fact that the waveguide modes themselves become lossy. Thus, $1/Q_{des}$ is design-dependent, while $1/Q_{wm}$ is largely ubiquitous, especially since the near-field profiles of Fig. 3.1 are very similar; the strong correlations with increasing σ then show that the losses become increasingly waveguide-mode dominated. Finally, we note that the A1-HS correlation is very high even for $\sigma = 0.0014a$, which highlights the fact that those two defect cavities are extremely similar.

3.1.3 Discussion and implications for cavity optimizations*

Our study of the disorder-induced losses provides insights that guided our subsequent work on optimizing PhC cavities (Chapter 4). It is evident from Fig. 3.3 that, despite the fact that the designs of the cavities studied here, as well as their theoretical Q_t-s, differ vastly, in the regime in which the disorder-induced losses are dominating ($Q_d < Q_t$), the statistics of $1/Q_d$ are to a good approximation design-independent. Thus, optimizing Q_t is important only if the measured Q (or, better, the $\langle Q \rangle$ measured over many samples) is not much lower than Q_t. If that is the case, there are just two ways to significantly increase the measured Q. One is to decrease the magnitude of disorder, which for all studied designs is related to the extrinsic losses via $\langle 1/Q_d \rangle \propto \sigma^2$. The second (albeit not reproducible) way is to explore the broad high-Q tail of the probability distribution, which is visible in Fig. 3.3(d)-(f). The thickness of the tail is related to the fact that in the disorder-dominated regime, the distribution of $1/Q_d$ is close to a squared Gaussian, as illustrated in Fig. 3.3(a)-(c). This results, for example, in a 5.7% chance to find an HS cavity with $Q = 7.4 \times 10^6$ – the average value with $\sigma = 0.001a$ – even within the $\sigma = 0.0014a$ case. Of course, it should be kept in mind that for such high values of the nominal Q, the measured value could be limited not only by disorder, but also by linear absorption, or two-photon absorption and other non-linear effects [70], which all introduce an additional effective loss rate.

Since the parameter space of hole positions and sizes in a typical PhC structure is not only large but also inseparable (i.e. the effect of hole fluctuations on Q is highly correlated among different holes), many local maxima of Q_t can be expected. The ideal tool for optimizing a design would thus be a *global* optimization algorithm – e.g. a *genetic optimization*. The computational speed of the GME allows us to perform such a global optimization, which will be presented in the next Chapter. In view of that, the take-away message of this Section can be stated as follows: once the Q_t of a

cavity has reached a certain value ($\approx 10^7$ for current silicon-based devices, and lower for other materials with higher magnitude of the fabrication imperfections), the best improvement strategy is not to push Q_t higher still, but instead to focus on additional features beyond the quality factor. For example, the H0, H1, and L3 cavities studied here all have a much smaller mode volume than the A3, A1, and HS, which is good, but it is combined with a much lower Q_t. Improving the quality factor of the former designs is thus of greater importance than just pushing for a world-record Q_t in **any** PhC cavity. Beyond the mode volume and the quality factor, an optimization could also focus on designs allowing for more sophisticated practical applications, as in e.g. Refs. [105–109].

3.2 Effect of irregular hole shapes on PhC waveguides

As shown in Section 3.1, disorder can be **the** factor determining the quality of PhC structures. It is by now well-known that fabrication imperfections also degrade the preformance of PhC waveguides by inducing extrinsic radiation losses [61, 62, 110, 111] and light localization [1, 63] in the vicinity of the guided band edge. Most of the theoretical works on disorder in PhCs [62, 63, 94, 95, 110], as well as Section 3.1 here, consider the simplest possible disorder model, namely circular holes with randomly fluctuating radii and/or positions, and study radiation losses, spectral properties, and light localization as a function of the fluctuation amplitude. Here, following our work in Ref. [81], we present an analysis based on more realistic assumptions, clarifying the role of the observed deviations from a perfectly circular shape of the PhC holes [103, 112]. We study numerically the interplay of angle correlation and radius fluctuations, and conclude, in agreement with recent experimental evidence [103], that the relevant parameter that quantifies the effect of disorder is the amplitude of *fluctuations in the hole area*. More specifically, we employ the Bloch-mode expansion (cf. Section 2.4 and references therein) to study the effect of irregular hole shapes on the properties of a W1 waveguide. We carry out a systematic analysis for two limiting assumptions within the hole-shape model, namely fixed radius fluctuation (within each single hole), or fixed hole area fluctuation (among different holes). The result clearly shows that varying the correlation angle has practically no effect on the spectrum and radiation losses in the second case, while it is highly determinant within the first assumption.

3.2.1 Disorder model

We consider a W1 waveguide as the one in Fig. 1.7, based on a triangular lattice of cylindrical holes of radius $R = 0.3a$ in a dielectric slab of thickness $d = 0.5a$, where a is the lattice parameter. The permittivity is set to $\varepsilon_2 = 12.11$ (relevant for Si) in the dielectric material and to $\varepsilon_1 = 1$ outside. Disorder is modeled in the form of fluctuations in the hole profile, given by $R(\phi) = R + \delta R(\phi)$, where ϕ is the polar angle

relative to the hole center. In particular, each hole is characterized by a different disorder realization (no correlation between hole shapes is assumed) defined through random Fourier expansion coefficients C_m as $\delta R(\phi) = \sum_{m=-\infty}^{+\infty} C_m e^{im\phi}$.

The Bloch modes of the regular waveguide are computed via the GME. In all computations we truncate the reciprocal space of guided modes to $G_{\max} = 3 \times 2\pi/a$, $\alpha_{\max} = 1$, and take a computational cell as in Fig. 2.8(a), of size a in the x-direction and $5\sqrt{3}a$ in the y-direction. To apply the BME, we need to compute the Fourier transforms of the dielectric profiles of both the regular structure, $\varepsilon(\mathbf{r})$, and the disordered one, $\varepsilon'(\mathbf{r})$. As usual in our study of slab-PhCs, the z dependence is trivial and can be taken care of analytically, thus the only nontrivial task is the evaluation of the 2D Fourier transforms of $\varepsilon(\boldsymbol{\rho})$ and $\varepsilon'(\boldsymbol{\rho})$ at $z = 0$ inside the slab. The former is readily computed [63]: let ζ be an index running over all holes included in the computational cell, with $\boldsymbol{\rho}_\zeta$ denoting their positions and R_ζ - their radii (i.e. we allow for different radii of the holes, while still assuming they are perfectly circular). Then, we have

$$\varepsilon(\mathbf{g}) = \varepsilon_2 \delta_{\mathbf{g},0} + \frac{\varepsilon_1 - \varepsilon_2}{A} \sum_\zeta e^{i\mathbf{g}\boldsymbol{\rho}_\zeta} \frac{2\pi R_\zeta}{g} J_1(gR_\zeta), \tag{3.2}$$

where J_1 denotes the Bessel function of the first kind and g is the magnitude of $\mathbf{g}$.

The computation of $\varepsilon'(\mathbf{g})$ is more involved, but we can also derive an analytical expression. First, we assume that the disordered dielectric profile is also constant in the z-direction, i.e. $\varepsilon'(\mathbf{r}) = \varepsilon(\boldsymbol{\rho}, 0)$. Then, we consider a slab with holes centered at the same positions $\boldsymbol{\rho}_\zeta$ ($\zeta = 1, 2, \dots$) as the holes of the regular guide, but of arbitrary shape given by a contour $R_\zeta(\phi)$ (in polar coordinates), i.e. we treat disorder due to irregular hole-edge. In such a setup we have

$$\varepsilon'(\boldsymbol{\rho}) = \varepsilon_2 + \sum_\zeta (\varepsilon_1 - \varepsilon_2) S_\zeta(\boldsymbol{\rho} - \boldsymbol{\rho}_\zeta), \tag{3.3}$$

where $S_\zeta(\boldsymbol{\rho})$ is a function defined as

$$S_\zeta(\rho, \phi) = \begin{cases} 1, & \rho \leq R_\zeta(\phi) \\ 0, & \rho > R_\zeta(\phi) \end{cases} \tag{3.4}$$

To compute the Fourier transform $\varepsilon'(\mathbf{g})$, we start from the Fourier transform of a single function $S(\boldsymbol{\rho})$ as defined above, for some hole profile $R(\phi)$:

$$S(\mathbf{G}) = \int_A e^{-i\mathbf{G}\boldsymbol{\rho}} d^2\boldsymbol{\rho} = \int_0^{2\pi} d\phi \int_0^{R(\phi)} \rho d\rho e^{-iG\rho\cos(\theta-\phi)}, \tag{3.5}$$

where $\mathbf{G} = (G, \theta)$ in polar coordinates. Assume that the hole profile can be represented

as deviating slightly from a circular shape, $R(\phi) = R_0 + \delta R(\phi)$. Then,

$$
S(\mathbf{G}) = \int_0^{2\pi} \mathrm{d}\phi \left[\int_0^{R_0} + \int_{R_0}^{R_0 + \delta R(\phi)} \right] \rho \mathrm{d}\rho e^{-iG\rho\cos(\theta - \phi)} = S_0(\mathbf{G}) + \delta S(\mathbf{G}), \qquad (3.6)
$$

where we split the result into a circular hole expression, $S_0(\mathbf{G})$ - which is well-known, and a correction term, $\delta S(\mathbf{G})$. For the latter we have,

$$
\begin{aligned}
\delta S(\mathbf{G}) &= \int_0^{2\pi} \mathrm{d}\phi \int_{R_0}^{R_0 + \delta R(\phi)} \rho \mathrm{d}\rho e^{-iG\rho\cos(\theta - \phi)} \\
&= \int_0^{2\pi} \mathrm{d}\phi \int_{R_0}^{R_0 + \delta R(\phi)} \rho \mathrm{d}\rho e^{iG\rho\sin\left(\theta - \phi + \frac{\pi}{2}\right)},
\end{aligned} \qquad (3.7)
$$

and we make use of the Jacobi-Anger expansion:

$$
e^{i\omega\sin\varphi} = \sum_{m=-\infty}^{\infty} J_m(\omega)e^{im\varphi}, \qquad (3.8)
$$

to get

$$
\begin{aligned}
\delta S(\mathbf{G}) &= \int_0^{2\pi} \mathrm{d}\phi \int_{R_0}^{R_0 + \delta R(\phi)} \rho \mathrm{d}\rho \sum_{m=-\infty}^{\infty} J_m(G\rho)e^{im\left(\theta - \phi + \frac{\pi}{2}\right)} \\
&= \int_0^{2\pi} \mathrm{d}\phi \sum_{m=-\infty}^{\infty} i^m e^{im(\theta - \phi)} \int_{R_0}^{R_0 + \delta R(\phi)} \rho \mathrm{d}\rho J_m(G\rho).
\end{aligned} \qquad (3.9)
$$

For δR small, we can expand the $\mathrm{d}\rho$ integrals to first order,

$$
\int_{R_0}^{R_0 + \delta R(\phi)} \rho \mathrm{d}\rho J_m(G\rho) \approx \delta R(\phi) R_0 J_m(GR_0). \qquad (3.10)
$$

Since $\delta R(\phi)$ is a 2π-periodic function, we can take its Fourier series expansion,

$$
\delta R(\phi) = \sum_{n=-\infty}^{\infty} C_n e^{in\phi}, \qquad (3.11)
$$

with reality condition $C_{-n} = C_n^*$. Plugging (3.10) and (3.11) in (3.9) yields

$$
\begin{aligned}
\delta S(\mathbf{G}) &= R_0 \sum_{m,n=-\infty}^{\infty} i^m e^{im\theta} J_m(GR_0) \int_0^{2\pi} \mathrm{d}\phi e^{-im\phi} C_n e^{in\phi} \\
&= 2\pi R_0 \sum_{m=-\infty}^{\infty} i^m e^{im\theta} C_m J_m(GR_0)
\end{aligned} \qquad (3.12)
$$

The Fourier expansion of the dielectric profile in presence of disorder can be directly

expressed using this result, since

$$\varepsilon'(\mathbf{g}) = \varepsilon_2 \delta_{\mathbf{g},0} + \frac{\varepsilon_1 - \varepsilon_2}{A} \sum_\zeta e^{i\mathbf{g}\boldsymbol{\rho}_\zeta} S_\zeta(\mathbf{g}), \tag{3.13}$$

where A is the area of the supercell, ζ runs over all the holes centered at $\boldsymbol{\rho}_\zeta$ present in the supercell, and $S_\zeta(\mathbf{g}) = S_{0,\zeta}(\mathbf{g}) + \delta S_\zeta(\mathbf{g})$ is the Fourier transform corresponding to a $R_\zeta(\phi) = R_{0,\zeta} + \delta R_\zeta(\phi)$ profile. In the computations done here, we further simplify this result by taking $R_{0,\zeta} = R_0$ – constant for all holes (both in the regular and in the disordered case), i.e. only the hole-edge disorder $\delta R(\phi)$ is different for every hole in the supercell. If we characterize this by a set of Fourier-expansion parameters $C_{m,\zeta}$ for hole number ζ, the expression is finally

$$\varepsilon'(\mathbf{g}) = \varepsilon_2 \delta_{\mathbf{g},0} + \frac{2\pi R_0}{A}(\varepsilon_1 - \varepsilon_2) \sum_\zeta e^{i\mathbf{g}\boldsymbol{\rho}_\zeta} \left[\frac{J_1(gR_0)}{g} + \sum_{m=-\infty}^{\infty} i^m e^{im\theta} C_{m,\zeta} J_m(gR_0) \right]. \tag{3.14}$$

 In the disorder model used here, we take the $\{C_m\}$ coefficients for each hole to be Gaussian random variables, whose distribution is fully determined by $\langle C_m \rangle$ and $\langle |C_m|^2 \rangle$. Note that $\langle C_{m\neq 0} \rangle = 0$, since it is an average over complex numbers with a random phase. We further assume Gaussian correlations along ϕ, such that $\langle \delta R(\phi)\delta R(\phi') \rangle = \sigma^2 e^{-\frac{(\phi-\phi')^2}{2\delta^2}}$, where δ is the correlation angle. We verified that assuming exponential correlations does not relevantly change our conclusions [75]. This sets $\langle \sum_m |C_m|^2 \rangle = \langle \delta R^2 \rangle = \sigma^2$, and the dependence with m of the second moments:

$$\langle |C_m|^2 \rangle = \sigma^2 \int_{-\pi}^{\pi} e^{-\frac{\phi^2}{2\delta^2}} e^{-im\phi} \mathrm{d}\phi. \tag{3.15}$$

Within this scheme, the quantities σ, δ and $\langle C_0 \rangle$ are still free parameters. To set them, we consider two different models. The first one consists in assuming, for varying δ, a given magnitude of the fluctuation of the hole radius, namely by setting $\langle \delta R \rangle = 0$ and $\langle \delta R^2 \rangle = const$, which sets $\langle C_0 \rangle = 0$ and $\sigma = \sqrt{\langle \delta R^2 \rangle}$. Fig. 3.5(a) illustrates one realization of a hole within this model with $\sigma = 0.006a$, computed for two different values of δ. The second model consists instead in assuming a given magnitude of the fluctuations in the hole area A, thus setting $\langle \delta A \rangle = 0$ and $\langle \delta A^2 \rangle = const$, which determines implicitly the parameters $\langle C_0 \rangle$ and σ. In panel (c) of Fig. 3.5, we show a hole realization when those conditions are imposed, with $\langle \delta A^2 \rangle = 0.004a^2$, for the same two values of δ as in panel (a). It can be seen that in this case the magnitude of the radius fluctuations $\langle \delta R^2 \rangle$ depends substantially on δ, and while the profile for $\delta = 0.06(2\pi)$ appears as a reasonable representation of what could be expected from a state-of-the-art PhC [103, 112], the $\delta = 0.005(2\pi)$ profile displays unrealistically large radius fluctuations.
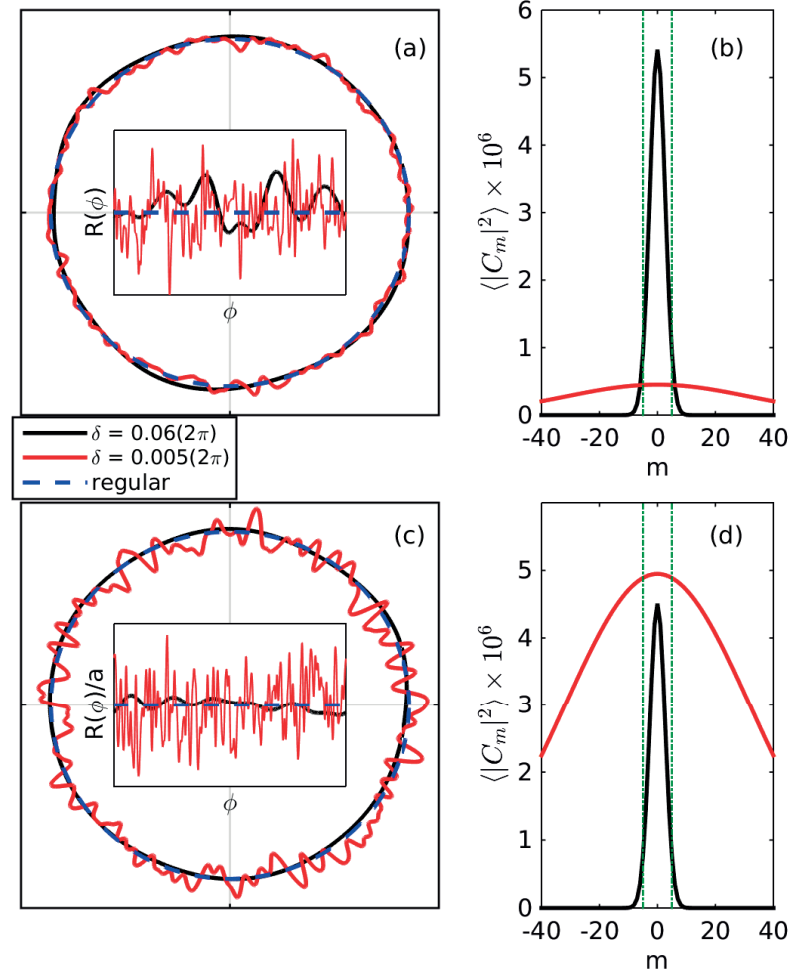
Figure 3.5: (a): Polar and Cartesian plots of a sample hole shape for two different correlation angles, assuming a fixed radius fluctuation $\sigma = 0.006a$; (b): The underlying distributions of $\langle |C_m|^2 \rangle$; the green dashed lines mark the region $|m| \leq 5$. (c), (d): same, assuming a fixed area fluctuation $\langle \delta A^2 \rangle = 0.004a^2$

3.2.2 Effects on the waveguide properties*

In Fig. 3.6 we plot the dispersion and radiative loss rates of the waveguide modes computed for one disorder realizaton in a waveguide of length $L = 256a$. Using the BME method, the rates were computed as explained in Section 2.4. The magnification in the insets shows the broad variation of the rates corresponding to modes very close to the band edge, which can be thought of as Anderson-localized cavity-like modes (cf. Section 1.3.1) with a broad distribution of Q-s (cf. Section 3.1).

Panel (a) of Fig. 3.6 presents the fixed-$\langle \delta R^2 \rangle$ model, with the four possible combinations of $\delta = 0.06(2\pi)$, $\delta = 0.005(2\pi)$, $\sigma = 0.006a$ and $\sigma = 0.002a$ (see the legend). As can be seen, within this model, changing δ can have an effect as dramatic as that

51
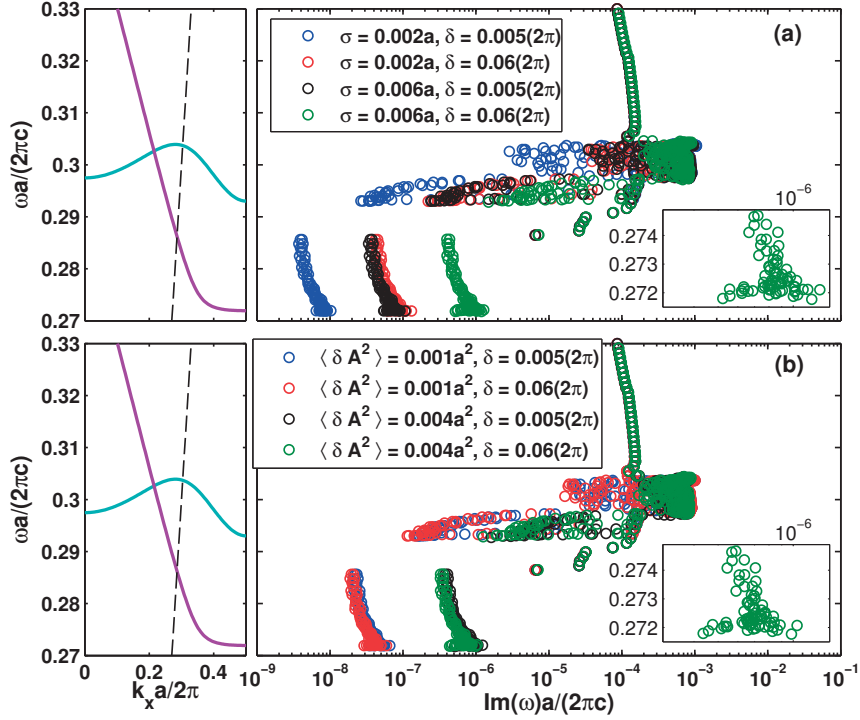
Figure 3.6: Computed radiation loss rates of the waveguides with disorder. (a): $\langle \delta R^2 \rangle = const$ model; (b): $\langle \delta A^2 \rangle = const$ model. Insets: detail of the rates close to the band edge. On the left, the guided bands of the regular structure (solid lines) and the light cone (dashed line) are displayed for reference.

of changing σ, with an order of magnitude difference present in the loss rates of the modes when going from the high $\delta = 0.06(2\pi)$ to the low $\delta = 0.005(2\pi)$. In panel (b) we show a similar plot but for the fixed-$\langle \delta A^2 \rangle$ model, with the same two values of δ and with $\langle \delta A^2 \rangle = 0.004a^2$ and $\langle \delta A^2 \rangle = 0.001a^2$. Here, in contrast, changing δ does not have a very pronounced effect, with the radiative rates being only very slightly higher in the low-δ case. This single-realization data, together with the sample profiles given in Fig. 3.5, suggest that **fine features** in the shape of the holes do not contribute as strongly to the disorder effects as do the smooth features.

To test this further, we computed the Density of States (DOS) of the modes close to the band edge, by a statistical average over 500 disorder realizations. The computed DOS is plotted in Fig. 3.7, panels (a)-(b) for the fixed-$\langle \delta R^2 \rangle$ model and panels (c)-(d) for the fixed-$\langle \delta A^2 \rangle$ one. To emphasize the role of the irregular hole shape, we also plot the DOS with the commonly adopted simple disorder model of constant radius fluctuations (corresponding to the limiting case $\delta \to \infty$). Oscillations in the high-frequency tails originate from the finite length of the simulated waveguide. All the computed histograms show a *Lifshitz tail* below the band edge. Modes in this region are spatially localized [63, 113], and slow-light propagation is consequently hindered.
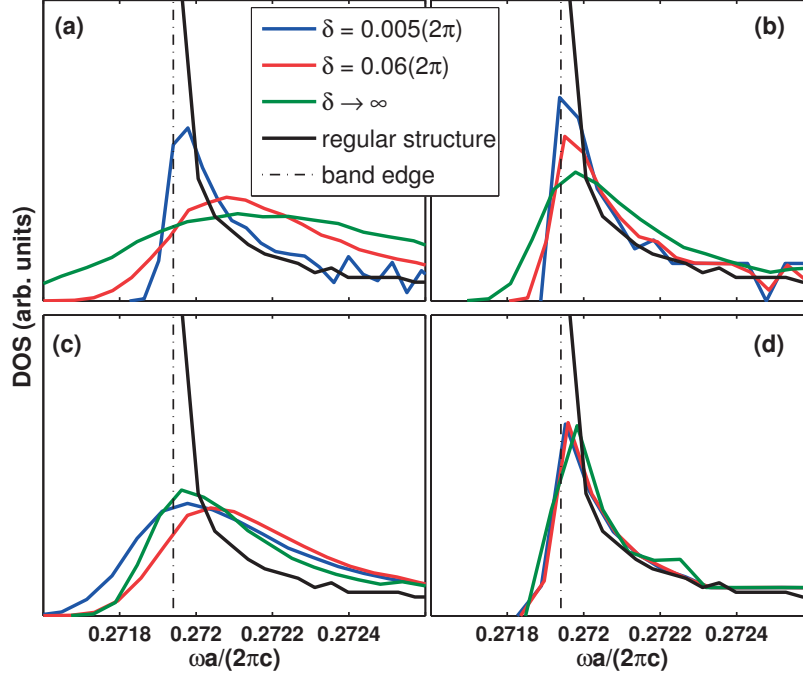
Figure 3.7: Density of states of the waveguide modes close to the band edge (marked by a dashed-dotted line), for (a): $\sigma = 0.006a$; (b): $\sigma = 0.002a$; (c): $\langle \delta A^2 \rangle = 0.004a^2$; (d): $\langle \delta A^2 \rangle = 0.001a^2$.

From the DOS it appears, once more, that the correlation angle δ has a strong effect on the distribution only in the $\langle \delta R^2 \rangle = const$ case, where the broadening of the band edge increases considerably for increasing δ. In this case, we also expect the parameter δ to affect significantly all effects due to disorder, such as Anderson localization and the resulting breakdown of slow-light propagation. We further note that in Ref. [99], a related model for waveguide disorder was studied, assuming holes divided into a number of constant-radius segments. Fixing the standard deviation of the radii, the dependence of the out-of-plane losses could thus be computed as a function of the number of segments N, which defines a correlation length $L_c = 2\pi R_0/N$. A maximum of the losses was found for $N = 5$, i.e. at a finite correlation length. Our results show instead that the disorder effects increase monotonously with increasing correlation angle, thus also with correlation length, which in our model can be defined as $L_c = R_0\delta$. We find this result more intuitive in view of the above discussion of hole-area fluctuations. The discrepancy could be simply due to the different disorder models that were used, but in principle further investigation is recommended.

In all our simulations, the sum in eq. (3.14) was restricted to $|m| \leq m_{\max}$. We have carefully checked that all results were well converged starting at $m_{\max} = 5$ (dashed-dotted lines in Fig. 3.5(b) and (d)). This remark corroborates our statement that fine features in the disorder are not as relevant as the smooth ones. Intuitively, this is due to the typical wavelength of the electromagnetic modes of the PhC, which produces a

spatial averaging of features in the dielectric profile on a much smaller spatial scale.

3.2.3 Implications for waveguide fabrication*

The main result presented here can be broken down in two statements. First – confirming the suggestion made in a recent experimental study [103] – it is indeed the magnitude of the fluctuations of the hole area, $\langle \delta A^2 \rangle$, which determines the magnitude of the disorder effects. This is evident from Figs. 3.6 and 3.7, in which the $\langle \delta A^2 \rangle = const$ model is virtually independent of δ. Second, when $\langle \delta R^2 \rangle = const$ is imposed instead, the disorder effects are strongly dependent on δ, with a small correlation angle corresponding to much smaller loss rates and spectral broadening. Insight is provided by comparing panels (b) and (d) of Fig. 3.5, where the average quantities $\langle |C_m|^2 \rangle$ are plotted for the corresponding hole models in panels (a) and (c). The dashed-dotted lines in panels (b) and (d) mark the convergence range $|m| \leq m_{max} = 5$. In the case of fixed radius fluctuation depicted in panel (b), the values of $\langle |C_m|^2 \rangle$ in this small-$|m|$ range vary considerably when varying δ. This is due to the fact that the parameters σ and δ determine respectively the integral and the width of the distribution $\langle |C_m|^2 \rangle$ as a function of m. In the case of fixed hole-area fluctuations shown in panel (d) instead, the two curves differ mainly in their width, while their values in the vicinity of $m = 0$ are closer than in the previous case. Thus, for fixed area fluctuations, the C_m coefficients relevant to the results vary less as a function of δ.

The fabrication process of a PhC does not correspond to either of the two limiting models considered here. The cross section of the e-beam used for lithography and the subsequent etching process are likely to set a *typical length scale* for the hole shape. For PhCs with nominally constant hole radii, this situation is however expected to be closer to the fixed-$\langle \delta R^2 \rangle$ assumption, as panels (a) and (c) of Fig. 3.5 also clearly suggest. We conclude that, while hole-area fluctuations are the single relevant parameter to quantify disorder effects, this parameter is only indirectly determined by the details of the fabrication process, which instead directly set the amplitude of radius fluctuations and their correlation angle. If any control over those two parameters is possible in the fabrication process, then, to increase the PhC quality, we propose to minimize the angular scale of the hole roughness δ, while keeping its amplitude constant.

4 Automated Optimization of Photonic Crystals

In this Chapter, we present the implementation of an automated, global optimization of photonic crystal devices, and apply it to various structures.

In Section 4.1, we focus on the L3, H0, and H1 cavities in silicon, which are very widespread designs due to their compactness, simplicity, and small mode volume. However, the best designs for these cavities prior to our work had Q-values of a few times 10^5 at most, namely one order of magnitude below the bound set by fabrication imperfections and material absorption in silicon. The Section is adapted from [78] (M. Minkov and V. Savona, "Automated optimization of photonic crystal slab cavities," *Scientific Reports* **4** (2014)), where we use a genetic algorithm to find a global maximum of the quality factor of these designs, by varying the positions of few neighboring holes. We consistently find Q-values above one million – one order of magnitude higher than in previous devices. Furthermore, we study the effect of disorder on the optimal designs (in the same way as presented in Section 3.1), and conclude that a similar improvement is also expected experimentally in state-of-the-art systems.

These outstanding predictions led to several collaborations with experimental groups. Two of the ensuing results are presented in Section 4.2. In Section 4.2.1, we report an experimental realization of an ultra-high-Q L3 cavity, using the design one of the designs obtained in Section 4.1. The cavity was fabricated by prof. Antonio Badolato and Yiming Lai at the University of Rochester, while the spectroscopy was performed by prof. Matteo Galli, prof. Dario Gerace, Giulia Urbinati, and Stefano Pirotta at the University of Pavia. The Section is adapted from our publication, Ref. [114] (Y. Lai et al., "Genetically designed L3 photonic crystal nanocavities with measured quality factor exceeding one million," *Appl. Phys. Lett.* **104** (2014)). The measured $Q = 2 \times 10^6$ is among the highest recorded in any PhC cavity, and is in particular one order of magnitude higher than that of previous L3 designs. In Section 4.2.2, adapted from Ref [115] (U. P. Dharanipathy et al., "High-Q silicon photonic crystal cavity for enhanced optical nonlinearities," *Appl. Phys. Lett.* **105** (2014)), we report on a similar experiment,

but utilizing an H0 cavity design also taken from Section 4.1. The cavity was fabricated and characterized by prof. Romuald Houdré, Dr. Perumal Dharanipathy, and Mario Tonin here in EPFL, and the measured Q-factor of $400,000$ is higher than the previous-best **theoretical** value for this cavity. Additionally, this design has the advantage of a tiny modal volume, several times smaller than that of the L3 design, which is in turn smaller than that of other ultra-high-Q designs like the A1 or HS (Section 3.1). The two cavities presented in Section 4.2 thus have some of the largest Q/V ratios ever reported – an important figure of merit for most applications. They thus hold great promise for the reliable fabrication of on-chip devices based on ultra-high-Q resonators for nonlinear and quantum photonics.

In Section 4.3, we present other cavity optimizations that we have performed, illustrating further the broad applicability of our procedure. In Section 4.3.1, we present a design for an L3 cavity in a Gallium Nitride (GaN) slab. This material has a lower refractive index than Si, resulting in lower Q values, but is very important for a variety of reasons, e.g. the fact that it is transparent at optical frequencies. The optimized cavities were fabricated by Dr. Noelia Vico-Triviño and Dr. Jean-François Carlin in the group of Prof. Nicolas Grandjean in EPFL, and optically characterized by Giulia Urbinati and Prof. Matteo Galli in the University of Pavia. The results, and the accompanying simulations that we performed, are published in Ref. [116] (N. Vico-Triviño et al., "Gallium nitride L3 photonic crystal cavities with an average quality factor of 16 900 in the near infrared," *Appl. Phys. Lett.* **105** (2014)). Section 4.3.1 is adapted from that publication. In Section 4.3.2, we report on the Q-optimization of an L3 cavity in a PhC formed in a silicon slab embedded in SiO_2. This design is important in view of integrating photonic devices with existing Complementary Metal–oxide–semiconductor (CMOS) technologies used for the fabrication of todays nano-electronic devices. Finally, in Section 4.3.3, we report on the optimization of a cavity with respect to a figure of merit other than the quality factor. In particular, we focus on a cavity used for the optical trapping of a dielectric particle [109], and try to maximize the electric field in the trapping region, thus boosting the efficiency of the device.

Section 4.4 presents another illustration of an optimization that goes beyond the quality factor of a cavity. The Section is adapted from Ref. [117] (M. Minkov and V. Savona, "Wide-band slow light in compact photonic crystal coupled-cavity waveguides," *Optica* **2** (2015)), where we propose a photonic crystal coupled-cavity waveguide with an ultra-compact arrangement of the constituent cavities in the propagation direction. We use the automatic optimization to tune several structural parameters to engineer slow light with a constant group index n_g over a wide bandwidth (see Section 1.3.1). We propose several specific silicon designs, including one with $n_g \approx 37$ over a 20nm wavelength range, and another one with $n_g \approx 116$ over a 8.8nm band, which yields a group index-bandwidth product of 0.66 – a record value among all slow-light devices. The design is experimentally beneficial because of its small footprint and straightforward fabrication and could find applications for optical storage or switching, and for

generating quantum states of light.

4.1 High-Q-optimized silicon air-bridge cavities: theory

4.1.1 Background to cavity optimization*

As discussed in Section 1.3, optical nonlinearities, the Purcell effect, and radiation-matter coupling all depend directly on the Q and inversely on the V of a cavity mode [47, 68, 69, 118]. For this reason, a major effort has been directed towards the maximization of Q and/or the minimization of V, i.e. to cavity *optimization*. To this purpose, three different approaches can be broadly defined. The first is the inverse problem approach [84, 88], where an effective equation for the dielectric profile is defined starting from the desired shape of the cavity mode, through a semi-analitical formalism. The second is the topology optimization method [119], where variations of the entire topology of the PhC are allowed, and the objective function (either Q or Q/V) is maximized numerically [120–122]. Although some of these works [118, 122] have achieved remarkably high values of Q and Q/V, the resulting cavity designs often pose a serious technological challenge in terms of manufacturability, as they present excessively small holes or holes with irregular pattern and sharp features. A third and completely different strategy consists in optimizing simple PhC cavity designs by tweaking only a few geometrical parameters (e.g. by shifting the positions and varying the radii of nearby holes), in order to preserve the small spatial footprint and ease of fabrication of the design. This approach has produced encouraging results, in particular for the three most widespread cavity designs, namely the L3 cavity [82, 101, 123, 124], the H0 cavity (also known as 'zero-cell' or 'point-shift' cavity) [89, 101], and the H1 cavity [101, 102, 125–127]. It brought in some cases an increase of the quality factor by more than one order of magnitude – reaching values of a few hundred-thousands, or even above one million for the H1 hexapole mode [126, 127] – while the mode volume was only slightly increased or sometimes even reduced. A common feature of all these optimization works however is the lack of an exhaustive exploration of the parameter space in search of a global maximum of the objective function.

Experimentally, the quality factor of PhC cavities is limited by extrinsic losses, due to absorption and fabrication imperfections [79, 94, 95, 100]. More precisely, the measured quality factor Q_e can be expressed as

$$\frac{1}{Q_e} = \frac{1}{Q_t} + \frac{1}{Q_a} + \frac{1}{Q_d}, \tag{4.1}$$

where Q_t is the theoretical quality factor expected from the ideal structure, while $1/Q_a$ and $1/Q_d$ are measures of the additional loss rates due to material absorption and to disorder-induced extrinsic losses respectively. This formula was extensively discussed in Section 3.1. For silicon PhCs and wavelengths in the 1.5 μm range, record

values of Q_e ranging between one and nine million were measured on cavity designs based on a modulation of a one-dimensional PhC waveguide [83, 85, 94, 127–129]. For these designs, Q_t ranges between 2×10^7 and 10^8, suggesting a value of several million for both Q_d and Q_a. These waveguide-based designs, however, have a considerably larger footprint and display a mode volume up to three times larger than that of defect cavities. There are no fundamental reasons that should prevent the quality factor of the latter from reaching values of several million, close to the current bound set by disorder and absorption.

Here, we adopt a simple optimization strategy. Similarly to several existing works [28, 82, 89, 101, 102, 123, 124, 126, 127], we choose a small set of variational parameters – typically the spatial shifts of a few holes next to the defect – thus producing designs that can be easily realized with current nanofabrication processes. Differently from these works however, we carry out a global exploration of the parameter space by means of an evolutionary algorithm. Here, by 'global' we mean the exhaustive search for the global maximum of the quality factor in the parameter space of choice. In this way we demonstrate that it is possible to systematically optimize L3, H0, and H1 cavities to values of Q_t well above 10^6 – typically more than one order of magnitude above previous optimal values – without a large increase of the mode volumes. The key to this drastic improvement is the exhaustive search that finds configurations overlooked by previous approaches, as exemplified by the simplest of the L3 designs considered here [123]. This optimization procedure is made computationally feasible thanks to the use of the guided-mode expansion (Section 2.3) that allows calculation of the modes and quality factors of each variation within minutes of computational time. Furthermore, we statistically analyze the influence of fabrication imperfections on the optimal designs and conclude that a considerable improvement in the **experimental** quality factor can be expected. This has actually been confirmed by the experiments [114, 115] discussed in Sections 4.2.1 and 4.2.2.

All cavities studied here are formed in the usual triangular lattice with pitch a of air-holes of radius R in a silicon ($n = 3.46$) slab of thickness d. All lengths are expressed in units of a, but we set the parameters such that, for the typically used thickness $d = 220$nm, the resonant modes lie in the telecommunication band around $\lambda = 1.55\mu$m. For the simulation of a single structure, we use the GME, whose reliability for modelling high-Q cavities was discussed extensively in Section 2.3. The computational parameters used here are $G_{\max} = 2.5 \times 2\pi/a$, $\alpha_{\max} = 1$ (4 in the simulations related to Fig. 4.2(f)), and $N_k = 3$ (cf. Section 2.3). As a further check of the validity of the results, all final (optimized) structures are also simulated using the 3D finite-difference time-domain method [73]. For each of the optimized designs presented here, we also analyze the probability density of Q_e in the presence of fabrication imperfections (and neglecting the absorption loss contribution $1/Q_a$). The disorder model is the same as in Section 3.1.
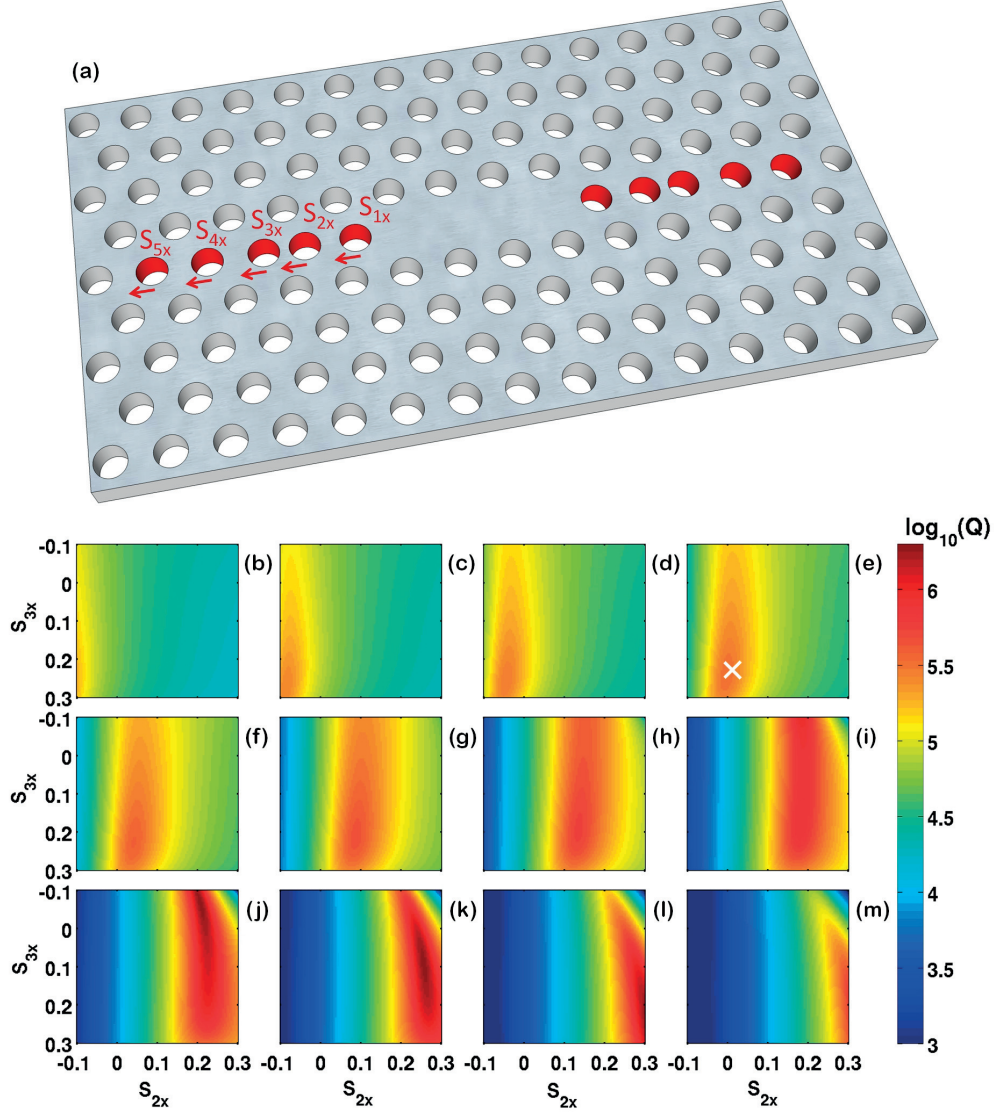
Figure 4.1: (a): The design of the L3 cavity. For quality factor optimization, shifts of the positions of the five neighbouring holes in the x-direction were introduced, labeled as $S_{1x}, S_{2x}, S_{3x}, S_{4x}$, and S_{5x} in the figure. (b)-(m): A parameter scan of the GME-computed quality factor values for different S_{1x}, S_{2x} and S_{3x}, where S_{1x} starts from $0.15a$ in panel (b) and increases in multiples of $0.02a$ in every consecutive panel, up to $0.37a$ in (m), and $S_{4x} = S_{5x} = 0$ in all panels.

4.1.2 Preliminary considerations*

The first cavity design we investigate is the L3 cavity that has been omnipresent in this thesis (Fig. 4.1(a)), with $d = 0.55a$ and $R = 0.25a$. The quality factor of this cavity has already been optimized [123] with respect to shifts of the positions of three neighbouring holes (marked $S_{1x}, S_{2x},$ and S_{3x} in the Figure), by using a simplified

approach in which, starting from the unshifted design, each of the three shifts has been varied once while keeping the two others constant. To explore the extent to which this approach is suitable, we compute a full map of the quality factor on a relevant region of the (S_{1x}, S_{2x}, S_{3x})-space. The map is displayed in Fig. 4.1(b)-(m). There, in each panel, Q_t is plotted as a function of S_{2x} and S_{3x}, while the value of S_{1x} increases from $0.15a$ to $0.37a$ in steps of $0.02a$ when going from panel (b) to panel (m). Technically, these plots already provide a global optimization of the cavity (a clear maximum of Q_t can be identified), although performed in the least practical, brute-force way. If applied to the panels of Fig. 1 (though approximately, given the coarse S_{1x} step used in this figure), the simplified optimization procedure in [123] leads to the point marked by a white cross in panel (e) (more precisely, $S_{1x} = 0.21a$, $S_{2x} = 0.01a$, $S_{3x} = 0.23a$), i.e. far off the maximum that can be seen in panel (k) at $S_{1x} = 0.33a$, $S_{2x} = 0.26a$, $S_{3x} = 0.10a$. It is also interesting to note that within the range of the plots in Fig. 4.1(b-m), two maxima are visible - a local one around $S_{1x} = 0.25a$, $S_{2x} = 0.09a$, $S_{3x} = 0.21a$ in panel (g) and another one which first appears at $S_{1x} = 0.29a$, $S_{2x} = 0.18a$, $S_{3x} = -0.10a$ in panel (i) and then shifts to become the global maximum at $S_{1x} = 0.327a$, $S_{2x} = 0.257a$, $S_{3x} = 0.116a$. In general, an even larger number of local extrema might in principle be present, especially for larger number of parameters, thus making the search for the global extremum more difficult. This highlights the need for a global optimization procedure instead of a more conventional algorithm (e.g. the conjugate gradient) that would almost inevitably find a local rather than a global maximum.

Ideally, we would like to apply a global, stochastic (since there is no general way to come up with a 'good' guess for a starting point) procedure to the problem of optimizing the cavity parameters. Thus, we choose to employ the genetic algorithm provided in the MATLAB® Global Optimization Toolbox [130], which starts from a random initial population (i.e. a set of points in parameter space) and goes on to create a sequence of generations (new sets of such points) where the 'fittest' individuals are kept. The algorithm incorporates an array of evolutionary inspired techniques, including cross-over, random mutations, and natural selection of individuals. An 'individual' in our case is simply one Q-computation for a particular set of cavity parameters, and the higher the quality factor, the higher the assigned 'fitness' of the individual (i.e. its probability to survive to the next generation and/or to be mixed with another individual to produce an 'offspring' lying in parameter space somewhere in between the two). With the increase of the number of free parameters, the number of generations needed for convergence increases. Here, the maximum number of parameters used is 8, in which case ≈ 300 generations each consisting of 120 individuals are needed for convergence. This can however be greatly improved if a rough optimization is first carried out (with a large allowed range for the free parameters), followed by a finer optimization centered around the rough maximum. The longest optimization we ran thus took about a week on twelve CPUs with 32GB of RAM. This would have taken more than ten years to finish using the same machine but employing an FDTD solver
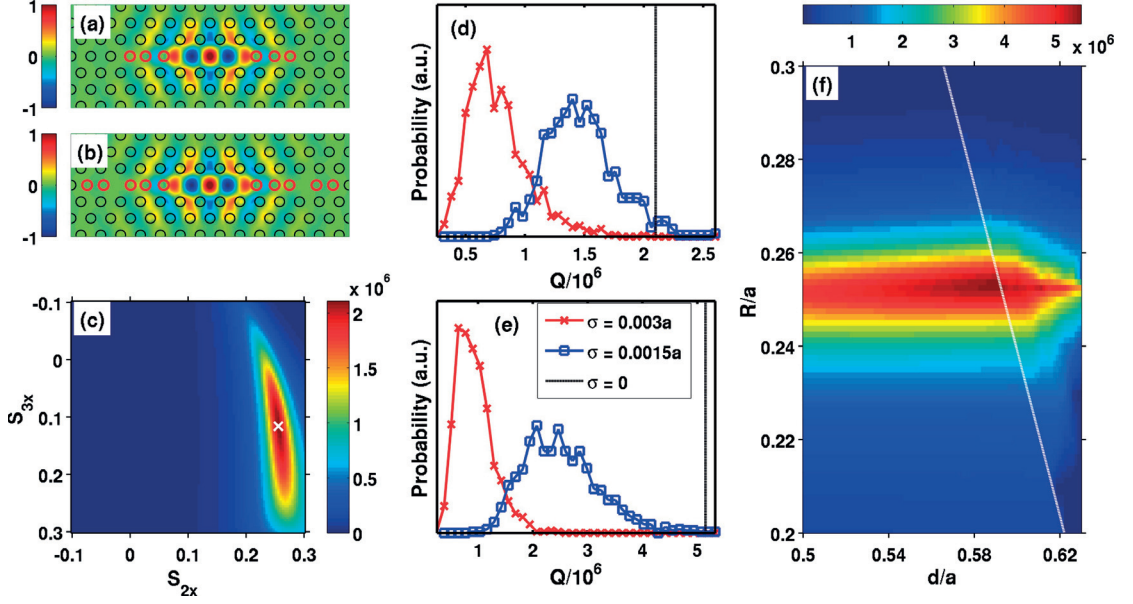
Figure 4.2: (a)-(b): Electric field (E_y) profiles of the two optimized L3 designs; the holes that were displaced are marked in red. (a): $S_{1x} = 0.327a$, $S_{2x} = 0.257a$, $S_{3x} = 0.116a$. (b): $S_{1x} = 0.337a$, $S_{2x} = 0.270a$, $S_{3x} = 0.088a$, $S_{4x} = 0.323a$, $S_{5x} = 0.173a$. (c): Dependence of Q_t on S_{2x} and S_{3x} for $S_{1x} = 0.327a$; the shifts in the design of panel (a) are marked by a white cross. (d): Histograms showing the probability of occurrence of different Q_e-values in the design of panel (a), for two different disorder magnitudes: $\sigma = 0.003a$ (red) and $\sigma = 0.0015a$ (blue). The black line indicates the ideal Q_t. (e): Same as (d), for the design of (b). (f): Dependence of Q_t on the overall radius and the slab thickness, for the values of $S_{1x} - S_{5x}$ corresponding to the optimal design in (b). On the right of the dashed line, the slab becomes multi-mode at the cavity frequency.

instead of the GME.

4.1.3 Optimized L3 cavity*

We choose the objective function of the optimization to be the GME-computed quality factor Q_t. When applied to the L3 with freedom in S_{1x}, S_{2x} and S_{3x}, the optimal design is found for $S_{1x} = 0.327a$, $S_{2x} = 0.257a$ and $S_{3x} = 0.116a$ (Fig. 4.2(a)). This yields $Q_t = 2.1 \times 10^6$ (FDTD: 1.6×10^6), which is an increase by a factor of ≈ 6 as compared to the previously highest value [123] of 3.3×10^5 (FDTD: 2.6×10^5), while the mode volume (defined as in eq. (1.17)) increases from $0.77(\lambda/n)^3$ to $0.94(\lambda/n)^3$. One obvious advantage of using evolutionary optimization rather than the brute-force parameter scan of Fig. 4.1 is the precision with which the maximum can be pinpointed; another one is that less than a thousand cavity computations are needed to reach this extremum, while each of the panels of Fig. 4.1 contains 10^4 computations. Moreover, the design can be further improved if two more shifts (S_{4x} and S_{5x} in Fig. 4.1(a)) are allowed in the optimization, which is still easily handled by the genetic algorithm,

61

although ≈ 100 generations of 80 individuals each are needed for convergence. In this case, the optimized design is found for $S_{1x} = 0.337a$, $S_{2x} = 0.270a$, $S_{3x} = 0.088a$, $S_{4x} = 0.323a$, and $S_{5x} = 0.173a$ (Fig. 4.2(b)), and has $Q_t = 5.1 \times 10^6$ (FDTD: 4.2×10^6) with mode volume $V = 0.95(\lambda/n)^3$, i.e. an increase in Q_t by one order of magnitude compared to the previous optimal values [123, 124], with an increase in the mode volume comparable to the three-shift case. The resonant frequency of the modes is at $\frac{\omega a}{2\pi c} = 0.259$ for both designs, which is slightly lower than the frequency $\frac{\omega a}{2\pi c} = 0.263$ of the unmodified $L3$ (i.e. with the same d/a and R/a but with no hole shifts).

The choice of the particular hole shifts presented here is not unique, but appears optimal for the given number of free parameters (3 or 5, respectively). A more intricate design including 8 parameters is presented in Section 4.1.4. Having only a few hole shifts as free parameters results in a technologically friendly structure, and in a more compact cavity defect, characterized by a much smaller footprint on the PhC, than waveguide-based ultrahigh-Q designs [83, 85, 88]. In addition, the present designs are as robust to fabrication imperfections as any other high-Q PhC cavity [79], as can be inferred from Fig. 4.2(c)-(f). In panel (c) we plot, for the three-shift L3, the dependence of Q_t on S_{2x} and S_{3x} as in Fig. 4.1, but for the value $S_{1x} = 0.327a$ corresponding to our optimal design (the white cross indicates where the design lies with respect to S_{2x} and S_{3x}). In this plot, we observe that the width of the maximum is larger than the typical uncertainty in the hole positions (smaller than $0.005a$ for Si [103]). Furthermore, in Fig. 4.2(d)-(e) we show, respectively for the three- and five-shift design, the computed probability of occurrence of Q_e-values in presence of disorder. Each of these histograms was obtained by simulating 1000 disordered realisations of the corresponding cavity design. The blue plot in panel (d) in particular shows that for a state-of-the-art disorder magnitude $\sigma = 0.0015a$ (i.e. about 0.6nm [94, 95], when assuming $a = 400$nm in a silicon slab), the average value lies at about $Q_e = 2.5 \times 10^6$, i.e. quality factors one order of magnitude larger than the previous **theoretical** maximum can be expected **in practice**, highlighting the significance of the design optimization. Finally we note that, for a given set of optimal values of the S_{nx} parameters, the designs are also robust to small changes in the overall hole radius R and slab thickness d, which can originate from an offset in the fabrication process and/or be introduced on purpose in order to e.g. tune the resonant frequency to a desired value. To show this, in panel (f) we plot the value of Q_t obtained by varying R and d while keeping the shifts $S_{1x} - S_{5x}$ constant and set to the values obtained for the optimal design computed at $d = 0.55a$ and $R = 0.25a$. We observe that $Q_t > 4 \times 10^6$ for a range of R and d values which is much larger than the fabrication uncertainty and which allows fine-tuning of the frequency. For certain values of d and R (to the right of the dashed line in the Figure), higher-order guided modes of the slab become non-negligible. More precisely, the second $\sigma_{xy} = 1$ guided band of the underlying slab (cf. Fig. 1.4) becomes resonant with the cavity mode and introduces a new loss channel [25]. We point out that, while Q_t appears to systematically increase with d in the single-mode region, it drops rapidly
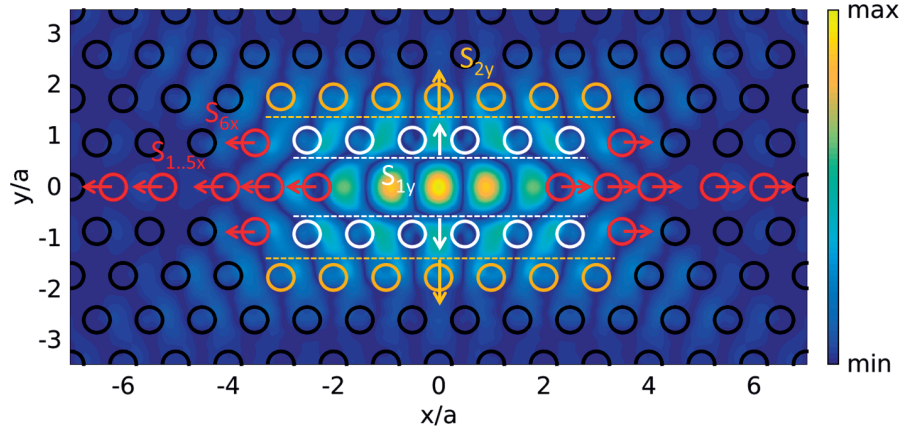
Figure 4.3: Design of the 8-shift L3 cavity. The shifts S_{1x} to S_{5x} are defined in the same way as for the design of Fig. 4.2(b). Additionally, a 6-th shift in the x-direction is introduced as marked, as well as two shifts in the y-direction. The latter consist of moving **all** holes marked in white by a distance S_{1y} in the y-direction, and all holes marked in brown – by a distance S_{2y}. The color map shows the absolute value of the y-component of the electric field of the fundamental cavity mode.

as soon as d increases into the multi-mode region. An analogous trend of the loss rates as a function of R/a and d/a is expected for the other cavity designs discussed in this study. In principle, one could consider d/a and/or R/a as free parameters in the optimization, but in that case setting a target wavelength, for a fixed value of d that might arise from technological requirements, becomes more difficult.

4.1.4 L3 cavity with a Q of 20 million

To increase the Q of the L3 cavity even further, we tried increasing the number of optimization parameters in various configurations. It was found that modifying the hole radius of the 5 holes used in the 5-shift design of Fig. 4.2(b) does not bring a significant improvement, and neither do position shifts in the holes further out along the $y = 0$ axis (intuitively, it is straightforward to expect that the holes closest to the cavity defect have the highest influence). We thus introduced shifts in the holes above and below the cavity, trying various parameter configurations and running the automated optimization for each one. The best result was obtained with the 8-parameter design illustrated in Fig. 4.3. Using the same PhC parameters as in Section 4.1.3, the best design was found for $S_{1-6x} = [0.312, 0.209, 0.040, 0.227, 0.177, -0.014]a$, $S_{1y} = 0.058a$, $S_{2y} = 0.037a$, with a GME-computed Q of 23.7×10^6. This result was obtained with the standard computation parameters, $G_{\max} = 2.5 \times 2\pi/a$, $\alpha_{\max} = 1$, which are however somewhat insufficient for this ultra-high-Q cavity, since the FDTD-computed result is 14.2×10^6. Of course, when increasing the parameters to $G_{\max} = 3 \times (2\pi)/a$, $\alpha_{\max} = 9$, the agreement is restored, with a GME-computed Q of 15.9×10^6. In the final analysis of this L3 cavity, it was found that the Q can be further increased by
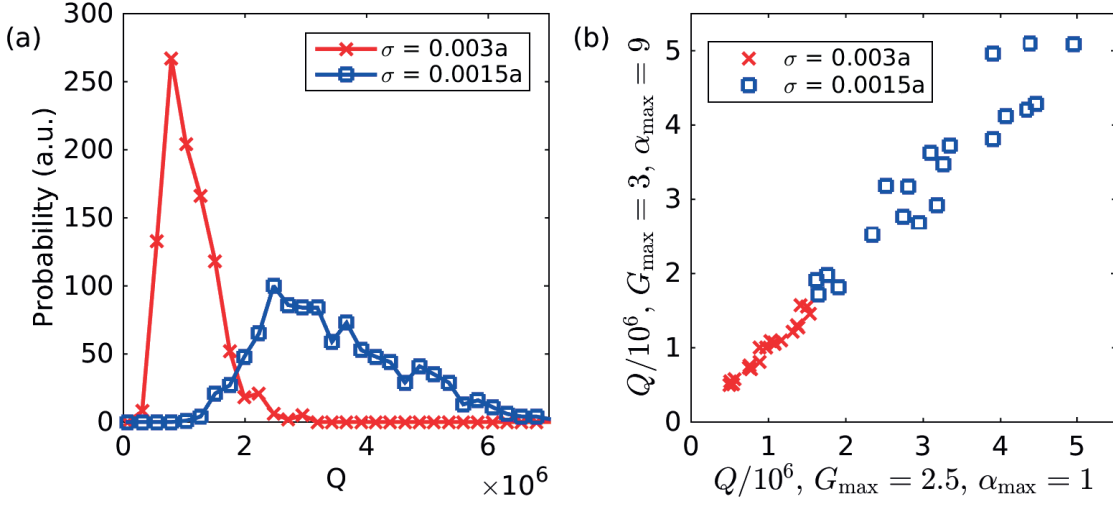
Figure 4.4: (a): Histograms of the probability distribution of the Q_e in presence of disorder for the optimized 8-shift cavity. 1000 disorder realizations were computed using the GME with $G_{max} = 2.5$ and $\alpha_{max} = 1$. (b): Correlation between the results of the $G_{max} = 2.5$ and $\alpha_{max} = 1$ and the $G_{max} = 3$ and $\alpha_{max} = 9$ computations for 20 disorder realizations for each of the two disorder magnitudes. The correlation coefficient is $\rho = 0.978$ for $\sigma = 0.003a$, and $\rho = 0.946$ for $\sigma = 0.0015a$.

a slight change of the overall hole radius. This brought the maximum Q of the design, obtained for $R = 0.255a$ instead of $0.25a$, to 20.0×10^6 (FDTD: 20.9×10^6).

In Fig. 4.4(a), we perform the same statistical analysis of the expected experimental Q_e as for the previous L3 designs of Section 4.1.3. We simulate 1000 disorder realizations for the two disorder magnitudes $\sigma = 0.003a$ and $\sigma = 0.0015a$. The mean value $\langle Q_e \rangle$ is higher than the one of the 5-shift design, but as expected in view of our discussion in Section 3.1, it does not increase by much, since the losses are disorder-dominated. The computations were performed with the parameters $G_{max} = 2.5 \times 2\pi/a$, $\alpha_{max} = 1$, and are in this case sufficiently accurate, since the Q is lowered by the disorder. This is illustrated in Fig. 4.4(b), where we plot the quality factor computed with those parameters vs. the one computed with $G_{max} = 3 \times 2\pi/a$, $\alpha_{max} = 9$, for 20 disorder realizations for each of the two disorder magnitudes. As can be seen, the values are very close and very strongly correlated, which justifies the use of the lower convergence parameters to obtain the statistics of the disorder-induced losses.

4.1.5 Far-field considerations

The far field of a cavity is defined as the electromagnetic field at a large distance (e.g. much larger than the resonant wavelength) away from the cavity region. A number of previous works on improving the cavity Q have discussed the far-field components of the resonant mode [83, 84, 88, 89, 101, 102, 123], and for a good reason. In a perfectly
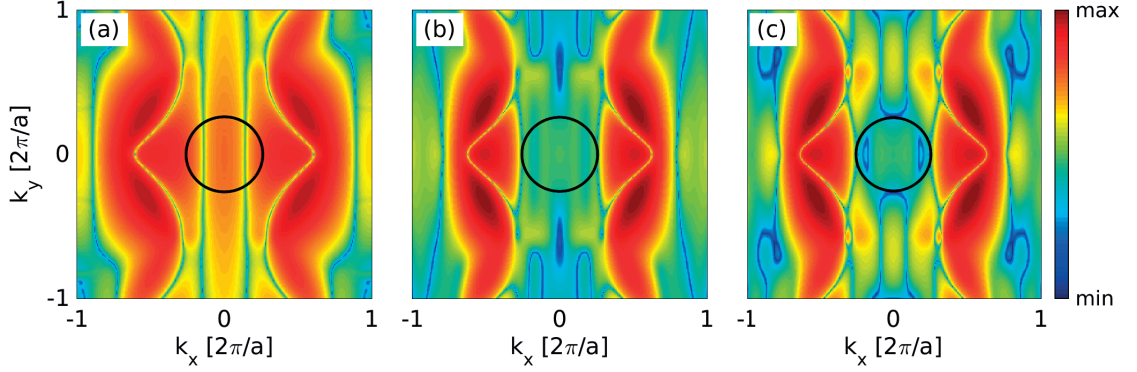
Figure 4.5: (a): Log-scale color map of the Fourier transform of the electric field E_y at a plane 70nm above the PhC slab for an un-optimized L3 cavity ($Q = 6900$). The light cone $k_x^2 + k_y^2 < \omega_0^2/c^2$ is shown with a black circle. (b): Same as (a), for the five-shift design of Section 4.1.3 ($Q = 4.2 \times 10^6$). (c): Same as (a), for the eight-shift design of Section 4.1.4 ($Q = 2.1 \times 10^7$).

loss-less cavity, i.e. one with an infinitely high quality factor, the far field is zero as all field components decay exponentially at large distances. In the case of slab-PhCs, as discussed in Chapter 1 and Section 1.3.2 in particular, this is not possible due to the fact that the band gap is only partial, and the cavity mode inevitably has components that are radiating in the direction orthogonal to the slab. This results in finite far-field components, and also in a finite Q. In fact, the latter can be obtained by integrating the electromagnetic energy radiated through the former [84, 131], and so the two concepts are intimately related. To put it simply, the quality factor describes the total power radiatively lost from the cavity, while the far field profile gives additional information on the directions in which the electromagnetic energy is radiated.

It should be clear, then, that the goals of maximizing the cavity Q and of minimizing the (integrated) far-field components are equivalent. If one cavity has a higher quality factor than another, then it must also have a weaker far-field emission. Restating the quality factor optimization into a far-field problem could still be beneficial as illustrated by the analytical inverse-design cavity proposals of Refs. [84, 88]. However, when it comes to the exploration of the parameter space in the framework of our optimization scheme, there is no advantage in computing the far field instead of the quality factor. Still, for completeness and comparison to previous works, in Fig. 4.5 we plot the Fourier transform of the electric field recorded in a plane 70nm above the slab, for an un-optimized and for two of the optimized L3 cavities. The far field can be computed from the Fourier components that lie inside the light cone (black circle in the Figure) through a simple transformation [84, 131]. As predicted and can be seen in the Figure, these components are more and more strongly suppressed as the Q of our optimal designs increases.
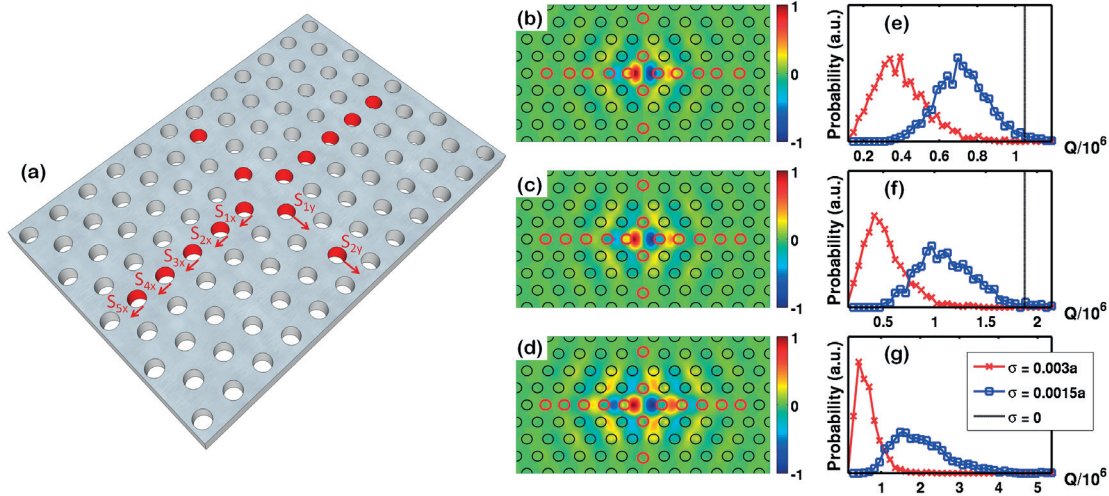
Figure 4.6: (a): The design of the H0 cavity. For quality factor optimization, shifts of the positions of the five neighboring holes in the x-direction and the two neighboring holes in the y-direction were introduced, labeled as $S_{1x}, S_{2x}, S_{3x}, S_{4x}, S_{5x}, S_{1y}$ and S_{2y} in the Figure. (b)-(d): Electric field (E_y) profiles of three optimized designs with increasing Q and V. (b): $S_{1x} = 0.216a$, $S_{2x} = 0.103a$, $S_{3x} = 0.123a$, $S_{4x} = 0.004a$, $S_{5x} = 0.194a$, $S_{1y} = -0.017a$, $S_{2y} = 0.067a$. (c): $S_{1x} = 0.280a$, $S_{2x} = 0.193a$, $S_{3x} = 0.194a$, $S_{4x} = 0.162a$, $S_{5x} = 0.113a$, $S_{1y} = -0.016a$, $S_{2y} = 0.134a$. (d): $S_{1x} = 0.385a$, $S_{2x} = 0.342a$, $S_{3x} = 0.301a$, $S_{4x} = 0.229a$, $S_{5x} = 0.116a$, $S_{1y} = -0.033a$, $S_{2y} = 0.093a$. (e): Histograms showing the probability of occurrence of different Q_e-values in the design of panel (b), for two different disorder magnitudes: $\sigma = 0.003a$ (red) and $\sigma = 0.0015a$ (blue). The black line indicates the value of Q_t. (f)-(g): Same as (e), for the designs of (c)-(d). The $\sigma = 0$ line in panel (g) is not visible as Q_t occurs beyond the axis boundary.

4.1.6 Optimized H0 cavity*

Often, obtaining the highest possible theoretical Q_t is not the main goal of optimization (see the Discussion in Section 3.1). In fact, when Q_t gets above a limit set by the material and the fabrication process (currently $\approx 5 \times 10^6$ in silicon [94]), the experimentally measured Q_e is always dominated by losses due to disorder and/or absorption, and so weakly affected by further increase in Q_t. The potential of an automated optimization procedure is therefore best exploited when applied to other attractive properties. One example consists in maximizing Q_t while having the smallest possible mode volume, so that Q_t/V is as high as possible, since the latter is a figure of merit for applications in both cavity QED [47, 68, 84] and non-linear optics [69]. With this in mind, the second design we focus on is the H0 cavity [89, 101], namely the simple defect cavity with the smallest known mode volume.

The design of the H0 is shown in 4.6(a); the defining defect is the shift of two holes away from each other (S_{1x}), the thickness of the slab taken here is $d = 0.5a$, while the hole radius is $R = 0.25a$. For the optimization, we also use the consecutive shifts $S_{2x} - S_{5x}$,

as well as two shifts in the vertical direction, S_{1y} and S_{2y}. Using S_{1x}, S_{2x}, S_{3x}, S_{1y} and S_{2y}, the cavity has already been optimized [89] (following the same approach already discussed for the L3 [123]) to a quality factor of $Q_t = 2.8 \times 10^5$, with a corresponding mode volume $V = 0.23(\lambda/n)^3$. Here, we improve on this result by on one hand using the genetic optimization, and on the other by including S_{4x} and S_{5x}. It should be mentioned that in the optimization, an allowed range of variation for each parameter is set. For the H0, we find that the maximum allowed S_{1x} is a very important parameter, increasing which produces several different optimized designs. All of those are interesting, as increasing S_{1x} increases the mode volume but also the Q_t of the cavity. More precisely, the designs in 4.6(b)-(d) were obtained by imposing the following restrictions in the genetic algorithm: $S_{1x} \leq 0.25a$, $S_{1x} \leq 0.3a$, and $S_{1x} \leq 0.4a$, respectively. The ensuing optimal parameters $[S_{1x}, S_{2x}, S_{3x}, S_{4x}, S_{5x}, S_{1y}, S_{2y}]$ are as follows: $[0.216a, 0.103a, 0.123a, 0.004a, 0.194a, -0.017a, 0.067a]$ (panel (b)); $[0.280a, 0.193a, 0.194a, 0.162a, 0.113a, -0.016a, 0.134a]$ (panel(c)); and $[0.385a, 0.342a, 0.301a, 0.229a, 0.116a, -0.033a, 0.093a]$ (panel(d)). The corresponding quality factors are $Q_t = 1.04 \times 10^6$ (FDTD: 1.04×10^6), $Q_t = 1.88 \times 10^6$ (FDTD: 1.66×10^6), and, remarkably, $Q_t = 8.89 \times 10^6$ (FDTD: 8.29×10^6), while the respective mode volumes are $V = 0.25(\lambda/n)^3$, $V = 0.34(\lambda/n)^3$, and $V = 0.64(\lambda/n)^3$. The first among these three designs (panel (b)) has a mode volume only slightly larger than the previous most optimal design [89], combined to a quality factor almost four times larger. The last of the three designs (panel (d)) instead shows a more significant increase of the mode volume, but associated to an almost 30-fold increase of Q_t with respect to the value obtained in Ref. [89]. The resonance frequencies of the three designs decrease with the increase of V and are $\frac{\omega a}{2\pi c} = 0.280$, $\frac{\omega a}{2\pi c} = 0.275$, and $\frac{\omega a}{2\pi c} = 0.269$, respectively, while the original cavity with $S_{1x} = 0.14$ (and no other shifts) of Ref. [101] has $\frac{\omega a}{2\pi c} = 0.292$.

Similarly to what we have done above for the L3 cavity, in Fig. 4.6(e)-(g) we present the probability of occurrence of Q_e values, computed using 1000 random disorder realizations for each design and each disorder magnitude. From these histograms it appears clearly that, even though design 3 has the highest theoretical Q_t/V, it might not be the best choice in practice. According to Eq. (4.1) in fact, depending on the amount of disorder, the maximum value of the actual ratio Q_e/V will in general be achieved for a design having an intermediate value of Q_t. For example, in the case with $\sigma = 0.003a$ (red curves in panels (e)-(g)), the average values of Q_e (neglecting absorption) computed from the simulations are 3.97×10^5, 5.23×10^5, and 6.49×10^5, respectively, meaning that the highest Q_e/V would in practice be achieved by design 1. On the other hand, for the smaller disorder $\sigma = 0.0015a$ (blue curves in panels (e)-(g)), the corresponding average values of Q_e are 7.22×10^5, 1.12×10^6, and 2.02×10^6, and the highest average Q_e/V is achieved by design 2. For both values of σ, the expected Q_e/V for the five-shift L3 cavity is lower than that for any of the three H0 designs, thus the latter should be the cavity of choice for applications where Q/V is the most important figure of merit. We expect that design 3 will dominate for yet smaller values of σ, which
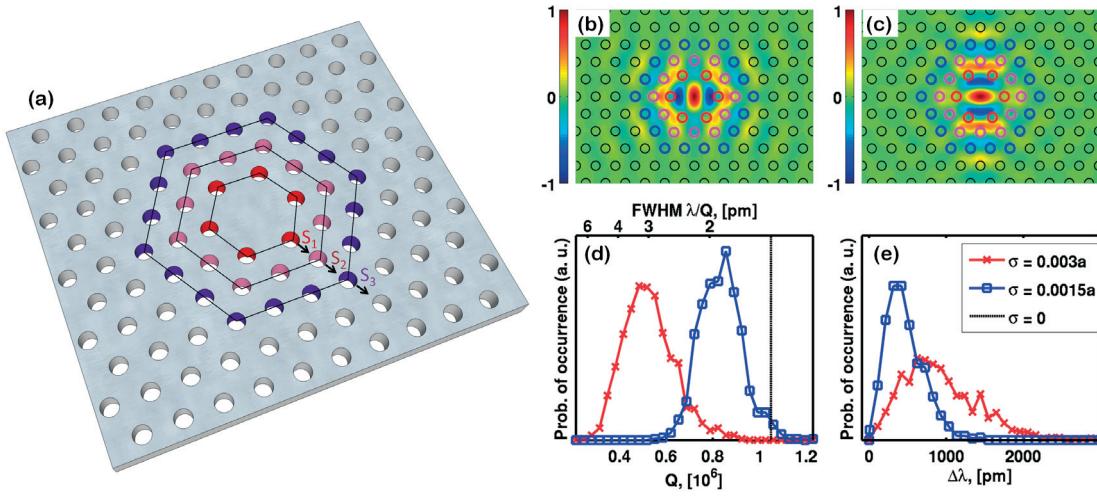
Figure 4.7: (a): The design of the H1 cavity. The size of the first three hexagonal "rings" of holes is varied for quality factor optimization, with the increase of the distance from a hexagon vertex to the center of the cavity given by S_1, S_2 and S_3 (marked). (b): Electric field (E_y) profile of the y-polarized and (c): electric field (E_x) profile of the x-polarized mode, for the optimal design $S_1 = 0.213a$, $S_2 = 0.070a$, $S_3 = -0.009a$. (d): Histograms showing the probability of occurrence of different Q_e-values for two different disorder magnitudes: $\sigma = 0.003a$ (red) and $\sigma = 0.0015a$ (blue). The black line indicates the ideal Q_t. (e): Histograms showing the probability of occurrence of the wavelength splitting $\Delta\lambda$ between the two modes, which are degenerate in the disorder-less cavity.

however appear to be currently not achievable in practice. Additionally, design 3 could be the preferred choice for purely manufacturing reasons if quantum dots are to be inserted in the cavity, as the field maxima are further away from the hole edges than in the other two cavities.

4.1.7 Optimized H1 cavity*

Another interesting cavity with potential applications for polarization-entangled photon generation [105, 132] and quantum dot spin readout [133] is the H1 [28, 101, 126] – also known as 'single point-defect cavity' – formed by one missing hole in the lattice (Fig. 4.7(a)). The modes of this cavity preserve the underlying hexagonal symmetry, and for a wide range of parameters, the fundamental (lowest-frequency) resonance is given by two degenerate dipole modes. Based on the electric field polarization in the center of the cavity, those are usually referred to as the y-polarized (Fig. 4.7 (b)) and x-polarized (Fig. 4.7 (c)) modes, although in fact the electric field of each of those modes also has a non-vanishing component oriented in the orthogonal direction; however, since the near-field in the very center of the cavity as well as the far-field emission in the z-direction (perpendicular to the slab plane) are both truly y (correspondingly x) polarized, this labeling is in many cases appropriate, in particular for applications

in which a quantum dot is placed in the center of the cavity. Here, we optimize the quality factor of the dipole mode. We take $d = 0.55a$ and $R = 0.23a$, and the parameters used for design optimization, labeled S_1, S_2, and S_3 in Fig. 4.7(a), are an increase in the side-length of the three consecutive hexagonal "rings" around the cavity (which is also equivalent to the increase of the distance from a vertex of a hexagon to the cavity center). The previously most-optimal design was achieved using only the holes at the vertices of the hexagons (but including variations of the hole radii), and has a moderate $Q_t = 6.2 \times 10^4$ and a mode volume $V = 0.47(\lambda/n)^3$ [102]. Here, using the genetic algorithm with the shifts as outlined in Fig. 4.7(a), we find an optimal design at $S_1 = 0.213a$, $S_2 = 0.070a$, and $S_3 = -0.009a$, with $Q_t = 1.05 \times 10^6$ (FDTD: 0.97×10^6) and $V = 0.62(\lambda/n)^3$, i.e. we find a 19-fold increase in Q_t coupled to an increase in V by 32%. For this cavity as well, the disorder analysis (panel (d)) suggests that Q_e-values close to a million can be expected experimentally in state-of-the-art silicon systems, i.e. more than an order of magnitude larger than the previous **theoretical** values. The modes lie at a frequency $\frac{\omega a}{2\pi c} = 0.253$, which is, as expected, slightly lower than that of the unmodified cavity, $\frac{\omega a}{2\pi c} = 0.270$.

We note that while the degeneracy of the two dipole modes is an attractive feature of the H1, it is lifted by disorder. This is why, in panel (e) of Fig. 4.7, we study the probability of occurrence of the splitting between the modes, based on the 1000 disorder realizations that were used for the disorder analysis in panel (d). It is important to note that there is no absolute way to define an x-y reference frame, as three equivalent frames (rotated $60°$ from one another) exist due to the hexagonal symmetry of the cavity. This symmetry is broken if the cavity presents preferential orientations of the axes (e.g. introduced by lithography). In the case where only random disorder is considered, x- and y-polarized modes can turn out to be oriented along either of the three x-y reference frames. Thus, what we plot in panel (e) is only the difference between the resonant wavelengths of the higher- and the lower-frequency modes, without any reference to their polarization. What is important to note is that the splitting is of the order of hundreds of picometers, i.e. two orders of magnitude larger than the linewidth corresponding to the typical Q_e-s (see top x-axis of panel (d)). This implies that for applications for which overlap in frequency between the two modes is needed, some form of post-fabrication tuning is required, the possibility for which has already been demonstrated [105, 134]. This can also be combined with an additional modulation of the neighboring holes which increases the emission in the vertical direction [135], which would decrease the Q_e and make the tuning easier while simultaneously increasing the intensity of the collected radiation, which is beneficial for entangled-photon generation [132, 136].

We finally address the hexapole mode of the H1 cavity, which typically lies at a higher frequency than the dipolar modes studied above. This mode has previously been optimized to $Q_t = 1.6 \times 10^6$ [126, 127] by varying only S_1, with $S_2 = S_3 = 0$ in the sketch of Fig. 4.7(a). Here, we run a global optimization of Q_t by varying the three shifts, with $d = 0.55a$ and $R = 0.22a$. We could improve the previous value to $Q_t = 3.2 \times 10^6$ (FDTD:

Cavity	$\frac{\omega a}{2\pi c}$	Q_t (GME)	Q_t (FDTD)	$V, \left(\frac{\lambda}{n}\right)^3$	$\frac{Q_t}{V}, \left(\frac{n}{\lambda}\right)^3$
L3 des. 1	0.259	2.1×10^6	1.6×10^6	0.94	2.2×10^6
L3 des. 2	0.259	5.1×10^6	4.2×10^6	0.95	5.4×10^6
L3 des. 3	0.254	2.0×10^7	2.1×10^7	0.94	2.1×10^7
H0 des. 1	0.280	1.0×10^6	1.0×10^6	0.25	4.2×10^6
H0 des. 2	0.275	1.9×10^6	1.7×10^6	0.35	5.4×10^6
H0 des. 3	0.269	8.9×10^6	8.3×10^6	0.64	1.4×10^7
H1 dip.	0.253	1.0×10^6	1.0×10^6	0.62	1.6×10^6
H1 hexap.	0.261	3.2×10^6	3.1×10^6	1.10	2.9×10^6

Table 4.1: Summary of the simulated resonant frequency, quality factor, mode volume, and Q_t/V ratio (taking the GME-computed Q_t) for all the optimal designs presented here. L3 des. 1 and 2 are shown in Fig. 4.1; L3 des. 3 – in Fig. 4.3; the three H0 designs – in Fig. 4.6; and the H1 designs are as in Fig. 4.7.

Cavity	$\langle Q_e \rangle_{\sigma_1}$	$\frac{\langle Q_e \rangle_{\sigma_1}}{V}, \left(\frac{n}{\lambda}\right)^3$	$\langle Q_e \rangle_{\sigma_2}$	$\frac{\langle Q_e \rangle_{\sigma_2}}{V}, \left(\frac{n}{\lambda}\right)^3$
L3 des. 1	7.7×10^5	8.2×10^5	1.5×10^6	1.6×10^6
L3 des. 2	9.3×10^5	9.8×10^5	2.5×10^6	2.6×10^6
L3 des. 3	1.1×10^6	1.2×10^6	3.5×10^6	3.7×10^6
H0 des. 1	4.0×10^5	1.6×10^6	7.2×10^5	3.0×10^6
H0 des. 2	5.2×10^5	1.5×10^6	1.1×10^6	3.1×10^6
H0 des. 3	6.5×10^5	1.0×10^6	2.0×10^6	3.1×10^6
H1 dip.	5.3×10^5	8.5×10^5	8.4×10^5	1.4×10^6
H1 hexap.	6.6×10^5	6.0×10^5	1.6×10^6	1.5×10^6

Table 4.2: Average values of Q_e and Q_e/V computed over 1000 disorder realizations, in which both hole radii and position are subject to Gaussian fluctuations with standard deviation $\sigma_1 = 0.003a$, or $\sigma_2 = 0.0015a$.

3.1×10^6), obtained for the optimal values $S_1 = 0.271a$, $S_2 = 0.039a$, and $S_3 = 0.018a$. The resonance frequency of this mode is $\frac{\omega a}{2\pi c} = 0.261$, while in the unmodified cavity of the same d and R, this mode is not present.

4.1.8 Discussion of the optimization results

The figures of merit of all designs that were presented in this Section are summarized in Table 4.1. In Table 4.2, we show the averaged values of Q_e and Q_e/V in the presence of disorder for the two disorder magnitudes used in the Figures. Notice that for the higher disorder σ_1, the values of $\langle Q_e \rangle$ do not differ dramatically among the different designs. This reflects the fact that, as was extensively discussed in Section 3.1, in the disorder-dominated regime (when $Q_d \gg Q_t$), the losses are nearly design-independent. Notice that, for the lower (but still experimentally achievable) disorder magnitude, all

the cavities presented here have a value of $\langle Q_e \rangle / V$ larger than 10^6 (in units of $(\lambda/n)^{-3}$), illustrating the relevance of the designs for future applications.

The designs obtained here show that the quality factor of the three most widespread PhC defect-cavities can be systematically optimized to well above 10^6 by adjusting only a few structural parameters (only shifts of hole positions were used here), with small increases in the mode volumes (within 50% with the exception of the third H0 design) as compared to those of the corresponding non-optimized designs. In carrying out our analysis, we have tried to include the radii of holes next to the cavity as additional free parameters, but this brought no significant improvement. We therefore restricted to shifts of hole positions only, as these are easily controlled in the fabrication process. Our scheme leaves the possibility open to use the hole radii as free parameters for independent optimization of an additional figure of merit. A very important conclusion of our analysis is that the parameter space of such structural variations has to be explored globally, using an automated optimization tool. We find that the genetic algorithm is an excellent tool to handle this task, even with seven or eight parameters included in the computation. Employing this algorithm was possible only due to the computational advantage of the GME – to compute the number of cavity configurations that was needed for the optimization using a first-principle tool like FDTD or a Finite-element Method (FEM) would require either an enormous computational power, or time of the order of years. This computational advantage made it also possible, for each cavity type, to vary more structural parameters than in previous optimization works, resulting in an even larger increase in the quality factors.

The statistical analysis of Q-factors including structural disorder shows clearly that the designs obtained here are as robust to disorder as other ultrahigh-Q designs [79]. In particular, for the L3 cavity with a theoretical Q-factor $Q_t = 5.1 \times 10^6$, state-of-the-art fabrication quality in silicon should easily result in experimental Q-factors around 2×10^6, in the same range as current ultrahigh-Q designs based on a PhC waveguide [94, 127, 128]. On the other hand, our experience shows that systematic structural variations can rapidly suppress the Q-factor of an optimal structure. Hence, an important conclusion of our analysis is that, whenever a design needs to be significantly varied (e.g. when strongly modifying the ratios R/a and/or d/a, or the refractive index n in order to, e.g., operate at a different wavelength), a **new** optimization must be carried out in order to obtain the best structural design adapted to the new requirements.

4.2 High-Q-optimized silicon air-bridge cavities: experiments

The two experiments presented in this section demonstrate the validity and importance of the optimization procedure outlined in Section 4.1.
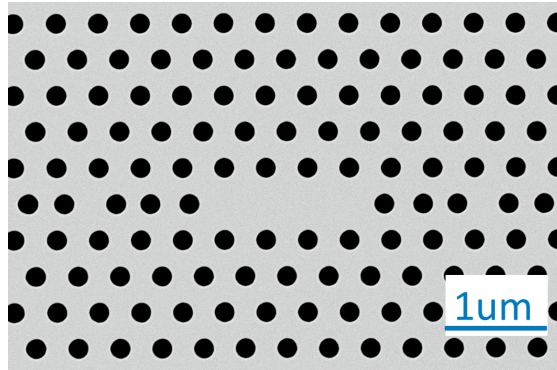
Figure 4.8: Scanning electron micrograph of one of the fabricated super-L3 cavities.

4.2.1 Ultra-high-Q L3 cavity*

In this experiment, the *five-shift* L3 cavity design of Section 4.1 (Fig. 4.2(b)) was fabricated by the group of Prof. Antonio Badolato in the University of Rochester, and spectrally characterized by the group of Prof. Matteo Galli in the University of Pavia. Eight groups of *super-L3* cavities were fabricated in commercially available Silicon-on-insulator (SOI) wafers. Each group comprised twenty-one nominally identical cavities, while the hole radius was slightly varied from one group to the next, resulting in a different nominal resonant wavelength for each group. Note that by varying only the radius instead of applying an overall scaling factor, the design moves away from its optimal configuration (Fig. 4.2). With our choice of fabrication parameters, the group number five was the one nominally corresponding to the optimal design.

The SOI wafer consisted of a 220nm top silicon layer and a 3μm buffer oxide layer on a silicon substrate. The PhC pattern was defined by 100kV electron beam lithography direct writing using positive e-beam resist. The pattern was transferred from the resist to the silicon top-layer by fluorine based inductively coupled plasma dry etching and the oxide layer was removed by dilute Hydroflouric-acid wet etching. Engineered lateral openings in the membrane made the suspended membrane free from buckling [137]. Fig. 4.8 shows a Scanning Electron Microscope (SEM) image of the super-L3 whereby we measured the standard deviation of the hole-radii to be < 1nm.

The fundamental cavity mode was measured by cross-polarization Resonant Scattering (RS) spectroscopy [138]. This technique is particularly well-suited for measuring PhC cavities with ultra-high Qs, because it does not require any evanescent coupling (e.g., through an integrated photonic crystal waveguide or an external fiber taper) and thus directly yields the intrinsic (unloaded) Q. A schematic of the experimental setup is shown in Fig. 4.9(a), where a 10MHz resolution tunable laser was used to excite resonantly the cavity mode, and the light scattered by the cavity was collected vertically in far-field with a NA = 0.9 objective. In this setting, the emission of the fundamental mode resulted to be linearly polarized (y-direction). Using the y-direction
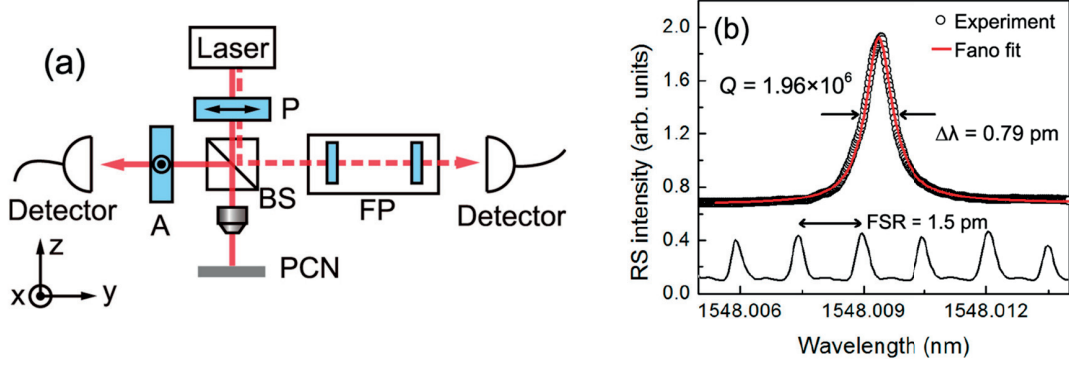
Figure 4.9: (a): Schematic of the cross-polarization resonant scattering setup. P: polarizer, A: polarization analyzer, BS: beam splitter, FP: Fabry-Pérot interferometer. (b): Resonant scattering spectrum of the super-L3 (open dots). Best-fitted Fano lineshape (red line) gives a linewidth of 0.79pm, i.e. $Q = 1.96 \times 10^6$. The Fabry-Pérot spectrum used for wavelength calibration is shown as a black line at the bottom of the plot.

as a reference, we excited the cavity mode with a laser beam linearly polarized at $+45°$ and collected at $-45°$, achieving precise control over the extinction of the reflected laser light. While scanning, the laser wavelength was calibrated through the simultaneous measurement of the interference fringes of a 0.8m long Fabry-Pérot interferometer with 1.5pm free spectral range. Fig. 4.9(b) shows the RS spectrum measured on the cavity displaying the highest Q out of the twenty-one devices in group five. The lower curve in Fig. 4.9(b) shows the measured transmission spectrum of the Fabry-Pérot interferometer. Fitting of the cavity resonance with a Fano lineshape [138] demonstrates $Q_e = 1.96 \times 10^6$, which is 20 times larger than the highest Q previously reported in an L3 cavity [95, 123]. This corresponds to an experimentally observed $Q_e/V > 2 \times 10^6 (\lambda/n)^{-3}$, which is more than 10 times larger than the values previously reported in an L3 cavity and ranks our design among those with the highest Q_e/V values ever reported in 2D PhCs. We note that around the time of the publication of this result, another experimental study of silicon L3 cavities [36], optimized using an educated-guess procedure, reported a measured Q-factor of 10^6 for the best cavity (and a value $Q = 0.5 \times 10^6$ averaged over several devices). Our result still outperforms these values by a factor of 2.

The other group-five L3-s all displayed a clear resonance, with Q-values lying systematically in the 10^6 range, as plotted in Fig 4.10. Spectra measured from devices belonging to groups other than group-five (data not shown) resulted in Q-values ranging from 0.4×10^6 to 1.1×10^6. This finding is consistent with group five being the one closest to the nominally optimal design. We notice that the Q-values measured in the non-optimal groups are all largely exceeding the highest Q-values previously measured for an L3, which also demonstrates the robustness of the optimized design to small
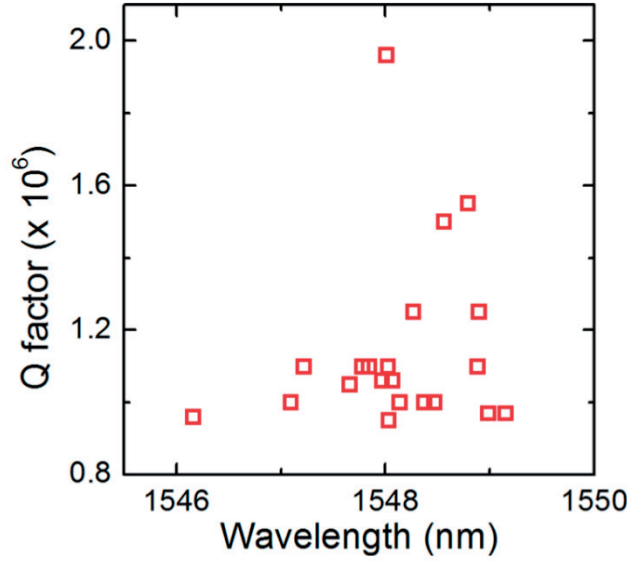
Figure 4.10: Scatter plot of the measured Q-values and resonant wavelengths from the twenty-one nominally identical cavities present in group five. All of them display a clear resonance, with Q-values lying in the 10^6 range. The highest value (spectrum in Fig. 4.9(b)) corresponds to $Q = 1.96 \times 10^6$.

variations of the overall hole radius.

The observed fluctuations in the values of Q and λ (Fig. 4.10) are expected and are due to disorder in the fabrication process, as was analyzed extensively in Section 3.1 (see also Fig. 4.2(d)). In Fig. 4.11, we report the occurrence histograms of the values of Q and λ measured on the group-five cavities. In both panels, we plot the theoretical occurrence histograms obtained through GME simulations with the same disorder model of Sections 3.1 and 4.1. The values of the disorder amplitude σ and of Q_a (see eq. 4.1) were empirically adjusted to $\sigma = 0.0014a$, corresponding to $(\langle 1/Q_d \rangle)^{-1} = 4.5 \times 10^6$, and $Q_a = 2.1 \times 10^6$, to reproduce at best the measured histograms. A fairly good agreement is found, although the measured Q seems to obey a narrower distribution than the simulated one. We argue that this discrepancy might be due partly to the limited number of experimental data, resulting in large statistical uncertainty, and partly to the simple disorder model, which neglects possible spatial correlations in the fluctuations of different holes. Moreover, additional aspects, such as slight surface oxidation of the silicon membrane upon air exposure as well as surface contamination by adsorption of water vapor molecules, may also affect the influence of disorder on the measured Q.

In conclusion, we presented an experimental confirmation of the viability of the transformative generation of L3 PhC cavities that were theoretically predicted in Section 4.1.
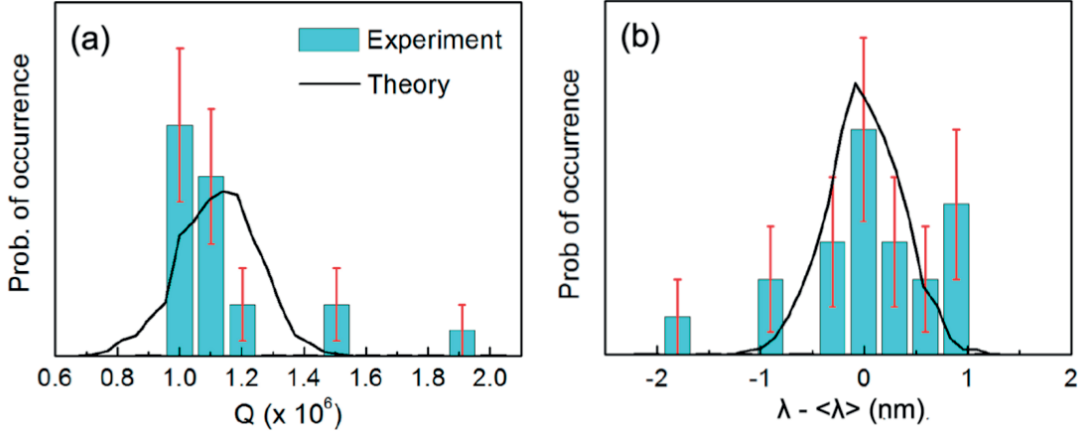
Figure 4.11: Occurrence histograms of (a): Q-values and (b): resonant wavelengths, as measured in group five. In both panels, the black lines denote the histogram computed over 1500 simulated realizations of the super-L3 design with disorder added as Gaussian fluctuations of the hole radii and positions. The red error bars indicate the statistical uncertainty in the experimental data.

4.2.2 Ultra-high-Q H0 cavity*

In this Section, the experimental characterization of the optimal H0 design derived in Section 4.1 is presented. The fabrication and spectroscopy was performed by the group of Prof. Houdré at EPFL [115].

The optimal cavity design that we used is the 'intermediate' one (in terms of Q and V), i.e. the one of Fig. 4.6(c), which is also illustrated in Fig. 4.12(a), with an SEM image of one fabricated cavity shown in panel (b). The thickness of the PhC slab is 220nm, while the radius of each hole is $0.25a$ (the lattice constant a was varied as in the L3 experiment of Section 4.2.1, see below). The GME-computed quality factor is $Q_t = 1.9 \times 10^6$. The computed mode profile (Fig. 4.12(c)) corresponds to an extremely small mode volume: $V = 0.34(\lambda/n)^3$. In Fig. 4.12(d), we plot the mean value of the quality factor and its standard deviation in the presence of disorder as a function of σ, where each point was computed based on 1000 random disorder realizations with the standard disorder model of this thesis (Section 3.1). Disorder reduces the Q-factor on average, as expected, but nonetheless very high quality factors for a reasonable fabrication disorder magnitude are predicted. Fig. 4.12(e) shows a histogram of the probability distribution of the Q-values for $\sigma = 0.003a$, which is a reasonable estimate of the largest fluctuations introduced in our fabrication process [103], and is consistent with the experimental results below.

Several cavities were fabricated following the optimal design with $a = 435$nm on a SOI wafer, which consists of a 220nm thick silicon layer and a 2μm thick silica (SiO_2) layer on a silicon substrate. The photonic crystal pattern is defined with electron
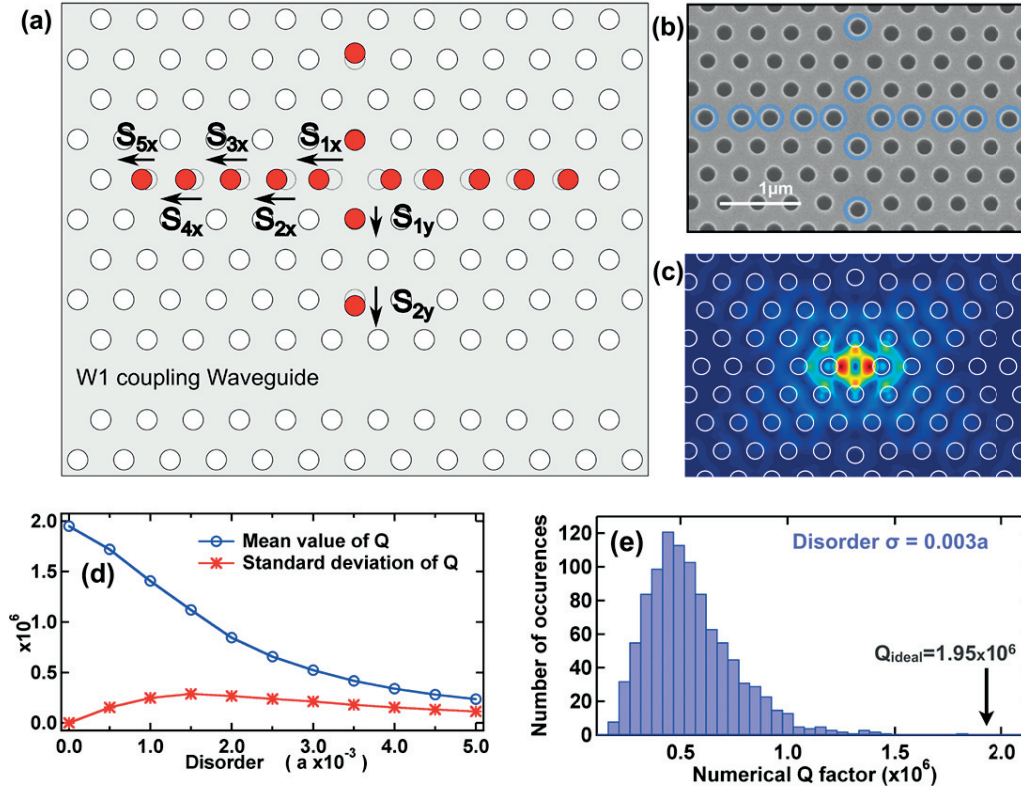
Figure 4.12: (a): Schematic of the proposed design, highlighting (in red) the holes whose positions have been optimized, with the displacement parameters correspondingly labeled. The coupling W1 waveguide, at a distance from the cavity, is shown. (b): Scanning electron micrograph of one of the fabricated cavities, with the displaced holes encircled in blue. (c): Electric field distribution in the cavity as computed with the guided-mode expansion. (d) Mean and standard deviation of Q in the presence of random structural disorder, as a function of the disorder magnitude σ, computed from 1000 simulated disorder realizations for each σ. (e): Histogram of the computed quality factor for $\sigma = 0.003a$; the ideal Q-factor without disorder is indicated.

beam lithography (VISTEC EBPG5000) on an electro-sensitive resist (ZEP520) and the developed pattern is further transferred into the silicon layer with an inductively coupled plasma (ICP) AMS200 dry etcher with a SF_6 and C_4F_8 gas mixture. The last step is the removal of the sacrificial SiO_2 layer with buffered HF (BHF) wet etching. Coupling of continuous-wave monochromatic light into the cavity was performed in a standard end-fire set-up with lensed fibres, adiabatically tapered ridge waveguides and photonic crystal W1 waveguides. The cavity couples either in a side-coupling (Fig. 4.12(a)) or in a cross-coupling (Fig. 4.14(b)) scheme, and was characterized by a different distance to the waveguide $D = n\frac{\sqrt{3}}{2}a$, $n = 5, \dots 15$. When measuring the Q-factors, the input light power was lowered until optical nonlinearities (see below) vanished and the device operated in a regime of linear response. Cavity emission

spectra are shown in Fig. 4.13(b) and (c) for $n = 11$ and $n = 15$, respectively. In panel (c), the coupling of light into the cavity is very weak, making the signal almost comparable to the noise, which is why we used a Fano fit instead of a Lorentzian (the former describes the spectral response of a resonance in a continuous background). Fig. 4.13(a) shows the change in measured (loaded) Q-factor, for the side-coupled cavities, as D is increased. The variation is due to the coupling waveguide that acts as an additional loss channel for the cavity. [123] The error bars of the data points (only visible for the last two points on the scale of the plot) come from the uncertainty in the Lorentzian/Fano fits, and do not take into account the variation in Q values that is expected among different cavities due to disorder. This, as suggested by Fig. 1(d) and (e), is expected to be much larger than the measurement error. The maximum measured value of $Q = 400,000$ was obtained for a coupling distance $n = 15$. The data in Fig. 4.13(a) suggest clearly that, at $n = 15$, the coupling waveguide still affects the measured Q-factor. A conservative way of extrapolating the unloaded Q-factor consists in assuming an exponential decay with distance of the cavity-waveguide coupling. More precisely, we assume $Q^{-1} = Q_{UL}^{-1} + C\exp(-\alpha D)$. A fit of the measured Q-values (with C, Q_{UL}, and α as free parameters), as plotted in Fig. 4.13(a), yields $Q_{UL} = 450,000$, which should be taken as a lower bound to the actual unloaded Q-factor. This value is in very good agreement with the maximum in the histogram of Fig. 4.12(e), computed for a disorder amplitude $\sigma = 0.003a$, which is a very reasonable estimate of the largest fluctuations introduced in the fabrication process. [103] Finally, we note that Fig. 4.13(a) also shows that at short distances, where the Q-factor is still very high ($\approx 100,000$), losses are fully dominated by coupling into the waveguide channel, which highlights the potential of this cavity for photonic applications.

The simulated modal volume $V = 0.34(\lambda/n)^3$ is a reliable estimate of the corresponding quantity for the fabricated structure [108, 139]. The present nanocavity has a maximum (loaded) $Q_e/V = 1.18 \times 10^6 (n/\lambda)^3$ and thus ranks among those with the highest Q/V ratio ever reported [34, 69, 82, 94, 98, 102, 140, 141]. The amount of disorder that appears to be present in our system suggests that the first H0 design of Section 4.1 might be slightly better in terms of this figure of merit (see Table 4.2). Thus, we also fabricated and characterized that cavity, which has $V = 0.25(\lambda/n)^3$. The maximum measured (loaded) Q-factor was $260,000$, corresponding to $Q_e/V = 1.04 \times 10^6 (n/\lambda)^3$, which is slightly lower but very close to the value for the first fabricated design. We note that both of those values are lower than what was measured in the super-L3 cavity (Section 4.2.1), but this is attributed to lower disorder in the L3 fabrication. Note also that the L3 experiment did not involve in- and out-coupling waveguides, while here, the intrinsic (unloaded) Q could not be directly measured, but instead had to be extrapolated.

The Q/V ratio is a measure of the enhancement of optical nonlinearities produced by a cavity. [69, 70, 142] To examine the nonlinear spectral properties of our design, in Fig. 4.14(a) we show the emission spectrum, measured under continuous-wave resonant excitation, of a cavity with measured Q-factor $Q = 150,000$ in the cross-
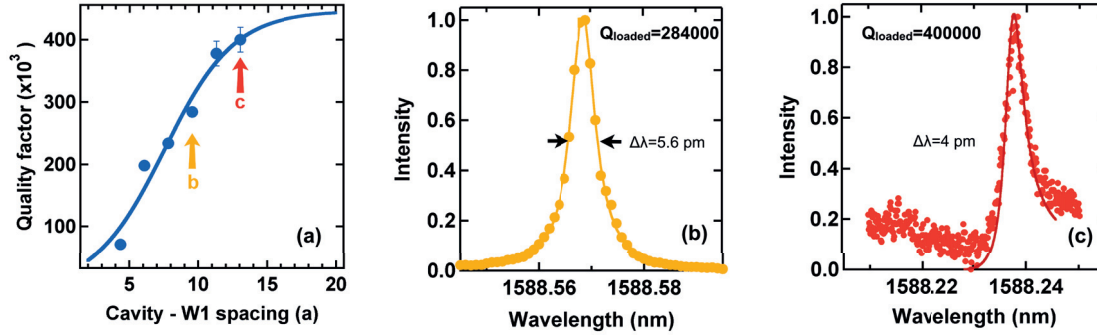
Figure 4.13: (a): Change in the measured Q-factor as the distance D from the side-coupling W1 waveguide is increased. The blue line shows the best fit of the experimental data to the model $Q^{-1} = Q_{UL}^{-1} + C\exp(-\alpha D)$, indicating an unloaded Q-factor $Q_{UL} = 450,000$. (b) and (c): Spectra (normalized to the maximum intensity) of the emission from the membrane surface measured for two values of the cavity-waveguide distance, indicated by arrows in panel (a). The experimental data are fitted with a Lorenzian curve in panel (b) and a Fano curve in panel (c), and the extracted full width at half maximum results respectively in loaded quality factors $Q_L = 284,000$ and $Q_L = 400,000$.

coupling configuration, at varying intra-cavity power. This configuration allows for a rough estimate of the power coupled into the PhC region where the cavity is located [127, 143]. For a given input and output power, we define the transmission coefficient $T = P_{output}/P_{input}$. For a symmetric system (Fig. 4.14(b)), the power available in the cavity region is then $P_{cavity} = \sqrt{T}P_{input}$ – i.e. it depends linearly on the actual input power – which can also be rewritten, using T from the previous expression, as $P_{cavity} = \sqrt{P_{input}P_{output}}$. In particular, for an input power from the laser $P_{input} = 4\mu W$, we measure a transmitted power $P_{output} \approx 2nW$ in the detector after the ridge waveguide at the cavity resonance wavelength. According to the above equation, for these values $P_{cavity} = 0.09\mu W$, which sets the proportionality factor $\sqrt{T}$ between P_{cavity} and P_{input} in our measurement. As shown in panel (a) of the Figure, at low power, a slight blue shift of the cavity mode is observed and attributed to free carrier dispersion. [69] Starting at $P_{cavity} = 0.6\mu W$, heating due to nonlinear absorption, and optical-Kerr nonlinearity result in a redshift. At higher input powers, a drop in the spectral response on the red side of the resonance indicates the onset of optical bistability. To characterize this bistable behaviour, we sweep the input power and record the steady-state emission intensity. A clear hysteresis with a large contrast and very low power threshold is observed in Figs. 4.14(c) and (d), where the input laser is respectively detuned by 20pm and 40pm above the cavity resonance. Switching power ratios P_{up}/P_{down} of respectively 2.0 ($P_{up} = 26\mu W$ and $P_{down} = 13\mu W$) and 4.5 ($P_{up} = 90\mu W$ and $P_{down} = 20\mu W$), and a contrast above 70% are obtained, demonstrating robust and controllable bistable behaviour. The present cavity displays one of the lowest power thresholds for optical bistability among 2D PhC silicon devices for which a similar power-dependent analysis
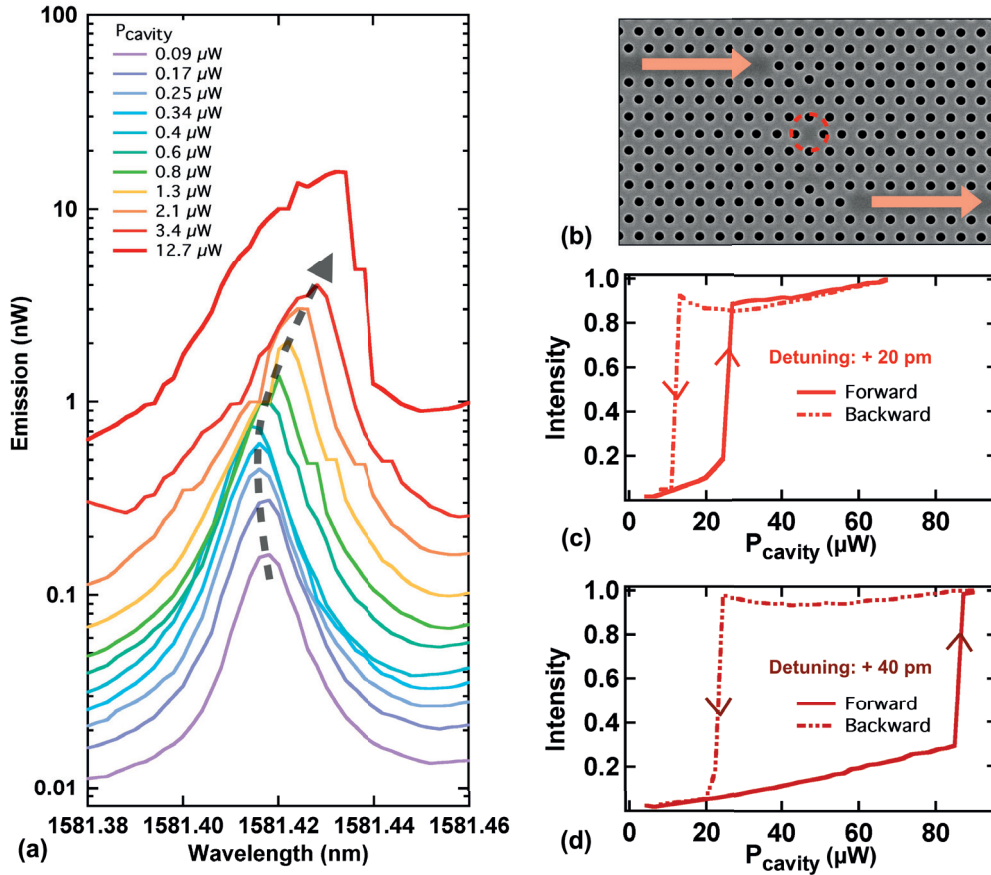
Figure 4.14: (a): Measured emission spectrum from the cavity, as the input power is increased. The dashed line is a guide to the eye to indicate the change in the resonance wavelength. (b): Scanning electron micrograph of the cross-coupled cavity structure used to measure optical nonlinearities. (c) and (d): Hysteresis plots, respectively for an excitation wavelength red-shifted by 20pm and 40pm from the cavity resonance.

was carried out. [127, 143]

4.3 Other cavity optimizations

The range of applicability of the optimization scheme presented in Section 4.1 is very broad. We note that the GME returns not only the quality factor but also the full mode profile of the cavity modes, thus the same procedure can be used for optimization of various quantities depending on the practical requirements. For example, notice that in Section 4.1, the Q was always the figure of merit for optimization, since V is much more weakly affected by the structural changes we considered. In the case of the H0, or in some even more specific cases, however, it might be worth considering Q/V – or, depending on the particular application, some other combination of those (see Section 1.3.2) as the objective function. This is all within the scope of our au-

tomated optimization procedure. In this section, we present several investigations that go beyond the quality factor of silicon air-bridge cavities. In Sections 4.3.1 and 4.3.2, we present again a Q-optimization, but in systems with a lower refractive index contrast between the slab and the claddings. In Section 4.3.3, we take advantage of the computed electric field profiles to optimize a cavity design for the enhanced trapping of a dielectric particle [109].

4.3.1   L3 in Gallium Nitride*

Over the past few years, there has been a strong effort, both in academia and industry, to combine the well-established Si technology with the optoelectronic properties of direct bandgap compound semiconductors [144, 145]. The aim is to unify different optoelectronic devices, with various functionalities and operating wavelengths, on the same chip while offering a reduced footprint. In this regard, GaN, Aluminum Nitride (AlN), Indium Nitride (InN) and their ternary alloys are excellent candidate materials for such platforms thanks to their wide direct bandgap ranging from the Ultra-violet (UV) to the Infra-red (IR) spectral range. Their unique optoelectronic properties are supported by the significant increase in the solid-state lighting market which mostly relies on III-nitride light-emitting diodes. Besides the design flexibility enabled by such a bandgap tunability, III-nitrides (III-N) possess a large second-order nonlinear susceptibility, which is highly desirable for second harmonic generation or frequency-doubling processes [146–151]. For instance, this should facilitate the integration of fluorescence-based biosensors working in the green spectral range together with devices operating in the NIR. Beyond enhanced light-matter interaction phenomena, this material family offers additional features such as chemical inertness, high thermal stability, and large mechanical resistance, making them well-suited for optomechanics, [149] and biocompatibility [152].

The development of high quality (Q) factor III-N based photonic crystal cavities – both in the 2D PhC slab and one-dimensional nanobeam geometries – was hindered by technological issues mainly arising from their mechanical hardness and the lack of an appropriate lattice-matched substrate. However, in recent years several groups have overcome such challenges by reporting the fabrication of III-N PhC cavities exhibiting comparatively large experimental Q factors. At short wavelengths, values up to 6,300 have been demonstrated both for nanobeam cavities [153] and for defect cavities in PhC slabs [154–156], whereas at $\lambda \sim 1.55\mu$m, Q values up to 34,000 where recently shown for GaN-on-Si PhC cavities based on the width-modulated waveguide structure [157, 158] and up to 146,000 for AlN nanobeam structures deposited by sputtering [159].

In view of applications, both the 2D slab and the nanobeam geometries hold great promise as platforms for investigating strong light-matter coupling at the nano-scale,

in a longer term perspective, the need for scalability and integrability hints at the 2D slab structure as the most suitable choice, where cavities and waveguides can be fabricated on a single slab and arranged in a circuit-like fashion. To this purpose, the minimization of the spatial footprint of PhC cavities is also a crucial requirement. In previous works, either L7 or width-modulated waveguide cavities were adopted at both visible [154–156] and IR wavelengths [158]. These designs systematically present a Q-factor larger than their smaller siblings, but only at the cost of a larger mode volume, and, in the case of waveguide-based designs, sub-optimal footprint. Previously, a measured Q of 2,200 in a smaller L3 GaN-on-Si cavity has been demonstrated [157]. Here, we take advantage of the automated optimization to obtain a cavity design with a theoretical $Q = 166,000$ at $\lambda \sim 1.3\mu$m. We fabricate several replicas of this design and characterize them optically. We demonstrate high reproducibility and an average measured (unloaded) Q-factor of $16,900$, with individual samples reaching $Q = 22,500$. We quantitatively explain the measured data – and in particular the gap to the expected theoretical Q-factor – by deploying a model that involves the simulation of hundreds of disorder realizations of the optimal design, and includes material absorption in the spirit of eq. (4.1).

The high-Q L3 cavity design (Fig. 4.15(a)) was optimized for a slab consisting of a 310nm GaN (refractive index $n = 2.35$) and a 40nm AlN (refractive index $n = 2.05$) layer. The values of n at 1.3μm were extrapolated using Sellmeier formula coefficients given by Antoine-Vincent and co-workers for GaN on Si (111) [160]. The lattice constant is $a = 467$nm, while the hole radius was kept as a free parameter. The general optimization scheme was the one described in Section 4.1. The present problem is however somewhat different, particularly due to the much lower refractive index contrast, and we found that including size variations of the neighboring holes results in significantly better designs. Thus, both the positions and the radii of the three holes nearest to the cavity in the ΓK direction (Fig. 4.15(a)) were chosen as the parameters for optimization. The optimal design was found for the following parameters: hole radius $r = 0.2553a$, outward shifts of the three nearest holes $S_{1-3} = [0.3482, 0.2476, 0.0573]a$, shrinkage of their corresponding radii $dr_{1-3} = [-0.0980, -0.0882, -0.0927]a$. The high Q of this optimized design was verified using an FDTD solver [74], resulting in $Q = 112,000$ at a resonance wavelength $\lambda = 1.329\mu$m. The simulated electric field E_y in the center of the slab is plotted in Fig. 4.15(b), while in panel (c) we compare the Fourier transform of this field for an un-optimized L3 cavity with the same overall hole radius (left) and for our optimized design (right). The Fourier components inside the light cone of our design are strongly suppressed, which is why the value of the quality factor is more than 65 times larger than that of the unmodified cavity ($Q = 1,700$).

A technical detail worth mentioning is that the GME as outlined in Section 2.3 cannot be applied to the exact structure, due to the 40nm AlN layer. A multi-layer guided-mode expansion is in principle possible and in fact conceptually straightforward, but so far it has been left for a potential future implementation. In the optimization, we
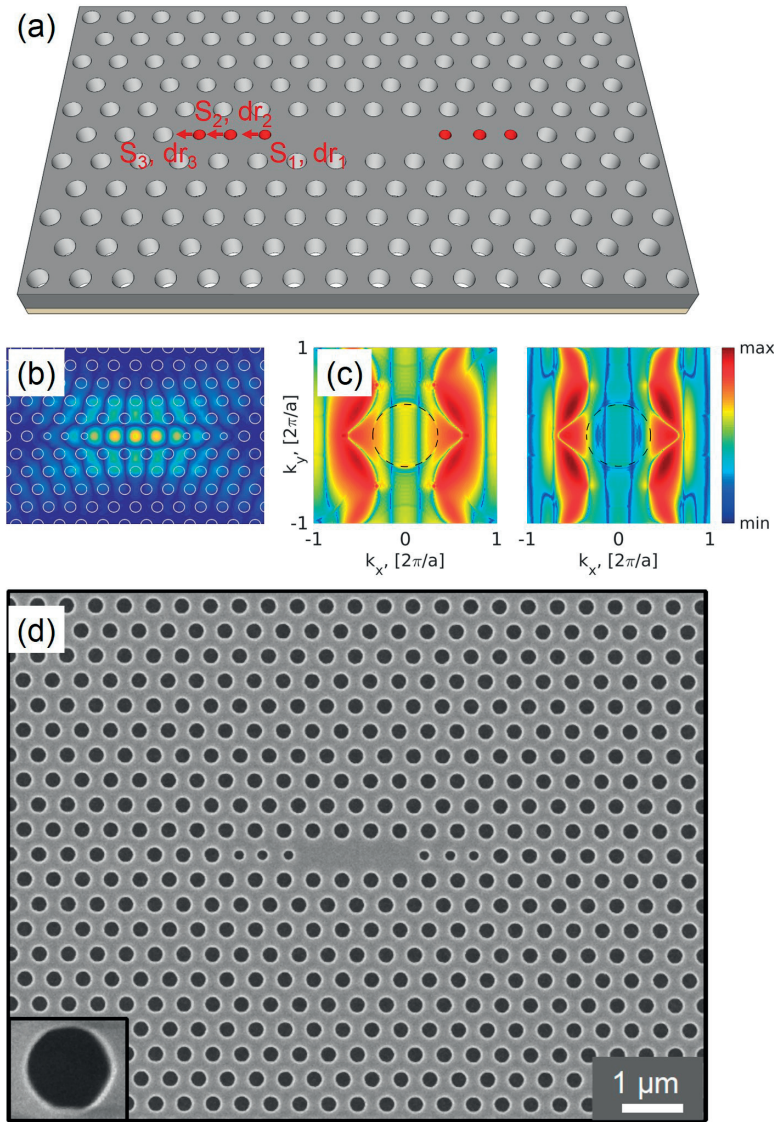
Figure 4.15: (a): Schematic of the photonic crystal cavity design, with the AlN buffer layer shown in beige. The three holes which were modified for the optimized Q are marked in red. (b): Simulated electric field ($|E_y|$) profile of the fundamental cavity mode. (c): Fourier components $\ln(|\mathrm{FT}(E_y)|)$ for an unmodified cavity (left) and the optimized one (right); the light cone is indicated by the black circle. (d): SEM top view of a fabricated cavity. Bottom left: close-up view of one of the holes illustrating a trend to a hexagonal shape.

thus assumed a GaN layer of thickness 350nm, which is a fairly good approximation due to the similar refractive indexes of GaN and AlN, and the fact that the electric field of the cavity is weaker close to the slab boundaries compared to the slab center. However, the AlN layer does break the σ_{xy} symmetry and thus it introduces resonant losses into the $\sigma_{xy} = -1$ modes (cf. Section 2.3), which are not taken into account by
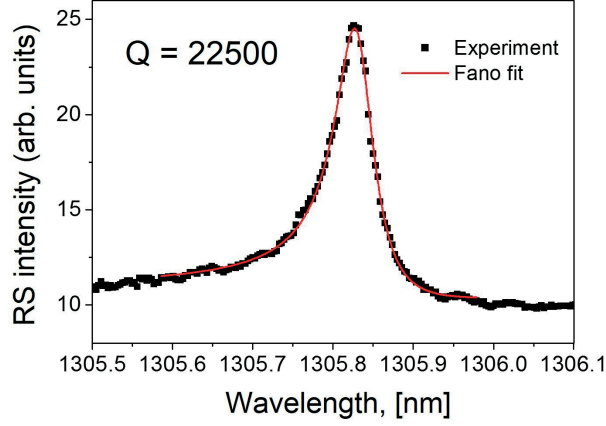
Figure 4.16: Resonant scattering spectrum and Fano fit of the cavity with the highest measured quality factor (see also Fig. 4.9).

the GME. Nevertheless, the optimization yields a very good result as testified by the 65-fold (FDTD-verified) improvement with respect to an unoptimized design. For for the sake of precision, however, all the simulations shown hereafter were performed with the FDTD solver.

The fabrication of the optimized cavity is first based on the growth on 2-inch Si (111) substrate by metal organic vapor phase epitaxy of a 40nm thick AlN buffer layer followed by a 310nm thick GaN layer. The PhC lattice is subsequently patterned by e-beam lithography using a SiO_2 hard mask and dry etching techniques. Finally, a membrane is obtained by undercutting the Si substrate, again by selective dry etching. With this processing methodology air gaps larger than $\approx 3\ \mu$m can be achieved. Further details on this fabrication procedure together with structural characterization can be found in Ref. [157]. Figure 4.15(d) displays a scanning electron microscope (SEM) image of one of the fabricated L3 cavities. As shown in the bottom left inset, one can observe a slight deviation toward a hexagonal shape for the holes instead of the designed circular one. This is ascribed to a crystallographic orientation-dependent selective etching which has been previously reported in similar III-nitride based PhC lattice structures [161]. In the present case, the cavity orientation is $[1\bar{2}10]$. Due to expected uncertainty in the etching, 20 groups of cavities (labeled $g_1 - g_{20}$) were fabricated to allow for lithographic tuning. Group g_{16} was targeted to have the nominal hole radius, while groups with lower (higher) number contain cavities where all radii are increasingly smaller (larger) in steps of 1nm. The spectroscopic characterization was performed in the same way as for the Si L3 cavity of Section 4.2.1, see Fig. 4.9(a) and its discussion in the text.

The measured resonance wavelength of the g_{16} group of cavities, which was the target nominal structure, was blue-shifted by more than 20nm from the simulated wavelength, 1.329μm. We attribute this shift to several possible effects: the deviation of
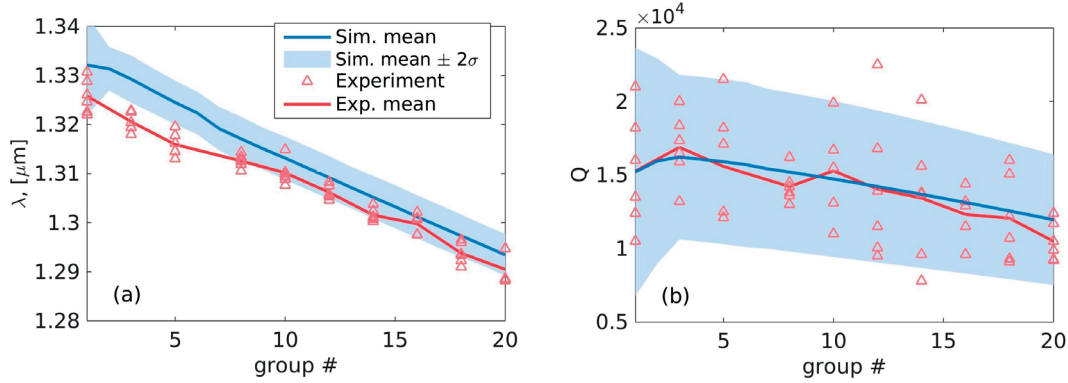
Figure 4.17: Simulated (blue) and measured (red) (a) resonance wavelengths and (b) quality factors as a function of the cavity group number.

the hole radius from the target value, the uncertainty in the slab thickness, and the uncertainty in the refractive index which comes from our Sellmeier's law extrapolation and potentially from free-carrier absorption. To fit the experimental data, the following assumptions were made: GaN refractive index $n = 2.33$, GaN layer thickness $d = 300$ nm (the AlN layer was kept unchanged). In addition, a diameter increase of the holes occurring during the etching process was observed, which resulted in group g_{10} having the nominal hole radius instead of g_{16}. We simulated the effect of disorder using our standard model (Section 3.1), with a disorder magnitude $\sigma_d = 5$nm. One hundred disorder realizations were simulated for each group g_x. In the experiment, 6 replicas within each of the following groups were measured: g_1, g_3, g_5, g_8, g_{10}, g_{12}, g_{16}, g_{18}, g_{20}, and in Fig. 4.17(a), we compare the results to the simulated wavelengths λ_{sim}. The blue shaded area shows the region $\langle \lambda_{sim} \rangle \pm 2\sigma(\lambda_{sim})$, where the averaging is done over the 100 disorder realizations and $\sigma()$ denotes the standard deviation. The agreement is excellent given all the above-mentioned uncertainties. We note that the refractive index dispersion was neglected here as the GaN PhC structures are designed for a frequency range far below that of the GaN bandgap. A fine-tuning of the simulated results to the experimental ones is in principle possible, but would not bring any further insight. It is noteworthy that over the full set of groups, the slope corresponding to the average of the experimental wavelength (red line in Fig. 4.17(a)) follows the expected theoretical trend (blue line) even when considering that there is a target hole diameter difference of only 2nm between two adjacent groups (g_x and g_{x+1}). This further confirms the reproducibility and maturity of this approach for the fabrication of III-nitride PhCs.

The measured quality factors could also be well matched to our disorder simulation (Fig. 4.17(b)). To this purpose, constant, systematic losses with an associated quality factor Q_a were additionally assumed (see eq. (4.1)). These could be due to absorption, but could also be related to scattering losses not captured in our disorder model, e.g. by the slab surface roughness. The value of $Q_a = 40,000$ was estimated for the best agreement between computed and experimental data. The simulated Q_{sim} was

computed as $Q_{sim}^{-1} = Q_d^{-1} + Q_a^{-1}$, where Q_d is the quality factor resulting from the simulations in the presence of disorder, and the mean and standard deviation were obtained by $\langle Q_{sim} \rangle = 1/(\langle Q_d^{-1} \rangle + Q_a^{-1})$, $\sigma(Q_{sim}) = \langle Q_{sim} \rangle^2 \sigma(Q_d^{-1})$. The light-blue region in Fig. 4.17(b) is given by $\langle Q_{sim} \rangle \pm 2\sigma(Q_{sim})$, and is thus the region within which, for a Gaussian statistical distribution, 95% of the data points are expected to lie. The scattering in the measured data matches this distribution very satisfactorily. Finally, it is interesting to note that the quality factor slightly increases with decreasing radius, reaching a maximum around group g_3, where the theoretical Q of the design with no disorder and no Q_a is $166,000$. This is, however, followed by a drop and spread of the Q-distribution for smaller radii, for which, in some disorder realizations, a degradation of the cavity mode is observed (the field is no longer concentrated in the three-missing-hole region). The existence of this super-optimal design we attribute to the non-trivial effect that of the AlN buffer layer on the cavity Q, which is not captured by GME and thus was not taken into account in the optimization.

In conclusion, we demonstrated a PhC L3 cavity optimized for fabrication in GaN, with a maximum theoretical quality factor of $166,000$ at wavelengths in the $\sim 1.3\mu$m window. The fabricated cavities consistently showed measured quality factors above $10,000$, and the maximum measured value was $Q = 22,500$. In addition, for the best group (g_3), the average measured Q was $16,900$, which demonstrates the growing technological maturity of GaN-based PhCs.

4.3.2 Silicon L3 'buried' in silica

For some of the potential applications of photonic crystals, e.g. in the field of optical data transfer and manipulation, it is highly desirable for the devices to be compatible with current CMOS technologies used in the fabrication of microprocessors. This is in principle possible since, as we have seen, silicon is a material that is very well-suited for PhC fabrication. In fact, the slabs used in e.g. Sections 4.2.1 and 4.2.2 were made starting from SOI wafers normally intended for electronic chips. With this in mind, several groups have already demonstrated the fabrication and characterization of CMOS-compatible PhC cavities [162, 163] and waveguides [164–166]. A characteristic feature of these devices is that the Si slab is no longer suspended in air, but is instead buried in a low-index material, typically SiO_2. This would allow for electric contacts to be integrated above or below the device, and in addition quite simply provides extra structural support (air-bridge PhCs can be easily broken and are thus not well-suited for technological applications). However, the SiO_2 also reduces the refractive index contrast between slab and claddings, which, as in the case of a GaN slab, makes it harder to obtain ultra-high-Q cavities. Nevertheless, our optimization is still relevant, and thus, for the sake of completeness, we provide here the best design that we could obtain for an L3 cavity in such a 'buried' PhC.

To maximize the Q, we used the 8-shift design of Fig. 4.4, assuming the standard parameters: $d = 0.55a$, $R = 0.25a$. The only change compared to Section 4.1.4 was thus the refractive index of the claddings, which was set to $n = 1.444$, relevant for SiO$_2$. The best design was found for $S_{1-6x} = [0.391, 0.431, 0.450, 0.378, 0.218, -0.002]a$, $S_{1y} = 0.045a$, $S_{2y} = 0.028a$, with a Q of 4.8×10^5 (FDTD: 3.9×10^5), at a resonance frequency $\omega a/2\pi c = 0.249$. We note that this optimization assumed that the SiO$_2$ is also permeating the holes of the PhC slab. A separate optimization was carried out assuming air-holes (but still SiO$_2$ claddings), but the best design had a significantly lower Q of 1.7×10^5. We give the design parameters nonetheless, since whether or not the SiO$_2$ enters the holes could depend on the fabrication and is not necessarily within the scope of experimental control. The parameters for the best air-hole cavity are as follows: $S_{1-6x} = [0.369, 0.403, 0.405, 0.290, 0.070, 0.000]a$, $S_{1y} = 0.050a$, $S_{2y} = 0.021a$.

4.3.3 Cavities for optical trapping

The possibility to use the light-matter interaction to 'trap' dielectric particles, atoms, or even organic molecules, has revolutionized many domains of experimental physics [167, 168]. The trapping of atoms in particular has been to various extents involved in at least three Nobel prizes, namely the one for laser cooling (Steven Chu, Claude Cohen-Tannoudji, William Daniel Phillips, 1997), for the achievement of Bose-Einstein condensation (Wolfgang Ketterle, Eric Allin Cornell, Carl Edwin Wieman, 2001), and for the cavity-quantum electrodynamics experiments (Serge Haroche, David J. Wineland, 2012). In its rudimentary form, the optical trapping, or 'tweezing', consists of using the radiation pressure exerted by the light to confine the target particle to some region of space. This naturally requires a strong light intensity impinging on the particle. Recently, another regime of trapping was realized in a 'hollow' PhC cavity [109], in which the effect of the particle on the electromagnetic mode used for confinement is non-negligible and leads to *back-action*. Interestingly, in that scenario it is possible for the particle to be trapped in a region where it 'sees' a very low local field intensity [169]. This could prove particularly important for *lab-on-chip* devices for biomedical sensing [170, 171] when a low intensity is required for the samples to not be destroyed.

In this Section, we present an optimization of the cavity used in Ref. [109], which is illustrated in Fig. 4.18(a). The device is based on an H2-type cavity, which is similar to the H1 of Section 4.1.7, but the holes in the first 'ring' around the defect (see Fig. 4.7) are also missing. In addition, there is an extra-large hole added in the center of the cavity (the big circle in Fig. 4.18(a)), which is where the dielectric particle gets optically trapped. The FDTD-computed electric field amplitude $\sqrt{|E_x|^2 + |E_y|^2}$ of the cavity mode that was used in Ref. [109] is plotted in the Figure. The units of the color map are $(\mu\text{m})^{-3/2}$, since the field is normalized as

$$\int_V \left(|E_x(\mathbf{r})|^2 + |E_y(\mathbf{r})|^2 \right) \varepsilon(\mathbf{r}) \mathrm{d}\mathbf{r} = 1. \tag{4.2}$$
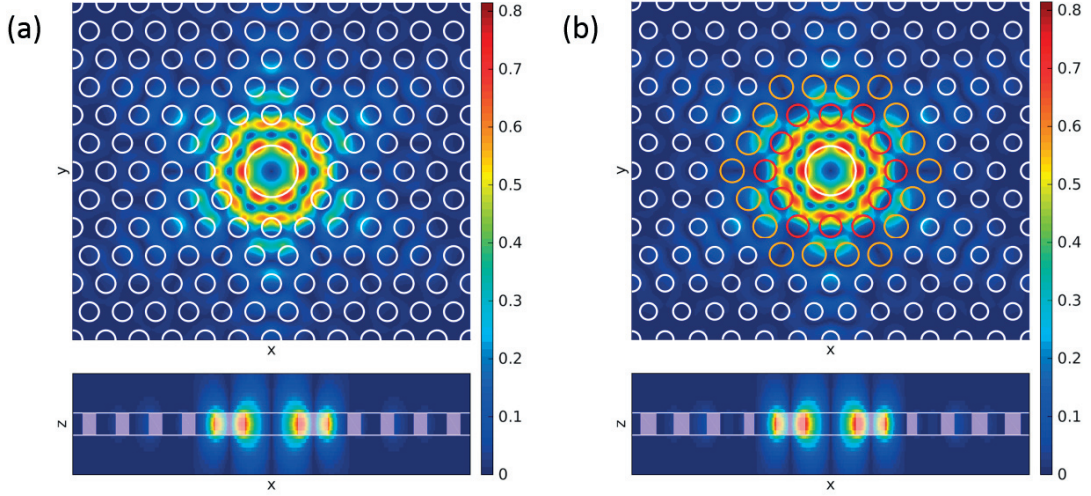
Figure 4.18: (a): Electric field amplitude $\sqrt{|E_x|^2 + |E_y|^2}$ of the cavity mode used for trapping in Ref. [109], shown in an xy-cross-section (at $z = 0$, i.e. in the center of the slab), and in an xz-cross-section (at $y = 0$; the shaded areas denote silicon). (b): Same as (a), but for the optimized design. The holes marked in red and orange are shifted outwards as described in Fig. 4.7 by an amount of S_2 and S_3, respectively, and their radius is changed by dr_2 and dr_3, respectively.

The trapping efficiency of this device is directly proportional to the electric field intensity penetrating the big central hole [109, 172]. The efficiency is also proportional to the quality factor of the cavity, but it should be noted that the experiment was performed with the PhC slab immersed in water to facilitate bringing the dielectric particle to the trapping region. The theoretical Q of the cavity with water in the claddings and in the holes (refractive index $n_w = 1.318$) is computed to be 5700 with GME (FDTD: 6400). However, the measured Q is limited by absorption losses in the water. The highest experimental Q was thus about 2000, while the typical values were around 1000. Taking this into consideration, we optimized a cavity for an increased field overlap with the trapping region without a considerable sacrifice of the Q. More precisely, the objective function F_h was defined as follows. For $Q_t > 2000$,

$$F_h = \frac{1}{R_H^2} \int_{\text{BH}} \left(|E_x(\boldsymbol{\rho}, z = 0)|^2 + |E_y(\boldsymbol{\rho}, z = 0)|^2 \right) \mathrm{d}\boldsymbol{\rho}, \tag{4.3}$$

where R_H is the radius of the big hole, which was kept as a free parameter (within some limits), and the integration is inside that hole and in the $z = 0$ plane only. For values of $Q_t < 2000$, the objective function of eq. (4.3) was simply rescaled by a factor of $Q_t/2000$, in order to suppress designs which would result in significantly lower Q-s than the experimentally measured one. Apart from R_H, the other free parameters chosen were the position and size of the two rings of nearby holes, which were shifted outwards in the same way as illustrated in Fig. 4.7, by an amount of S_2 and S_3, respectively,
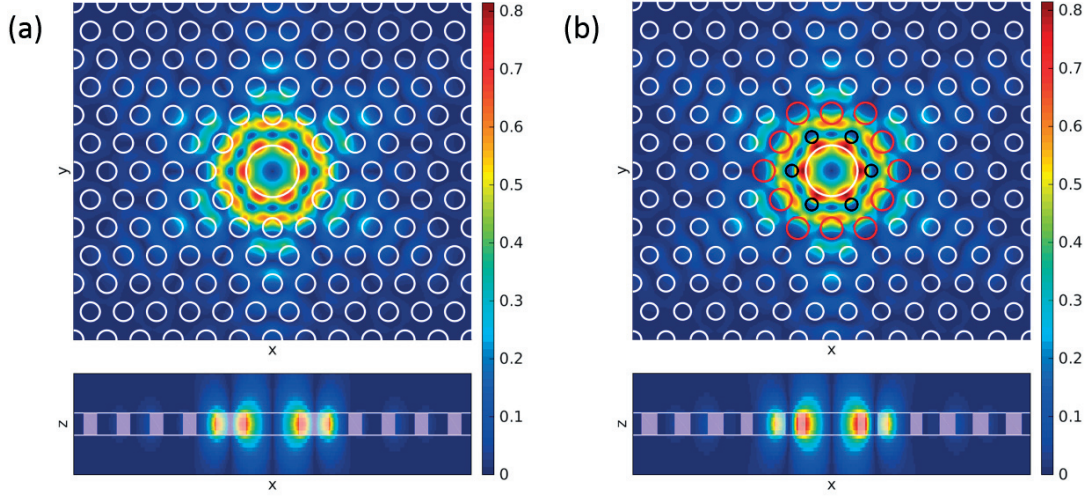
Figure 4.19: (a): Same as panel (a) in Fig. 4.18, replotted here for comparison to (b). (b): The optimized H1 design. The holes marked in black and red are shifted outwards as described in Fig. 4.7 by an amount of S_1 and S_2, respectively, and their radius is changed by dr_1 and dr_2, respectively.

and whose radius was changed by an amount dr_2 and dr_3, respectively (Fig. 4.18(b)). The general PhC parameters were set to $d = 220$nm, $a = 430$nm, $R = 110$nm, as for the experimental setup of Ref. [109]. The optimal design was found for $S_1 = -0.015a$, $S_2 = -0.009a$, $dr_1 = 0.072a$, $dr_2 = 0.099a$, $R_H = 0.076a$. The fact that the holes around the cavity need to be pushed towards the center and increased in size can be understood intuitively, since the electric field mostly concentrates in the high-index material. The modification then 'pushes' more electric field into the big hole, by leaving less space for the field to spread in the dielectric. The objective function defined as in eq. (4.3) for this optimized design is $F_h = 0.137$ (FDTD: $F_h = 0.182$), which is only a marginal increase from the starting, unmodified design, which has $F_h = 0.126$ (FDTD: $F_h = 0.172$). Still, the improvement is visible in Fig. 4.18.

To further improve the device, we also designed another structure based on an H1-type cavity, as illustrated in Fig. 4.19(b). The parameters used in this optimization are R_H, as well as the outward shifts and radius changes S_1, S_2, dr_1, dr_2, as illustrated in the Figure. The overall PhC parameters were taken as in the first optimization. The optimal design was found for $S_1 = 0.201a$, $S_2 = 0.022a$, $dr_1 = -0.072a$, $dr_2 = 0.075a$, $R_H = 0.074a$. This results in $F_h = 0.160$ (FDTD: $F_h = 0.206$), which is now a significant improvement of $\approx 25\%$ over the unmodified design, and is clearly visible in Fig. 4.19. We note that the quality factors of both optimized designs are higher than 2000, thus, experimentally, similar Q-values to the ones measured in the seminal experiment [109] can be expected. The values of F_h and Q for the three cavities discussed here are summarized in Table 4.3.

Cavity	F_h (GME)	F_h (FDTD)	Q (GME)	Q (FDTD)
H2 unopt.	0.126	0.172	5700	6400
H2 opt.	0.137	0.182	2100	2500
H1 opt.	0.160	0.209	2100	2400

Table 4.3: A comparison of the three trapping cavities: unoptimized H2 (used in [109]), optimized H2, and optimized H1. The electric field integral inside the big hole F_h, as defined in eq. (4.3), and the theoretical quality factor Q are given, computed both with GME and with FDTD.

The optimization presented here is an important illustration of the applicability of our scheme, and the GME in particular, to optimizing PhC systems for a quality that goes beyond the cavity Q. The new designs and their qualities were communicated to the group of prof. Houdré, where the seminal experiment was performed, and a new sample employing both of them is planned for fabrication and characterization. It is also worth noting that a similar cavity can be used for other applications, such as stimulated emission from colloidal quantum dots [173]. This would also benefit from our optimization, since the dots are in the hollow region, and the light-matter coupling increases with increasing electric field amplitude of the cavity mode.

4.4 Optimized coupled-cavity waveguide

4.4.1 Preliminary considerations*

In Section 1.3.1, we discussed the importance of slow light as a means to enhance the effects due to optical non-linearities. Periodic photonic structures like the W1 waveguide are particularly suited for applications in that domain, since the group index n_g can be made arbitrarily large in the vicinity of the band edge. Additionally, a significant control over the dispersion is possible through suitable engineering of the photonic structure. Because of this, silicon PhCs have led to impressive slow-light results [52], in particular in line-defect waveguide systems [53, 54, 66, 174], and in Coupled-cavity Waveguides (CCWs) (also called coupled-resonator optical waveguides or CROWs) [46, 55, 58, 175–178].

There is no unique figure of merit for a slow-light system, but there are several important (and not always independent) parameters. The group index $n_g = c/v_g$, with v_g the group velocity, is the slow-down factor as compared to the light propagation in vacuum, and non-linear effects typically scale with this quantity. While it is hard to significantly change the refractive index n of a material using simple manipulations, the group index can be dramatically modified through engineering of the material dispersion, since $v_g = d\omega/dk$. Although this value can be theoretically arbitrarily small in PhCs, it is inevitably restricted in practice by effects of localization and light losses due to disorder

(see discussion in Section 1.3.1). Localization for high n_g in particular has been shown to severely restrict the length-scale on which one could meaningfully talk about light transport [61, 62, 179]. In practice, the best achieved n_g values are of a few hundred at a given frequency [176, 177], while $n_g \lesssim 100$ in wide-band devices [66]. For a realistic system, it is thus natural to restrict the target n_g values to a similar magnitude, and focus instead on improving other figures of merit. These include: low Group Velocity Dispersion (GVD) (i.e. second-order dispersion $d^2\omega/dk^2$), which is necessary for pulsed operation; high Delay-Bandwidth Product (DBP), which, for a fixed group index means a wide operational bandwidth; and low-loss/high-transmission propagation.

In view of these parameters, PhC CCW systems used thus far have some major pros and cons. The advantages are that a very high n_g with a reasonably low GVD can be achieved, and that losses can be made extremely low using $Q \approx 10^6$ cavities. The disadvantages are that the operational bandwidth is typically small, and that having sufficiently many cavities in order to obtain a continuous spectrum requires very long ($> 100\mu m$) structures, which are very challenging to fabricate. In this Section, we show how to overcome both of those difficulties in an ultra-compact PhC CCW design, which we optimize for a high, constant n_g within a large bandwith, for several different, experimentally-relevant values of the group index.

A few remarks are in order. Following Ref. [180], from here on we use the Group Index-Bandwith Product (GBP) (also referred to as the normalized DBP) instead of the DBP as a figure of merit of the CCW performance, and we compute the loss due to out-of-plane radiation in units of $[dB/ns]$ instead of the more standard choice, $[dB/cm]$. This brings the advantage of using quantities which are independent of the device length, and also facilitates the comparison to other systems. In addition, the requirement for low GVD is translated to the related (but not equivalent) requirement [66, 180] for an approximately constant n_g: we define a relative variation Δ_R and require $|n_g - \langle n_g \rangle|/\langle n_g \rangle < \Delta_R$. Finally, we remark that for an approximately constant $n_g \approx \langle n_g \rangle$ within a bandwith $\Delta\omega$, the GBP is $n_g\Delta\omega/\omega \approx \Delta k/\omega$, where Δk is the range of momenta associated to the bandwidth $\Delta\omega$ centered at ω. Thus, in a periodic structure of period L in the propagation direction, the maximum achievable GBP is given by $\pi/(L\omega)$, and ω is fixed by the target operational wavelength.

Motivated by this consideration, we propose a PhC coupled-cavity array with an extremely short spatial periodicity (Fig. 4.20(a)). The structure is based on a chain of L3 cavities, and the underlying PhC has the exact same parameters as in Section 4.1.3. With this particular zig-zag arrangement, the unit cell size in the propagation direction y is $2\sqrt{3}a$, but in fact, due to the symmetry with respect to the $x = 0$ axis, the effective periodicity is of half this pitch, $L_y = \sqrt{3}a$. Intuitively this is to say that no gap can open at the boundary of the first Brillouin zone (at $\pi/(2L_y)$), and a larger $k-$space of twice the width can be considered. This can be more formally illustrated within a tight-binding model for a chain of cavities. To do that, we use the operator
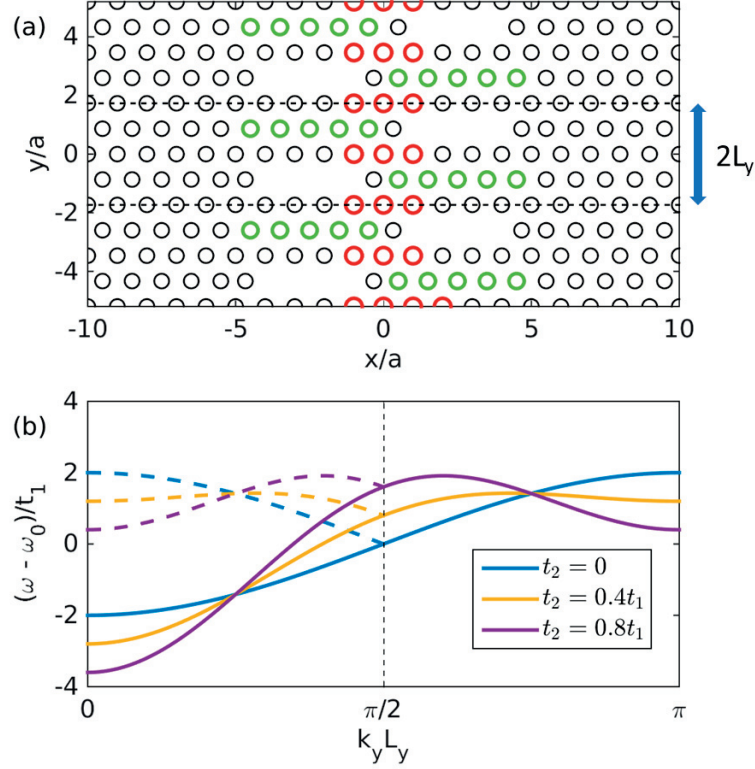
Figure 4.20: (a): CCW composed of coupled L3 PhC cavities; the propagation direction is the vertical, y-axis. The unit cell of the infinite structure is marked by dashed lines. For dispersion optimization, the radius of all holes marked in red is varied by an amount Δr_1, and that of all holes marked in green – by Δr_2. (b): Tight-binding dispersion of a chain of cavities with first- and second-neighbor coupling, t_1 and t_2. The dashed lines show the folded bands in the case of two cavities included in the unit cell, which is an equivalent representation.

formalism that is standard in quantum mechanics, since it is concise and intuitive to read out, but we note that we are not discussing any quantum effects – the formalism is equally well suited to classical field propagation. We denote with c_i and $c_i^\dagger$ the ladder operators for cavity i, with L_i the position of cavity i, and with L_y – the inter-cavity spacing. With first- and second-neighbor coupling and one cavity per unit cell, the Hamiltonian reads

$$H = \sum_i \left[\frac{\omega_0}{2} c_i^\dagger c_i - t_1(c_i^\dagger c_{i+1}) - t_2 c_i^\dagger c_{i+2} \right] + h.c. \tag{4.4}$$

Fourier transforming to k-space through $c_j = \sum_k e^{ikL_j} c_k$, this becomes

$$H(k) = \omega_0 - 2t_1 \cos(L_y k) - 2t_2 \cos(2L_y k), \tag{4.5}$$

91

and so the dispersion $\omega(k)$ is given by

$$\omega(k) - \omega_0 = -2t_1 \cos(L_y k) - 2t_2 \cos(2L_y k), \tag{4.6}$$

where the Brillouin zone for k is from $-\pi/L_y$ to π/L_y. If we consider instead the same system but written in terms of two cavities A and B in the unit cell, the Hamiltonian reads

$$H = \sum_i \left[\frac{\omega_0}{2}(c_{Ai}^\dagger c_{Ai} + c_{Bi}^\dagger c_{Bi}) - t_1(c_{Ai}^\dagger c_{Bi} + c_{Bi}^\dagger c_{Ai+1}) \right.$$
$$\left. -t_2(c_{Ai}^\dagger c_{Ai+1} + c_{Bi}^\dagger c_{Bi+1}) \right] + h.c. \tag{4.7}$$

Defining $C_k = (c_{Ak}, c_{Bk})^T$, the Fourier space Hamiltonian is $H(k) = C_k^\dagger \mathcal{H}(k) C_k$, with

$$\mathcal{H}(k) = \begin{pmatrix} \omega_0 - 2t_2 \cos(2L_y k) & -t_1(1 + e^{i2L_y k}) \\ -t_1(1 + e^{-i2L_y k}) & \omega_0 - 2t_2 \cos(2L_y k) \end{pmatrix} \tag{4.8}$$

Diagonalizing this 2-by-2 matrix gives the dispersion, which now consists of two bands but the Brillouin zone is twice smaller: k from $-\pi/(2L_y)$ to $\pi/(2L_y)$. Since the system is physically the same, when 'unfolded', the two bands match the band obtained in eq. (4.6). This is illustrated in Fig. 4.20(b) for the structure of panel (a), using generic first- and second-neighbor couplings t_1 and t_2. Note that these coefficients are identical for the cavities on the left and on the right of the $x = 0$ plane. The dispersion curves computed with periodicity L_y (one cavity in the unit cell) or $2L_y$ (two cavities in the unit cell) are plotted for comparison, for several values of t_1 and t_2.

For dispersion optimization, we would like to be able to tune the cavity couplings. To a first approximation, we can imagine that modifying the radius of the red and green holes in Fig. 4.20(a) can be used to control t_1 and t_2, respectively. We see from Fig. 4.20(b) that when t_2 becomes comparable to t_1, a degeneracy appears within a finite frequency domain, which prevents low-GVD propagation. To verify that this can be avoided in our design, in Fig. 4.21 we show the results of a simulation of a system with two cavities only, arranged in each of the two possible ways as shown in the top insets of each panel. The simulation was performed using the GME, and also verified with an FDTD solver [74]. The fundamental modes of the cavities are coupled, producing an anti-symmetric and a symmetric mode, and the splitting $\Delta\omega = \omega_S - \omega_{AS}$ is twice the coupling constant t (as can be inferred from eq. (4.7), considering just two cavities). Thus, t_1 and t_2 as a function of the radius of the modified holes can be computed, and are plotted in Fig. 4.21. An interesting observation was recently made [181] that in PhCs, the frequency splitting can be either positive or negative, and moreover could be tuned from one sign to the other – crossing zero – by a simple modulation, which we also observe in Fig. 4.21(b). This is in fact crucial for the compactness of our design, since it allows us to arrange the cavities as shown in Fig. 4.21(a) – with second
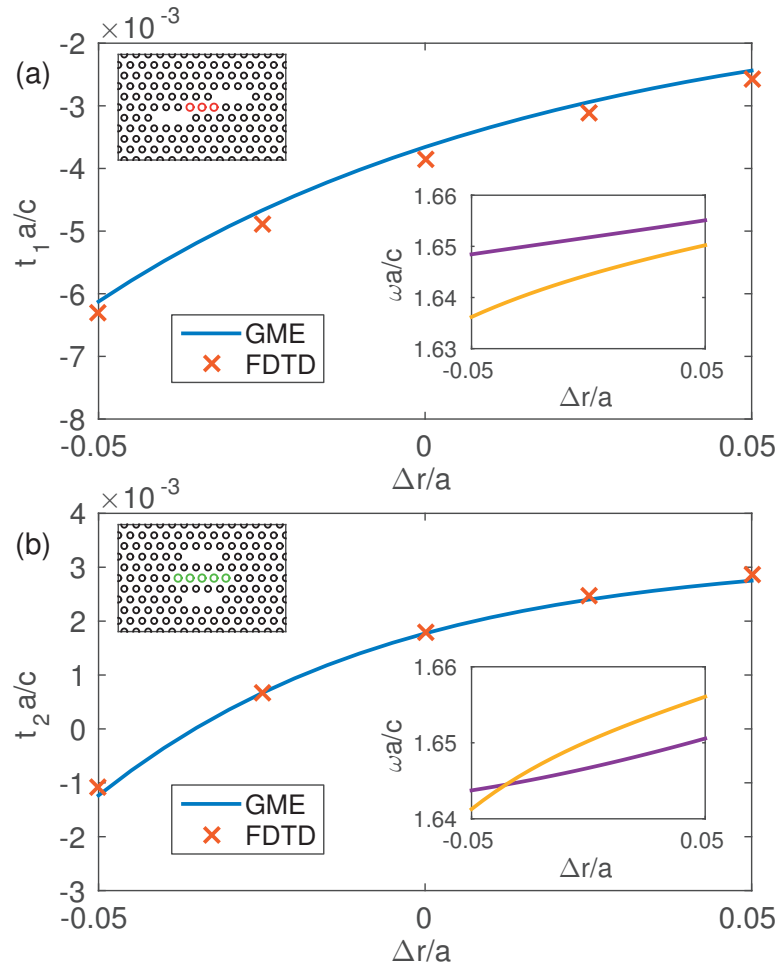
Figure 4.21: (a): Cavity-cavity coupling in a system of two cavities arranged as shown in the top inset, depending on the radius change Δr of the holes marked in red. Values obtained with the guided-mode expansion (blue line) and the finite-difference time-domain (red crosses) methods are shown. Bottom right inset: frequency of the symmetric (yellow) and anti-symmetric (purple) modes vs. Δr. (b): Same as (a) but for a different arrangement, shown in the top left inset.

neighbors separated by a small physical distance – and still have an arbitrarily small t_2, which, as can be seen in Fig. 4.21(b), crosses 0 for a given radius change. To conclude this discussion, we note that the tight-binding approximation provides important insights but is rather crude, and so for all simulations below, we use the guided-mode expansion to find the true PhC eigenmodes.

4.4.2 Optimization of the PhC CCW*

Encouraged by the considerations of Section 4.4.1, we proceed with an optimization of the GBP, using the genetic algorithm to find the optimal PhC parameters in the same
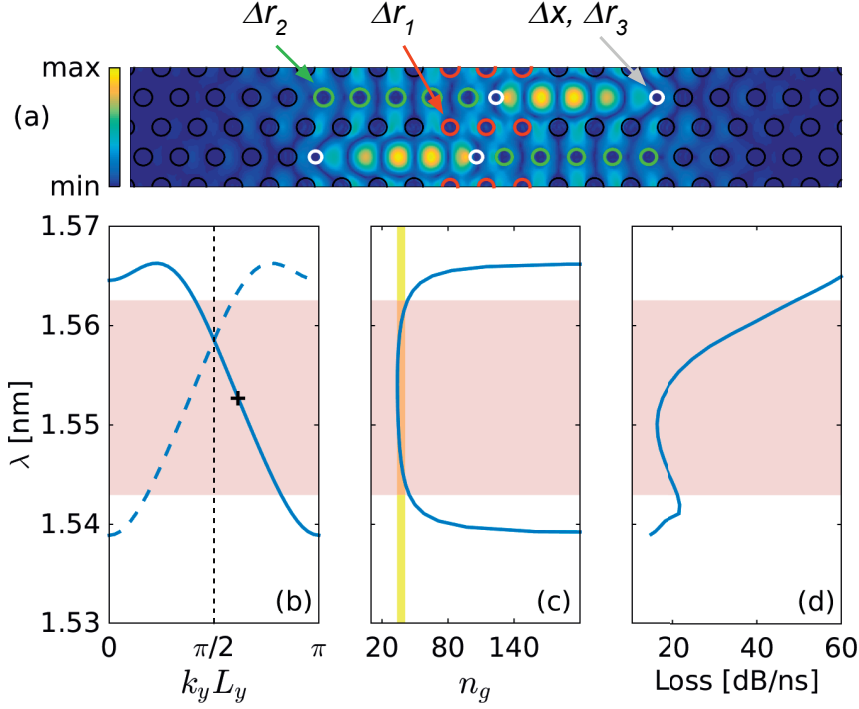
Figure 4.22: (a): Electric field $|E_y|$ profile of the mode marked by a black cross in (b). The green and red holes are modified as in Fig. 4.20(a), while the white holes are shifted outwards by an amount Δx, and have a radius changed by Δr_3. (b) Wavelength dispersion of the optimized design; the black dashed line marks the Brillouin zone for periodicity $2L_y$. Modes from the dashed-line band propagate in the direction opposite to the one of the solid-line band. The operational band-width $\Delta\omega$ is marked by a light-red region (extending into panels (c) and (d)). (c): Group index dispersion; in light yellow, the region $\langle n_g \rangle (1 \pm \Delta_R)$ is marked. (d): Dispersion of the radiative losses.

manner that has already been successfully applied throughout this Chapter. Note that the GME is particularly well-suited for dispersion computations as it is an expansion on the basis of propagating modes, and as it assumes periodic boundary conditions. Of course, as illustrated in the preceeding Sections, the method is also accurate for computing the light loss due to radiation outside of the slab. This is important, since the basic L3 cavity has a modest quality factor of a few thousand [25, 82], but, as illustrated in Section 4.1.3, this can be increased by several orders of magnitude using some simple modifications of the neighboring holes. Thus, to include the possibility for minimizing losses in the optimization, we allow for a change of radius Δr_3 and an outward shift Δx of the holes on each side of each cavity (marked in white in Fig. 4.22(a)). Our free parameters are thus $(\Delta r_1, \Delta r_2, \Delta r_3, \Delta x)$, but we still have freedom in defining the objective function.

We demonstrate several optimizations below, to highlight the flexibility of our method. For all computations, we take the standard choice [180] for the maximum allowed
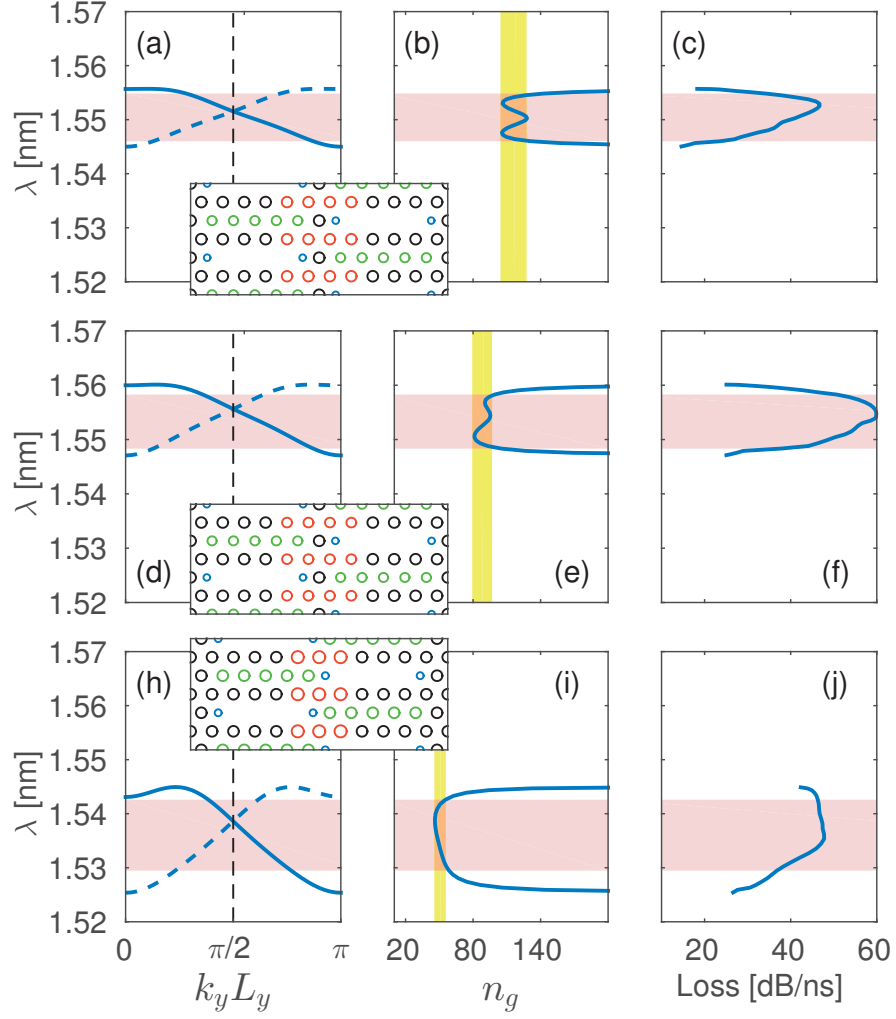
Figure 4.23: Designs with (a)-(c): $\langle n_g \rangle = 116$, $G = 0.66$; (d)-(f): $\langle n_g \rangle = 88$, $G = 0.56$; (h)-(j): $\langle n_g \rangle = 51$, $G = 0.43$. Same plotting and color scheme is employed as in Fig. 4.22(b)-(d)

relative variation of the group index, $\Delta_R = 10\%$, i.e. we consider the operational band-with $\Delta\omega$ to be the one within which $|n_g - \langle n_g \rangle|/\langle n_g \rangle < \Delta_R$ for some value of $\langle n_g \rangle$ (not necessarily the arithmetic average). Thus, for a given design, after computing $n_g(\omega)$, we define the GBP as $G = \langle n_g \rangle \Delta\omega/\omega$, where $\langle n_g \rangle$ is defined such that $\Delta\omega$ is largest. To also account for the radiative losses L_r, the objective function for the design shown in Fig. 3 was set to $f(\Delta r_1, \Delta r_2, \Delta r_3, \Delta x) = G$ for $\max(L_r) < 50 \mathrm{dB/ns}$, and to $G \times (50\mathrm{dB/ns}/\max(L_r))$ otherwise. The cut-off in the maximum allowed losses was chosen based on the experimentally demonstrated loss in PhC waveguide systems [180].

With this objective function, the optimization results in a design with parameters $(\Delta r_1, \Delta r_2, \Delta r_3, \Delta x) = (-0.0385, -0.0279, -0.0759, 0.1642)a$ (Fig. 4.22(a)). The wave-

Table 4.4: Parameters and figures of merit of the optimized CCW designs presented in this Section.

CCW	$\Delta r_1/a$	$\Delta r_2/a$	$\Delta r_3/a$	$\Delta x/a$	GBP	$\langle n_g \rangle$	$\Delta\lambda, [nm]$
Des. 1	-0.0385	-0.0279	-0.0759	0.1642	0.47	37	19.5
Des. 2	-0.0049	-0.0340	-0.1016	0.2204	0.66	116	8.8
Des. 3	-0.0221	-0.0341	-0.1200	0.2500	0.56	88	9.9
Des. 4	0.0323	-0.0002	-0.0877	0.2131	0.43	51	13.1

length dispersion plotted in Fig. 4.22(b) is obtained by setting $a = 400$nm; as can be seen, the CCW guided band has very low GVD within a very wide wavelength range of 19.5nm. The average group index is $\langle n_g \rangle = 37$, which results in a GBP of 0.47. This value is more than twice higher than that of previous CCW systems [176, 177] and is close to the highest theoretical value of any existing proposal. In fact, the only system to our knowledge which has a higher theoretical GBP is a topology-optimized PhC waveguide [182] with a GBP of 0.5 at $n_g = 50$, which has the significant disadvantage of requiring non-circular holes with fine features, which are challenging to fabricate. In another proposal using a coupled-waveguide system [183], the group index and so the GBP vary spatially along the device. A position-averaged GBP value attaining a maximum of approximately 0.5 was estimated for such a system, but the spatial dependence of n_g remains a significant disadvantage as compared to our design.

In order to look for a higher group index n_g, we perform another optimization but aiming at a smaller first-neighbor coupling, which, intuitively, results in a smaller frequency width of the guided bands, and thus – slower light. Practically we impose this by increasing the distance in the x-direction (refer to Fig. 4.20(a)) between consecutive cavities by one lattice constant a, as illustrated in the inset of Fig. 4.23(a). Notice that this results in 4 holes marked in red (radii changed by Δr_1) between consecutive cavities, instead of 3. Running an optimization with the same objective function as above results in a design with parameters $(\Delta r_1, \Delta r_2, \Delta r_3, \Delta x) = (-0.0049, -0.0340, -0.1016, 0.2204)a$, with $\langle n_g \rangle = 116$ within a 8.8nm band, thus with a GBP of 0.66 (Fig. 4.23(a)-(c)). This is the highest theoretical GBP among all existing slow-light designs.

Finally, we also obtain designs with an intermediate group index by optimizing each of the two basic designs with a different objective function, defined as $G \times (|\langle n_g \rangle - n_{g,t}|/n_{g,t})$, for some target $n_{g,t}$ (notice that we drop the loss-dependence of the objective function). Setting $n_{g,t} = 80$ results in the design shown in Fig. 4.23(d)-(f), with parameters $(\Delta r_1, \Delta r_2, \Delta r_3, \Delta x) = (-0.0208, -0.0350, -0.0950, 0.2443)a$, with $\langle n_g \rangle = 88$ over a 9.9nm wavelength range (GBP = 0.56). Setting $n_{g,t} = 50$ yields a better design if the three-red-hole scheme of Fig. 4.22(a) is used; the optimal design (Fig. 4.23(h) inset) is found for $(\Delta r_1, \Delta r_2, \Delta r_3, \Delta x) = (0.0323, -0.0002, -0.0877, 0.2131)a$, with $\langle n_g \rangle = 51$ over a 13.1nm bandwidth (GBP = 0.43). The parameters and figures of merit of all designs are summarized in Table 4.4.
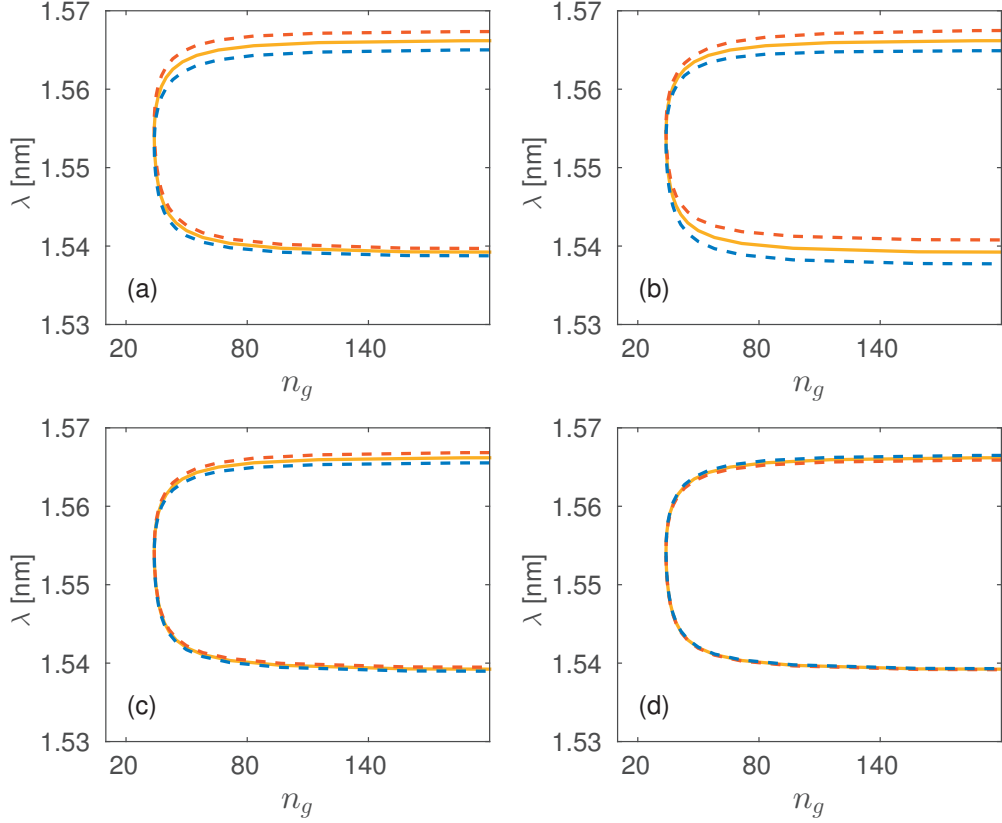
Figure 4.24: Group index vs. wavelength for Design 1. Shown is the nominal structure (yellow solid line), and a -2nm (red dashed line) or a +2nm (blue dashed line) deviation in (a): Δr_1, (b): Δr_2, (c): Δr_3, and (d): Δx.

The parameters are given with a high precision in case it is needed, but a sub-nanometer control is by no means a requirement to keep the outstanding dispersion properties. This is illustrated in Fig. 4.24, where we plot the effect of small variations of the optimization parameters on the wavelength dependence of the group index, for the design of Fig. 4.22. In the Figure, panel (a) shows variation in Δr_1, panel (b) – in Δr_2, panel (c) – in Δr_3, and panel (d) – in Δx. The red dashed line shows a variation of -2nm of the respective parameter, while the blue dashed line – of $+2$nm. This variation is larger than the state-of-the-art precision in Silicon devices. We note that Δr_1 and Δr_2 have a much more pronounced effect than Δr_3 and Δx, which can be expected since the latter were introduced mostly to minimize losses. Most importantly, the effect of all parameters is to slightly shift the operational band up or down in wavelength, but the important property of the designs – high, approximately constant $\langle n_g \rangle$ – is conserved. We checked that all these conclusions hold for the other designs as well.

Of course, as discussed above, random disorder in all holes of the structure introduces unavoidable losses both in the vertical and in the counter-propagating direction [61, 62, 179], but this was the reason for which we aimed for values of the group index and

the extrinsic losses which have been observed in practice in similar systems [66, 176]. Finally, we note that we checked that small variations of the material refractive index also preserve the outstanding properties of the proposed designs, thus they can also be implemented in materials of similar permittivity as silicon, e.g. gallium arsenide.

4.4.3 Experimental outlook

In conclusion, we presented highly optimized designs for silicon coupled-cavity waveguides with a record-high group index-bandwith product, low variation of the group index, and low out-of-plane losses. The waveguides are straightforward to fabricate and can find a variety of applications, including high-bit-rate optical storage (very short pulses can be used due to the large bandwidth) [52, 58], enhanced non-linear effects like four-wave mixing (e.g. for entangled photon pair generation) [46, 54, 56] and third-harmonic generation [53, 184], and enhanced radiative coupling between distant quantum dots for quantum information processing [59, 60].

The outstanding properties predicted for the designs presented here, together with the many possibilities for applications, are a strong incentive to realize these structures in practice. To do this, we are collaborating with the group of prof. Houdré at EPFL and prof. Badolato in Rochester. A preliminary sample has in fact been fabricated, and very promising spectroscopic results have already been measured. The current state of this project is that a new sample is in preparation, in which some structural challenges that seem to have affected the first sample will be tackled. We expect this to lead to an experimental demonstration of the highest-quality slow-light device ever reported, opening up various possibilities for future experiments.

4.5 The impact of PhC optimization

The results presented in this Chapter could easily be considered the core of this thesis. It is fair to argue that our optimization procedure constitutes a paradigm shift, in that it reveals the enormous room left for exploration in the domain of photonic crystals. Because of this, our scheme has attracted interest from research groups all over the world and will undoubtedly be useful for years to come. This is best illustrated by the sheer variety of the results presented here[1], as well as some other results that are part of currently ongoing projects. As an outlook, we list a few of those: one example is a cavity with resonant modes at ω and 2ω that we have developed [185], useful for Second-harmonic Generation (SHG). For that same application, we have also developed GaN and AlN cavity designs with high Q and efficient vertical extraction, which are currently under fabrication. Another idea is to optimize a self-filtering,

---

[1]Two of the results of this Chapter were featured on the cover of Applied Physics Letters [114, 115], as well as in several press releases.

highly efficient Four-wave Mixing (FWM) device for frequency conversion. Yet another project is optimizing GaAs cavities at various frequencies for quantum dot integration. We are also developing an acoustic GME code that will enable us to optimize structures for optomechanics [186, 187]. All in all, the research directions that the optimization scheme opens are countless.

5 Radiative Coupling of Quantum Dots in Photonic Crystals

In this Chapter, we derive a general formalism to model the polariton states resulting from the radiation-matter interaction between an arbitrary number of excitonic transitions in semiconductor Quantum Dots (QDs) and photon modes in a photonic crystal structure in which the quantum dots are embedded. The Chapter is adapted from two of our publications, Refs. [60] (M. Minkov and V. Savona, "Radiative coupling of quantum dots in photonic crystal structures," *Phys. Rev. B* **87** (2013)) and [188] (M. Minkov and V. Savona, "Long-distance radiative excitation transfer between quantum dots in disordered photonic crystal waveguides," *Phy. Rev. B (R)*, **88** (2013)).

This Chapter is organized as follows: Section 5.1 gives some background to the study of QDs in photonic structures. In Section 5.2 we lay down the semi-classical linear response theory for a system of N distinct, spatially localized excitonic transitions in QDs, coupled to M photonic modes of an arbitrary photonic structure. In particular, we frame the underlying Maxwell equations into an eigenvalue problem, describing the polariton modes of the system in analogy with the polariton formalisms for a bulk semiconductor [189], for quantum wells [190], and for QDs in an unstructured photonic environment [191, 192]. In Section 5.3, we apply the formalism to Ln cavities (with n missing holes in a row) and W1 waveguides in a PhC slab. For the computation of the photonic modes, the Bloch-mode expansion is employed (cf. [63] and Section 2.4), although any other method which provides reliable field profiles (e.g. GME, FDTD) can also be used. We show how known single-dot radiative properties – such as the vacuum Rabi splitting in a microcavity and the Purcell enhancement and β-factor in a waveguide – are well reproduced. The main focus of the Section however is the quantitative characterization of radiative coupling between **two** dots in those same structures. To this purpose, we characterize the spectra of the polariton eigenmodes, the time-evolution of a starting excitation in one of the dots, and the distance-dependence of the radiative excitation transfer in a spatially extended structure. In Section 5.4, we extend our simulations to realistic systems with different magnitudes of fabrication disorder, both in the PhC and in the QD positioning. We

show that, while disorder-induced light localization has a profound effect on both the range and the magnitude of the dot-dot excitation transfer rate, this latter is still large when compared to typical decoherence rates. Finally, Section 5.5 gives some concluding remarks.

5.1 Motivation for studying the QD-PhC system*

In the last two decades, the design and implementation of devices for quantum information processing has been a major goal of condensed matter physics. An essential requirement of the quantum information paradigm is the possibility for two *qubits* to interact coherently in a controlled fashion, in order to achieve controlled gate operations [193]. This must in principle be possible for each arbitrarily chosen pair of qubits in the system. Most of the technologies, however, employ qubits which are at all times spatially separated and do not interact directly [194–196]. The interaction can then be achieved by means of a *quantum bus*, namely a spatially extended degree of freedom interacting with all localized qubits. In a more general picture, these spatially extended degrees of freedom might even form a quantum network connecting distant quantum information systems [197]. A quantum bus can be of several kinds – two common examples being phonons in chains of trapped ions [198] and microwave photons in superconducting circuits [199, 200]. Photons are the most natural choice in a solid-state system, given their low decoherence rate, high velocity, and the recent advances in the on-chip photonic technology, especially in the photonic crystal domain.

Semiconductor QDs have long been considered as viable qubit candidates [201], as they naturally fulfill the criteria of scalability and integrability required in a quantum information technology. Facing the remarkable advance made in the system of spin qubits in lateral QDs [196] – where electron spins are controlled electronically with ohmic contacts – optical excitations in self-organized QDs have only recently caught up in the race towards controlled quantum operations. On one hand, in fact, full single-qubit optical control has been successfully demonstrated [202–211]. On the other, integrating QDs in photonic structures has made significant progress, and both single-dot Purcell enhancement in cavities [212–217] and waveguides [218–225], and strong coupling to a cavity mode [47, 226, 227] have been demonstrated. Single-dot coupling to light modes is in itself important for practical applications, as suggested by the possibility of non-classical light generation [42, 43, 228, 229], or single-photon optical switching [44]. Beyond that, short-distance coupling in quantum dot 'molecules' has been demonstrated [230–235], where however the coupling is enforced by the direct overlap of the QD wave-functions and/or the electrostatic Förster dipole-dipole interaction [236, 237], rather than by any long-distance mechanism. Altogether, these advances suggest that the field has reached the milestone, following which the process of **long-distance**, photon-mediated interaction between two or more quantum dots should also be addressed. It has been shown that the light-matter interaction between

a QD and the electromagnetic modes of a non-structured photonic environment is very weak [191, 192, 238, 239], thus photonic structures are needed in order to tailor the density of optical modes and thus enhance the radiative coupling between spatially separated quantum dots. Indeed, short-range radiative coupling has already been achieved in several experiments involving small optical cavities, where strong coupling of two quantum dots to the same cavity mode was detected [240–242], and, most recently, its coherent nature was demonstrated [243]. A photonic structure has also brought the experimental demonstration of long-distance transfer of photons emitted by an embedded QD. [41]

On the theoretical side, specific aspects of structures with one or more quantum dots in a photonic environment have been studied. These include the strong coupling regime and emission spectrum of one [68, 90, 244–246] or more [247–249] dots in a microcavity, as well as the possibility of performing cavity-mediated qubit operations through coherent excitation exchange in such a system [50, 250–253]. In addition, the spontaneous emission enhancement of one dot coupled to a single waveguide mode has been estimated [254–256], and non-trivial dynamics of single-dot cavity-QED in presence of coupling to a second, distant cavity, have been predicted [59]. There are, however, only a few studies of the dot-dot interaction at a mesoscopic (i.e. more than one wavelength) inter-dot distance – which is a main focus of this Chapter. Most notably, the possibility to generate entangled states between distant QDs in a coupled-cavity system was recently demonstrated [257], as well as the non-trivial decay dynamics[1] of two distant dots in a photonic crystallite [258]. Here, we present a general formalism accounting for an arbitrary number of quantum dots coupled to arbitrarily many photonic modes, which allows us to analyze the distance dependence of the radiative interaction, the influence of fabrication disorder, and the competition between excitation transfer at-a-distance and radiation losses.

5.2 Theoretical formalism*

Starting from Maxwell's equations with the assumptions of a non-magnetic medium and no free charges, but with a non-zero polarizability $\mathbf{P}$, the electric field in the frequency domain obeys the equation

$$\nabla \times \nabla \times \mathbf{E}(\mathbf{r}, \omega) - \frac{\omega^2}{c^2} \left(\varepsilon(\mathbf{r})\mathbf{E}(\mathbf{r}, \omega) + 4\pi\mathbf{P}(\mathbf{r}, \omega) \right) = 0 \,. \tag{5.1}$$

In our study, the underlying photonic structure is as usual characterized by the spatial dependence of the dielectric constant, $\varepsilon(\mathbf{r})$, while the optical response of the quantum dots is included in the polarization vector through a non-local susceptibility tensor

---

[1]Here we prefer not to use the term 'superradiant', in order to avoid ambiguity with the concept of Dicke superradiance, which has a radically different physical nature.

[259], such that

$$\mathbf{P}(\mathbf{r}, \omega) = \int d\mathbf{r}' \hat{\chi}(\mathbf{r}, \mathbf{r}', \omega) \mathbf{E}(\mathbf{r}', \omega) \, . \tag{5.2}$$

In what follows, we will consider the specific case of excitons originating from the heavy-hole band of a semiconductor with cubic symmetry (e.g. Indium Arsenide (InAs)), for which only the x- and y-components of the polarization couple to the electromagnetic field according to the following susceptibility tensor [190, 260, 261]

$$\hat{\chi}(\mathbf{r}, \mathbf{r}', \omega) = \frac{\mu_{cv}^2}{\hbar} \sum_{\alpha=1}^{N} \frac{\Psi_\alpha^*(\mathbf{r}) \Psi_\alpha(\mathbf{r}')}{\omega^\alpha - \omega} \begin{pmatrix} 1 & 0 & 0 \\ 0 & 1 & 0 \\ 0 & 0 & 0 \end{pmatrix} \, . \tag{5.3}$$

The formalism can be easily generalized to different forms of the susceptibility tensor. Here, α runs over all QDs, μ_{cv}^2 is the squared dipole matrix element of the inter-band optical transition, $\Psi_\alpha(\mathbf{r}) = \Psi_\alpha(\mathbf{r}_e = \mathbf{r}, \mathbf{r}_h = \mathbf{r})$, and $\Psi_\alpha(\mathbf{r}_e, \mathbf{r}_h)$ is the excitonic wave-function, normalized as

$$\int d\mathbf{r}_e \int d\mathbf{r}_h |\Psi_\alpha(\mathbf{r}_e, \mathbf{r}_h)|^2 = 1 \, . \tag{5.4}$$

We denote the frequencies of the bare excitons by a *superscript* α, in order to distinguish them from the frequencies of the photonic resonances, which we will later on index with *subscripts*, e.g. as ω_m. Notice also that here all frequencies are assumed to be complex quantities, e.g. $\omega^\alpha = \Re(\omega^\alpha) - i\frac{\gamma^\alpha}{2}$, where γ^α represents the overall decay rate of the exciton state, including any possible non-radiative mechanism and the rate of radiative decay into photon modes that are **not** included among the M modes treated exactly.

In order to turn the Maxwell equation into a self-adjoint form, we introduce the quantities [262] $\mathbf{Q}(\mathbf{r}, \omega) = \sqrt{\varepsilon(\mathbf{r})} \mathbf{E}(\mathbf{r}, \omega)$. Eq. (5.1) then becomes

$$\Upsilon \mathbf{Q}(\mathbf{r}, \omega) - \frac{\omega^2}{c^2} \mathbf{Q}(\mathbf{r}, \omega) = \frac{4\pi}{\sqrt{\varepsilon(\mathbf{r})}} \frac{\omega^2}{c^2} \int d\mathbf{r}' \hat{\chi}(\mathbf{r}, \mathbf{r}', \omega) \frac{\mathbf{Q}(\mathbf{r}', \omega)}{\sqrt{\varepsilon(\mathbf{r}')}}, \tag{5.5}$$

which is an inhomogeneous differential equation defined for the *self-adjoint* differential operator

$$\Upsilon = \frac{1}{\sqrt{\varepsilon(\mathbf{r})}} \nabla \times \nabla \times \frac{1}{\sqrt{\varepsilon(\mathbf{r})}} \, . \tag{5.6}$$

The susceptibility tensor as given in eq. (5.3) decouples the z-polarized fields. We then define the two-dimensional field $\mathbf{Q} = (Q_x, Q_y)$. We can solve the problem using a

Green's function approach [263], in which the formal solution to eq. (5.5) is

$$\mathbf{Q}(\mathbf{r},\omega) = \mathbf{Q}_0(\mathbf{r},\omega) + \frac{4\pi}{\sqrt{\varepsilon(\mathbf{r})}} \frac{\omega^2}{c^2} \int d\mathbf{r}' \int d\mathbf{r}'' \hat{G}(\mathbf{r},\mathbf{r}',\omega) \frac{\hat{\chi}(\mathbf{r}',\mathbf{r}'',\omega)}{\sqrt{\varepsilon(\mathbf{r}'')}} \mathbf{Q}(\mathbf{r}'',\omega). \quad (5.7)$$

The Green's tensor can be expanded onto the basis of field eigenmodes using the resolvent representation, following Fredholm's theory [264]

$$\hat{G}(\mathbf{r},\mathbf{r}',\omega) = \sum_m \frac{\mathbf{Q}_m(\mathbf{r}) \otimes \mathbf{Q}_m^*(\mathbf{r}')}{\frac{\omega_m^2}{c^2} - \frac{\omega^2}{c^2}}, \quad (5.8)$$

where the $\mathbf{Q}_m$-s are the *orthonormal* eigenfunctions of Υ corresponding to eigenvalues ω_m^2/c^2, and $\otimes$ is an outer product defined as

$$\mathbf{A} \otimes \mathbf{B} = \begin{pmatrix} A_x B_x & A_x B_y \\ A_y B_x & A_y B_y \end{pmatrix}. \quad (5.9)$$

The sum in eq. (5.8) runs in principle over the infinite set of eigenmodes. In most situations of interest, however, this sum is dominated by the resonant modes of the photonic crystal that are closest to the frequency range characterizing the excitonic transitions. In addition, in all structures of interest (e.g. a PhC [47,48], pillar cavity [226] or a microdisc [227]), the dots are typically embedded within the dielectric medium, i.e. their wave-functions are non-negligible only in a region where $\varepsilon(\mathbf{r}) = \varepsilon_\infty$, the permittivity of the semiconductor. Thus, as the $\mathbf{r}$-dependence of all quantities will eventually enter through overlap integrals with the QD wave-functions, in eq. (5.7) we can safely substitute $\sqrt{\varepsilon(\mathbf{r})} = \sqrt{\varepsilon(\mathbf{r}'')} = \sqrt{\varepsilon_\infty}$. Finally, in typical situations, all QD transition frequencies lie within a small range originating from the inhomogeneous distribution of QD sizes. A very good approximation consists then in replacing the ω on the r.h.s. of (5.7), as well as the $(\omega_m + \omega)/2$ obtained by factoring the denominator in (5.8), with an average exciton transition frequency ω_0. In order to compute the complex frequency poles, corresponding to the resonances of the coupled system, we consider the homogeneous problem associated with eq. (5.7). Then, by defining

$$\mathbf{Q}^\alpha(\omega) = \int d\mathbf{r} \Psi_\alpha(\mathbf{r}) \mathbf{Q}(\mathbf{r},\omega), \quad (5.10)$$

we obtain

$$\mathbf{Q}(\mathbf{r},\omega) = \frac{2\pi\omega_0}{\varepsilon_\infty} \frac{\mu_{cv}^2}{\hbar} \sum_{\alpha=1}^N \sum_{m=1}^M \frac{\mathbf{Q}_m(\mathbf{r}) \otimes \mathbf{Q}_m^{\alpha*}}{(\omega_n - \omega)(\omega^\alpha - \omega)} \mathbf{Q}^\alpha(\omega). \quad (5.11)$$

By integrating eq. 5.7 with $\int d\mathbf{r} \Psi_\beta(\mathbf{r})$ and defining additionally $\tilde{\mathbf{Q}}^\alpha(\omega) = \mathbf{Q}^\alpha(\omega)/(\omega^\alpha -$

ω), we finally obtain a set of equations (labeled by β) for the complex frequency poles

$$(\omega^\beta - \omega)\tilde{\mathbf{Q}}^\beta(\omega) = \frac{2\pi\omega_0}{\varepsilon_\infty}\frac{\mu_{cv}^2}{\hbar}\sum_{\alpha=1}^N\sum_{m=1}^M\frac{\mathbf{Q}_m^\beta\otimes\mathbf{Q}_m^{\alpha*}}{(\omega_n-\omega)}\tilde{\mathbf{Q}}^\alpha(\omega)\,. \tag{5.12}$$

We now define the quantities

$$\mathbf{g}_m^\alpha = (g_{m,x}^\alpha, g_{m,y}^\alpha) = \left(\frac{2\pi\omega_0}{\varepsilon_\infty}\frac{\mu_{cv}^2}{\hbar}\right)^{1/2}\mathbf{Q}_m^\alpha\,, \tag{5.13}$$

which should be interpreted as the coupling strengths between the m-th mode of the PhC and the α-th QD. To this end, we notice that the $2N$ equations in (5.12) can be solved only for those values of ω for which the $N\times N$ matrix

$$\Lambda_1 = \begin{pmatrix} \omega_x^1 - \omega - \sum_{m=1}^M\frac{g_{m,x}^1 g_{m,x}^{1*}}{\omega_m-\omega} & \cdots & -\sum_{m=1}^M\frac{g_{m,x}^1 g_{m,x}^{N*}}{\omega_m-\omega} & -\sum_{m=1}^M\frac{g_{m,x}^1 g_{m,y}^{N*}}{\omega_m-\omega} \\ -\sum_{m=1}^M\frac{g_{m,y}^1 g_{m,x}^{1*}}{\omega_m-\omega} & \cdots & -\sum_{m=1}^M\frac{g_{m,y}^1 g_{m,x}^{N*}}{\omega_m-\omega} & -\sum_{m=1}^M\frac{g_{m,y}^1 g_{m,y}^{N*}}{\omega_m-\omega} \\ \vdots & \ddots & \cdots & \vdots \\ -\sum_{m=1}^M\frac{g_{m,y}^N g_{m,x}^{1*}}{\omega_m-\omega} & \cdots & -\sum_{m=1}^M\frac{g_{m,y}^N g_{m,x}^{N*}}{\omega_m-\omega} & \omega_y^N - \omega - \sum_{m=1}^M\frac{g_{m,y}^N g_{m,y}^{N*}}{\omega_m-\omega} \end{pmatrix} \tag{5.14}$$

is singular. This is a nonlinear equation, but we notice that it can be transformed into a more familiar form, since it is mathematically equivalent to finding the eigenvalues of the matrix

$$\Lambda_2 = \begin{pmatrix} \omega_x^1 & 0 & \cdots & 0 & g_{1,x}^1 & \cdots & g_{M,x}^1 \\ 0 & \omega_y^1 & \cdots & 0 & g_{1,y}^1 & \cdots & g_{M,y}^1 \\ \vdots & \cdots & \ddots & \vdots & \vdots & \cdots & \vdots \\ 0 & 0 & \cdots & \omega_y^N & g_{1,y}^N & \cdots & g_{M,y}^N \\ g_{1,x}^{1*} & g_{1,y}^{1*} & \cdots & g_{1,y}^{N*} & \omega_1 & \cdots & 0 \\ \vdots & \cdots & \ddots & \vdots & \vdots & \cdots & \vdots \\ g_{M,x}^{1*} & g_{M,y}^{1*} & \cdots & g_{M,y}^{N*} & 0 & \cdots & \omega_M \end{pmatrix}\,. \tag{5.15}$$

More precisely, solving $\det(\Lambda_1) = 0$ is equivalent to solving $\det(\Lambda_2 - \omega I_{(2N\times M)\times(2N\times M)}) = 0$, whenever $\omega \neq \omega_m\,\forall\,m = 1\ldots M$. The proof can be easily obtained by, on one hand, multiplying the equation for Λ_1 by $\prod_{m=1}^M(\omega_m - \omega)$, and on the other, using in the eigenvalue problem for Λ_2 the following identity for the determinant of a block-matrix:

$$\det\begin{pmatrix} A & B \\ C & D \end{pmatrix} = \det(D)\det(A - BD^{-1}C)\,. \tag{5.16}$$

The poles $\omega = \omega_m$ will generally exist as solutions only when a photonic mode $\mathbf{Q}_m$ is

fully decoupled from the system, i.e. when $\mathbf{g}_m^\alpha = 0 \,\forall\, \alpha$, in which case this mode can safely be excluded from the very beginning. The $2N + M$ complex eigenvalues of Λ_2 then define the frequencies (real part) and the loss rates ($-2\times$ imaginary part) of the *polariton modes* of the system, while the eigenvectors

$$\boldsymbol{\lambda} = (\lambda_x^1, \lambda_y^1, \dots \lambda_x^N, \lambda_y^N, \lambda_1 \dots, \lambda_M) \tag{5.17}$$

define the corresponding Hopfield coefficients [189], which, for each eigenstate, give the probability amplitude of finding an excitation in the corresponding bare-exciton or bare-photon mode. Notice in addition that the matrix of eq. (5.15) corresponds to a Tavis-Cummings Hamiltonian [265] in the weak excitation regime, when only transitions from the ground state to the manifold of states with a single excitation are considered. Thus, notice that our approach has a straightforward extension to treating non-linear quantum dot dynamics, as the coupling constants in the off-diagonal terms of eq. (5.15) can be used to write the Tavis-Cummings Hamiltonian in its most general from, i.e. including transitions among all excitation-number manifolds. This describes the system whenever the quantum dots behave as two-level systems, which is indeed the case for small dots under resonant excitation. Our semi-classical formalism instead treats all degrees of freedom as harmonic oscillators with linear couplings. The two regimes give equivalent predictions in the limit of weak exciton saturation, as in a quantum well [266]. In the quantum-dot case, the saturation is strong but the predictions are still expected to coincide in the weak-excitation regime, when the quantum Hamiltonian can be truncated to the single-excitation subspace.

The present formalism applies to a large variety of photonic structures and to an arbitrary spatial distribution of QDs. In this sense, it generalizes the results that were obtained for specific configurations [59, 68, 254–258]. As an illustrating application, in Section 5.3 we present results obtained for the case of two quantum dots embedded in several of the most widely studied photonic crystal structures: the L3 and Ln cavities and the W1 waveguide.

5.3 Application: from cavities to waveguides

5.3.1 Model parameters*

In order to quantify the susceptibility of eq. (5.3), we need an appropriate model of the exciton wave-function evaluated at equal electron and hole positions, $\Psi_\alpha(\mathbf{r}) = \Psi_\alpha(\mathbf{r}_e = \mathbf{r}, \mathbf{r}_h = \mathbf{r})$. This function is **not** properly normalized as a function of $\mathbf{r}$ (the correct normalization is over $\mathbb{R}^3 \times \mathbb{R}^3$ as given in eq. (5.4)). In fact, similarly to the quantum well case [260, 261], the oscillator strength of the exciton transition in the QD

depends on the dimensionless quantity

$$C^2 = \left| \int d\mathbf{r} \Psi_\alpha(\mathbf{r}) \right|^2 . \tag{5.18}$$

The particular *shape* of the wave-function enters through the overlap integrals with the electric field, as given in eq. (5.10). As long as the size of the QDs is much smaller than the characteristic wavelength, the electric field varies very weakly in the region where Ψ_α is non-negligible, and thus the point dipole assumption, $\Psi_\alpha(\mathbf{r}) = C\delta(\mathbf{r} - \mathbf{r}_\alpha)$, is a very good approximation. In what follows we will mostly use parameters typical of self-organized InGaAs QDs [267], whose size lies in the $10 - 20$nm range, with a typical exciton recombination energy of 1.3eV ($\lambda \approx 950$nm). For these values, we checked that assuming a Gaussian shape for $\Psi_\alpha(\mathbf{r})$ introduces little change with respect to the Dirac-delta assumption. Notice, however, that the strong dependence [268, 269] of the QD oscillator strength with its size is still present, carried by the normalization constant C. One way to estimate this constant is through a microscopic model of $\Psi_\alpha(\mathbf{r})$ [270, 271]. Here, instead, we take a more pragmatic approach, and compute C based on the measured radiative decay rate of QDs. Following Ref. [191], this is given by twice the imaginary part of the quantity

$$G_\alpha = i\frac{2\pi^2\mu_{cv}^2}{\hbar\varepsilon_\infty} \int_0^\infty dk |\Psi_{\alpha k}|^2 \frac{k(2k_0^2 - k^2)}{k_z} , \tag{5.19}$$

where $\Psi_{\alpha k}$ is the Fourier transform of $\Psi_\alpha(\mathbf{r})$. With the assumption $\Psi_\alpha(\mathbf{r}) = C\delta(\mathbf{r} - \mathbf{r}_\alpha)$, the decay rate is thus

$$\Gamma^\alpha = \frac{4}{3}\frac{k_0^3}{\hbar\varepsilon_\infty}d^2 , \tag{5.20}$$

where $k_0 = (\omega_0/c)\sqrt{\varepsilon_\infty}$, and we defined the dipole moment d of the dot (also labeled $\mathcal{D}$ [272] or μ [90]) as

$$d^2 = \mu_{cv}^2 C^2 . \tag{5.21}$$

eq. (5.20) coincides with the expression that is commonly adopted [68, 90, 272]. For typical QDs [42, 43, 49], with radiative lifetime of 1ns and exciton transition energy $\hbar\omega^\alpha \approx 1.3$eV, we obtain a squared dipole moment $d^2 \approx 0.51$eV $\times$ nm^3.

The last requirement of the problem is the knowledge of the modes of the PhC structure, i.e. the set of orthonormal functions $\{\mathbf{Q}_m(\mathbf{r})\}$ and their corresponding eigenfrequencies ω_m. Here, we use the BME to compute those, with the Bloch modes of a regular W1 waveguide computed via GME (cf. Section 2.4). This approach is particularly well suited for elongated PhC cavities as considered in the present work. The orthogonality

relation is then given by

$$\int_S \mathrm{d}^2\rho \int_{-\infty}^{\infty} \mathrm{d}z \, \mathbf{Q}_m(\boldsymbol{\rho}, z)\mathbf{Q}_n^*(\boldsymbol{\rho}, z) = \delta_{mn} \,. \tag{5.22}$$

where S is the area of the 2D computational cell in the slab plane. All the photonic crystals we consider are based on a triangular lattice of circular holes in a dielectric slab suspended in air. The specific parameters we chose are relevant to GaAs structures [42, 43, 49], namely: lattice constant $a = 260$nm, hole radius 65nm, and slab thickness 120nm, with a real part of the refractive index $\sqrt{\varepsilon_\infty} = 3.41$. In this Section we consider only ideal PhC structures i.e. in the absence of any fabrication imperfections. As discussed in detail in Chapter 3, disorder in PhCs has two important effects. First, it determines the extrinsic radiation loss rates of otherwise fully guided modes in waveguides, and suppresses the quality factors of high-quality PhC cavities. This effect is here taken into account through the inclusion of a constant phenomenological loss rate for the modes under study, related to their quality factor by $\gamma = \omega/Q$. For the L3 cavity of Section 5.3.2, we set $Q = 10000$ or 30000. For the longer Ln cavities (section 5.3.3) and the W1 waveguide (section 5.3.4), we set $Q = 50000$ for all modes. The second way disorder affects the results is by modifying the spatial profiles of the electric field modes, especially in the case of waveguides. This effect is studied in detail in Section 5.4.

5.3.2 Application to an L3 cavity*

The system of one quantum dot coupled to an L3 cavity has been widely studied [43, 47, 49] and is thus a good starting point for testing the present formalism.

The cavity is a modified L3 [43, 49], where the two holes on each side of the cavity are shifted outwards by $0.15a$, and their radii are decreased by 80%. This design improves the quality factor by more than one decade compared to that of a standard L3 cavity, while changing the field profile only marginally. We include in the computation only the fundamental cavity mode, shown in Fig. 5.1. We further assume the QDs to lie on the in-plane symmetry axis of the cavity, where $Q_x = 0$. The diagonalization of the matrix (5.15) is then equivalent to the well-known expression

$$\det \begin{pmatrix} \omega_y - \omega & g_c \\ g_c^* & \omega_c - \omega \end{pmatrix} = 0 \,. \tag{5.23}$$

The coupling constant g_c, through eq. (5.13), is

$$g_c = \left(\frac{2\pi\omega_0}{\varepsilon_\infty \hbar}\right)^{1/2} d\, Q_y(\mathbf{r}_\alpha) \,, \tag{5.24}$$

which matches previous theoretical results [68] when the dot is sitting in the center
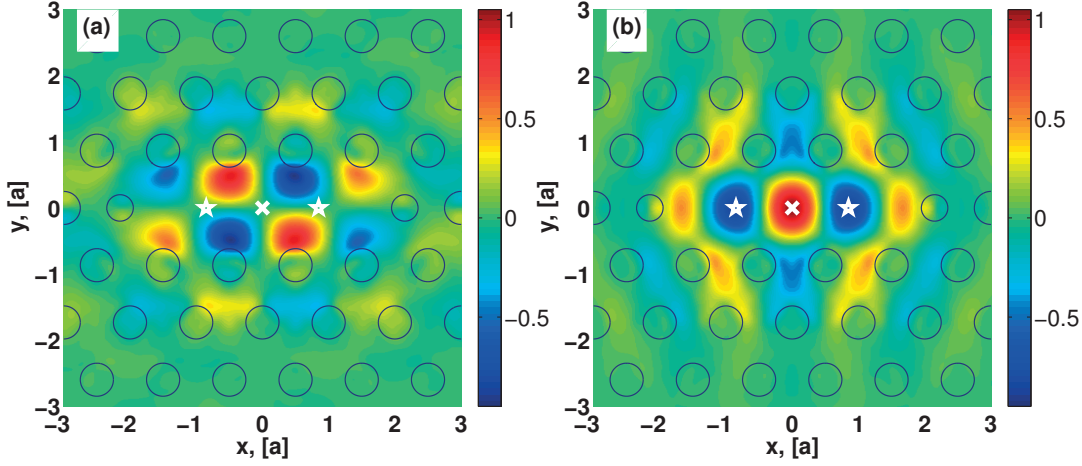
Figure 5.1: Electric field of the fundamental mode of an L3 cavity, (a): $Q_x(\mathbf{r})$ and (b): $Q_y(\mathbf{r})$. In the one-QD simulation, the dot was placed in the central maximum of the y-field (dot position marked by a white cross). For the two-QD simulations, the dots were placed in the corresponding secondary maxima (positions marked by white stars).

$\mathbf{r}_0$ of the cavity and the mode volume is defined as $\frac{1}{V} = |Q_y(\mathbf{r}_0)|^2$. As expected from eq. (5.23), for $|g_c|^2 > |\gamma_c - \gamma_y|^2/16$, vacuum-field Rabi splitting appears between two polariton modes. The energy splitting at zero dot-cavity detuning is given by $2\hbar\Omega$, where the Rabi frequency Ω is

$$\Omega = \sqrt{|g_c|^2 - \frac{(\gamma_c - \gamma_y)^2}{16}} \, . \tag{5.25}$$

Using the PhC and QD parameters we already introduced, the coupling constant was computed to be $\hbar|g_c| = 147\mu\text{eV}$, which compares perfectly with the most recently reported result for that system [43].

After showing the way the standard one-dot cavity-QED results are reproduced with our formalism, we now proceed to the situation of two dots coupled to the same cavity mode (see Fig. 5.1), and so radiatively coupled to each other. We assume a symmetric spatial configuration of the two dots with respect to the cavity center (see Fig. 5.1), resulting in equal coupling constants $\hbar|g_c| = 125\mu\text{eV}$ for the two dots. Since usually $\gamma_c \gg \gamma_y$, i.e. the losses through the cavity mode are significantly larger than the QD losses through other channels (both non-radiative and radiative through modes other than the cavity mode), we set here and in all following sections $\gamma_y^{1,2} = 0$. Given the phenomenological way these rates enter the formalism, calculations can easily be generalized to include finite QD loss rates. Let us first consider the case of zero dot-dot detuning $\delta = \omega_y^1 - \omega_y^2$. The relevant exciton states are in this case the symmetric and antisymmetric linear combinations of the two QD states, whose coupling to the cavity mode depends on the symmetry of the electric field profile. As discussed extensively in Ref. [95], the L3 cavity symmetry is described by the D_{2h} point

Figure 5.2: (a): Eigenfrequencies (solid lines) and radiative rates (dashed lines) for two QDs with no dot-dot detuning, strongly coupled to an L3 cavity mode with $Q = 10000$. With a dashed-dotted line, the bare cavity resonance is also indicated. The Hopfield coefficients for each solution, correspondingly color-coded, are presented in panels (b): equal (in absolute value) QD coefficients and (c): cavity coefficient.

group, and its fundamental mode belongs to the B_{2u} irreducible representation, which is even with respect to the $\hat{\sigma}_{yz}$ symmetry operation (mirror reflection with respect to the yz plane) – as can also be seen from Fig. 5.1. Hence, the antisymmetric QD state remains dark, while the symmetric one behaves as a single exciton with a coupling constant $\sqrt{2}g_c$.

In Fig. 5.2 (a) we plot the eigenfrequencies of the system as a function of the detuning between the exciton resonance frequency ω_y (same for both dots) and the cavity resonance frequency ω_c, as computed for a cavity quality factor of $Q = 10000$. We observe vacuum Rabi splitting between an upper and a lower polariton in exactly the same way we would for a single dot coupled to the cavity, but in addition we see a

dark mode which is a trivial solution, $\omega = \omega_y$. The splitting between the lower and the upper polaritons at zero dot-cavity detuning is $2\hbar\Omega_c = 347\mu\text{eV}$, which for $Q = 10000$ corresponds exactly to an effective coupling constant of $\sqrt{2} \times 125\mu\text{eV}$. The system is further characterized in panels (b) and (c), where we plot the Hopfield coefficients for each of the three eigenmodes (correspondingly color-coded). This clear collective behavior has been observed experimentally in a QD-cavity system [240–243], while the more general dependence of the effective coupling constant with the number of coupled two-level systems N – given by $\sqrt{N}|g_c|$ – has also been observed in a circuit-QED system [273]. It is very important to remark that this dependence has nothing to do with the $\sqrt{N}|g_c|$ energy splitting of different rungs in a Jaynes-Cummings model, where N would be the number of photons in the system: on the contrary, as discussed before, here we restrict to the linear response only, which holds in the limit of vacuum electromagnetic field. The effect in our case is simply due to the collective behavior of the N resonant quantum dots.

The major experimental challenges to the radiative coupling of two spatially separated quantum dots is achieving both spatial control (to ensure strong overlap between each of the dots and the cavity mode) and spectral control (to ensure as small dot-dot and dot-cavity detuning as possible). Typically, QDs are characterized by an inhomogeneous distribution of exciton energies with a width of several meV. Then, two QDs are very likely to be detuned. In Fig. 5.3, we study the same system, but assuming a detuning $\delta = 300\mu\text{eV}$. Close to resonance, all of the eigenmodes acquire a finite component from the cavity mode. Additionally, they have both a significant $|\lambda_y^1|$ coefficient (panel (b)), and a significant $|\lambda_y^2|$ coefficient (panel (c)), implying that there is a sizable radiative coupling present. The radiative coupling is expected to vanish as the cavity-dot detunings become much larger than the coupling constant, and an expression for an effective coupling strength in this limit was derived in [50, 274].

We now address the question of how the excitation transfer process depends on time. This aspect is of particular importance to assess the usefulness of the radiative excitation transfer as a coupling mechanism between different qubits in a semiconductor-based quantum gate architecture. In the present case, when polaritonic features are spectrally resolved, one correspondingly expects the excitation to oscillate between the different basis states, including the photon state. To illustrate this aspect, we compute the time-dependent amplitudes of the various basis states, assuming that one QD is excited at $t = 0$. From these amplitudes, we extract time-dependent probabilities of finding the excitation in each of the basis modes, expressed in vector form as

$$\mathbf{P}(t) = \left|e^{-i\Lambda_2 t}\boldsymbol{\lambda}_{in}\right|^2 , \tag{5.26}$$

where Λ_2 is the matrix of eq. (5.15). These probabilities are properly normalized if one accounts also for the probability $P_{out}(t)$ of the excitation to have radiated out of the system, i.e. $\sum P_i(t) = 1 - P_{out}(t)$. In Fig. 5.4 we plot these time-resolved probabilities
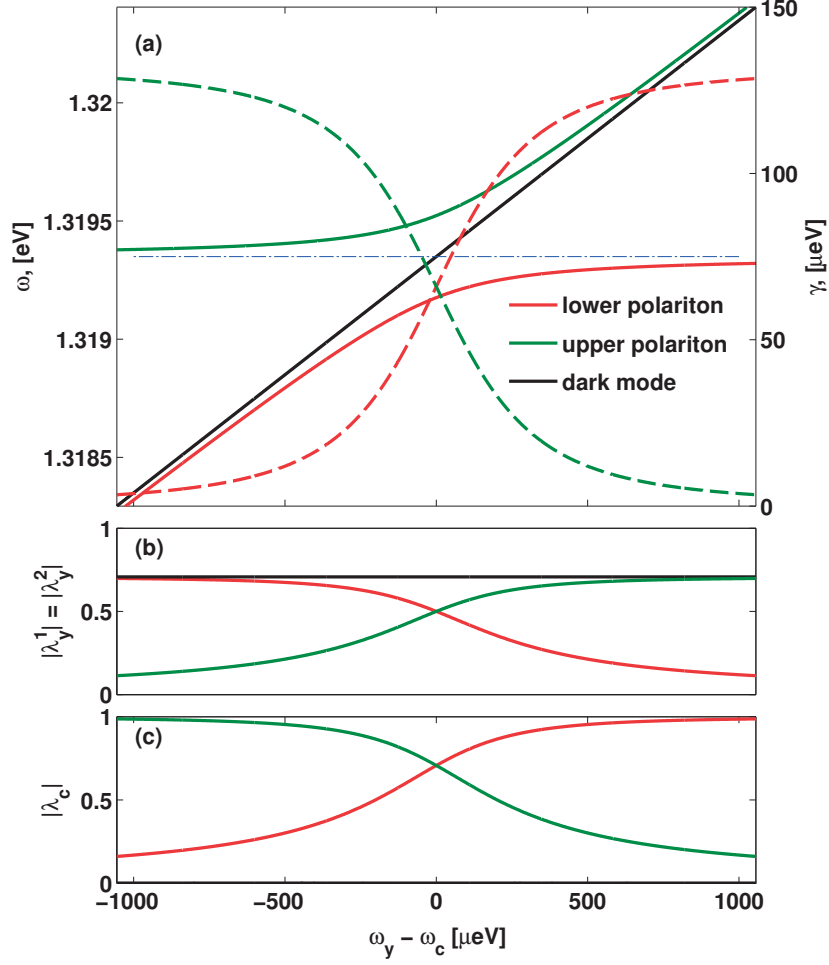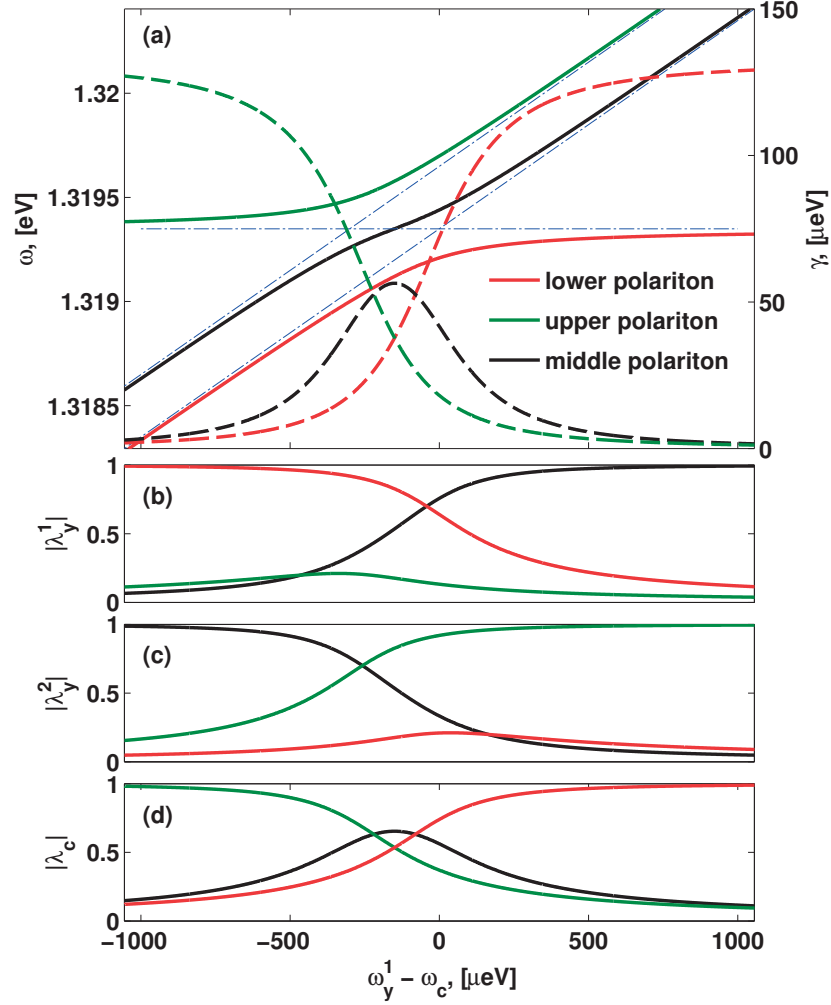
Figure 5.3: (a): Eigenfrequencies (solid lines) and radiative rates (dashed lines) for two QDs with a dot-dot detuning of 300μeV, strongly coupled to an L3 cavity mode with $Q = 10000$. With dashed-dotted lines, the bare excitons and the bare cavity resonances are also shown. The Hopfield coefficients for each solution, correspondingly color-coded, are presented in panels (b): first exciton coefficient, (c): second exciton coefficient, and (d): cavity coefficient.

for a starting excitation in one of the QDs, i.e. $\boldsymbol{\lambda}_{in} = (1, 0, 0)$. We study four different cases: either zero dot-dot and dot-cavity detuning, or $\hbar\delta = 300\mu$eV (with the cavity frequency tuned at the average of the two exciton frequencies), and cavity Q-factor equal to either 10000 or 30000. In panels (a) and (b), where $\delta = 0$, the probabilities never decay to zero due to the presence of a dark state and the fact that no non-radiative decay mechanism was included. In panels (c) and (d) a dark state no longer exists, and a clear decay of the excitation with a characteristic lifetime depending on the Q-factor is visible. All plots show that the excitation oscillates between the three possible states, on a time scale defined through the radiative coupling strength. In particular, the

113
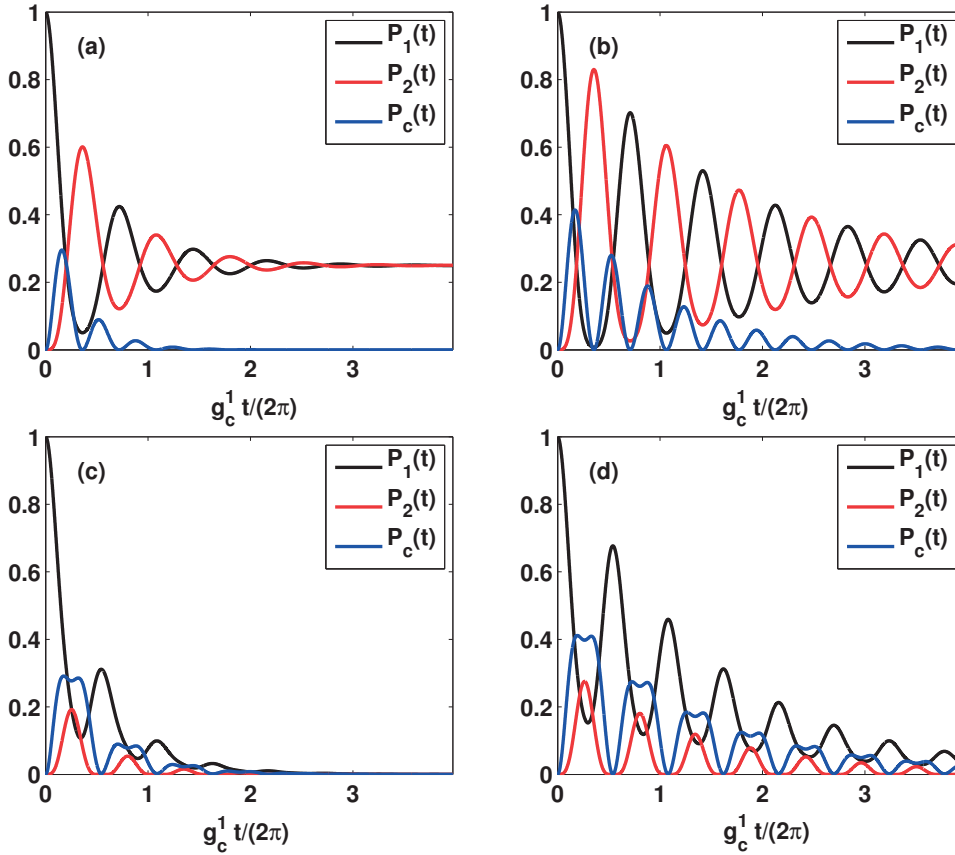
Figure 5.4: Time evolution of the probability of an excitation in one dot to be transferred to the second dot or to the cavity. (a): $\delta = 0$, $Q = 10000$; (b): $\delta = 0$, $Q = 30000$; (c) $\hbar\delta = 300\mu\text{eV}$, $Q = 10000$; (d) $\hbar\delta = 300\mu\text{eV}$, $Q = 30000$.

probability of finding the system in an excited state of the second QD remains sizable over several oscillation periods, showing that a significant dot-dot interaction can be achieved with experimentally feasible parameters. These results generally agree with specific setups of radiatively coupled QDs in photonic crystals that have been recently studied in the literature [257, 258].

5.3.3   Application to Ln cavities*

Recently, using Ln cavities with $n > 3$ to achieve light-matter coupling has spurred interest [88, 275, 276], as these generally have a larger quality factor than the L3 – though at the expense of a larger mode volume and thus a smaller dot-cavity coupling strength.

Here, we investigate cavities of varying length n with a common setup, illustrated in Fig. 5.5 for $n = 11$. In the figure, we show the first four modes, M_{1-4}, of the L11 cavity, with resonant energies 1.3065eV, 1.3125eV, 1.3269eV, and 1.3565eV, respectively. In all
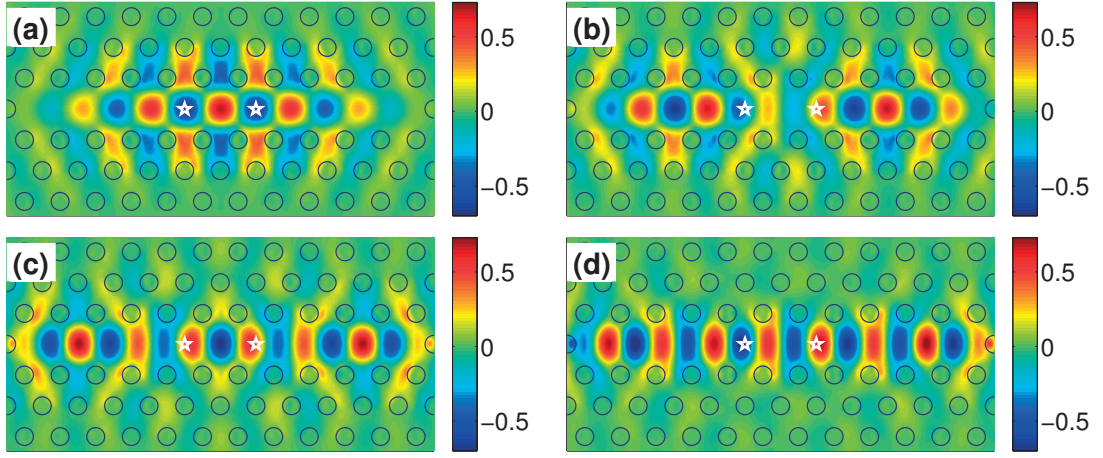
Figure 5.5: $Q_y(\mathbf{r})$ for the four lowest-energy modes of the *L11* cavity; (a): Fundamental mode M_1, at $\hbar\omega_1 = 1.3065\text{eV}$, (b): M_2, $\hbar\omega_2 = 1.3125\text{eV}$, (c): M_3, $\hbar\omega_3 = 1.3269\text{eV}$, (d): M_4, $\hbar\omega_4 = 1.3565\text{eV}$. The positions of the quantum dots are marked with white stars.

the results to follow, for all n, the two dots were placed in the center of an elementary cell on each side of the center of the defect (i.e. at a distance a from the center of the cavity and so $2a$ from each other), where the coupling constants for each of them in the $n = 11$ case are $|\hbar g_1| = 94\mu\text{eV}$, $|\hbar g_2| = 55\mu\text{eV}$, $|\hbar g_3| = 65\mu\text{eV}$, and $|\hbar g_4| = 89\mu\text{eV}$. Since the smallest energy difference between the cavity resonances in this case is between ω_1 and ω_2, and is $\approx 6\text{meV}$, i.e. much larger than all the coupling strengths, it is reasonable to expect that the dots will never couple significantly to more than one mode. Thus, the phenomenology of the system will be, qualitatively, the same as the one described in Section 5.3.2, which was also verified by our computations.

The situation should change significantly when increasing the length n of the photonic defect. Then, we expect the energy spacing between the resonant frequencies of the Ln cavity to decrease and eventually become comparable to the typical coupling strength. In this situation, the radiative transfer process is no longer mediated by an isolated cavity mode, and a smooth transition to a multi-mode coupling regime is expected. In order to determine at which cavity length this crossover occurs, one should also consider the fact that the coupling of a dot to each individual mode decreases with the increase of the mode volume. As a result, the crossover length is increased with respect to what would be given by a simple assumption of constant coupling strength per mode.

In Fig. 5.6, we plot the minimum mode-separation $\omega_2 - \omega_1$ vs. the length n of the cavity, and in addition show the coupling strengths $|g_m^1|$ for $m = 1\dots10$. For all n, the dots were placed as in Fig. 5.5 – at a distance a on each side of the center of the cavity. The fact that half of the coupling constants decay much faster as a function of n is again
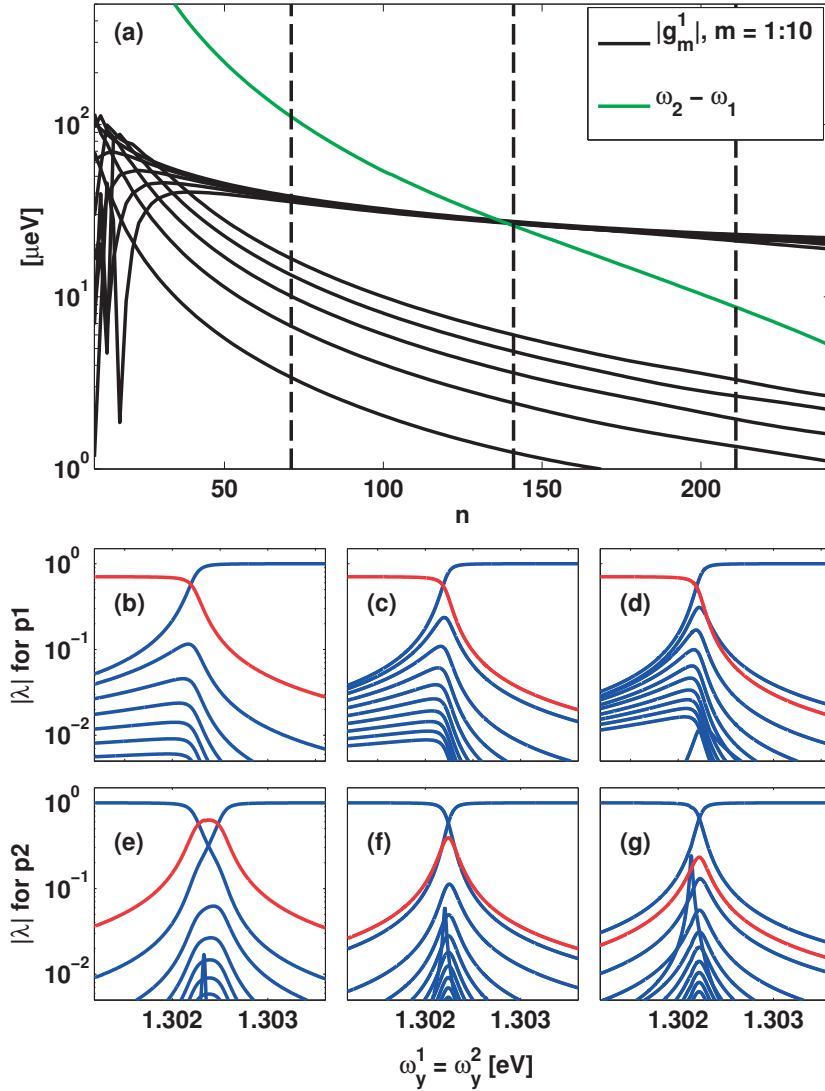
Figure 5.6: (a): Black lines – coupling constants between one QD and the ten lowest modes of an Ln cavity, vs. n; green line – energy separation between the lowest two cavity modes. (b)-(d): Hopfield coefficients of one polariton eigenstate as a function of the bare exciton frequency ω_y^1 with no dot-dot detuning, for $n = 71$, $n = 141$, $n = 211$ (the values marked by dashed vertical lines in (a)). The red line shows the dot coefficients, while the blue lines belong to the many cavity modes. (e)-(g): Same as (b)-(d) but for another polariton state.

explained by the particular symmetry of the field profiles. It turns out that for every n, the modes alternate between symmetric and antisymmetric w.r.t. $\hat{\sigma}_{yz}$, as can be seen in Fig. 5.5 for the L11 case. In the limit of large n, the antisymmetric modes have a small amplitude at the QD positions close to the node, resulting in a small radiative coupling strength.

116
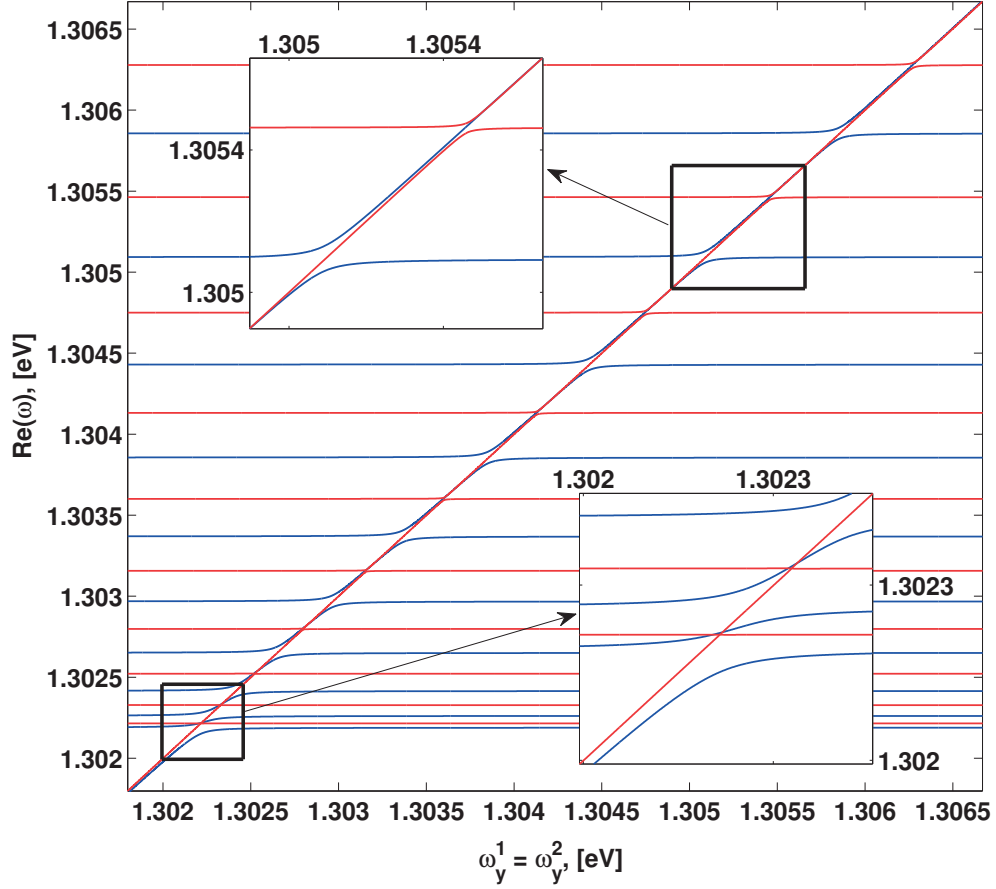
Figure 5.7: Eigenfrequencies for two QDs with no dot-dot detuning in an L141 cavity ($Q = 50000$ for each mode) vs. the resonant frequency of the excitons. The insets show close-ups over two selected regions. Blue (red) lines denote a symmetric (anti-symmetric) combination of the QD states.

The crossover from a single-mode to a many-mode regime occurs around $n = 150$, as clearly visible in Fig. 5.6. In panels (b)-(g), we show the corresponding Hopfield coefficients for three different values of n, given by $n = 71$, $n = 141$, and $n = 211$, also indicated by dashed lines in panel (a), and for two different polariton modes. Consequently, for $n = 71$, the Hopfield coefficients of two different polariton eigenstates, shown in panels (b) and (e) respectively, are still largely dominated by one cavity and one dot component. On the other hand, for $n = 211$ – panels (d) and (g) – the value of several photonic fractions λ_m is non-negligible.

In Fig. 5.7 we plot the polariton energies as a function of QD-exciton energy in the case of the L141 cavity, for $\delta = 0$. As mentioned already, the photon modes alternate between symmetric and anti-symmetric w.r.t. the $\hat{\sigma}_{yz}$ operator, hence coupling to either the symmetric or anti-symmetric linear combination of the QD states is present. In the Figure, the polaritons due to a combination of symmetric states are denoted
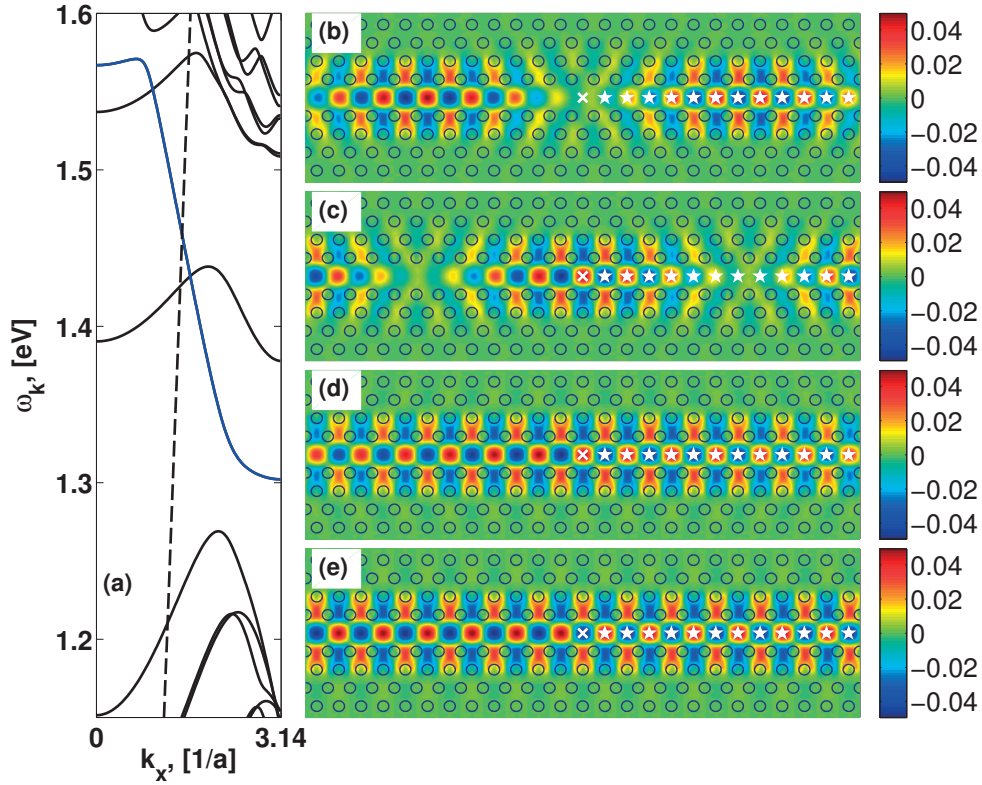
Figure 5.8: (a): Band structure of the $W1$ waveguide; the dashed line shows the light cone. The QD resonant energies are close to the band-edge energy of the main guided band (blue). The field profiles of four guided modes in that spectral region are shown, over a small stretch of the waveguide: (b), (c): the two degenerate modes at $\hbar\omega_k = 1.30308\text{eV}$ (anti-symmetric combination in (b), symmetric in (c)); (d): the symmetric mode at $\hbar\omega_k = 1.30224\text{eV}$ (e): the symmetric mode at $\hbar\omega_k = 1.30218\text{eV}$ (at the band edge). In all computations, one QD was placed in the center of the waveguide (white cross), while the second one was placed in the center of one of the successive elementary cells (white stars).

by blue lines, while the anti-symmetric combinations are represented by red lines. In the symmetric case, the exciton-photon coupling strength is always large, and an anti-crossing occurs at every mode. In the anti-symmetric case, the results show a transition from weak coupling (close to the lowest ω_m) to strong coupling (anti-crossing is visible in the higher-ω inset), due to the fact that the coupling strengths there become larger than $\omega_m/4Q$. It is clear both from Figs. 5.6 and 5.7 that for $n \to \infty$, the dots couple to a structured continuum of photon modes, reproducing the physics of a W1 waveguide. This situation is studied below.

5.3.4 Application to a W1 waveguide*

The results obtained for the Ln cavities indicate that the radiative coupling is still sizable in very long structures and might be effective even at very long distance between the two QDs. Here, we investigate this possibility in more detail, by considering QDs embedded in a W1 photonic crystal waveguide.

Coupling of a single dot to a W1 waveguide (or a similar structure) with the purpose of spontaneous emission enhancement (and the potential application as a single-photon source) has already been widely discussed theoretically [255, 256, 277], and achieved experimentally [218–224]. The fact that it is already possible to couple efficiently a dot to the guided modes of the waveguide is promising in view of achieving radiative coupling between **two** dots that could – due to the spatial extension of the structures and the modes they support – extend to inter-dot distances for which targeting each dot individually by a laser pulse is possible.

We begin our study by looking at the modes of the W1 waveguide. The band structure is presented in Fig. 5.8(a), where two guided bands in the band-gap of the regular crystal are visible. Strongest dot-PhC coupling is typically achieved for the smallest group velocity (largest local density of states of the photonic modes), and so the spectral range we concentrate on is around the band-edge of the main guided band (blue line), where the group velocity of the ideal photonic structure vanishes. The second guided band is spatially odd with respect to a $\hat{\sigma}_{xz}$ reflection [25], and would not couple to the exciton state of a QD located at the center of the waveguide. In the simulations below, we compute the $W1$ modes for 2048 k-points in the interval $(-\pi/a, \pi/a]$, which is equivalent to simulating a waveguide of length 2048 elementary cells with periodic boundary conditions. In panels (b)-(e) of Fig. 5.8, we show the electric field profiles of four modes lying close in energy to the band edge of the main guided band. As is the case with all structures we considered so far, this band has vanishing Q_x component on the symmetry axis of the waveguide, allowing us again to include the y-polarized fields only. Furthermore, modes at $\pm k$ are degenerate – one propagating and one counter-propagating – with real-space profiles proportional to $\exp(ikx)$ and $\exp(-ikx)$, respectively. As basis states, we take the symmetric and the anti-symmetric combination of the degenerate guided modes, representing the fields by their 'standing wave' profiles: one with a maximum and one with a zero amplitude in the center of the guide (compare panels (b)-(c)). Without loss of generality (due to the PBC), we place one dot at that position, so that it couples to one of the modes only. The second dot is then placed in the center of a successive elementary cell, and will, in general, couple to every mode in the basis thus constructed, so even for zero dot-dot detuning, no fully dark state is present.

In Fig. 5.9(a), we show the polariton structure in the spectral range close to the band edge of two dots with dot-dot detuning $\delta = 0$, with the second dot placed at the closest
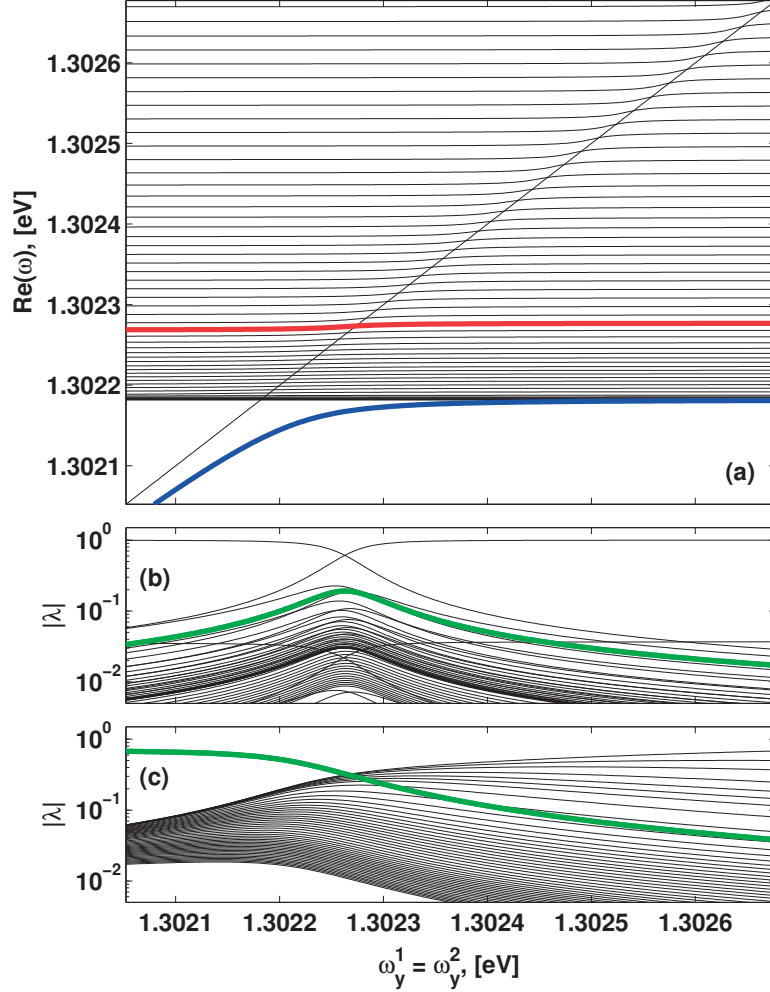
Figure 5.9: (a): Eigenfrequencies for two QDs in the waveguide, with no dot-dot detuning. The Hopfield coefficients for the red line of (a) are shown in (b), where the green line shows the QD coefficients $|\lambda_y^1| = |\lambda_y^2|$, and the black lines show all the waveguide coefficients $|\lambda_m|$. The same in (c), but for the blue line of (a). The loss rate of each mode is $\gamma_\mathrm{w} = \omega_y^1/50000 \approx 26\mu\mathrm{eV}$.

possible distance, a, from the first one. The quality factor of each of the photonic modes was again set to $Q = 50000$ for all modes. While a strong dependence of the $W1$ loss rates on the group velocity close to the band edge has been shown in transmission measurements [278], this dependence is heavily influenced by back-scattering due to disorder. In our case, we model stationary modes rather than transport, and the only relevant radiative loss is the one out of the plane of the PhC slab. Then, the assumption of approximately constant Q-s is realistic, as seen from microscopic modeling of extrinsic disorder-induced losses [63,110], and Section 3.2. Polariton modes originating from antisymmetric photon modes are essentially uncoupled and are not displayed (although, they were still included in the computation). The coupling constants of

each of the dots to each of the symmetric modes varies very little, and is $\hbar|g_m^{1,2}| \approx 7\mu\text{eV}$. The $\omega = \omega_y^1$ solution (straight diagonal in panel (a)) is due to the anti-symmetric QD combination, which is almost dark. The strongest anti-crossing behavior is exhibited by the polariton lying below the band edge (blue line), whose Hopfield coefficients are given in panel (c). The remaining polariton modes display similar behavior, so the Hopfield coefficients of just one of them (the red line of (a)) are given in panel (b). For completeness, the same plots but for $\hbar\delta = 100\mu\text{eV}$ are given in Fig. 5.10. In this case, no dark modes are present and Hopfield coefficient corresponding to the two QDs are generally different from each other, as seen in panels (b) and (c). In both Figs. 5.9 and 5.10 we observe that anti-crossings are still present – though characterized by a very small energy splitting – where the exciton becomes resonant with the various guided modes. This situation can be understood as the precursor to the structured continuous spectrum of modes that would arise in the limit of infinite waveguide length, analogous, for example, to the polariton modes arising from the interaction between an exciton in a two-dimensional quantum well and the three-dimensional continuum of electromagnetic modes [190, 260].

The present formalism provides a detailed quantitative account of the effect of the guided electromagnetic field on the radiation properties of few QDs. In particular, we now derive the Purcell enhancement of the radiative rate characterizing a single QD, and the distance-dependence of the radiative excitation transfer process between two distant QDs. We compute these properties both numerically, and analytically. To this purpose, let us consider the elements of the matrix Λ_1 introduced by eq. (5.14):

$$\Lambda_1^{\alpha\beta} = (\omega^\alpha - \omega)\delta_{\alpha\beta} - G^{\alpha\beta}(\omega)\,, \tag{5.27}$$

where the coupling matrix elements $G^{\alpha\beta}$ are proportional to the Green's function of eq. (5.8):

$$G^{\alpha\beta}(\omega) = \sum_{m=1}^{M} \frac{g_m^\alpha g_m^{\beta*}}{\omega_m - \omega} = d^2 \frac{2\pi}{\epsilon_\infty \hbar} \frac{\omega^2}{c^2} G(\mathbf{r}_\alpha, \mathbf{r}_\beta, \omega). \tag{5.28}$$

For a structure with no sharp resonances – like the waveguide – we can take advantage of the exciton-pole approximation and substitute $\omega = \omega_0$ in the denominator, in which case $G^{\alpha\alpha}(\omega_0)$ is the self-interaction energy of each dot, while $|G^{12}(\omega_0)|$ is an effective coupling constant for the case of two dots with zero dot-dot detuning, i.e. $\omega_y^1 = \omega_y^2 = \omega_0$. In order to derive an analytical expression for the coupling, let us replace the sum with an integral over $k = k_x$, and use the fact that, in accordance with Bloch's theorem, when $\mathbf{r}_\alpha$ and $\mathbf{r}_\beta$ are in the center of an elementary cell, $g_k(\mathbf{r}_\beta) = \exp(-\mathrm{i}kx)g_k(\mathbf{r}_\alpha)$:

$$G^{\alpha\beta}(\omega_0) = \frac{a}{2\pi} \int_{-\frac{\pi}{a}}^{\frac{\pi}{a}} \mathrm{d}k \frac{|g_k|^2 e^{\mathrm{i}kx}}{\omega(k) - \omega_0}\,. \tag{5.29}$$

121
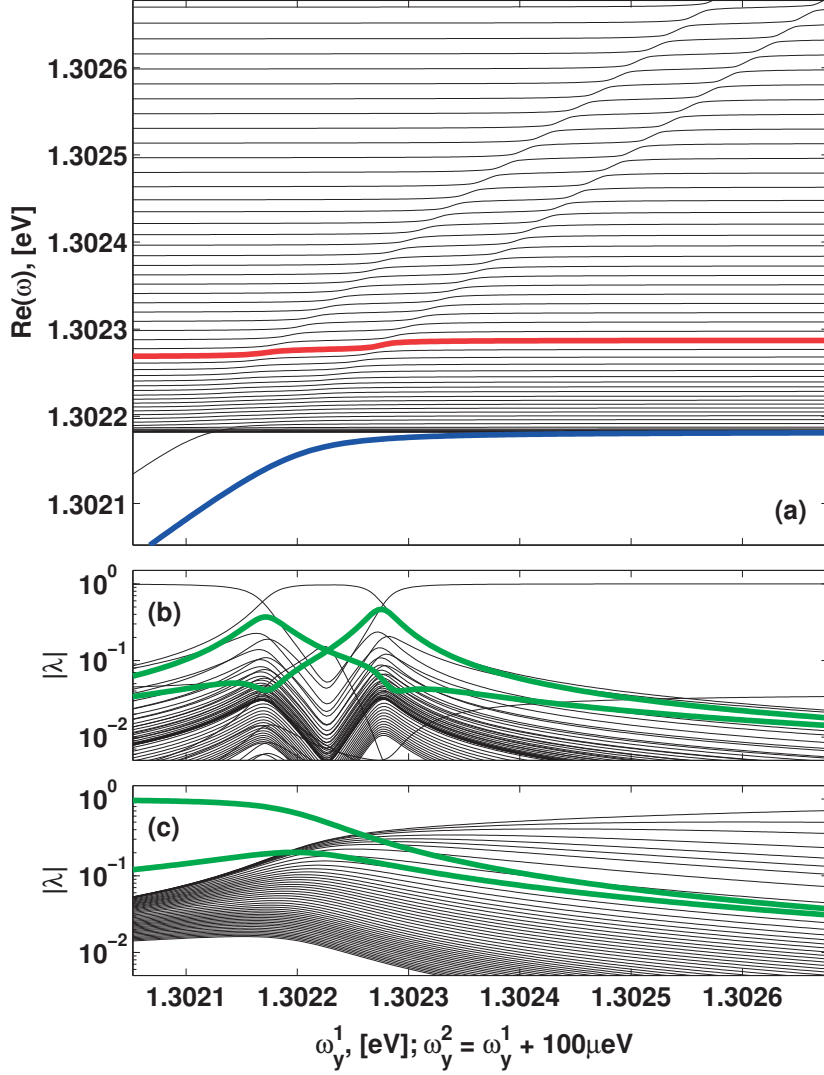
Figure 5.10: (a): Eigenfrequencies for two QDs in the waveguide, with dot-dot detuning $\hbar\delta = 100\mu\text{eV}$ and γ_{w} as in Fig. 5.9. The Hopfield coefficients for the red line of (a) are shown in (b), where the two green lines show the QD coefficients $|\lambda_y^{1,2}|$, and the black lines – all the waveguide coefficients $|\lambda_m|$. Same in (c), but for the blue line of (a).

A few simplifications are due. First, we write $\omega_k = \Re(\omega(k))$ and $\gamma_{\text{w}} = -2\Im(\omega(k))$, and assume the latter is constant, equal to ω_0/Q. Furthermore, we assume $|g_k|^2 = |g|^2$, i.e. the coupling strength has weak dependence on k. This feature is due to the small spatial extension of the exciton wave function, resulting in a very broad distribution in Fourier space with approximately constant overlap with all guided modes, and is also confirmed by our numerical results. Finally, by taking k_0 as the positive Bloch momentum for which the guided mode is resonant with the exciton frequency ω_0, and

defining the corresponding group velocity

$$v_g = - \left. \frac{\mathrm{d}\omega_k}{\mathrm{d}k} \right|_{k_0} , \tag{5.30}$$

we get

$$G^{\alpha\beta}(\omega_0) \approx \frac{a}{\pi} \frac{|g|^2}{v_g} \int_0^{\frac{\pi}{a}} \mathrm{d}k \frac{\cos(kx)}{k - k_0 - \mathrm{i}\frac{\gamma_{\mathrm{w}}}{2v_g}} . \tag{5.31}$$

This expression holds in the limit where the resulting spectral linewidth is small enough so that the group velocity is still well defined. It can now be applied for example to obtain the radiative lifetime of a single dot embedded in the waveguide as $\Gamma^\alpha = 2\Im(G^{\alpha\alpha})$, and so

$$\Gamma^\alpha = \frac{2a}{\pi} \frac{|g|^2}{v_g} \tan^{-1} \left(\frac{2(k - k_0)v_g}{\gamma_{\mathrm{w}}} \right) \Bigg|_{k=0}^{k=\pi/a} . \tag{5.32}$$

The Purcell factor for the enhancement of the single-dot spontaneous emission rate is then given by the ratio between eq. (5.32) and eq. (5.20). This result takes into account the detailed structure of the photonic environment due to the waveguide. In this respect, it generalizes the result obtained by assuming that only one Bloch mode at wave vector $k = k_0$ determines the radiation loss process [255, 256]. This simplified result is recovered by taking the limit $\gamma_{\mathrm{w}} \to 0$ in the integral (5.28), namely by assuming that the guided Bloch mode has vanishing extrinsic radiation loss rate. The emission rate Γ^l of the dot into leaky modes can also be estimated numerically by restricting the summation in eq. (5.28) to the modes which lie above the light-cone only. Then, the β-factor in the absence of non-radiative decay mechanisms can also be computed as

$$\beta = \frac{\Gamma^\alpha}{\Gamma^\alpha + \Gamma^l} , \tag{5.33}$$

and a further generalization to the case in which non-radiative processes are also present follows straightforwardly.

As a development from the previous works, which consider just one dot in the waveguide, we now proceed to quantify the radiative excitation transfer process between **two** QDs and its dependence on inter-dot distance. The closed-form expression for the cross-coupling term G^{12}, obtained by carrying out the integral (5.31) reads

$$\begin{aligned} G^{12} = \frac{a}{\pi} \frac{|g|^2}{v_g} \Bigg[&\cosh\left(\frac{x}{r_{12}} - \mathrm{i}k_0 x \right) \mathrm{Ci}\left(-\mathrm{i}\frac{x}{r_{12}} + (k - k_0)x \right) \\ &+ \mathrm{i}\sinh\left(\frac{x}{r_{12}} - \mathrm{i}k_0 x \right) \mathrm{Si}\left(\mathrm{i}\frac{x}{r_{12}} - (k - k_0)x \right) \Bigg] \Bigg|_{k=0}^{k=\frac{\pi}{a}} , \end{aligned} \tag{5.34}$$

where $\mathrm{Ci}(z)$ and $\mathrm{Si}(z)$ are respectively the cosine integral and the sine integral functions, and we defined $r_{12} = 2v_g/\gamma_w$. The quantity r_{12} is simply the decay length associated to the propagation of light along the resonant guided mode. We expect this decay to characterize also the distance dependence of the radiation transfer process. Indeed, under the ideal assumption of vanishing radiation loss rate for the guided mode, in a one-dimensional geometry one would expect the radiative transfer process to be **independent of the distance**. For comparison, as has already been shown, the coupling strength decays as $R_{\alpha\beta}^{-1}$ in 3D bulk semiconductor [191], and as $R_{\alpha\beta}^{-1/2}$ in a 2D planar cavity system [192]. In Fig. 5.11, we display the absolute value of G^{12} computed numerically through eq. (5.28), for four different values of the exciton frequency ω_0 of the two QDs, in a waveguide of length $2048a$. This quantity is compared to the result obtained from the analytical model of eq. (5.34) and to the simpler assumption of an exponential dependence $|G^{12}| = |G^{11}|e^{-x/r_{12}}$. In panel (d), where ω_0 is taken to lie below the edge of the guided band, the group velocity cannot be properly defined, and thus the analytical models do not apply.

Apart from this case, it is clear that the distance dependence of the inter-dot coupling is perfectly captured by the simple exponential-decay model. The oscillations of the numerical curve in panel (a) are due to the finite length of the waveguide and reproduce the spatial behavior of the Bloch mode at $k = k_0$ that dominates the transfer process. These oscillations cannot obviously be reproduced by the analytical model that implicitly assumes an infinitely extended waveguide. As anticipated, the numerical results show that the distance dependence of the transfer rate is expressed by the decay associated to the light propagation, and quantified by the decay length r_{12}. It is interesting to note that even for very small group velocities, e.g. $v_g < c/500$, the interaction distance is still of the order of $100a = 26\mu\mathrm{m}$, i.e. of mesoscopic scale, thus confirming the potential of the PhC waveguide for very long-distance dot-dot coupling.

More generally, eq. (5.34) suggests that there is a compromise, enforced by the group velocity, between strength and distance dependence of the transfer process. The overall strength of the transfer rate depends inversely on the group velocity. This expresses the magnitude of the local density of states at the QD exciton frequency or, in a more suggestive picture, the fact that slow light interacts with a QD over a longer time lapse. However, a smaller group velocity also implies a shorter characteristic decay length r_{12}, as we are assuming a constant radiation loss rate. In a realistic system, including disorder, we further expect the group velocity picture to break down at frequencies close to the band edge, where disorder-induced localization of light dominates and the spatial decay associated to the localization length becomes shorter than r_{12}. This calls for an analysis including disorder effects, which we present in Section 5.4.

We conclude this Section by studying the time-dependent probability amplitudes of the excitation lying in each mode. These quantities are plotted in Fig. 5.12, assuming that one QD is excited at $t = 0$, for three different inter-dot distances and three different
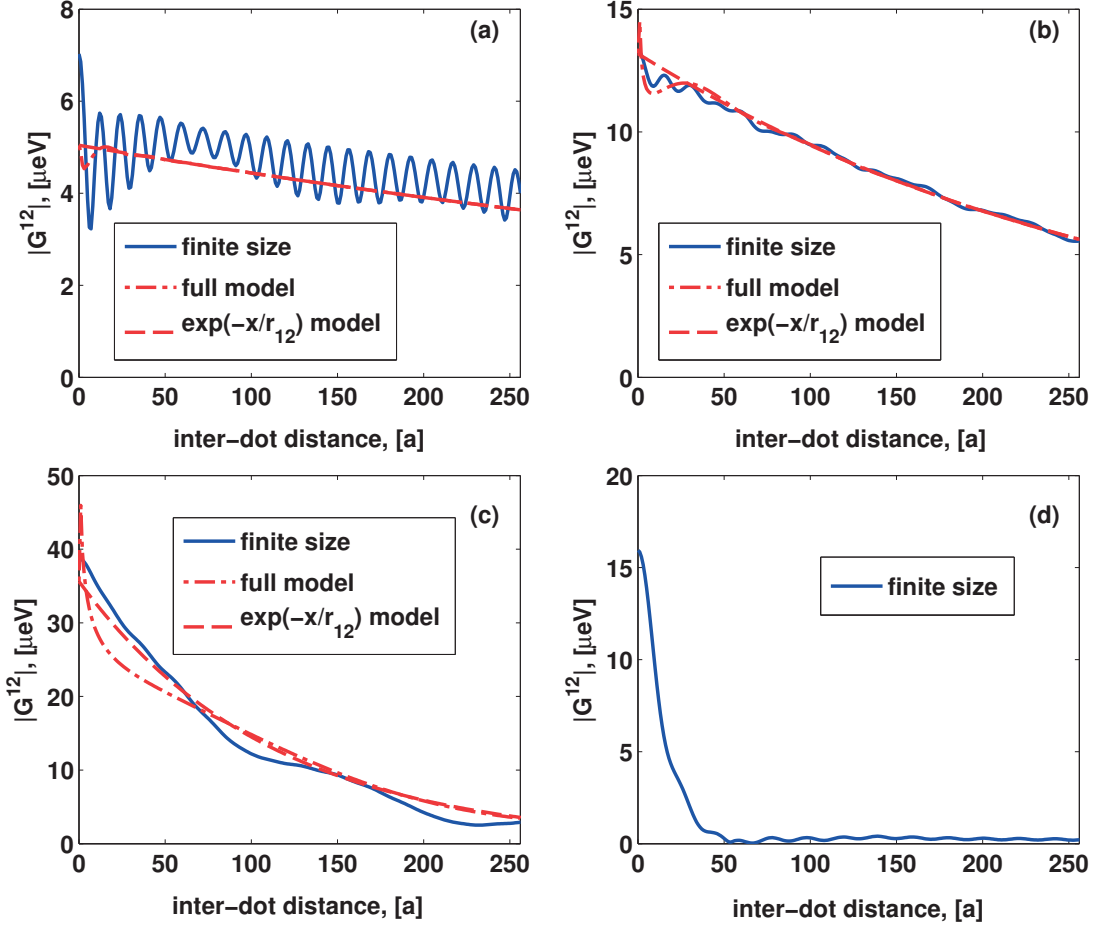
Figure 5.11: Absolute value of the off-diagonal term of the matrix in eq. (5.14), in the exciton-pole approximation, computed numerically for a finite-size waveguide (solid line), analytically through eq. (5.34) (dashed-dotted line), and through an exponential decay model with characteristic distance $r_{12} = 2v_g/\gamma_{\rm w}$ (dashed line, $\gamma_{\rm w}$ as in Fig. 5.9). In (a): $\hbar\omega_0 = 1.30353\text{eV}$, $n_g = 74$, (b): $\hbar\omega_0 = 1.30240\text{eV}$, $n_g = 195$, (c): $\hbar\omega_0 = 1.30220\text{eV}$, $n_g = 525$, (d): $\hbar\omega_0 = 1.30208\text{eV}$, i.e. 100 μeV below the band edge.

values of ω_y^1. In all cases, $\hbar\delta = 100\mu\text{eV}$ was imposed. As discussed above, the transfer mechanism is driven by several light modes. The plots show that the radiative transfer process still occurs and, in particular, the marked oscillations are characterized on average by a period that can be associated to an effective transfer rate $\hbar\Omega = 50 - 60\mu\text{eV}$. As in short Ln cavities, this rate is quite sizable and should be observable in state-of-the-art GaAs-based photonic structures [218–225, 276].
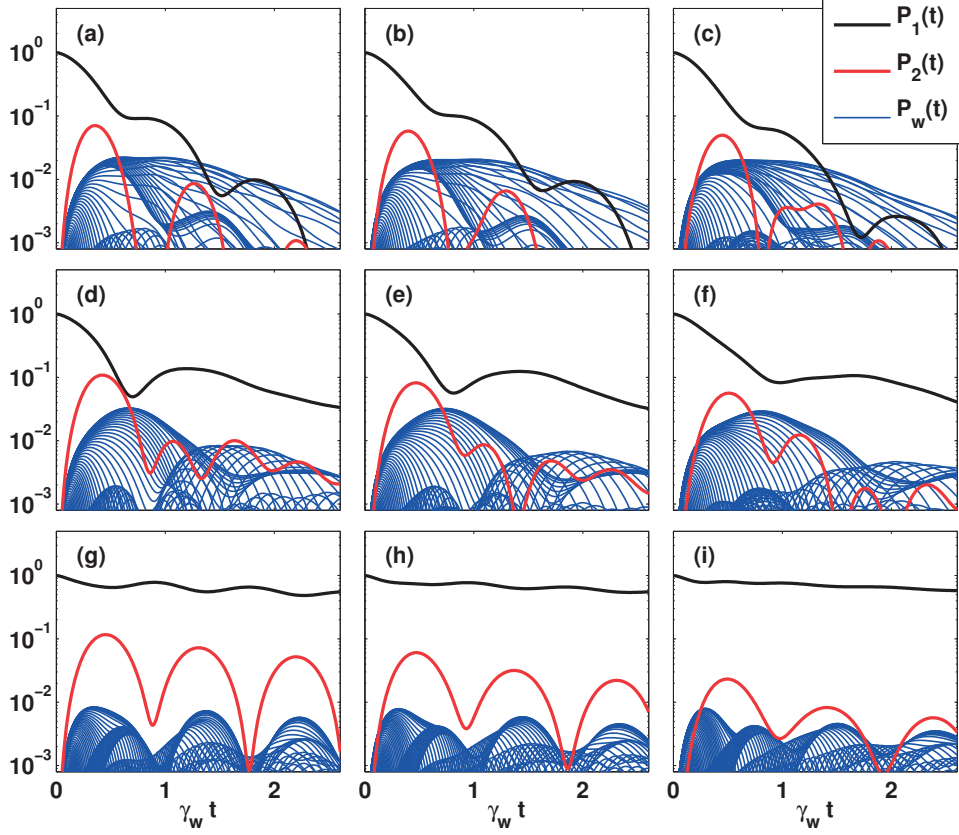
Figure 5.12: Time evolution of the probability of an excitation in one dot to be transfered to the second dot or to the many PhC modes (blue lines). The dot-dot detuning is $\hbar\delta = 100\mu eV$. Horizontally across the panels, the inter-dot distance changes from 260nm to 2.6μm to 5.2μm. Vertically across the panels, the exciton frequency of the first dot changes from (a)-(c): $\hbar\omega_y^1 = 1.30224eV$ (close to the band edge), through (d)-(f): $\hbar\omega_y^1 = 1.30218eV$ (at the band edge), to (g)-(i): $\hbar\omega_y^1 = 1.30208eV$ (100μeV below the band edge energy, which is then resonant with $\hbar\omega_y^2$).

5.4 Radiative coupling in a disordered waveguide*

In Section 5.3.4, we included only partially the effects of disorder, by introducing a phenomenological loss rate γ to each of the ideally lossless waveguide mods. However, the effect of Anderson localization of light (see discussion in Section 1.3.1) was not included. In this Section, we simulate realistic systems with different magnitudes of disorder. We show that, while light localization indeed has a profound effect on both the range and the magnitude of the dot-dot excitation transfer rate, this latter is still sizable, compared to typical decoherence rates, even at several μm distance.

We study the same W1 waveguide as in Section 5.3.4, and we again focus on the main guided band in the spectral range close to the band edge (Fig. 5.13(a)-(b)). Fabrication

Figure 5.13: (a): Band structure of the regular waveguide; the main guided band is shown in blue, and the light cone – in dashed black. (b): Zoom-in close to the edge of the guided band. (c)-(d): For a waveguide with disorder, y-component of the electric field (E_y) of a mode at frequency (c): $\omega = 1.2980$eV (dashed line in (b)); and (d): $\omega = 1.2993$eV (dashed-dotted line in (b)). In (c), the white crosses indicate the elementary cell centers, where we assume a quantum dot can be placed. (e): Disorder-averaged zero-distance coupling $\langle |G^{11}(\omega_0)| \rangle$, plotted as a function of the exciton frequency ω_0. (f): Characteristic decay length of the disorder-averaged coupling $\langle |G^{12}(\omega_0)| \rangle$ as a function of ω_0. Full lines: Including disorder-induced localization. Dashed lines: No localization; the decay length is simply given by $2v_g/\gamma$. In both panels (e) and (f), three different magnitudes of disorder are shown (see legend). The vertical dot-dashed line denotes the band-edge of the regular waveguide. For $\sigma = 0.002a$, the $2v_g/\gamma$-curve in (f) cannot be distinguished from the band edge line on the scale of the plot. The inset in (e) shows the disorder-averaged $\langle |G^{12}(\omega_0)| \rangle$ as a function of distance, for three different values of the exciton frequency ω_0, and $\sigma = 0.004a$.

disorder is introduced in the same way as in Chapters 3 and 4, i.e. random fluctuations in the x and y positions and the radius of each hole, drawn from a Gaussian random distribution with zero mean standard deviation σ. A waveguide of length $512a$ using the BME.

As discussed in Section 1.3.1, disorder limits the maximum group index, which for an ideal waveguide goes to infinity at the band edge. It is also worth noting that disorder introduces modes that lie **below** the band edge of the regular structure, i.e.

the density of states of the disordered guide presents a Lifshitz tail below the van Hove singularity [63, 279]. In addition, disorder induces Anderson localization of light [63, 64, 113], which for states close to or below the band edge can be extremely strong. This is illustrated in Fig. 5.13 (c), where one mode of a disordered waveguide is shown, and the electric field is localized over several elementary cells. The field profile resembles those of PhC cavities, and both strong Purcell enhancement [64] and cavity-like vacuum Rabi splitting [65] of a single QD coupled to such a mode has already been observed. Modes slightly higher in frequency become more extended, and present more than one lobes (Fig. 5.13 (d)), and in fact provide the ideal compromise between strength and range of the dot-dot excitation transfer. Just as in Section 5.3.4, here we always consider two dots in the waveguide, which are placed in the center of an elementary cell (Fig. 5.13 (c)), and so at a distance multiple of a from each other.

To quantify the QD-W1 and the effective QD-QD coupling, we use the same Green's function formalism as in Section 5.3.4. The effective coupling strength is given as in eq. (5.28), the only difference being that we use the disordered waveguide modes in the summation, which depend on the particular configuration. In other words, while localized modes always appear in the presence of disorder, their particular shape, and the position of the localized lobes, differs vastly among disorder realizations. Thus, here we perform the analysis using a *configuration average* over 400 different realizations of the waveguide disorder, and a *running average* over the position of the first dot in each particular waveguide. The dependence with inter-dot distance of the averaged magnitude of the excitation transfer rate $\langle|G^{12}|\rangle$ is shown in the inset of panel (e) of Fig. 5.13 for three different exciton transition frequencies ($\omega_0 = 1.2980$eV, $\omega_0 = 1.2987$eV and $\omega_0 = 1.3000$eV, with band edge at $\omega = 1.2982$eV) and for $\sigma = 0.004a$. These plots show some deviation from an exponential law at large distances, but this is an unphysical result originating form the finite size of our simulation domain, and occurs at very small values of G^{12}, which are scarcely relevant to our conclusions. For each ω_0, an exponential function can thus be fitted in the region where the decay is a straight line on a logarithmic plot, and an attenuation length can be extracted. On this basis, panels (e) and (f) give detailed information about the dot-dot interaction for three different disorder magnitudes. The interaction strength is quantified in panel (e), through the averaged zero-distance term $\langle|G^{11}|\rangle$, while the range – in panel (f) through the interpolated attenuation length. Finally, even though the group index n_g cannot be well-defined in the presence of localization, its value in the ideal-PhC case is given on the top x-axis in both panels.

Some previous experimental works [64, 65], in which single-dot coupling to a PhC waveguide has been demonstrated, take advantage of large PhC disorder as a means to have strongly localized modes. That this is beneficial is not directly obvious from the large-disorder result shown in Fig. 5.13(e), which never exceeds 10μeV. It should be kept in mind however that this result represents the configuration-averaged zero-distance coupling. In few individual configurations in which the dot is sitting exactly

on top of a strongly localized mode, the same coupling can exceed 100μeV. In any case, such a strong disorder makes it very unlikely to have long-distance dot-dot interaction, as can be seen from panel (f). For $\sigma = 0.004a$ ($\approx$ 1nm in typical systems, realistically achievable), however, the attenuation length becomes sizable – of the order of $100a$, which corresponds to the $10\ \mu$m range. Notice, though, that the localization still has a drastic effect as compared to the case studied in Section 5.3.4, i.e. when including extrinsic losses only. This is illustrated by the dashed lines in panel (f) showing the distance-dependence of the transfer rate in this case, which is simply determined by the ratio $2v_g/\gamma$. In the Figure, γ was taken as the average over the loss rates, computed through Bloch-mode expansion, for each of the disorder magnitudes, and corresponds to a quality factor of $Q = 95000$ for each mode in the $\sigma = 0.004a$ case. The drastic influence of Anderson localization emerges in the fact that modes at a given frequency are characterized by a localization length which also determines the spatial decay of the light transport process at that frequency. The corresponding decay length is generally much smaller than that associated to ballistic propagation in presence of a phenomenological extrinsic loss rate.

While the configuration average gives a good estimate of the interaction strength, it is also important to understand the underlying statistics, to know what one could expect in an actual experiment. In Fig. 5.14(a), we plot the coupling $|G^{12}(\omega_0)|$ as a function of the dot-dot distance, for $\sigma = 0.004a$ and $\omega_0 = 1.2985$eV (indicated by an arrow in panel (b)). The full line is the configuration-averaged quantity, the dashed line represents the $\exp(-x/(2v_g/\gamma))$-dependence (i.e. neglecting localization effects), while the dot-dashed line represents a single disorder realization. As a first remark, when neglecting localization effects the coupling decays very slowly, illustrating again their importance. When accounting for localization instead, the coupling decays significantly with distance, but its magnitude at short distances is increased. This enhancement is due to the presence of modes localized on a short spatial range that behave similarly to resonant cavity modes. The plotted single disorder configuration and the position of the first dot were selected from the statistical ensemble in order to have a large zero-distance coupling, exceeding 100μeV. This is suggestive of the fact that the statistics is characterized by a large variance. As a better illustration, we compute the statistical distribution of the values of $|G^{11}|$ (for the same parameters as in panel (a)) and plot it in Fig. 5.14(c). The distribution exhibits a very long tail towards high values, suggesting that there is a sizable probability of having large radiative coupling. This is highlighted in panel (b) where we plot, as a function of ω_0, the configuration-averaged value of $|G^{11}|$ (full line), and compare it to the value for which the Cumulative Distribution Function (CDF) is equal to 0.95 (dashed line). Put simply, the dashed line in Fig. 5.14(b) gives the magnitude of the coupling that one can expect from one in every 20 samples. It is then clear that $|G^{11}|$ can exceed 70μeV, and a value of above 30μeV can be expected even for frequencies for which the interaction range is of the order of $100a$.
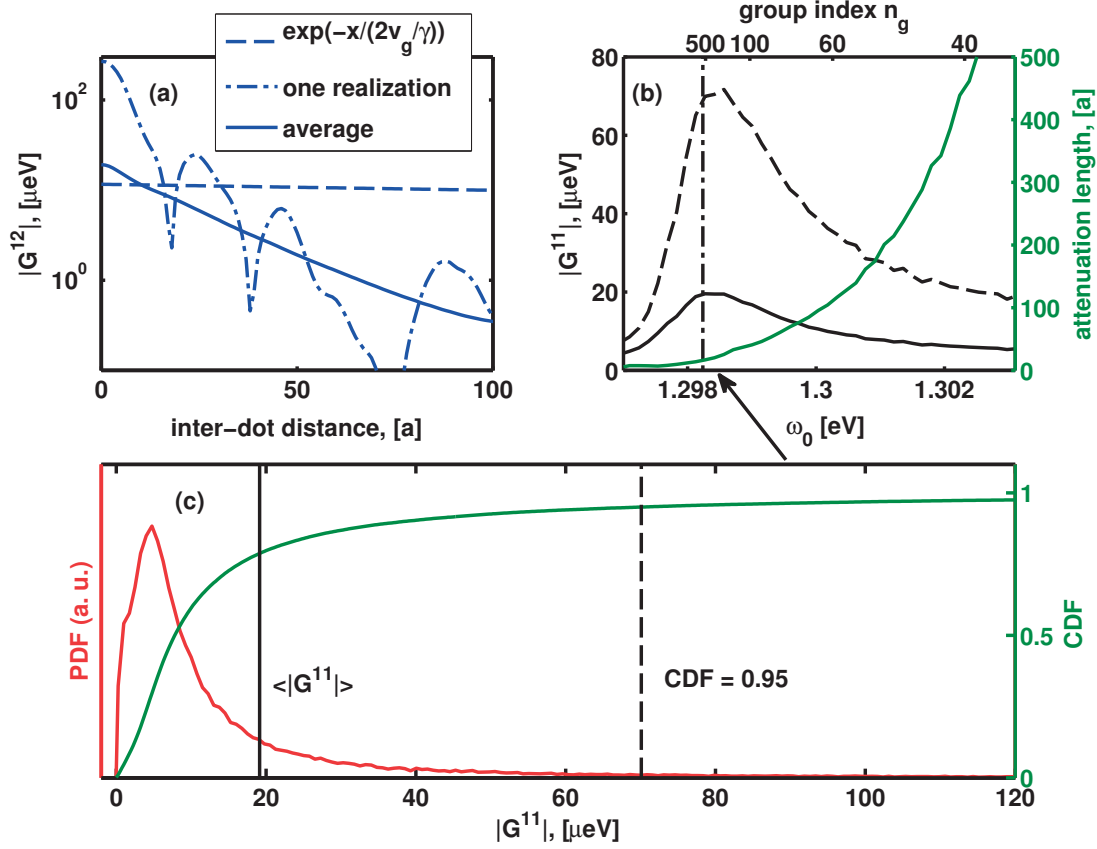
Figure 5.14: (a): Excitation transfer rate vs. distance without light localization (dashed), or with, for a single disorder realization (dashed-dotted) and the configuration average (solid), for $\sigma = 0.004a$ and $\omega_0 = 1.2985$eV (indicated by an arrow in (b)). (b): The two solid lines are the same as the $\sigma = 0.004a$ lines in panels (e) and (f) of Fig. 5.13; the dashed line shows the value of $|G^{11}|$ for which the CDF (panel (c)) is 0.95. (c): PDF and CDF of $|G^{11}|$, with $\langle|G^{11}|\rangle$ and the CDF = 0.95 values explicitly indicated.

Finally, we note that the PhC disorder plays a more important – and non-trivial – role than the imperfect positioning of the quantum dots. To illustrate this fact, we take one specific disorder realization of the PhC waveguide, place one QD at the center of an elementary cell of the waveguide, while for the second QD – located in another elementary cell of the guide – we assume a random displacement from the center of the cell, characterized by a Gauss distribution with standard deviation σ_D. In Fig. 5.15, panels (a) and (b) show the computed dot-dot coupling $|G^{12}(\omega_0)|$ for one realization of the PhC disorder and with the first dot respectively placed in two different elementary cells, as a function of the inter-dot distance. The parameters are $\sigma = 0.004a$ and $\omega_0 = 1.2985$eV. In both panels, the green line denotes the corresponding quantity averaged over the disorder realizations, while the other curves are computed for a single realization and different values of σ_D, and are averaged over the position of the second QD. The only effect of a finite value of σ_D is a rescaling of the interdot coupling
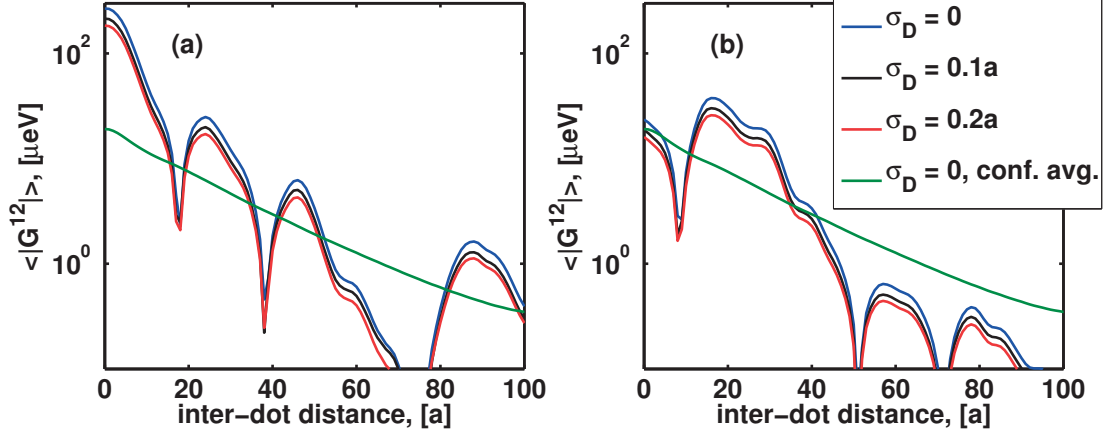
Figure 5.15: (a), (b): For two different positions of the first dot, the excitation transfer rate as a function of dot-dot distance, for the dots placed exactly at the center of the elementary cells (blue line) and with some positioning disorder corresponding to a finite value of σ_D (black and red lines, averaged over dot positioning). The configuration average over PhC disorder is also shown (green line).

by a factor not far from unity, which is expected, as the electric field does not vary strongly on the length-scale of a few tens of nanometers.

5.5 Summary and outlook for the QD-PhC system

We have developed a general formalism of linear radiation-matter coupling in systems of many QDs embedded in a photonic crystal structure. The formalism is an extension of the exciton-polariton formalism well known for bulk semiconductors and quantum wells. It provides a quantitative account of a variety of radiative effects, starting from the basic microscopic parameters of the QD-PhC system. It is important to establish a relation between the present approach and previous works that use the photonic Green's function [59, 254, 255, 257, 258]. The equations obtained there have the advantage of highlighting the importance of each single mode in determining the effects under study, but, on the other hand, incorporate either single-mode approximations or perturbative expansions. Our approach is in a sense complementary, with the main advantage coming from the fact that the problem is framed into a simple matrix diagonalization form, and that we make use of the Bloch-mode expansion to obtain the exact electric field profile for each mode, which allows us to compute the couplings independently of any approximations.

As examples of application, the main results presented of this Chapter concern radiative effects in the systems of one or two QDs embedded in Ln cavities and the W1 waveguide. In the case of one QD, we recover the known results for the Purcell enhancement of the radiative rate and the vacuum Rabi splitting in the strong coupling

regime. In the two-QD case, we quantify the strength of the radiative excitation transfer between **spatially separated** QDs, which lies in the $100 \ \mu eV$ range at short distance. The comparison of the single-mode coupling strength and the energy spacing between modes in Ln cavities of increasing length clearly shows that a crossover occurs – around $n = 150$ for GaAs-based systems – between single-mode and multi-mode radiative coupling. In the multi-mode case, the radiative coupling strength through each photonic mode is smaller but the overall effective excitation transfer rate still ranges at about $50 \ \mu eV$, thus suggesting that the W1 is an ideal structure for the realization of long-range radiative dot-dot coupling. This conclusion still holds even when accounting for disorder, both in the PhC and in the QD positioning. Due to the unavoidable randomness in this case, a statistical study was needed and performed. We find that, in a 1-out-of-20 setting, the rate still reaches $50 \mu eV$ and more. The transfer time to which this corresponds is of the order of $10 ps$ – close to the single-qubit operation time and much shorter than the decoherence time measured in these systems.

These results illustrate that the QD-PhC system is a candidate system to operate as a quantum bus and achieve controlled entangling interaction between distant qubits. This perspective is corroborated by the two following remarks. First, semiconductor QDs have recently seen a tremendous progress [202–210] towards the physical implementation of qubits that rely on the electron or hole spin as the computational degree of freedom, and on the interband optical transition as the main handle for single-qubit operations. Second, the optical quantum bus technology has already been successfully applied to achieve controlled two-qubit operations in the system of superconducting qubits [194]. The controlled operation in that case has been achieved by moving in and out of the anti-crossing region in the polariton spectrum arising from radiation-matter coupling. In view of a similar development in the semiconductor QD case, at least three steps have to be considered. First, the ability to fabricate site-controlled QDs, in order to position them with respect to the PhC structure. This is nowadays possible thanks to various kinds of growth on a patterned substrate [280–284]. Second, a clear experimental proof of the radiative excitation transfer mechanism at long distance, that might only come from ad-hoc technique such as, for example, the single-QD two-dimensional four-wave-mixing spectroscopy [239]. Third, a reliable scheme for dynamically controlling the exciton-photon detuning at sufficiently high speed. For this latter task, extremely promising results are already available on the optical control of the resonant frequency of high-Q PhC cavities [93, 127].

In short, given the rapid development of the field, the progress in all relevant directions, and the analysis presented here, it is realistic to believe that an experimental demonstration of dod-dot coupling at-a-distance is imminent.

6 Quantum Hall Effect for Light in an Array of Resonators

The last Chapter of this thesis is not restricted to the domain of photonic crystals, and is in the scope of the newly emerging field of *topological photonics.* The results presented here pertain to an array of resonators, which is represented by some generic parameters, and which could be implemented in various platforms. However, we do note that a PhC slab is one of the most promising structures to implement the model that will be discussed below. In that sense, this Chapter can also be seen as yet another research direction in which the optimization procedure of Chapter 4 will be relevant.

In the following Sections, we show how an analogue of the Haldane Quantum Hall model can be achieved in a Kagomé lattice of photonic resonators using a time-periodic modulation of the resonant frequencies, where *only the phase of the modulation varies among different sites, in a spatially periodic manner*. In Section 6.1, we present a brief introduction to the field of topological insulators and topological photonics. In Section 6.2, we introduce the model system, and the Floquet theory we use to solve the time-dependent Hamiltonian. We also discuss two possible geometries – the honeycomb and the Kagomé lattices – and explain the advantages of the latter. Finally, in Section 6.3, we compute the 2D Floquet bands for several systems, and show that they have non-zero Chern numbers, revealing their topological nature. We further show the existence of back-scattering-immune edge states, and discuss the possibilities for a practical implementation of the system.

6.1 Introduction to topological photonics

Topological order has opened a new frontier in the classification of distinctive phases of matter, and is thus a center of attention of theoretical and condensed matter physics [285]. Its study has also reached the field of photonics [286], for two main reasons. First, photonic analogues of topological systems are a promising route to bridging theory and experiment. Second, a signature of a topologically non-trivial material is the presence

of one-directional edge states providing energy transport immune to disorder. This could prove extremely valuable for slow-light photonic devices, which find a variety of applications, but whose performance is severely limited by back-scattering due to fabrication imperfections (cf. discussions in Sections 1.3.1 and 5.4).

Historically, topological order was first recognized in relation to the Quantum Hall effect [285, 287]. In that area, Haldane had a ground-breaking contribution in demonstrating that the effect can arise even with zero magnetic field averaged over a primitive cell. The research into topological photonics was also started by Haldane in two theoretical studies [288, 289], which were quickly followed by an experimental realization of a photonic topological insulator using gyromagnetic media [290]. This result was however obtained in the GHz frequency range. Due to the lack of suitable materials, reproducing this scheme in the visible or the near-infrared spectrum – which are the most interesting for applications – is still a major challenge. The milestone of an experimental realization of topological edge states for light in the near-infrared has been reached using coupled microring resonators [291, 292] or coupled waveguides [293] by taking advantage of the symmetry-induced degeneracy of rotating and counter-rotating modes. More specifically, these systems are characterized by a preserved Time-reversal Symmetry (TRS), which leads to an important limitation of the topological protection. The ground-breaking result (which is now known as the Spin Quantum Hall effect) of Kane and Mele [294] that, for electrons, this protection is still present in TRS systems, relies on the anti-unitarity of the time-reversal operator ($T^2 = -1$). For photons, this operator is unitary, and the result no longer holds [286], at least not in its full strength. Instead, the protection relies on the symmetry that prevents the mixing of propagating and counter-propagating modes in a waveguide, which in practice may be broken by disorder. This suggests the need for systems where TRS is broken [288, 289, 295–300]. Recently, the possibility to use a fine-tuned dynamic modulation of a system to engineer a gauge field for photons has been shown both theoretically [298] and experimentally [301, 302]. This scheme is employed here to induce a Haldane-like magnetic flux for photons on a lattice of optical resonators.

6.2   Floquet theory and lattice geometries

The seminal work by Haldane [303] considered a honeycomb lattice (Fig. 6.1(a)) with real first-neighbor and complex second-neighbor couplings. In the absence of the latter, the band structure of the lattice has six Dirac points, and no band gap (Fig. 6.1(b)). Haldane showed that the complex second-neighbor hopping terms, which result in zero average magnetic field over the unit cell, but non-zero magnetic flux through a triangle enclosed by second-neighbor hopping, break the TRS and open a topological band gap. Recently, this was successfully observed in a system of cold atoms in a 'shaken' optical lattice [304], which, together with previous research in that field [305–307], inspired the results presented here.
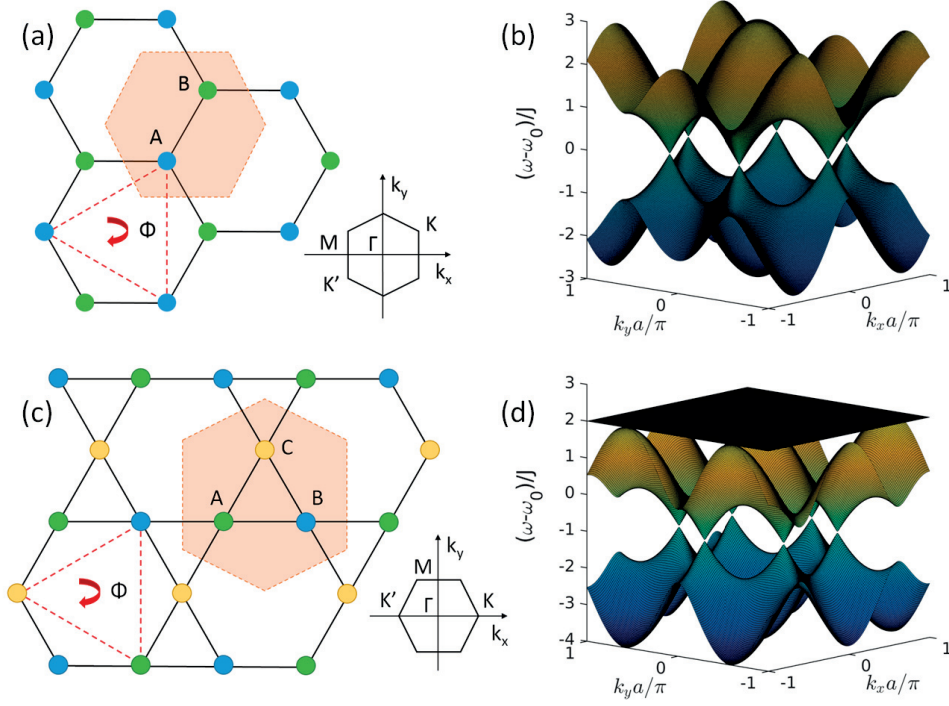
Figure 6.1: (a): Honeycomb lattice with two sites A and B in the primitive cell (highlighted in orange). The Haldane model involves a complex second-neighbor hopping, which results in a magnetic flux enclosed in the red triangle. The Brillouin zone in reciprocal space is also shown. (b): Band structure of the lattice with first-neighbor coupling J and zero flux Φ. Six Dirac cones at the K-points are present. (c): Kagomé lattice with three sites in the primitive cell, and the corresponding Brillouin zone. Effective magnetic flux through a hexagon, similar to the one of the original Haldane model, is used here to open topological band gaps. (d): The corresponding band-structure with first-neighbor coupling J and zero flux Φ. There are again six Dirac cones, and in addition a flat band.

For our photonic system, we start from the most general, linear, time-independent Hamiltonian for photons on a lattice ($\hbar = 1$):

$$H_S = H_0 + H_J = \sum_i \omega_i a_i^\dagger a_i - \sum_{i \neq j} J_{ij} a_i^\dagger a_j, \tag{6.1}$$

with $a_i^\dagger$, the photon creation operator, and with no particular requirements for the couplings J_{ij} (these will come later depending on the chosen lattice geometry). We add an on-site, time-dependent, periodic modulation of the resonant frequency with a position-dependent intensity and phase

$$H_t = \sum_i A_i \cos(\Omega t + \phi_i) a_i^\dagger a_i. \tag{6.2}$$

This can be achieved for example through electro-optic modulation [308,309], optically-induced material non-linearities [310], or optomechanical interaction with phonon modes [186]. The total Hamiltonian $H_S + H_t$ is particle-number preserving, thus it describes the system with any fixed number of photons (sub-spaces of different photon numbers are decoupled). The equation also applies to classical light, since it is a concise way to write the coupled-mode theory that can be used for an array of optical resonators.

6.2.1 Expansion on the Floquet basis

For times much larger than the period $T = 2\pi/\Omega$, it becomes meaningful to apply the Floquet theory of quasi-energies [311, 312]. In particular, the solutions to the time-dependent Schrödinger equation can be written as $|\psi_n(t)\rangle = \exp(-i\varepsilon_n t)|u_n(t)\rangle$, with $u_n(t)$ a T-periodic function which is a solution to

$$[H_S + H_t - i\partial_t]|u_n(t)\rangle = \varepsilon_n|u_n(t)\rangle \tag{6.3}$$

The spectrum ε_n has a Brillouin-zone like structure with Ω the width of the first zone, i.e. for any solution $|u_n(t)\rangle$ of quasi-energy ε_n, and any integer m, $\exp(im\Omega t)|u_n(t)\rangle$ is also a solution, with eigenvalue $\varepsilon_n + m\Omega$. The states $|u_n(t)\rangle$ form a Hilbert space of T-periodic functions. The inner product in this space can be defined starting from the standard bra-ket inner product $\langle\bullet|\bullet\rangle$ for time-independent states, and reads

$$\langle\langle\bullet|\bullet\rangle\rangle = \frac{1}{T}\int_0^T \mathrm{d}t\langle\bullet|\bullet\rangle. \tag{6.4}$$

The states can be expanded on the Floquet basis given by

$$|\{n_i\}, m\rangle = U_t(t)|\{n_i\}\rangle\exp(im\Omega t) \tag{6.5}$$

$$=|\{n_i\}\rangle\exp\left(-\frac{i}{\Omega}\sum_i A_i\sin(\Omega t + \phi_i)n_i + im\Omega t\right),$$

where n_i denotes the occupation number of site i, and

$$U_t(t) = \exp\left(-i\int_{t_0}^t H_t(t')\mathrm{d}t'\right) \tag{6.6}$$

is the time-evolution operator corresponding to the time-dependent Hamiltonian H_t, and we assume an adiabatic switching of the modulation in order to disregard the phase offset due to the starting time t_0. Since the Hamiltonian is particle-number-preserving, we need only consider the subspace of a single excitation in the system, $\sum_i n_i = 1 \,\forall\, \{n_i\}$. Equation (6.3) is then an eigenvalue problem with matrix elements

in this basis given by

$$\langle\langle\{n'_j\}, m'|H_S + H_t - i\partial_t|\{n_i\}, m\rangle\rangle = \delta_{m,m'}\left[\langle\{n'_j\}|H_0 + m\Omega|\{n_i\}\rangle\right] + \qquad (6.7)$$
$$\int_0^T e^{i(m-m')\Omega t}\exp\left(\frac{iA_j}{\Omega}\sin(\Omega t + \phi_j) - \frac{iA_i}{\Omega}\sin(\Omega t + \phi_i)\right)\langle\{n_j\}|H_J|\{n_i\}\rangle.$$

These matrix elements are then equal to

$$\langle\langle n'_i, m'|H_S + H_t - i\partial_t|n_i, m\rangle\rangle = \delta_{m,m'}(m\Omega + \omega_i), \qquad (6.8)$$

when the particle stays on the same site, and to

$$\langle\langle n'_j, m'|H_S + H_t - i\partial_t|n_{i\neq j}, m\rangle = \int_0^T e^{i(m-m')\Omega t}J_{ij}\times$$
$$\exp\left(\frac{i}{\Omega}(A_j\sin(\Omega t + \phi_j) - A_i\sin(\Omega t + \phi_i))\right), \qquad (6.9)$$

when the particle hops from site i to site j. In eqs. (6.8) and (6.9), we label by n_i the only non-zero occupation number of $\{n_i\}$. We can further use the Jacobi-Anger expansion to simplify eq. (6.9) to

$$\langle\langle n'_j, m'|H_S + H_t - i\partial_t|n_{i\neq j}, m\rangle = -\mathcal{J}_{m'-m}(\rho_{ij})e^{i(m'-m)\phi_{ij}}J_{ij}, \qquad (6.10)$$

with $\mathcal{J}_n(x)$ the n-th Bessel function of the first kind, and the definition

$$\rho_{ij}e^{i\phi_{ij}} = (A_je^{i\phi_j} - A_ie^{i\phi_i})/\Omega. \qquad (6.11)$$

6.2.2 Floquet perturbation theory

Some additional intuition can be found in writing the Floquet perturbation theory [304, 313] for the effective time-independent Hamiltonian H_{eff} that describes the time evolution for timescales greater than T, in the sense that the time-evolution operator is

$$U(t + T, t) = \exp\left(-i\int_t^{t+T}(H_S + H_t)\mathrm{d}t\right) = \exp\left(-iH_{\text{eff}}T\right). \qquad (6.12)$$

For a Fourier-expanded time-periodic Hamiltonian,

$$H(t) = \sum_m H_m e^{im\Omega t}, \qquad (6.13)$$

we can write a perturbation expansion for H_{eff} in orders of $1/\Omega$. Up to first order, this reads

$$
\begin{aligned}
H_{\text{eff}} &= H_{0\Omega} + H_{1\Omega} + \mathcal{O}\left(\frac{1}{\Omega^2}\right) \\
&= H_{m=0} + \frac{1}{\Omega} \sum_{m=1}^{\infty} \frac{1}{m} [H_m, H_{-m}] + \mathcal{O}\left(\frac{1}{\Omega^2}\right).
\end{aligned}
\tag{6.14}
$$

In our dynamically-modulated lattice, after the unitary transformation

$$
H' = U_t^{\dagger}[H_S + H_t - i\partial_t]U_t = \sum_i \omega_i a_i^{\dagger} a_i - \sum_m \sum_{ij} \mathcal{J}_m\left(\rho_{ij}\right) e^{im(\Omega t + \phi_{ij})} J_{ij} a_i^{\dagger} a_j, \tag{6.15}
$$

with the definitions of $\mathcal{J}, \rho$, and ϕ as above, the Fourier components H_m can be easily read out. The zero-th order of the perturbative expansion of eq. (6.14) is

$$
H_{0\Omega} = H_0 + H_J' = \sum_i \omega_i a_i^{\dagger} a_i - \sum_{ij} J_{ij}' a_i^{\dagger} a_j,
$$

$$
J_{ij}' = J_{ij} \mathcal{J}_0\left(\rho_{ij}\right), \tag{6.16}
$$

i.e. similar to the starting H_S of the static lattice, but with rescaled (but still real) couplings J_{ij}'. The first-order term is

$$
\begin{aligned}
H_{1\Omega} &= \sum_{m=1}^{\infty} \frac{(-1)^m}{\Omega m} \sum_{ijpq} \mathcal{J}_m(\rho_{ij}) \mathcal{J}_m(\rho_{pq}) J_{ij} J_{pq} e^{im(\phi_{ij} - \phi_{pq})} \times [a_i^{\dagger} a_q \delta_{jp} - a_p^{\dagger} a_j \delta_{iq}] \\
&= \sum_{ij} 2i \sum_{m=1}^{\infty} \frac{(-1)^m}{\Omega m} \sum_p \mathcal{J}_m(\rho_{ip}) \mathcal{J}_m(\rho_{pj}) J_{ip} J_{pj} \times \sin(m(\phi_{ip} - \phi_{pj})) a_i^{\dagger} a_j, \tag{6.17}
\end{aligned}
$$

The (purely imaginary) term after the first sum sign can obviously be interpreted as a new coupling amplitude, J_{ij}'', which is added to J_{ij}', thus introducing a complex phase. The obvious interpretation of these terms is hopping from one site to another through one intermediate site. In the same way, terms of higher order in $1/\Omega$ represent hopping through an increasing number of intermediate sites. The imaginary J_{ij}'' thus can be used to introduce the magnetic flux required for the Haldane effect.

6.2.3 Honeycomb lattice

In the recent experimental observation of the Haldane model with cold atoms [304], the honeycomb lattice confining the atoms was 'shaken' by a periodic, elliptical modulation. In the reference frame of the lattice, this results in an inertial force on the atoms, which can be written as a site-dependent potential in the Hamiltonian. The strongest

effect is obtained for circular modulation, in which case the Hamiltonian reads

$$H_{lat} = \sum_{ij} t_{ij} c_i^\dagger c_j + \sum_i (C_i \cos(\Omega t) + S_i \sin(\Omega t)) c_i^\dagger c_i, \tag{6.18}$$

with t_{ij} the coupling constants, $c_i^\dagger, c_i$ the fermion creation and annihilation operators, Ω the frequency of the modulation, and C_i, S_i – site-dependent constants. This can obviously also be implemented through a modulation of the form of eq. (6.2), with the remark that since both Hamiltonians are particle-number preserving, the particle statistics (bosons or fermions) are not important. Thus, all the considerations of Ref. [304] also hold for a lattice of optical resonators – and, in particular, a Haldane model for photons on a honeycomb lattice can be implemented by choosing the A_i and ϕ_i so as to match the C_i and S_i that can be read out of Ref. [304], i.e. setting

$$A_i \cos(\Omega t + \phi_i) = C_i \cos(\Omega t) + S_i \sin(\Omega t), \qquad \forall\, i. \tag{6.19}$$

However, we note that the circular 'shaking' implies an inertial force which is the same for all lattice sites, which, written in terms of a potential in the Hamiltonian, implies a spatial *gradient*. In other words, the C_i and S_i arising from this circular modulation in the cold-atom case are proportional to the position vector $\mathbf{r}_i$ of site i, which would then also be the case for A_i when derived from eq. (6.19). Thus, replicating the cold atom system requires a gradient in the amplitude of the modulation of the frequency of the optical resonators, which is on one hand experimentally challenging, and on the other limits the scalability of such a system. Ideally, we would like to have a modulation which shares the spatial periodicity of the underlying lattice: this is, however, impossible in the case of the honeycomb lattice, for the following reason. This lattice has two sites in the unit cell (marked A and B in Fig. 6.1(a)). Assuming a modulation with the same periodicity, we are limited to two arbitrary amplitudes A_A and A_B, and two arbitrary phases φ_A, φ_B. Whatever their values, however, looking at eq. (6.11), it is obvious that $\phi_{12} = \pi + \phi_{21}$, which means that $\phi_{12} - \phi_{21} = \pi$. Since all terms in the second-neighbor imaginary hoppings (eq. (6.17)) that come out of this modulation are proportional to $\sin(m(\phi_{12} - \phi_{21}))$ with m an integer, they are all zero.

In short, the Haldane model can be achieved in a dynamically modulated honeycomb lattice, but only through a spatially-varying amplitude of the modulation. This breaks the spatial periodicity and makes it impossible to analyze the system in momentum space, which is a significant theoretical disadvantage. In addition, in view of potential experimental realizations, this feature introduces an extra challenge, since the maximum amplitude of the modulation is inevitably limited, which in turn would limit the maximum system size. Fortunately, this problem can be easily overcome by choosing a slightly different geometry – namely, by considering the Kagomé lattice illustrated in Fig. 6.1(c).

6.2.4 Kagomé lattice

The Kagomé lattice (Fig. 6.1(c)) has three lattice sites per elementary cell, and the band structure (Fig. 6.1(d)) is similar to the one of the honeycomb lattice in that there are six Dirac cones. The main difference comes from the additional flat band. Importantly, in the presence of a flux similar to the one of the Haldane model, topologically non-trivial band gaps can be opened between the first and the second and/or the second and the third bands [314, 315].

Using this lattice, it is possible to produce a non-zero Haldane-like flux through a **spatially-periodic** dynamic modulation. In fact, we can even impose a constant modulation amplitude A_0, and have spatial dependence only in the phase. As mentioned above, such a simple realization has the advantage of experimental scalability, and is also much easier to analyze theoretically, through two-dimensional Floquet band diagrams. To make matters simpler still, we set the phase of the modulation to φ, 2φ, and 3φ on A, B, C, respectively, for some constant φ, which is the second free parameter of our system (together with A_0).

For the starting Hamiltonian, we assume a constant resonant frequency ω_0 on all sites, and a constant first-neighbor coupling J (along the black lines in Fig. 6.1(c)). In the presence of the modulation, the effective Hamiltonian of eq. (6.14) up to first order in perturbation theory can then be written in k-space as

$$\tilde{H} = \sum_{\mathbf{k}} \mathcal{A}_{\mathbf{k}}^{\dagger} \left(\omega_0 + \mathcal{H}(\mathbf{k}) \right) \mathcal{A}_{\mathbf{k}} \tag{6.20}$$

with

$$\mathcal{A}_{\mathbf{k}}^{\dagger} = (a_{A,\mathbf{k}}^{\dagger}, a_{B,\mathbf{k}}^{\dagger}, a_{C,\mathbf{k}}^{\dagger}), \tag{6.21}$$

where $a_{A,\mathbf{k}}^{\dagger}$ is the Fourier transform of the $a_A^{\dagger}$ operator creating a particle on site A, and correspondingly for B and C. The coupling matrix is given by

$$\mathcal{H}(\mathbf{k}) = -2J \begin{pmatrix} 0 & t_{AB}(\mathbf{k}) & t_{AC}(\mathbf{k}) \\ t_{AB}^*(\mathbf{k}) & 0 & t_{BC}(\mathbf{k}) \\ t_{AC}^*(\mathbf{k}) & t_{BC}^*(\mathbf{k}) & 0 \end{pmatrix}, \tag{6.22}$$

where the (dimensionless) couplings can be split into

$$\begin{aligned}
t_{AB}(\mathbf{k}) &= (t_{AB,0} + t_{AB,1}) \cos(\mathbf{k}\mathbf{a}_1) + t_{AB,1}' \cos(\mathbf{k}(\mathbf{a}_2 + \mathbf{a}_3)), \\
t_{AC}(\mathbf{k}) &= (t_{AC,0} + t_{AC,1}) \cos(\mathbf{k}\mathbf{a}_2) + t_{AC,1}' \cos(\mathbf{k}(\mathbf{a}_1 - \mathbf{a}_3)), \\
t_{BC}(\mathbf{k}) &= (t_{BC,0} + t_{BC,1}) \cos(\mathbf{k}\mathbf{a}_2) + t_{BC,1}' \cos(\mathbf{k}(\mathbf{a}_1 + \mathbf{a}_2)),
\end{aligned} \tag{6.23}$$

where, in the first line, $t_{AB,0}$ is the first-neighbor coupling from site A to site B, $t_{AB,1}$
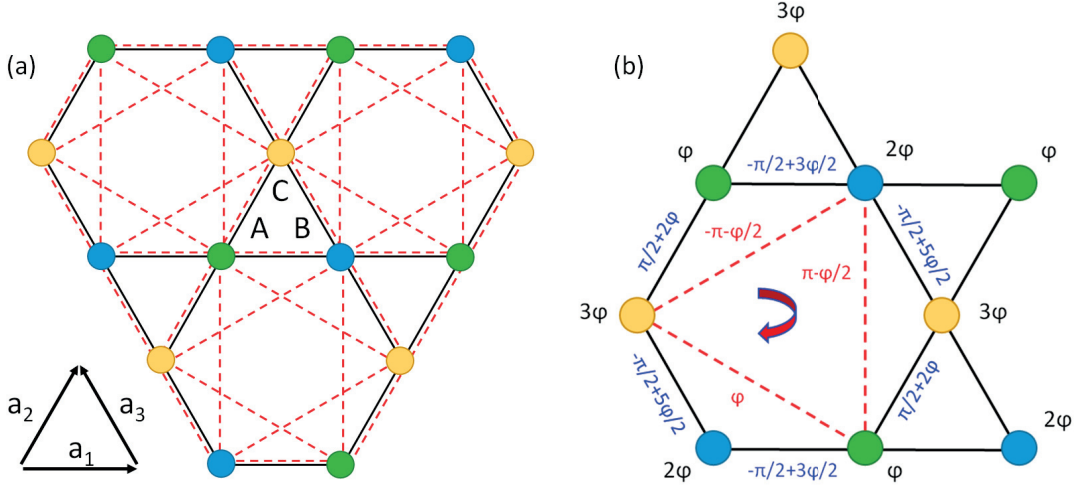
Figure 6.2: (a): Kagomé lattice, see also Fig. 6.1. In the presence of the dynamic modulation, the zero-order terms of the perturbation-theory effective Hamiltonian are first-neighbor couplings (black lines), while the first-order terms are both first- and second-neighbor couplings (red dashed lines), induced by hopping through one intermediate site. (b): Definition of various phases under a modulation of constant amplitude, and phases (marked in black): φ on site A, 2φ on site B, and 3φ on site C. In blue, the phase ϕ_{ij} as defined in eq. (6.11) is given for a clockwise hopping direction (indicated by the arrow in the center of the hexagon). With red, the phase $\phi_{ip} - \phi_{pj}$ entering eq. (6.17) is given, for the same hopping direction.

is the double-hop coupling (through site C) to a first-neighbor site B, and $t'_{AB,1}$ is the double-hop coupling (again through site C, but in a different direction) to a second-neighbor site B. The vectors $\mathbf{a}_i$ are defined such that $\mathbf{a}_1$ points from A to B, $\mathbf{a}_2$ points from A to C, and $\mathbf{a}_3$ points from B to C (see Fig. 6.2(a)). Simply put, the zero-th order effective Hamiltonian results in re-scaled first-neighbor couplings (black lines in Fig. 6.2(a)), while the first order results in all the couplings marked in dashed red lines in the Figure, which always involve an intermediate hopping, but are both first- and second-neighbor. The values of those couplings computed through (eq. (6.17)) are

$$t_{AC,0} = \mathcal{J}_0(2\rho_\varphi), \quad t_{AB,0} = t_{BC,0} = \mathcal{J}_0(\rho_\varphi)$$

$$t_{AB,1} = t'_{AB,1} = 2i\frac{J}{\Omega}\sum_m \frac{(-1)^m}{m}\mathcal{J}_m(\rho_{2\varphi})\mathcal{J}_m(\rho_\varphi)\sin(m(\varphi/2 - \pi))$$

$$t_{AC,1} = t'_{AC,1} = 2i\frac{J}{\Omega}\sum_m \frac{(-1)^m}{m}\mathcal{J}_m(\rho_\varphi)\mathcal{J}_m(\rho_\varphi)\sin(m\varphi) \tag{6.24}$$

$$t_{BC,1} = t'_{BC,1} = 2i\frac{J}{\Omega}\sum_m \frac{(-1)^m}{m}\mathcal{J}_m(\rho_{2\varphi})\mathcal{J}_m(\rho_\varphi)\sin(m(\pi + \varphi/2)),$$

where $\rho_\varphi = 2(A_0/\Omega)|\sin(\varphi/2)|$ and $\rho_{2\varphi} = 2(A_0/\Omega)|\sin(\varphi)|$ are the amplitudes computed through eq. (6.17) for a phase difference between sites i and j of φ and 2φ,
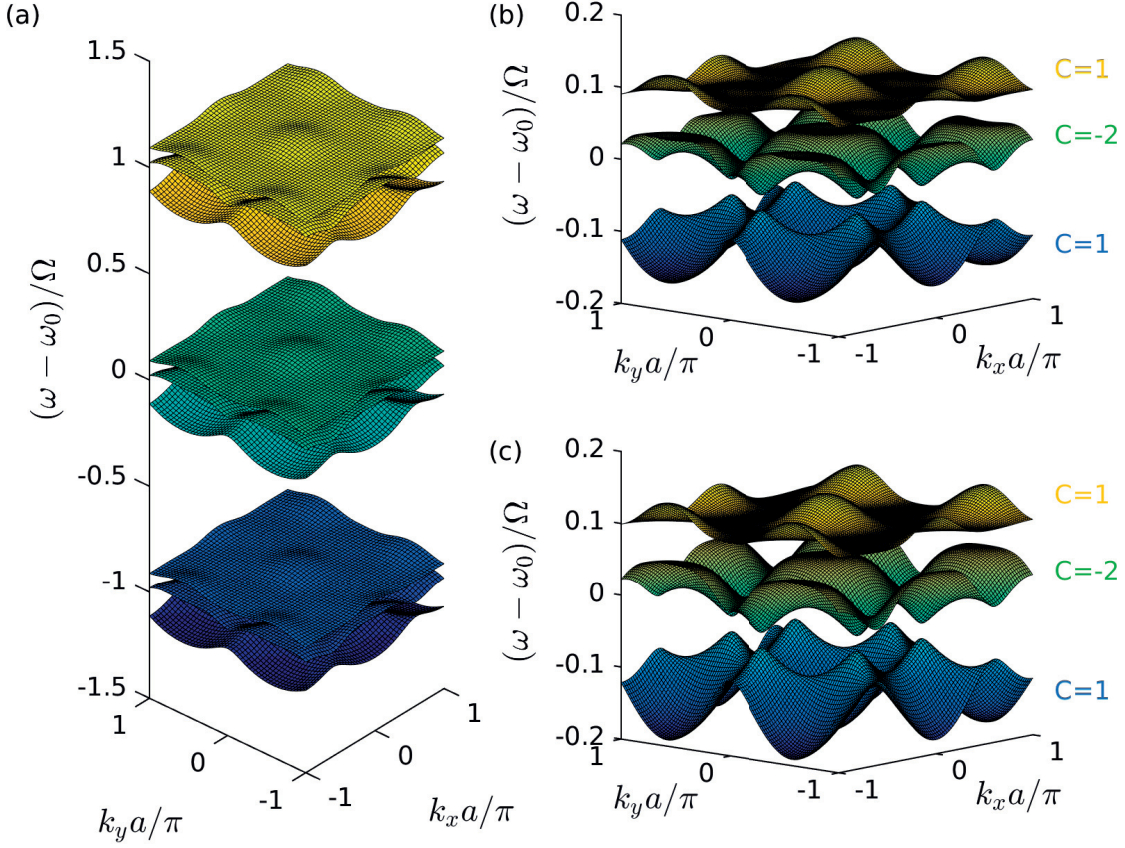
Figure 6.3: (a): Quasi-energy bands computed through diagonalization on the Floquet basis, for $J = 0.1\Omega$, $A_0 = 0.9\Omega$, $\varphi = 2.1$. The bands are repeated in orders of $m\Omega$, with m an integer. (b): Zoom-in on the $m = 0$ region of (a). (c): Bands computed through a perturbative expansion of the effective time-independent Hamiltonian. In (b) and (c), the Chern number for each band is indicated.

respectively. In Fig. 6.2(b), we illustrate the computation of the phases that enter the sine functions of eq. (6.24). Starting from the modulation phases (marked in black), one first computes the value of ϕ_{ij} (marked in blue) as defined in eq. (6.11) for all first neighbors, and then the values of $\phi_{ip} - \phi_{pj}$ (marked in red) that enter eq. (6.17).

6.3   Qauntum Hall effect on the Kagomé lattice

6.3.1   Floquet bands

The exact solution for the Floquet two-dimensional quasi-energy bands of the dynamically modulated Kagomé lattice can be computed with the diagonalization explained
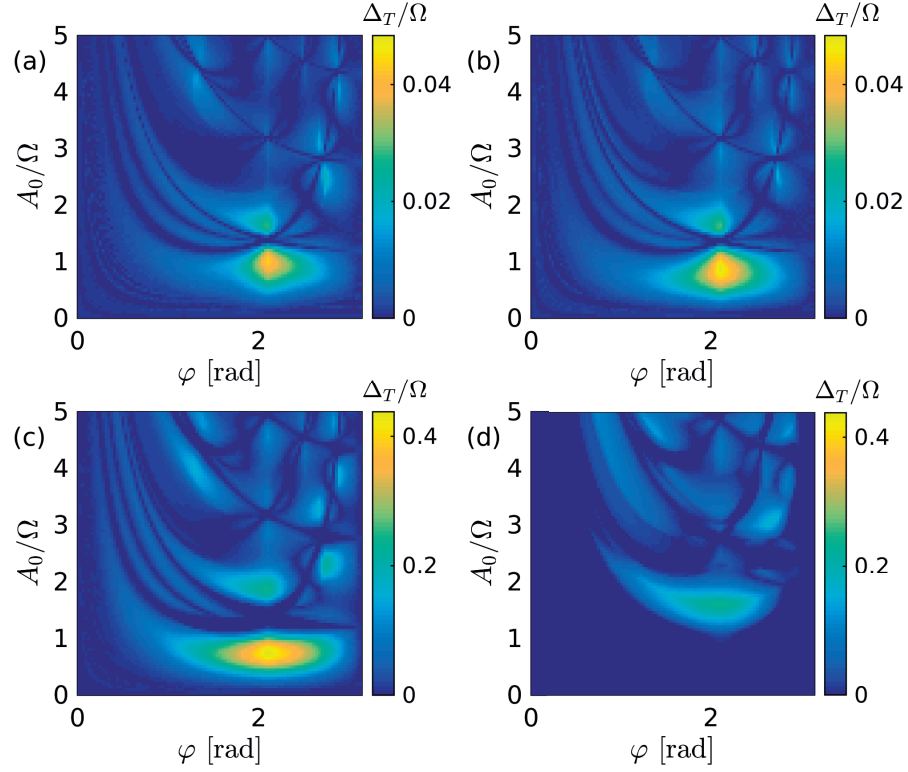
Figure 6.4: The (largest) width of the opened band gap due to the dynamic modulation of frequency Ω vs. the amplitude A_0 and the phase angle φ for the Kagomé lattice with first-neighbor coupling $J = 0.1\Omega$, (a): Floquet perturbation theory; (b): expansion on the Floquet basis. (c)-(d): Same as (a)-(b), but for $J = 0.5\Omega$. The color scheme is the same in panels (a) and (b), as well as in panels (c) and (d).

in Section 6.2.1. The eigenstates can be written as

$$u_n(\mathbf{k}, t) = \sum_{i,m} v_{m,i}(\mathbf{k}, n) e^{-i\mathbf{k}\mathbf{R}_i} e^{im\Omega t}, \tag{6.25}$$

with $v_{i,m}(\mathbf{k}, n)$ the eigenvectors from the diagonalization, and $\mathbf{R}_i$ the position of site i.

The band diagram of the system for $J = 0.1\Omega$, $A_0 = 0.9\Omega$, $\varphi = 2.1$ is shown in Fig. 6.3(a)-(b). As discussed in Section 6.2.1 and displayed in panel (a), the bands are repeated in frequency space at an interval of Ω. In panel (b), which shows a close-up of the zero-th order bands of panel (a), we see that band gaps are opened due to the dynamic modulation. To quantify their topological properties, we compute the Chern number for all bands by integrating the Berry curvature $\mathcal{F}(\mathbf{k})$ [316, 317] over the Brillouin zone:

$$C = \frac{1}{2\pi} \int_{BZ} d\mathbf{k} \mathcal{F}(\mathbf{k}) \tag{6.26}$$

Numerically, we compute $\mathcal{F}(\mathbf{k})$ on a discrete mesh in $\mathbf{k}$-space using the eigenvectors

$v_{m,i}(\mathbf{k}, n)$ [318, 319]. The non-zero Chern numbers (1, -2 and 1 for the three bands, respectively) confirm the non-trivial nature of the band gaps.

We can also compute the bands of the system through the perturbative expansion, as described in Sections 6.2.2 and 6.2.4. As mentioned above, this has the advantage of making the connection between this system and the Haldane model manifest, since the first-order terms in the expansion are imaginary couplings that introduce a flux in the red triangle of Fig. 6.1(c). In Fig. 6.3(c), we show the bands computed by diagonalizing this effective Hamiltonian, which agree very well with the exact solution of panel (b), and the computed Chern numbers are the same.

Topological invariants like the Chern number cannot change as long as the band gap remains open. Hence, the width of the band gap is an important parameter, giving an energy scale to the topological protection against disorder (only fluctuations on a larger scale can destroy the topological properties). Thus, in Fig. 6.4, we plot maps of the gap width Δ_T (if two gaps are present, the largest value is taken), versus the parameters A_0 and φ. The data in panels (a) and (b) are computed for $J = 0.1\Omega$, with the perturbation theory Hamiltonian in (a), and the full diagonalization in (b), and show very good agreement. In panels (c) and (d), $J = 0.5\Omega$ was used, and the agreement is no longer present. It is natural that the perturbative expansion works well for small J/Ω when the Floquet bands of different orders are well-separated (Fig 6.3(a)), but has limited reliability as J increases. Importantly, however, the topological effect is present even beyond perturbation theory: a gap of width larger than 0.2Ω is opened for $J = 0.5\Omega$, $A_0 = 1.6\Omega$, $\varphi = 2.1$. Notice that for any value of the parameters in this system, the band gap is inevitably limited to a fraction of Ω due to the higher-order Floquet bands.

In Fig. 6.5, we show the band structures with the largest band gaps for $J = 0.3\Omega$, $J = 0.5\Omega$ and $J = 0.7\Omega$, with parameters A_0 and φ chosen for the largest Δ_T. Topologically, there is a difference between the bands in Fig. 6.3(b) and 6.5(b), with Chern numbers 1, -2, and 1, and those of Fig. 6.5(d), (f) with Chern numbers 1, 0, and -1. What is important, however, is that in both cases there are bands with a non-zero topological invariant. The bulk-boundary correspondence principle [285, 286] then applies, guaranteeing the existence of gapless edge states at an interface between the topological material and a topologically trivial one (e.g. empty space). In terms of practical applications, propagating modes robust to disorder are thus expected to appear in a finite system.

6.3.2 Edge states

The existence of the topological edge modes is illustrated in Fig. 6.6 for a ribbon geometry, with a finite number of sites in one direction, and periodic boundary conditions in the other. The one-dimensional Floquet band structure can again be computed by expanding on the Floquet basis, and is shown in panel (a) and (d) for $J = 0.5\Omega$,
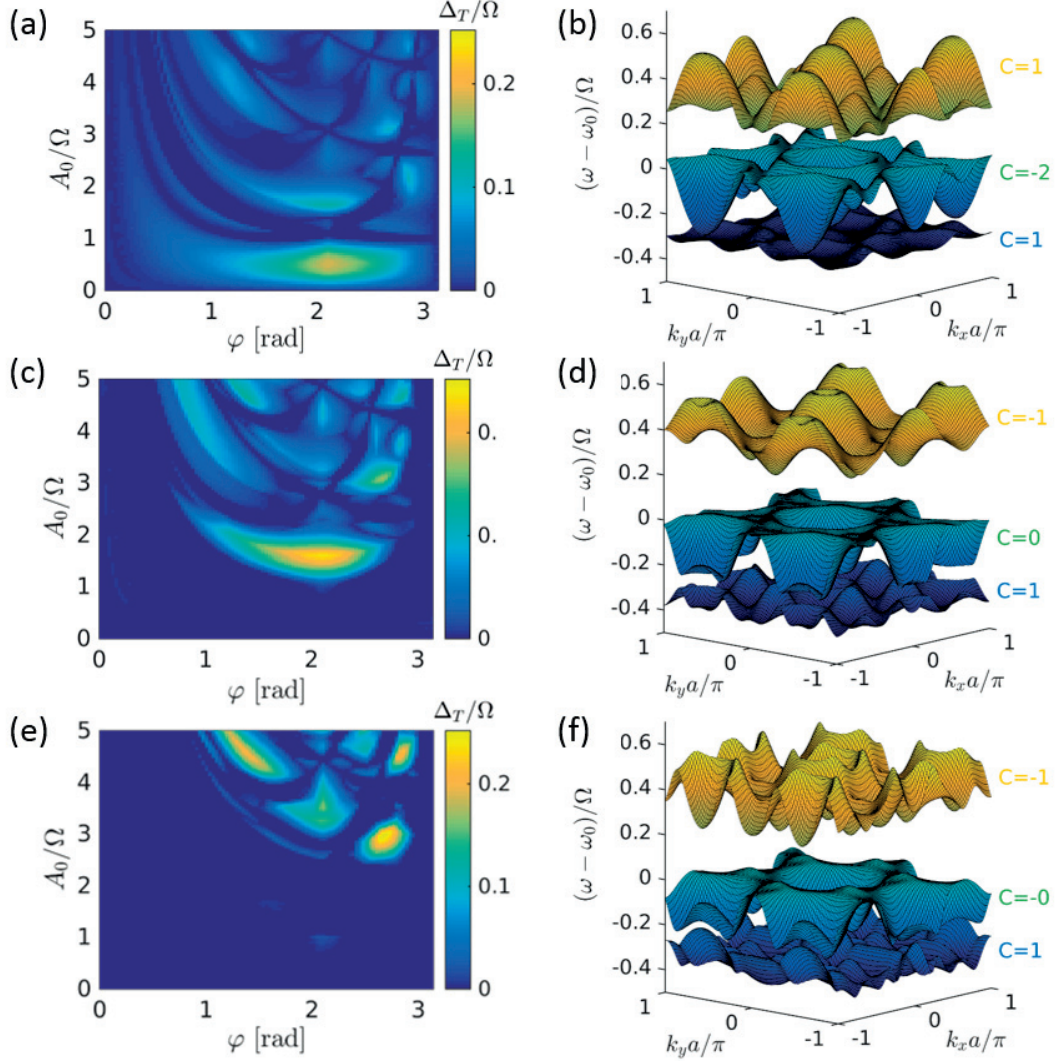
Figure 6.5: (a): Width of the opened band gap vs. A_0 and φ, for $J = 0.3\Omega$. (b): The band structure with the largest possible band gap for $J = 0.3\Omega$, with $A_0 = 0.5\Omega$, $\varphi = 2.1$. (c)-(d): Same as (a)-(b), for $J = 0.5\Omega$. In (d), $A_0 = 1.6\Omega$, $\varphi = 2.1$. (e)-(f): Same as (a)-(b), for $J = 0.7\Omega$. In (f), $A_0 = 3.05\Omega$, $\varphi = 2.67$. The Chern number for each band is indicated.

$A_0 = 1.6\Omega$, $\varphi = 2.1$. The difference between the two panels comes from the truncation at the edges – compare panels (b) and (e). Regardless of how we truncate, there is a band that closes the band gap of the bulk structure, due to the non-zero topological invariants. Modes belonging to that band are localized close to the boundaries of the ribbon; the important point, however, is that the modes at k_x and $-k_x$ are localized at opposite edges. This is illustrated in panels (c) and (f), where we plot the position dependence of the magnitude of the eigenvectors of the two states indicated by a blue
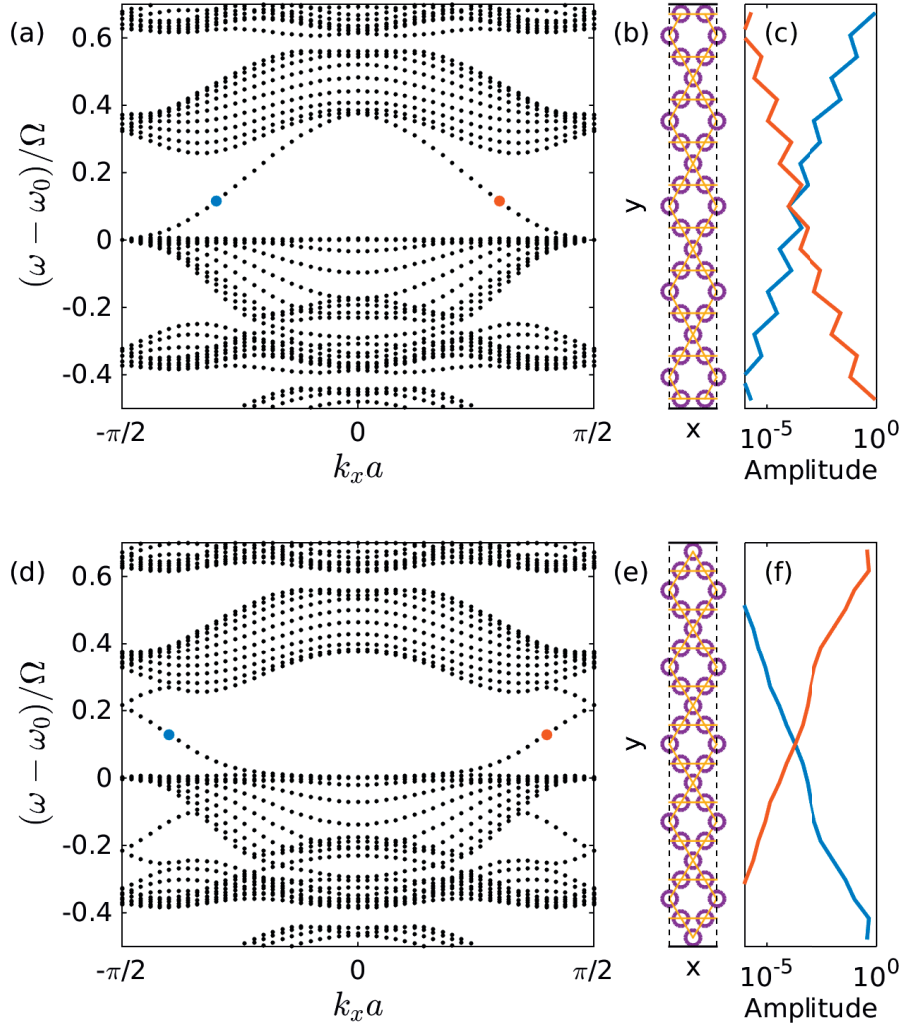
Figure 6.6: (a): Floquet bands for the ribbon geometry shown in (b), with a finite number of sites in one direction (the system is truncated at the solid black lines), and periodic boundary conditions in the other (along the dashed black lines). The parameters are as in Fig. 6.5(d): $J = 0.5\Omega$, $A_0 = 1.6\Omega$, $\phi = 2.1$. (c): The spatial dependence of the eigenstates marked in blue and red, respectively, in panel (a). The y-axis is aligned with the y-axis of panel (b). (d)-(f): Same as (a)-(c), but for a different truncation (compare (b) and (e)).

and a red dot in panels (a) and (d), respectively. The amplitude on the x-axis is the quantity $\sum |v_{m,i}(\mathbf{k}, n)|^2$, where the sum is over all m, and over all sites at the same position along y. The edge modes are exponentially localized at the boundaries (notice the logarithmic scale on the x-axes of panels (c) and (f)), thus the overlap between the forward and backward-propagating modes decreases exponentially with the width of the ribbon in the y-direction. This is only possible due to the broken TRS, and ensures protection against back-scattering in the presence of disorder.

6.3.3 Outlook for a potential realization

Several considerations have to be made for the results presented here to have practical implications. We have not considered the loss rate κ of the optical resonators, which is in practice always non-zero. To be able to meaningfully talk about light transport, this must be smaller than the coupling constant J. In addition, κ must also be smaller than the band gap Δ_T, so that the latter can be resolved. By extension, this also implies $\kappa \ll \Omega$. In state-of-the-art photonic crystal cavities, κ/ω_0 of the order of 10^{-6} can now be routinely achieved [114, 129, 176] at telecommunication frequencies $\omega_0/2\pi \approx 200\mathrm{THz}$, thus $\kappa/2\pi = 0.5\mathrm{GHz}$ is a reasonable and conservative assumption. The coupling constant J is the easiest parameter to control by varying the distance between resonators. Thus the more important challenge is to have a sufficiently high Δ_T. In fact, independently of κ, Δ_T is a general figure of merit for the magnitude of the topological protection that should be maximized.

In Ref. [298], electro-optic modulation was suggested as the practical tool for driving the resonant-frequency oscillation. This offers sufficient control over the phase, and has been shown to be scalable [298, 320]. The maximum achievable modulation frequency $\Omega/2\pi$ is of the order of several GHz. A band-gap Δ_T of the order of $1\mathrm{GHz}$ could thus be achieved, which lies just above the limit set by κ. We note that this challenge holds both for our proposal and for that of Ref. [298]. Very recently [299], it was suggested to use the coupling of the optical resonators to localized phonon modes to induce the frequency modulation. In this scheme, Ω is fixed by the phonon resonant frequency, which can be as high as $\Omega/2\pi = 10\mathrm{GHz}$ in two-dimensional optomechanical crystals [321]. This is sufficiently large for our scheme, and the required phase control can be easily implemented through the phase of the lasers driving the mechanical oscillations [186, 299]. We note that, when compared to Refs. [298] and [299], our proposal has a significant structural advantage, as it involves identical resonators with no intermediate (link) elements. Another recent optomechanical scheme [300] investigated the Kagomé lattice of resonators, focusing on creating and probing topological states for sound (i.e. phonons). Within that proposal, it is also possible to create topological states of light, but the size of the band gap is shown to be proportional to the phonon hopping coefficient. This is typically orders of magnitude smaller than the phonon resonant frequency, and thus also smaller than the best optical loss rate κ that could possibly be achieved in state-of-the-art photonic devices.

While both of the modulation schemes mentioned above could be employed for an experimental realization of our system, a third option is also worth mentioning. Using the optically-induced Kerr nonlinearity, repeated switching at a THz rate has been recently demonstrated in a micropillar cavity [310]. The maximum amplitude in such a scheme is limited to only a fraction of Ω, but assuming $\Omega/2\pi = 1\mathrm{THz}$, $A_0 = 0.05\Omega$ (which can be read out of the sine-like dependence of the cavity resonant frequency measured in Ref. [310]), $J = 0.2\Omega$, and $\varphi = 2.1$, we obtain for our Kagomé lattice a

topological band gap of width 0.033Ω, i.e. $\Delta_T/2\pi = 33\mathrm{GHz}$. This value is very similar to the magnitude of the disorder-induced fluctuations in the resonant frequencies of nominally identical photonic crystal cavities [79, 100], and, furthermore, the latter can in principle be reduced by post-processing techniques [322, 323]. The predicted Δ_T is thus, on one hand, two orders of magnitude larger than the loss rate of state-of-the-art cavities, and on the other high enough to ensure a truly sizable protection against disorder.

Conclusion and Outlook

Photonic crystals are in many ways similar to their electronic counterparts, i.e. materials with a well-defined crystalline lattice and an electron cloud. We have seen throughout this thesis how many of the concepts of solid-state physics are revisited in the PhC domain, but with light as the main actor. In particular, we have discussed in detail the Bloch modes and band structures of various PhCs, as well as the way they are affected by defects. Indeed, it is fair to say that the main object of study of this thesis was defects in a periodic photonic environment. The study of fabrication disorder, i.e. *unintentional* defects in the structure, which was presented in Chapter 3, is just one example. Beyond that, the PhC cavities and waveguides that were omnipresent here must also be recognized as defects breaking the PhC periodicity, the only difference being that they are *introduced on purpose*. Just as with electronic states in a semiconductor, in a band-gap photonic material localized electromagnetic modes are created around the defects. Examples of these are the guided modes of a waveguide as well as the confined cavity modes, but also the Anderson-localized modes in a waveguide with random disorder. Thus, the basic element connecting all the results presented here (with the exception of Chapter 6) is the study of the phenomenology of photonic modes created by defects in a band-gap PhC.

Electronic and photonic crystals are indeed conceptually very similar, but they differ greatly in some aspects. The numerical study of the former is extremely complicated, as it requires solving the many-body Schrödinger equation: a partial differential equation defined on a domain whose dimension grows exponentially with the number of particles included in the computation. This is then impossible to solve exactly, and the development and testing of various numerical methods is central in solid-state physics research. On the other hand, the number of studied materials is fairly limited, as nature provides us with just so many possible compounds, and the chemical composition of a substance defines its underlying crystal lattice – and no (or very limited) further control is possible. The situation is in a way inverted in the photonic case. The fact that light does not interact strongly with itself makes solving the Maxwell equations quite straightforward. Of course, some non-linear behavior can be present – and is in fact often sought after – but this can usually be studied perturbatively and/or iteratively. In any case, exact solutions, which are impossible to obtain for electrons, are com-

monplace in the PhC case. The second difference is that, in the photonic case, given the rate of improvement of our technological abilities, the number of experimentally feasible structures is more limited by imagination than anything else. Better yet, we have the extraordinary possibility to tailor functional elements out of the PhCs, and to control many parameters that influence their performance. All in all, this makes the number of structures with possible importance for applications dazzlingly high. This is a great opportunity, but one that is difficult to explore comprehensively. One could then summarize that the biggest challenge of solid-state physics is correctly predicting the material properties, while the biggest challenge in the study of photonic crystals is exploring the tremendous number of potentially useful structures.

We thus believe that this thesis is a step in the right direction. Slab-PhCs, which were the focus here, are particularly interesting, as they are straightforward to fabricate while still holding enormous potential for applications. Most importantly, we have shown that, through a combination of an insightful choice of a starting system and a global optimization algorithm, a truly significant improvement can be obtained in various devices. This illustrates the need for a continued exploration in that field.

There are a lot of future research perspectives that this work has opened. We enumerate those below, loosely following the structure of the thesis itself. With respect to numerical methods (Chapter 2), we have made the first steps towards implementing a GME solver for the acoustic (phononic) modes of a PhC slab. This is of interest to the emerging field of optomechanics, which has been developing lightning-fast [186, 187], as it will allow the optimization of structures with respect to both their photonic and their phononic properties. Regarding fabrication disorder (Chapter 3), we note that its study has shifted to the background of our attention, and has recently been used only as a means to understand experimental results, rather than being a focus of research in itself. Nevertheless, some open problems that could be explored are worth noting. One example is the effect of irregular holes on PhC cavities, i.e. a combination of Sections 3.1 and 3.2, which is straightforward to make. Other examples include the effect of surface roughness of the slab, as well as of non-vertical holes, and, more fundamentally, a study of Anderson localization of light in *two dimensions*.

The future applications of our optimization procedure (Chapter 4) are multi-fold, and more are expected to come. One example of a currently ongoing project is an experimental characterization of the CCW devices of Section 4.4.2. These have in fact already been fabricated by the group of Prof. Badolato, and preliminary measurements in the group of Prof. Houdré confirm their outstanding properties. Another ongoing project is the fabrication of GaN and AlN H0-type cavities optimized for a high quality factor and far-field emission concentrated close to the vertical direction. The goal is to demonstrate highly efficient second-harmonic generation useful for frequency conversion, with a second-harmonic signal in the visible range. The cavities are very well-suited for that purpose due to their ultra-high Q/V ratio, while the vertical emis-

sion allows for efficient in- and out-coupling of light. A preliminary sample has been fabricated in collaboration with Prof. Houdré and Prof. Grandjean, and its characterization by the group of Prof. Galli in the University of Pavia is pending. Another project where some preliminary theoretical results have already been obtained is the optimization of a device for spontaneous four-wave mixing with high efficiency due to the Q/V enhancement, which in addition filters out the pump wavelength efficiently. With sufficient pump suppression, this can serve as an on-chip, compact, heralded single-photon source for applications in quantum optics and quantum information. We expect finalizing a concrete proposal in the coming months.

The optimization scheme should also be beneficial for the integration of quantum dots in PhCs (Chapter 5). In that direction, we have optimized L3 cavity designs for a GaAs slab, targeting a high Q at two different resonant wavelengths: $980\mathrm{nm}$ and $1180\mathrm{nm}$. The former one is very commonly used when working with InGaAs QDs on a GaAs PhC platform [42–44, 219–225]. However, the Q-values for cavities at this resonant energy are always in the tens of thousands range, and the likely explanation is nonnegligible absorption at the surface of the slab and the holes. This problem is expected to be stronger for light of energy close to that of the GaAs band gap, and can thus be overcome by increasing the operational wavelength, and in fact, QDs emitting at $1200\mathrm{nm}$ or more have already been demonstrated and integrated in PhCs [47, 217, 222]. Preliminary results for the optimized GaAs cavities fabricated in the group of Prof. Badolato have shown a Q-factor close to half a million at $\lambda = 1180\mathrm{nm}$. Integrating QDs in such cavities would constitute a significant improvement in the solid-state cavity-QED domain, as such a system would be deep into the strong-coupling regime. Finally, regarding the topological photonics proposal (Chapter 6), we note that PhCs are once again the most promising platform, as they offer a combination of high Qs, scalability, and control over the inter-cavity couplings. The most challenging part of this proposal is the implementation of the dynamic modulation, which will require a clever setup for which the optimization could prove useful in many ways. Devising a concrete proposal taking all the experimental features and limitations into account is a challenging yet exciting outlook of our work.

Bibliography

[1] S. John, "Strong localization of photons in certain disordered dielectric superlattices," *Phys. Rev. Lett.*, vol. 58, pp. 2486–2489, Jun 1987.

[2] P. W. Anderson, "Absence of diffusion in certain random lattices," *Physical review*, vol. 109, no. 5, p. 1492, 1958.

[3] E. Yablonovitch, "Inhibited spontaneous emission in solid-state physics and electronics," *Phys. Rev. Lett.*, vol. 58, pp. 2059–2062, May 1987.

[4] California Institute of Technology, Minearl Spectroscopy Server (http://minerals.caltech.edu/), May 2015.

[5] J. Zi, X. Yu, Y. Li, X. Hu, C. Xu, X. Wang, X. Liu, and R. Fu, "Coloration strategies in peacock feathers." *Proceedings of the National Academy of Sciences of the United States of America*, vol. 100, no. 22, pp. 12576–12578, 2003.

[6] R. O. Prum, T. Quinn, and R. H. Torres, "Anatomically diverse butterfly scales all produce structural colours by coherent scattering.," *The Journal of experimental biology*, vol. 209, no. Pt 4, pp. 748–765, 2006.

[7] E. Yablonovitch, T. J. Gmitter, and K. M. Leung, "Photonic band structure: The face-centered-cubic case employing nonspherical atoms," *Phys. Rev. Lett.*, vol. 67, pp. 2295–2298, Oct 1991.

[8] H. S. Sözüer and J. W. Haus, "Photonic bands: simple-cubic lattice," *Journal of the Optical Society of America B*, vol. 10, no. 2, pp. 296–302, 1993.

[9] K. Ho, C. Chan, C. Soukoulis, R. Biswas, and M. Sigalas, "Photonic band gaps in three dimensions: New layer-by-layer periodic structures," *Solid State Communications*, vol. 89, no. 5, pp. 413–416, 1994.

[10] K. Sakoda, *Optical Properties of Photonic Crystals.* Springer-Verlag Berlin Heidelberg, 2005.

[11] J. D. Joannopoulos, S. G. Johnson, J. N. Winn, *et al.*, *Photonic Crystals: Molding the Flow of Light.* Princeton University Press, 2008.

Bibliography

[12] C. Kittel, *Introduction to solid state physics.* John Wiley & Sons, Inc., 1971.

[13] N. W. Ashcroft and N. D. Mermin, *Solid state physics.* Saunders College, 1976.

[14] K. M. Ho, C. T. Chan, and C. M. Soukoulis, "Existence of a photonic gap in periodic dielectric structures," *Phys. Rev. Lett.*, vol. 65, pp. 3152–3155, Dec 1990.

[15] I. Tarhan and G. Watson, "Photonic band structure of fcc colloidal crystals.," *Physical review letters*, vol. 76, no. 2, pp. 315–318, 1996.

[16] J. E. Wijnhoven, "Preparation of Photonic Crystals Made of Air Spheres in Titania," *Science*, vol. 281, no. 5378, pp. 802–804, 1998.

[17] K. Busch and S. John, "Photonic band gap formation in certain self-organizing systems," *Physical Review E*, vol. 58, no. 3, pp. 3896–3908, 1998.

[18] Y. a. Vlasov, X. Z. Bo, J. C. Sturm, and D. J. Norris, "On-chip natural assembly of silicon photonic bandgap crystals.," *Nature*, vol. 414, no. 6861, pp. 289–293, 2001.

[19] S. Y. Lin, J. G. Fleming, D. L. Hetherington, B. K. Smith, R. Biswas, K. M. Ho, M. M. Sigalas, W. Zubrzycki, S. R. Kurtz, and J. Bur, "A three-dimensional photonic crystal operating at infrared wavelengths," *Nature*, vol. 394, no. 6690, pp. 251–253, 1998.

[20] J. G. Fleming, S. Y. Lin, I. El-Kady, R. Biswas, and K. M. Ho, "All-metallic three-dimensional photonic crystals with a large infrared bandgap.," *Nature*, vol. 417, no. 6884, pp. 52–55, 2002.

[21] J. Schilling, J. White, a. Scherer, G. Stupian, R. Hillebrand, and U. Gösele, "Three-dimensional macroporous silicon photonic crystal with large photonic band gap," *Applied Physics Letters*, vol. 86, no. 1, pp. 2003–2006, 2005.

[22] S. R. Huisman, R. V. Nair, L. a. Woldering, M. D. Leistikow, A. P. Mosk, and W. L. Vos, "Signature of a three-dimensional photonic band gap observed on silicon inverse woodpile photonic crystals," *Physical Review B - Condensed Matter and Materials Physics*, vol. 83, no. 20, pp. 32–34, 2011.

[23] S. Noda, "Full Three-Dimensional Photonic Bandgap Crystals at Near-Infrared Wavelengths," *Science*, vol. 289, no. 5479, pp. 604–606, 2000.

[24] M. Qi, E. Lidorikis, P. T. Rakich, S. G. Johnson, J. D. Joannopoulos, E. P. Ippen, and H. I. Smith, "A three-dimensional optical photonic crystal with designed point defects.," *Nature*, vol. 429, no. 6991, pp. 538–542, 2004.

[25] L. C. Andreani and D. Gerace, "Photonic-crystal slabs with a triangular lattice of triangular holes investigated using a guied-mode expansion method," *Phys. Rev. B*, vol. 73, p. 235114, 2006.

[26] J. Jackson, *Classical Electrodynamics*. Wiley, 3rd edition, 1998.

[27] G. Bjork and Y. Yamamoto, "Analysis of semiconductor microcavity lasers using rate equations," *Quantum Electronics, IEEE Journal of*, vol. 27, pp. 2386–2396, Nov 1991.

[28] O. Painter, R. K. Lee, A. Scherer, A. Yariv, J. D. O'Brien, P. D. Dapkus, and I. Kim, "Two-dimensional photonic band-gap defect mode laser," *Science*, vol. 284, no. 5421, pp. 1819–1821, 1999.

[29] H.-G. Park, S.-H. Kim, S.-H. Kwon, Y.-G. Ju, J.-K. Yang, J.-H. Baek, S.-B. Kim, and Y.-H. Lee, "Electrically driven single-cell photonic crystal laser," *Science*, vol. 305, no. 5689, pp. 1444–1447, 2004.

[30] S. Matsuo, A. Shinya, T. Kakitsuka, K. Nozaki, T. Segawa, T. Sato, Y. Kawaguchi, and M. Notomi, "High-speed ultracompact buried heterostructure photonic-crystal laser with 13 fj of energy consumed per bit transmitted," *Nat Photon*, vol. 4, pp. 648–654, Sep 2010.

[31] B. Ellis, M. A. Mayer, G. Shambat, T. Sarmiento, J. Harris, E. E. Haller, and J. Vuckovic, "Ultralow-threshold electrically pumped quantum-dot photonic-crystal nanocavity laser," *Nat Photon*, vol. 5, pp. 297–300, May 2011.

[32] Y. Takahashi, Y. Inui, M. Chihara, T. Asano, R. Terawaki, and S. Noda, "A micrometre-scale Raman silicon laser with a microwatt threshold.," *Nature*, vol. 498, pp. 470–4, June 2013.

[33] K. Hirose, Y. Liang, Y. Kurosaka, A. Watanabe, T. Sugiyama, and S. Noda, "Watt-class high-power, high-beam-quality photonic-crystal lasers," *Nat Photon*, vol. 8, pp. 406–411, May 2014. Article.

[34] K. Nozaki, T. Tanabe, A. Shinya, S. Matsuo, T. Sato, H. Taniyama, and M. Notomi, "Sub-femtojoule all-optical switching using a photonic-crystal nanocavity," *Nature Photonics*, vol. 4, pp. 477–483, JUL 2010.

[35] K. Nozaki, A. Shinya, S. Matsuo, Y. Suzaki, T. Segawa, T. Sato, Y. Kawaguchi, R. Takahashi, and M. Notomi, "Ultralow-power all-optical ram based on nanocavities," *Nature Photonics*, vol. 6, pp. 248–252, APR 2012.

[36] E. Kuramochi, K. Nozaki, A. Shinya, K. Takeda, T. Sato, S. Matsuo, H. Taniyama, H. Sumikura, and M. Notomi, "Large-scale integration of wavelength-addressable all-optical memories on a photonic crystal chip," *Nature Photonics*, vol. 8, pp. 2–9, May 2014.

[37] M. Lončar, A. Scherer, and Y. Qiu, "Photonic crystal laser sources for chemical detection," *Applied Physics Letters*, vol. 82, no. 26, pp. 4648–4650, 2003.

[38] I. D. Block, L. Chan, and B. Cunningham, "Photonic crystal optical biosensor incorporating structured low-index porous dielectric," in *Sensors, 2005 IEEE*, pp. 4 pp.–, Oct 2005.

[39] A. Di Falco, L. O'Faolain, and T. F. Krauss, "Chemical sensing in slotted photonic crystal heterostructure cavities," *Applied Physics Letters*, vol. 94, no. 6, pp. –, 2009.

[40] G. Shambat, S.-R. Kothapalli, J. Provine, T. Sarmiento, J. Harris, S. S. Gambhir, and J. Vučković, "Single-cell photonic nanocavity probes," *Nano Letters*, vol. 13, no. 11, pp. 4999–5005, 2013. PMID: 23387382.

[41] D. Englund, A. Faraon, B. Zhang, Y. Yamamoto, and J. Vučković, "Generation and transfer of single photons on a photonic crystal chip," *Opt. Express*, vol. 15, pp. 5550–5558, Apr 2007.

[42] A. Faraon, I. Fushman, D. Englund, N. Stoltz, P. Petroff, and J. Vuckovic, "Coherent generation of non-classical light on a chip via photon-induced tunnelling and blockade," *Nature Physics*, vol. 4, pp. 859–863, NOV 2008.

[43] A. Reinhard, T. Volz, M. Winger, A. Badolato, K. J. Hennessy, E. L. Hu, and A. Imamoglu, "Strongly correlated photons on a chip," *Nature Photonics*, vol. 6, pp. 93–96, FEB 2012.

[44] T. Volz, A. Reinhard, M. Winger, A. Badolato, K. J. Hennessy, E. L. Hu, and A. Imamoglu, "Ultrafast all-optical switching by single photons," *Nature Photonics*, vol. 6, pp. 605–609, SEP 2012.

[45] N. Matsuda, H. Takesue, K. Shimizu, Y. Tokura, and M. Notomi, "Slow light enhanced correlated photon pair generation in photonic-crystal coupled-resonator optical waveguides," vol. 21, no. 7, pp. 8596–8604, 2013.

[46] H. Takesue, N. Matsuda, E. Kuramochi, and M. Notomi, "Entangled photons from on-chip slow light.," *Scientific reports*, vol. 4, p. 3913, Jan. 2014.

[47] T. Yoshie, A. Scherer, J. Hendrickson, G. Khitrova, H. M. Gibbs, G. Rupper, C. Ell, O. B. Shchekin, and D. G. Deppe, "Vacuum rabi splitting with a single quantum dot in a photonic crystal nanocavity," *Nature*, vol. 432, pp. 200–203, Nov. 2004.

[48] A. Badolato, K. Hennessy, M. Atatüre, J. Dreiser, E. Hu, P. M. Petroff, and A. Imamoğlu, "Deterministic coupling of single quantum dots to single nanocavity modes," *Science*, vol. 308, no. 5725, pp. pp. 1158–1161, 2005.

[49] K. Hennessy, A. Badolato, M. Winger, D. Gerace, M. Atatuere, S. Gulde, S. Faelt, E. L. Hu, and A. Imamoglu, "Quantum nature of a strongly coupled single quantum dot-cavity system," *Nature*, vol. 445, pp. 896–899, FEB 22 2007.

[50] A. Imamoglu, D. D. Awschalom, G. Burkard, D. P. DiVincenzo, D. Loss, M. Sherwin, and A. Small, "Quantum information processing using quantum dot spins and cavity qed," *Phys. Rev. Lett.*, vol. 83, pp. 4204–4207, Nov 1999.

[51] T. F. Krauss, "Why do we need slow light?," *Nature Photonics*, vol. 2, no. August, pp. 448–450, 2008.

[52] T. Baba, "Slow light in photonic crystals," *Nature Photonics*, vol. 2, pp. 465–473, Sept. 2008.

[53] B. Corcoran, C. Monat, C. Grillet, D. J. Moss, B. J. Eggleton, T. P. White, L. O'Faolain, and T. F. Krauss, "Green light emission in silicon through slow-light enhanced third-harmonic generation in photonic-crystal waveguides," *Nature Photonics*, vol. 3, no. April, pp. 206–210, 2009.

[54] C. Monat, M. Ebnali-Heidari, C. Grillet, B. Corcoran, B. J. Eggleton, T. P. White, L. O'Faolain, J. Li, and T. F. Krauss, "Four-wave mixing in slow light engineered silicon photonic crystal waveguides.," *Optics express*, vol. 18, no. 22, pp. 22915–22927, 2010.

[55] N. Matsuda, T. Kato, K.-i. Harada, H. Takesue, E. Kuramochi, H. Taniyama, and M. Notomi, "Slow light enhanced optical nonlinearity in a silicon photonic crystal coupled-resonator optical waveguide," *Optics Express*, vol. 19, p. 19861, Oct. 2011.

[56] S. Azzini, D. Grassani, M. J. Strain, M. Sorel, L. G. Helt, J. E. Sipe, M. Liscidini, M. Galli, and D. Bajoni, "Ultra-low power generation of twin photons in a compact silicon ring resonator.," *Optics express*, vol. 20, pp. 23100–7, Oct. 2012.

[57] F. Morichetti, A. Melloni, C. Ferrari, and M. Martinelli, "Error-free continuously-tunable delay at 10 gbit/s in a reconfigurable on-chip delay-line," *Opt. Express*, vol. 16, pp. 8395–8405, Jun 2008.

[58] H. Takesue, N. Matsuda, E. Kuramochi, W. J. Munro, and M. Notomi, "An on-chip coupled resonator optical waveguide single-photon buffer.," *Nature communications*, vol. 4, p. 2725, Jan. 2013.

[59] S. Hughes, "Coupled-cavity qed using planar photonic crystals," *Phys. Rev. Lett.*, vol. 98, p. 083603, Feb 2007.

[60] M. Minkov and V. Savona, "Radiative coupling of quantum dots in photonic crystal structures," *Phys. Rev. B*, vol. 87, p. 125306, Mar 2013.

[61] M. Patterson, S. Hughes, S. Combrié, N. V. Q. Tran, a. De Rossi, R. Gabet, and Y. Jaouën, "Disorder-induced coherent scattering in slow-light photonic crystal waveguides," *Physical Review Letters*, vol. 102, no. 25, pp. 1–4, 2009.

Bibliography

[62] S. Mazoyer, J. P. Hugonin, and P. Lalanne, "Disorder-induced multiple scattering in photonic-crystal waveguides," *Phys. Rev. Lett.*, vol. 103, p. 063903, Aug 2009.

[63] V. Savona, "Electromagnetic modes of a disordered photonic crystal," *Phys. Rev. B*, vol. 83, p. 085301, Feb 2011.

[64] L. Sapienza, H. Thyrrestrup, S. r. Stobbe, P. D. Garcia, S. Smolka, and P. Lodahl, "Cavity quantum electrodynamics with Anderson-localized modes.," *Science (New York, N.Y.)*, vol. 327, pp. 1352–5, Mar. 2010.

[65] J. Gao, S. Combrie, B. Liang, P. Schmitteckert, G. Lehoucq, S. Xavier, X. Xu, K. Busch, D. L. Huffaker, A. De Rossi, and C. W. Wong, "Strongly coupled slow-light polaritons in one-dimensional disordered localized states.," *Scientific reports*, vol. 3, p. 1994, Jan. 2013.

[66] J. Li, T. P. White, L. O'Faolain, A. Gomez-Iglesias, and T. F. Krauss, "Systematic design of flat band slow light in photonic crystal waveguides.," *Optics express*, vol. 16, no. 9, pp. 6227–6232, 2008.

[67] E. M. Purcell, "Spontaneous emission probabilities at radio frequencies," vol. 69, pp. 681+, 1946.

[68] L. C. Andreani, G. Panzarini, and J.-M. Gérard, "Strong-coupling regime for quantum boxes in pillar microcavities: Theory," *Phys. Rev. B*, vol. 60, pp. 13276–13279, Nov 1999.

[69] P. Barclay, K. Srinivasan, and O. Painter, "Nonlinear response of silicon photonic crystal microresonators excited via an integrated waveguide and fiber taper," *Opt. Express*, vol. 13, pp. 801–820, Feb. 2005.

[70] T. Uesugi, B.-S. Song, T. Asano, and S. Noda, "Investigation of optical nonlinearities in an ultra-high-q si nanocavity in a two-dimensional photonic crystal slab," *Opt. Express*, vol. 14, pp. 377–386, Jan. 2006.

[71] A. Taflove, *Computational Electrodynamics: The Finite-Difference Time-Domain Method.* Artech House (third edition), 2005.

[72] Lumerical Solutions, Inc., "FDTD Introduction," *https://kb.lumerical.com/en/index.html.*

[73] A. F. Oskooi, D. Roundy, M. Ibanescu, P. Bermel, J. D. Joannopoulos, and S. G. Johnson, "MEEP: A flexible free-software package for electromagnetic simulations by the FDTD method," *Computer Physics Communications*, vol. 181, pp. 687–702, January 2010.

[74] Lumerical Solutions, Inc., "FDTD Solutions," *http://www.lumerical.com/tcad-products/fdtd/.*

[75] M. Minkov, "Numerical treatment of disorder in phc slabs (arxiv:1508.04630)," Master's thesis, Ecole Polytechnique Federale de Lausanne, 2012.

[76] W. Trench, "An algorithm for the inversion of finite Toeplitz matrices," *J. Soc. Indust. Appl. Math.*, vol. 12, no. 3, 1964.

[77] M. Wax and T. Kailath, "Efficient inversion of Toeplitz-blcok Toeplitz matrix," *Acoustics, Speech and Signal Processing, IEEE Transactions on*, vol. 31, 1983.

[78] M. Minkov and V. Savona, "Automated optimization of photonic crystal slab cavities.," *Scientific reports*, vol. 4, p. 5124, Jan. 2014.

[79] M. Minkov, U. P. Dharanipathy, R. Houdré, and V. Savona, "Statistics of the disorder-induced losses of high-q photonic crystal cavities," *Opt. Express*, vol. 21, pp. 28233–28245, Nov 2013.

[80] V. Savona, "Erratum: Electromagnetic modes of a disordered photonic crystal [phys. rev. b 83, 085301 (2011)]," *Phys. Rev. B*, vol. 86, p. 079907(E), Aug 2012.

[81] M. Minkov and V. Savona, "Effect of hole-shape irregularities on photonic crystal waveguides," *Opt. Lett.*, vol. 37, pp. 3108–3110, Aug 2012.

[82] Y. Akahane, T. Asano, B. Song, and S. Noda, "High-Q photonic nanocavity in a two-dimensional photonic crystal," *Nature*, vol. 425, pp. 944–947, OCT 30 2003.

[83] B. Song, S. Noda, T. Asano, and Y. Akahane, "Ultra-high-Q photonic double-heterostructure nanocavity," *Nature Materials*, vol. 4, pp. 207–210, MAR 2005.

[84] D. Englund, I. Fushman, and J. Vuckovic, "General recipe for designing photonic crystal cavities," *Opt. Express*, vol. 13, pp. 5961–5975, Aug 2005.

[85] E. Kuramochi, M. Notomi, S. Mitsugi, A. Shinya, T. Tanabe, and T. Watanabe, "Ultrahigh-Q photonic crystal nanocavities realized by the local width modulation of a line defect," *Applied Physics Letters*, vol. 88, no. 4, p. 041112, 2006.

[86] T. Tanabe, M. Notomi, E. Kuramochi, A. Shinya, and H. Taniyama, "Trapping and delaying photons for one nanosecond in an ultrasmall high-Q photonic-crystal nanocavity," *Nature Photonics*, vol. 1, no. 1, pp. 49–52, 2007.

[87] Y. Tanaka, T. Asano, and S. Noda, "Design of photonic crystal nanocavity with Q-factor of $\sim 10^9$," *J. Lightwave Technol.*, vol. 26, pp. 1532–1539, Jun 2008.

[88] M. Felici, K. A. Atlasov, A. Surrente, and E. Kapon, "Semianalytical approach to the design of photonic crystal cavities," *Phys. Rev. B*, vol. 82, p. 115118, Sep 2010.

[89] M. Nomura, K. Tanabe, S. Iwamoto, and Y. Arakawa, "High-q design of semiconductor-based ultrasmall photonic crystal nanocavity," *Opt. Express*, vol. 18, pp. 8144–8150, Apr 2010.

[90] G. Khitrova, H. Gibbs, M. Kira, S. Koch, and A. Scherer, "Vacuum rabi splitting in semiconductors," *Nature Physics*, vol. 2, pp. 81–90, FEB 2006.

[91] H. Carmichael, *Statistical Methods in Quantum Optics 2: Non-Classical Fields*. Springer, 2008.

[92] C. Husko, A. D. Rossi, S. Combrie, Q. V. Tran, F. Raineri, and C. W. Wong, "Ultrafast all-optical modulation in GaAs photonic crystal cavities," *Applied Physics Letters*, vol. 94, no. 2, p. 021111, 2009.

[93] Y. Sato, Y. Tanaka, J. Upham, Y. Takahashi, T. Asano, and S. Noda, "Strong coupling between distant photonic nanocavities and its dynamic control," *Nature Photonics*, vol. 6, pp. 56–61, JAN 2012.

[94] Y. Taguchi, Y. Takahashi, Y. Sato, T. Asano, and S. Noda, "Statistical studies of photonic heterostructure nanocavities with an average q factor of three million," *Opt. Express*, vol. 19, pp. 11916–11921, Jun 2011.

[95] S. L. Portalupi, M. Galli, M. Belotti, L. C. Andreani, T. F. Krauss, and L. O'Faolain, "Deliberate versus intrinsic disorder in photonic crystal nanocavities investigated by resonant light scattering," *Phys. Rev. B*, vol. 84, p. 045423, JUL 12 2011.

[96] Y. Tanaka, T. Asano, Y. Akahane, B.-S. Song, and S. Noda, "Theoretical investigation of a two-dimensional photonic crystal slab with truncated cone air holes," *Applied Physics Letters*, vol. 82, no. 11, pp. 1661–1663, 2003.

[97] U. K. Khankhoje, S.-H. Kim, B. C. Richards, J. Hendrickson, J. Sweet, J. D. Olitzky, G. Khitrova, H. M. Gibbs, and A. Scherer, "Modelling and fabrication of gaas photonic-crystal cavities for cavity quantum electrodynamics," *Nanotechnology*, vol. 21, no. 6, p. 065202, 2010.

[98] T. Asano, B.-S. Song, and S. Noda, "Analysis of the experimental Q factors (1 million) of photonic crystal nanocavities," *Opt. Express*, vol. 14, pp. 1996–2002, Mar 2006.

[99] D. Gerace and L. C. Andreani, "Effects of disorder on propagation losses and cavity q-factors in photonic crystal slabs," *Photonics and Nanostructures – Fundamentals and Applications*, vol. 3, pp. 120–128, 2005.

[100] H. Hagino, Y. Takahashi, Y. Tanaka, T. Asano, and S. Noda, "Effects of fluctuation in air hole radii and positions on optical characteristics in photonic crystal heterostructure nanocavities," *Phys. Rev. B*, vol. 79, p. 085112, Feb 2009.

[101] Z. Zhang and M. Qiu, "Small-volume waveguide-section high q microcavities in 2d photonic crystal slabs," *Opt. Express*, vol. 12, pp. 3988–3995, Aug 2004.

[102] H. Takagi, Y. Ota, N. Kumagai, S. Ishida, S. Iwamoto, and Y. Arakawa, "High q h1 photonic crystal nanocavities with efficient vertical emission," *Opt. Express*, vol. 20, pp. 28292–28300, Dec 2012.

[103] N. L. Thomas, Z. Diao, H. Zhang, and R. Houdre, "Statistical analysis of sub-nanometer residual disorder in photonic crystal waveguides: Correlation between slow light properties and structural properties," *J. Vac. Sci. Technol. B*, vol. 29, no. 5, p. 051601, 2011.

[104] K. Welna, S. Portalupi, M. Galli, L. O'Faolain, and T. Krauss, "Novel dispersion-adapted photonic crystal cavity with improved disorder stability," *IEEE Journal of Quantum Electronics*, vol. 48, no. 9, pp. 1177–1183, 2012. cited By (since 1996)5.

[105] K. Hennessy, C. Hogerle, E. Hu, A. Badolato, and A. Imamoglu, "Tuning photonic nanocavities by atomic force microscope nano-oxidation," *Appl. Phys. Lett.*, vol. 89, no. 4, p. 041118, 2006.

[106] D. Dorfner, T. Zabel, T. Hürlimann, N. Hauke, L. Frandsen, U. Rant, G. Abstreiter, and J. Finley, "Photonic crystal nanostructures for optical biosensing applications," *Biosensors and Bioelectronics*, vol. 24, no. 12, pp. 3688 – 3692, 2009.

[107] J. Jágerská, H. Zhang, Z. Diao, N. L. Thomas, and R. Houdré, "Refractive index sensing with an air-slot photonic crystal nanocavity," *Opt. Lett.*, vol. 35, pp. 2523–2525, Aug 2010.

[108] S. Vignolini, F. Riboli, D. S. Wiersma, L. Balet, L. H. Li, M. Francardi, A. Gerardino, A. Fiore, M. Gurioli, and F. Intonti, "Nanofluidic control of coupled photonic crystal resonators," *Applied Physics Letters*, vol. 96, no. 14, p. 141114, 2010.

[109] N. Descharmes, U. P. Dharanipathy, Z. Diao, M. Tonin, and R. Houdré, "Observation of backaction and self-induced trapping in a planar hollow photonic crystal cavity," *Phys. Rev. Lett.*, vol. 110, p. 123601, Mar 2013.

[110] D. Gerace and L. C. Andreani, "Disorder-induced losses in photonic crystal waveguides with line defects.," *Optics Letters*, vol. 29, no. 16, pp. 1897–1899, 2004.

[111] S. Hughes, L. Ramunno, J. F. Young, *et al.*, "Extrinsic optical scattering loss in photonic crystal waveguides: Role of fabrication disorder and photon group velocity," *Phys. Rev. Lett.*, vol. 94, p. 033903, Jan 2005.

[112] M. Skorobogatiy, G. Bégin, and A. Talneau, "Statistical analysis of geometrical imperfections from the images of 2d photonic crystals," *Opt. Express*, vol. 13, pp. 2487–2502, Apr 2005.

[113] J. Topolancik, B. Ilic, and F. Vollmer, "Experimental observation of strong photon localization in disordered photonic crystal waveguides," *Phys. Rev. Lett.*, vol. 99, p. 253901, Dec 2007.

Bibliography

[114] Y. Lai, S. Pirotta, G. Urbinati, D. Gerace, M. Minkov, V. Savona, A. Badolato, and M. Galli, "Genetically designed L3 photonic crystal nanocavities with measured quality factor exceeding one million," *Appl. Phys. Lett.*, vol. 104, p. 241101, June 2014.

[115] U. P. Dharanipathy, M. Minkov, M. Tonin, V. Savona, and R. Houdré, "High-Q silicon photonic crystal cavity for enhanced optical nonlinearities," *Applied Physics Letters*, vol. 105, p. 101101, Sept. 2014.

[116] N. Vico Triviño, M. Minkov, G. Urbinati, M. Galli, J.-F. Carlin, R. Butté, V. Savona, and N. Grandjean, "Gallium nitride L3 photonic crystal cavities with an average quality factor of 16 900 in the near infrared," *Applied Physics Letters*, vol. 105, no. 23, pp. –, 2014.

[117] M. Minkov and V. Savona, "Wide-band slow light in compact photonic crystal coupled-cavity waveguides," *Optica*, vol. 2, pp. 631–634, Jul 2015.

[118] D. Englund, D. Fattal, E. Waks, G. Solomon, B. Zhang, T. Nakaoka, Y. Arakawa, Y. Yamamoto, and J. Vučković, "Controlling the spontaneous emission rate of single quantum dots in a two-dimensional photonic crystal," *Physical Review Letters*, vol. 95, p. 013904, July 2005.

[119] J. Jensen and O. Sigmund, "Topology optimization for nano-photonics," *Laser & Photonics Reviews*, vol. 5, no. 2, p. 308–321, 2011.

[120] W. R. Frei, H. T. Johnson, and K. D. Choquette, "Optimization of a single defect photonic crystal laser cavity," *Journal of Applied Physics*, vol. 103, no. 3, pp. –, 2008.

[121] X. Liang and S. G. Johnson, "Formulation for scalable optimization of microcavities via the frequency-averaged local density of states," *Optics Express*, vol. 21, p. 30812, Dec. 2013.

[122] D. Wang, Z. Yu, Y. Liu, X. Guo, C. Shu, S. Zhou, and J. Zhang, "Ultrasmall modal volume and high q factor optimization of a photonic crystal slab cavity," *Journal of Optics*, vol. 15, p. 125102, Dec. 2013.

[123] Y. Akahane, T. Asano, B.-S. Song, and S. Noda, "Fine-tuned high-q photonic-crystal nanocavity," *Opt. Express*, vol. 13, pp. 1202–1214, Feb. 2005.

[124] T. W. Saucer and V. Sih, "Optimizing nanophotonic cavity designs with the gravitational search algorithm," *Optics Express*, vol. 21, pp. 20831–20836, Sept. 2013.

[125] O. Painter, J. Vučkovič, and A. Scherer, "Defect modes of a two-dimensional photonic crystal in an optically thin dielectric slab," *J. Opt. Soc. Am. B*, vol. 16, pp. 275–285, Feb 1999.

[126] T. Tanabe, A. Shinya, E. Kuramochi, S. Kondo, H. Taniyama, and M. Notomi, "Single point defect photonic crystal nanocavity with ultrahigh quality factor achieved by using hexapole mode," *Applied Physics Letters*, vol. 91, no. 2, p. 021110, 2007.

[127] M. Notomi, "Manipulating light with strongly modulated photonic crystals," *Reports on Progress in Physics*, vol. 73, no. 9, p. 096501, 2010.

[128] Z. Han, X. Checoury, D. Néel, S. David, M. El Kurdi, and P. Boucaud, "Optimized design for 2x106 ultra-high q silicon photonic crystal cavities," *Optics Communications*, vol. 283, pp. 4387–4391, Nov. 2010.

[129] H. Sekoguchi, Y. Takahashi, T. Asano, and S. Noda, "Photonic crystal nanocavity with a q-factor of ~9 million," *Opt. Express*, vol. 22, pp. 916–924, Jan. 2014.

[130] "MATLAB and Global Optimization Toolbox Release 2012b, The MathWorks, Inc., Natick, Massachusetts, United States.."

[131] J. Vuckovic, M. Loncar, H. Mabuchi, and A. Scherer, "Optimization of the q factor in photonic crystal microcavities," *Quantum Electronics, IEEE Journal of*, vol. 38, pp. 850–856, Jul 2002.

[132] M. Larque, T. Karle, I. Robert-Philip, and A. Beveratos, "Optimizing h1 cavities for the generation of entangled photon pairs," *New Journal of Physics*, vol. 11, p. 033022, 2009.

[133] R. J. Coles, N. Prtljaga, B. Royall, I. J. Luxmoore, A. M. Fox, and M. S. Skolnick, "Waveguide-coupled photonic crystal cavity for quantum dot spin readout," *arXiv:1310.7848 [physics]*, Oct. 2013.

[134] I. J. Luxmoore, E. D. Ahmadi, A. M. Fox, M. Hugues, and M. S. Skolnick, "Unpolarized h1 photonic crystal nanocavities fabricated by stretched lattice design," *Applied Physics Letters*, vol. 98, no. 4, pp. –, 2011.

[135] S. L. Portalupi, M. Galli, C. Reardon, T. Krauss, L. O'Faolain, L. C. Andreani, and D. Gerace, "Planar photonic crystal cavities with far-field optimization for high coupling efficiency and quality factor," *Opt. Express*, vol. 18, pp. 16064–16073, Jul 2010.

[136] J. Hagemeier, C. Bonato, T.-A. Truong, H. Kim, G. J. Beirne, M. Bakker, M. P. van Exter, Y. Luo, P. Petroff, and D. Bouwmeester, "H1 photonic crystal cavities for hybrid quantum information protocols," *Opt. Express*, vol. 20, pp. 24714–24726, Oct. 2012.

[137] E. Iwase, P.-C. Hui, D. Woolf, A. W. Rodriguez, S. G. Johnson, F. Capasso, and M. Lončar, "Control of buckling in large micromembranes using engineered support structures," *Journal of Micromechanics and Microengineering*, vol. 22, no. 6, p. 065028, 2012.

Bibliography

[138] M. Galli, S. L. Portalupi, M. Belotti, L. C. Andreani, L. O'Faolain, and T. F. Krauss, "Light scattering and fano resonances in high-q photonic crystal nanocavities," *Applied Physics Letters*, vol. 94, no. 7, pp. –, 2009.

[139] M. Burresi, T. Kampfrath, D. van Oosten, J. C. Prangsma, B. S. Song, S. Noda, and L. Kuipers, "Magnetic light-matter interactions in a photonic crystal nanocavity," *Phys. Rev. Lett.*, vol. 105, p. 123901, Sep 2010.

[140] P. B. Deotare, M. W. McCutcheon, I. W. Frank, M. Khan, and M. Lončar, "High quality factor photonic crystal nanobeam cavities," *Applied Physics Letters*, vol. 94, pp. 121106–121106–3, Mar. 2009.

[141] Y. Takahashi, Y. Tanaka, H. Hagino, T. Asano, and S. Noda, "Higher-order resonant modes in a photonic heterostructure nanocavity," *Applied Physics Letters*, vol. 92, pp. 241910–241910–3, June 2008.

[142] M. Notomi, A. Shinya, S. Mitsugi, G. Kira, E. Kuramochi, and T. Tanabe, "Optical bistable switching action of si high-q photonic-crystal nanocavities," *Opt. Express*, vol. 13, pp. 2678–2687, Apr. 2005.

[143] Y. Zhang, D. Li, C. Zeng, Y. Shi, Z. Huang, J. Yu, and J. Xia, "Ultralow power nonlinear response in an si photonic crystal nanocavity," *IEEE Photonics Journal*, vol. 5, no. 4, pp. 6601409–6601409, 2013.

[144] T. Li, M. Mastro, and A. Dadgar, *III-V Compound Semiconductors: Integration with Silicon-Based Microelectronics*. CRC Press, Dec. 2010.

[145] G. Roelkens, L. Liu, D. Liang, R. Jones, A. Fang, B. Koch, and J. Bowers, "III-v/silicon photonics for on-chip and intra-chip optical interconnects," *Laser Photon. Rev.*, vol. 4, pp. 751–779, Nov. 2010.

[146] P. M. Lundquist, W. P. Lin, Z. Y. Xu, G. K. Wong, E. D. Rippert, J. A. Helfrich, and J. B. Ketterson, "Ultraviolet second harmonic generation in radio-frequency sputter-deposited aluminum nitride thin films," *Appl. Phys. Lett.*, vol. 65, pp. 1085–1087, Aug. 1994.

[147] G. Vecchi, J. Torres, D. Coquillat, M. L. V. d'Yerville, and A. M. Malvezzi, "Enhancement of visible second-harmonic generation in epitaxial GaN-based two-dimensional photonic crystal structures," *Appl. Phys. Lett.*, vol. 84, pp. 1245–1247, Feb. 2004.

[148] C. Xiong, W. Pernice, K. K. Ryu, C. Schuck, K. Y. Fong, T. Palacios, and H. X. Tang, "Integrated GaN photonic circuits on silicon (100) for second harmonic generation," *Opt. Express*, vol. 19, p. 10462–10470, May 2011.

[149] C. Xiong, W. H. P. Pernice, X. Sun, C. Schuck, K. Y. Fong, and H. X. Tang, "Aluminum nitride as a new material for chip-scale optomechanics and nonlinear optics," *New J. Phys.*, vol. 14, p. 095014, Sept. 2012.

[150] C. Xiong, W. H. P. Pernice, and H. X. Tang, "Low-loss, silicon integrated, aluminum nitride photonic circuits and their use for electro-optic signal processing," *Nano Lett.*, vol. 12, pp. 3562–3568, July 2012.

[151] M. Stegmaier, J. Ebert, J. M. Meckbach, K. Ilin, M. Siegel, and W. H. P. Pernice, "Aluminum nitride nanophotonic circuits operating at ultraviolet wavelengths," *Appl. Phys. Lett.*, vol. 104, p. 091108, Mar. 2014.

[152] M. Stutzmann, J. A. Garrido, M. Eickhoff, and M. S. Brandt, "Direct biofunctionalization of semiconductors: A survey," *Phys. Status Solidi A*, vol. 203, pp. 3424–3437, Nov. 2006.

[153] S. Sergent, M. Arita, S. Kako, K. Tanabe, S. Iwamoto, and Y. Arakawa, "High-q AlN photonic crystal nanobeam cavities fabricated by layer transfer," *Appl. Phys. Lett.*, vol. 101, p. 101106, Sept. 2012.

[154] N. Vico Triviño, G. Rossbach, U. Dharanipathy, J. Levrat, A. Castiglia, J.-F. Carlin, K. A. Atlasov, R. Butté, R. Houdré, and N. Grandjean, "High quality factor two dimensional GaN photonic crystal cavity membranes grown on silicon substrate," *Appl. Phys. Lett.*, vol. 100, p. 071103, Feb. 2012.

[155] D. Sam-Giao, D. Néel, S. Sergent, B. Gayral, M. J. Rashid, F. Semond, J. Y. Duboz, M. Mexis, T. Guillet, C. Brimont, S. David, X. Checoury, and P. Boucaud, "High quality factor AlN nanocavities embedded in a photonic crystal waveguide," *Appl. Phys. Lett.*, vol. 100, p. 191104, May 2012.

[156] M. Arita, S. Kako, S. Iwamoto, and Y. Arakawa, "Fabrication of AlGaN two-dimensional photonic crystal nanocavities by selective thermal decomposition of GaN," *Appl. Phys. Express*, vol. 5, p. 126502, Dec. 2012.

[157] N. Vico Triviño, U. Dharanipathy, J.-F. Carlin, Z. Diao, R. Houdré, and N. Grandjean, "Integrated photonics on silicon with wide bandgap GaN semiconductor," *Applied Physics Letters*, vol. 102, no. 8, p. 081120, 2013.

[158] I. Roland, Y. Zeng, Z. Han, X. Checoury, C. Blin, M. El Kurdi, A. Ghrib, S. Sauvage, B. Gayral, C. Brimont, T. Guillet, F. Semond, and P. Boucaud, "Near-infrared gallium nitride two-dimensional photonic crystal platform on silicon," *Appl. Phys. Lett.*, vol. 105, p. 011104, July 2014.

[159] W. H. P. Pernice, C. Xiong, C. Schuck, and H. X. Tang, "High-q aluminum nitride photonic crystal nanobeam cavities," *Appl. Phys. Lett.*, vol. 100, p. 091105, Feb. 2012.

[160] N. Antoine-Vincent, F. Natali, M. Mihailovic, A. Vasson, J. Leymarie, P. Disseix, D. Byrne, F. Semond, and J. Massies, "Determination of the refractive indices of AlN, GaN, and AlxGa1-xN grown on (111)si substrates," *J. Appl. Phys.*, vol. 93, pp. 5222–5226, May 2003.

Bibliography

[161] M. Arita, S. Ishida, S. Kako, S. Iwamoto, and Y. Arakawa, "AlN air-bridge photonic crystal nanocavities demonstrating high quality factor," *Appl. Phys. Lett.*, vol. 91, no. 5, p. 051106, 2007.

[162] K. K. Mehta, J. S. Orcutt, O. Tehar-Zahav, Z. Sternberg, R. Bafrali, R. Meade, and R. J. Ram, "High-Q CMOS-integrated photonic crystal microcavity devices," *Scientific Reports*, vol. 4, pp. 1–6, 2014.

[163] Y. Ooka, T. Tetsumoto, A. Fushimi, W. Yoshiki, and T. Tanabe, "CMOS compatible high-Q photonic crystal nanocavity fabricated with photolithography on silicon photonic platform," *Scientific Reports*, vol. 5, no. February, p. 11312, 2015.

[164] M. Settle, M. Salib, A. Michaeli, and T. F. Krauss, "Low loss silicon on insulator photonic crystal waveguides made by 193nm optical lithography.," *Optics express*, vol. 14, no. 6, pp. 2440–2445, 2006.

[165] L.-D. Haret, T. Tanabe, E. Kuramochi, and M. Notomi, "Extremely low power optical bistability in silicon demonstrated using 1D photonic crystal nanocavity.," *Optics express*, vol. 17, no. 23, pp. 21108–21117, 2009.

[166] M. Shinkawa, N. Ishikura, Y. Hama, K. Suzuki, and T. Baba, "Nonlinear enhancement in photonic crystal slow light waveguides fabricated using CMOS-compatible process," *Optics Express*, vol. 19, no. 22, p. 22208, 2011.

[167] A. Ashkin, "History of optical trapping and manipulation of small-neutral particle, atoms, and molecules," *Selected Topics in Quantum Electronics, IEEE Journal of*, vol. 6, pp. 841–856, Nov 2000.

[168] K. C. Neuman and S. M. Block, "Optical trapping," *Rev Sci Instrum*, vol. 75, pp. 2787–2809, Sep 2004. 16878180[pmid].

[169] L. Neumeier, R. Quidant, and D. E. Chang, "Theory of self-induced back-action optical trapping in nanophotonic systems," 2015.

[170] C. D. Chin, V. Linder, and S. K. Sia, "Lab-on-a-chip devices for global health: Past studies and future opportunities," *Lab Chip*, vol. 7, no. 1, pp. 41–57, 2007.

[171] B. Troia, A. Paolicelli, F. D. Leonardis, and V. M. N. Passaro, "Photonic Crystals for Optical Sensing : A Review," *Advances in Photonic Crystals*, pp. 241–295, 2013.

[172] U. P. Dharanipathy, *On the Investigation of Light-Matter Interactions in Slab Photonic Crystal Cavities.* PhD thesis, Ecole Polytechnique Federale de Lausanne (EPFL), 2014.

[173] S. Vignolini, F. Riboli, F. Intonti, M. Belotti, M. Gurioli, Y. Chen, M. Colocci, L. Andreani, and D. Wiersma, "Local nanofluidic light sources in silicon photonic crystal microcavities," *Physical Review E*, vol. 78, no. 4, p. 045603, 2008.

[174] Y. a. Vlasov, M. O'Boyle, H. F. Hamann, and S. J. McNab, "Active control of slow light on a chip with photonic crystal waveguides.," *Nature*, vol. 438, no. November, pp. 65–69, 2005.

[175] D. O'Brien, M. D. Settle, T. Karle, a. Michaeli, M. Salib, and T. F. Krauss, "Coupled photonic crystal heterostructure nanocavities.," *Optics express*, vol. 15, no. 3, pp. 1228–1233, 2007.

[176] M. Notomi, E. Kuramochi, and T. Tanabe, "Large-scale arrays of ultrahigh-Q coupled nanocavities," *Nature Photonics*, vol. 2, pp. 741–747, 2008.

[177] J. Jágerská, N. Le Thomas, V. Zabelin, R. Houdré, W. Bogaerts, P. Dumon, R. Baets, J. JÃ¡gersk A¡, R. HoudrÃ©, and J. Jagerska, "Experimental observation of slow mode dispersion in photonic crystal coupled-cavity waveguides," *Opt. Lett.*, vol. 34, pp. 359–361, Feb. 2009.

[178] J. Jágerská, H. Zhang, N. Le Thomas, and R. Houdŕ, "Radiation loss of photonic crystal coupled-cavity waveguides," *Applied Physics Letters*, vol. 95, no. 11, pp. 2007–2010, 2009.

[179] E. Kuramochi, M. Notomi, S. Hughes, a. Shinya, T. Watanabe, and L. Ramunno, "Disorder-induced scattering loss of line-defect waveguides in photonic crystal slabs," *Physical Review B - Condensed Matter and Materials Physics*, vol. 72, no. 16, pp. 2–5, 2005.

[180] S. a. Schulz, L. O'Faolain, D. M. Beggs, T. P. White, a. Melloni, and T. F. Krauss, "Dispersion engineered slow light in photonic crystals: a comparison," *Journal of Optics*, vol. 12, p. 104004, 2010.

[181] S. Haddadi, P. Hamel, G. Beaudoin, I. Sagnes, C. Sauvan, P. Lalanne, J. a. Levenson, and a. M. Yacomotti, "Photonic molecules: tailoring the coupling strength and sign," *Optics Express*, vol. 22, no. 10, p. 12359, 2014.

[182] F. Wang, J. S. n. Jensen, J. Mø rk, and O. Sigmund, "Systematic design of loss-engineered slow-light waveguides.," *Journal of the Optical Society of America. A, Optics, image science, and vision*, vol. 29, no. 12, pp. 2657–66, 2012.

[183] D. Mori and T. Baba, "Wideband and low dispersion slow light by chirped photonic crystal coupled waveguide.," *Optics express*, vol. 13, no. 23, pp. 9398–9408, 2005.

[184] M. Galli, D. Gerace, K. Welna, T. F. Krauss, L. O'Faolain, G. Guizzetti, and L. C. Andreani, "Low-power continuous-wave generation of visible harmonics in silicon photonic crystal nanocavities.," *Optics express*, vol. 18, pp. 26613–24, Dec. 2010.

Bibliography

[185] M. Minkov and V. Savona, "Optimizing doubly resonant photonic crystal cavity modes for second harmonic generation," 2014.

[186] M. Aspelmeyer, T. J. Kippenberg, and F. Marquardt, "Cavity optomechanics," *Rev. Mod. Phys.*, vol. 86, pp. 1391–1452, Dec 2014.

[187] M. Metcalfe, "Applications of cavity optomechanics," *Applied Physics Reviews*, vol. 1, no. 3, pp. –, 2014.

[188] M. Minkov and V. Savona, "Long-distance radiative excitation transfer between quantum dots in disordered photonic crystal waveguides," *Physical Review B*, vol. 88, no. 8, p. 081303, 2013.

[189] J. J. Hopfield, "Theory of the contribution of excitons to the complex dielectric constant of crystals," *Phys. Rev.*, vol. 112, pp. 1555–1567, Dec 1958.

[190] F. Tassone, F. Bassani, and L. C. Andreani, "Quantum-well reflectivity and exciton-polariton dispersion," *Phys. Rev. B*, vol. 45, pp. 6023–6030, Mar 1992.

[191] G. Parascandolo and V. Savona, "Long-range radiative interaction between semi-conductor quantum dots," *Phys. Rev. B*, vol. 71, p. 045335, JAN 2005.

[192] G. Tarel, G. Parascandolo, and V. Savona, "Ultralong-range radiative excitation transfer between quantum dots in a planar microcavity," *phys. stat. sol. (b)*, vol. 245, no. 6, pp. 1085–1088, 2008.

[193] M. A. Nielsen and I. L. Chuang, *Quantum Computation and Quantum Information (Cambridge Series on Information and the Natural Sciences)*. Cambridge University Press, 1 ed., Jan. 2004.

[194] L. DiCarlo, J. M. Chow, J. M. Gambetta, L. S. Bishop, B. R. Johnson, D. I. Schuster, J. Majer, A. Blais, L. Frunzio, S. M. Girvin, and R. J. Schoelkopf, "Demonstration of two-qubit algorithms with a superconducting quantum processor," *Nature*, vol. 460, pp. 240–244, July 2009.

[195] M. Riebe, H. Haffner, C. F. Roos, W. Hansel, J. Benhelm, G. P. T. Lancaster, T. W. Korber, C. Becher, F. Schmidt-Kaler, D. F. V. James, and R. Blatt, "Deterministic quantum teleportation with atoms," *Nature*, vol. 429, pp. 734–737, June 2004.

[196] I. van Weperen, B. D. Armstrong, E. A. Laird, J. Medford, C. M. Marcus, M. P. Hanson, and A. C. Gossard, "Charge-state conditional operation of a spin qubit," *Phys. Rev. Lett.*, vol. 107, p. 030506, Jul 2011.

[197] H. J. Kimble, "The quantum internet," *Nature*, vol. 453, pp. 1023–1030, June 2008.

[198] J. I. Cirac and P. Zoller, "Quantum computations with cold trapped ions," *Phys. Rev. Lett.*, vol. 74, pp. 4091–4094, May 1995.

[199] M. A. Sillanpaeae, J. I. Park, and R. W. Simmonds, "Coherent quantum state storage and transfer between two phase qubits via a resonant cavity," *Nature*, vol. 449, pp. 438–442, SEP 27 2007.

[200] J. Majer, J. M. Chow, J. M. Gambetta, J. Koch, B. R. Johnson, J. A. Schreier, L. Frunzio, D. I. Schuster, A. A. Houck, A. Wallraff, A. Blais, M. H. Devoret, S. M. Girvin, and R. J. Schoelkopf, "Coupling superconducting qubits via a cavity bus," *Nature*, vol. 449, pp. 443–447, SEP 27 2007.

[201] D. Loss and D. P. DiVincenzo, "Quantum computation with quantum dots," *Phys. Rev. A*, vol. 57, pp. 120–126, Jan 1998.

[202] B. Patton, U. Woggon, and W. Langbein, "Coherent control and polarization readout of individual excitonic states," *Phys. Rev. Lett.*, vol. 95, p. 266401, Dec 2005.

[203] D. Press, T. D. Ladd, B. Zhang, and Y. Yamamoto, "Complete quantum control of a single quantum dot spin using ultrafast optical pulses," *Nature*, vol. 456, pp. 218–221, NOV 13 2008.

[204] J. Berezovsky, M. H. Mikkelsen, N. G. Stoltz, L. A. Coldren, and D. D. Awschalom, "Picosecond coherent optical manipulation of a single electron spin in a quantum dot," *SCIENCE*, vol. 320, pp. 349–352, APR 18 2008.

[205] A. Greilich, S. E. Economou, S. Spatzek, D. R. Yakovlev, D. Reuter, A. D. Wieck, T. L. Reinecke, and M. Bayer, "Ultrafast optical rotations of electron spins in quantum dots," *Nature Physics*, vol. 5, pp. 262–266, APR 2009.

[206] A. Greilich, S. G. Carter, D. Kim, A. S. Bracker, and D. Gammon, "Optical control of one and two hole spins in interacting quantum dots," *Nature Photonics*, vol. 5, pp. 703–709, NOV 2011.

[207] E. Poem, O. Kenneth, Y. Kodriano, Y. Benny, S. Khatsevich, J. E. Avron, and D. Gershoni, "Optically induced rotation of an exciton spin in a semiconductor quantum dot," *Phys. Rev. Lett.*, vol. 107, p. 087401, Aug 2011.

[208] K. Müller, A. Bechtold, C. Ruppert, C. Hautmann, J. S. Wildmann, T. Kaldewey, M. Bichler, H. J. Krenner, G. Abstreiter, M. Betz, and J. J. Finley, "High-fidelity optical preparation and coherent larmor precession of a single hole in an (in,ga)as quantum dot molecule," *Phys. Rev. B*, vol. 85, p. 241306, Jun 2012.

[209] T. M. Godden, J. H. Quilter, A. J. Ramsay, Y. Wu, P. Brereton, S. J. Boyle, I. J. Luxmoore, J. Puebla-Nunez, A. M. Fox, and M. S. Skolnick, "Coherent optical control of the spin of a single hole in an $\mathrm{InAs/GaAs}$ quantum dot," *Phys. Rev. Lett.*, vol. 108, p. 017402, Jan 2012.

[210] Y. Kodriano, I. Schwartz, E. Poem, Y. Benny, R. Presman, T. A. Truong, P. M. Petroff, and D. Gershoni, "Complete control of a matter qubit using a single picosecond laser pulse," *Phys. Rev. B*, vol. 85, p. 241304, Jun 2012.

[211] W. B. Gao, a. Imamoglu, H. Bernien, and R. Hanson, "Coherent manipulation, measurement and entanglement of individual solid-state spins using optical fields," *Nature Photonics*, vol. 9, no. 6, pp. 363–373, 2015.

[212] J. M. Gerard, B. Sermage, B. Gayral, B. Legrand, E. Costard, and V. Thierry-Mieg, "Enhanced spontaneous emission by quantum boxes in a monolithic optical microcavity," *Physical Review Letter*, vol. 81, pp. 1110–1113, AUG 3 1998.

[213] G. S. Solomon, M. Pelton, and Y. Yamamoto, "Single-mode spontaneous emission from a single quantum dot in a three-dimensional microcavity," *Phys. Rev. Lett.*, vol. 86, pp. 3903–3906, Apr 2001.

[214] T. D. Happ, I. I. Tartakovskii, V. D. Kulakovskii, J.-P. Reithmaier, M. Kamp, and A. Forchel, "Enhanced light emission of $in_x ga_{1-x}As$ quantum dots in a two-dimensional photonic-crystal defect microcavity," *Phys. Rev. B*, vol. 66, p. 041303, Jul 2002.

[215] G. Ramon, U. Mizrahi, N. Akopian, S. Braitbart, D. Gershoni, T. L. Reinecke, B. D. Gerardot, and P. M. Petroff, "Emission characteristics of quantum dots in planar microcavities," *Phys. Rev. B*, vol. 73, p. 205330, May 2006.

[216] M. Munsch, A. Mosset, A. Auffeves, S. Seidelin, J. P. Poizat, J. M. Gerard, A. Lemaitre, I. Sagnes, and P. Senellart, "Continuous-wave versus time-resolved measurements of purcell factors for quantum dots in semiconductor microcavities," *Physical Review B*, vol. 80, p. 115312, SEP 2009.

[217] M. Petruzzella, T. Xia, F. Pagliano, S. Birindelli, L. Midolo, Z. Zobenica, L. H. Li, E. H. Linfield, and A. Fiore, "Fully tuneable, purcell-enhanced solid-state quantum emitters," *Applied Physics Letters*, vol. 107, no. 14, pp. –, 2015.

[218] E. Viasnoff-Schwoob, C. Weisbuch, H. Benisty, S. Olivier, S. Varoutsis, I. Robert-Philip, R. Houdré, and C. J. M. Smith, "Spontaneous emission enhancement of quantum dots in a photonic crystal wire," *Phys. Rev. Lett.*, vol. 95, p. 183901, Oct 2005.

[219] T. Lund-Hansen, S. Stobbe, B. Julsgaard, H. Thyrrestrup, T. Sünner, M. Kamp, A. Forchel, and P. Lodahl, "Experimental realization of highly efficient broadband coupling of single quantum dots to a photonic crystal waveguide," *Phys. Rev. Lett.*, vol. 101, p. 113903, Sep 2008.

[220] H. Thyrrestrup, L. Sapienza, and P. Lodahl, "Extraction of the beta-factor for single quantum dots coupled to a photonic crystal waveguide," *Applied Physics Letters*, vol. 96, no. 23, p. 231106, 2010.

[221] A. Schwagmann, S. Kalliakos, I. Farrer, J. P. Griffiths, G. A. C. Jones, D. A. Ritchie, and A. J. Shields, "On-chip single photon emission from an integrated semiconductor quantum dot into a photonic crystal waveguide," *Applied Physics Letters*, vol. 99, no. 26, p. 261108, 2011.

[222] T. B. Hoang, J. Beetz, L. Midolo, M. Skacel, M. Lermer, M. Kamp, S. Hofling, L. Balet, N. Chauvin, and A. Fiore, "Enhanced spontaneous emission from quantum dots in short photonic crystal waveguides," *Applied Physics Letters*, vol. 100, no. 6, p. 061122, 2012.

[223] A. Laucht, T. Gunthner, S. Putz, R. Saive, S. Frederick, N. Hauke, M. Bichler, M.-C. Amann, A. W. Holleitner, M. Kaniber, and J. J. Finley, "Broadband purcell enhanced emission dynamics of quantum dots in linear photonic crystal waveguides," *Journal of Applied Physics*, vol. 112, no. 9, p. 093520, 2012.

[224] A. Laucht, S. Pütz, T. Günthner, N. Hauke, R. Saive, S. Frédérick, M. Bichler, M.-C. Amann, A. W. Holleitner, M. Kaniber, and J. J. Finley, "A waveguide-coupled on-chip single-photon source," *Phys. Rev. X*, vol. 2, p. 011014, Mar 2012.

[225] M. Arcari, I. Söllner, A. Javadi, S. L. Hansen, S. Mahmoodian, J. Liu, H. Thyrrestrup, E. H. Lee, J. D. Song, S. Stobbe, and P. Lodahl, "Near-Unity Coupling Efficiency of a Quantum Emitter to a Photonic Crystal Waveguide," vol. 093603, no. August, pp. 1–5, 2014.

[226] J. P. Reithmaier, G. Sek, A. Loffler, C. Hofmann, S. Kuhn, S. Reitzenstein, L. V. Keldysh, V. D. Kulakovskii, T. L. Reinecke, and A. Forchel, "Strong coupling in a single quantum dot–semiconductor microcavity system," *Nature*, vol. 432, pp. 197–200, Nov. 2004.

[227] E. Peter, P. Senellart, D. Martrou, A. Lemaître, J. Hours, J. M. Gérard, and J. Bloch, "Exciton-photon strong-coupling regime for a single quantum dot embedded in a microcavity," *Phys. Rev. Lett.*, vol. 95, p. 067401, Aug 2005.

[228] J. Kasprzak, S. Reitzenstein, E. A. Muljarov, C. Kistner, C. Schneider, M. Strauss, S. Hoefling, A. Forchel, and W. Langbein, "Up on the jaynes-cummings ladder of a quantum-dot/microcavity system," *Nature Materials*, vol. 9, pp. 304–308, APR 2010.

[229] A. Dousse, J. Suffczynski, A. Beveratos, O. Krebs, A. Lemaitre, I. Sagnes, J. Bloch, P. Voisin, and P. Senellart, "Ultrabright source of entangled photon pairs," *Nature*, vol. 466, pp. 217–220, JUL 8 2010.

[230] M. Bayer, P. Hawrylak, K. Hinzer, S. Fafard, M. Korkusinski, Z. Wasilewski, O. Stern, and A. Forchel, "Coupling and entangling of quantum states in quantum dot molecules," *Science*, vol. 291, pp. 451–453, JAN 19 2001.

[231] P. Borri, W. Langbein, U. Woggon, M. Schwab, M. Bayer, S. Fafard, Z. Wasilewski, and P. Hawrylak, "Exciton dephasing in quantum dot molecules," *Phys. Rev. Lett.*, vol. 91, p. 267401, Dec 2003.

[232] B. D. Gerardot, S. Strauf, M. J. A. de Dood, A. M. Bychkov, A. Badolato, K. Hennessy, E. L. Hu, D. Bouwmeester, and P. M. Petroff, "Photon statistics from coupled quantum dots," *Phys. Rev. Lett.*, vol. 95, p. 137403, Sep 2005.

[233] H. J. Krenner, M. Sabathil, E. C. Clark, A. Kress, D. Schuh, M. Bichler, G. Abstreiter, and J. J. Finley, "Direct observation of controlled coupling in an individual quantum dot molecule," *Phys. Rev. Lett.*, vol. 94, p. 057402, Feb 2005.

[234] E. Stinaff, M. Scheibner, A. Bracker, I. Ponomarev, V. Korenev, M. Ware, M. Doty, T. Reinecke, and D. Gammon, "Optical signatures of coupled quantum dots," *Science*, vol. 311, pp. 636–639, FEB 3 2006.

[235] L. Robledo, J. Elzerman, G. Jundt, M. Atatüre, A. Högele, S. Fält, and A. Imamoglu, "Conditional dynamics of interacting quantum dots," *Science*, vol. 320, no. 5877, pp. 772–775, 2008.

[236] A. O. Govorov, "Spin and energy transfer in nanocrystals without tunneling," *Phys. Rev. B*, vol. 68, p. 075315, Aug 2003.

[237] A. O. Govorov, "Spin-förster transfer in optically excited quantum dots," *Phys. Rev. B*, vol. 71, p. 155323, Apr 2005.

[238] M. Scheibner, T. Schmidt, L. Worschech, A. Forchel, G. Bacher, T. Passow, and D. Hommel, "Superradiance of quantum dots," *Nature Physics*, vol. 3, pp. 106–110, FEB 2007.

[239] J. Kasprzak, B. Patton, V. Savona, and W. Langbein, "Coherent coupling between distant excitons revealed by two-dimensional nonlinear hyperspectral imaging," *Nature Photonics*, vol. 5, pp. 57–63, JAN 2011.

[240] S. Reitzenstein, A. Löffler, C. Hofmann, A. Kubanek, M. Kamp, J. P. Reithmaier, A. Forchel, V. D. Kulakovskii, L. V. Keldysh, I. V. Ponomarev, and T. L. Reinecke, "Coherent photonic coupling of semiconductor quantum dots," *Opt. Lett.*, vol. 31, pp. 1738–1740, Jun 2006.

[241] A. Laucht, J. M. Villas-Bôas, S. Stobbe, N. Hauke, F. Hofbauer, G. Böhm, P. Lodahl, M.-C. Amann, M. Kaniber, and J. J. Finley, "Mutual coupling of two semiconductor quantum dots via an optical nanocavity," *Phys. Rev. B*, vol. 82, p. 075305, Aug 2010.

[242] H. Kim, D. Sridharan, T. C. Shen, G. S. Solomon, and E. Waks, "Strong coupling between two quantum dots and a photonic crystal cavity using magnetic field tuning," *Opt. Express*, vol. 19, pp. 2589–2598, Jan 2011.

[243] F. Albert, K. Sivalertporn, J. Kasprzak, M. Strauß, C. Schneider, S. Höfling, M. Kamp, A. Forchel, S. Reitzenstein, E. A. Muljarov, and W. Langbein, "Microcavity controlled coupling of excitonic qubits," *Nature Communications*, vol. 4, p. 1747, 2013.

[244] F. Milde, A. Knorr, and S. Hughes, "Role of electron-phonon scattering on the vacuum rabi splitting of a single-quantum dot and a photonic crystal nanocavity," *Phys. Rev. B*, vol. 78, p. 035330, Jul 2008.

[245] G. Tarel and V. Savona, "Linear spectrum of a quantum dot coupled to a nanocavity," *Phys. Rev. B*, vol. 81, p. 075305, FEB 2010.

[246] S. Hughes, P. Yao, F. Milde, A. Knorr, D. Dalacu, K. Mnaymneh, V. Sazonova, P. J. Poole, G. C. Aers, J. Lapointe, R. Cheriton, and R. L. Williams, "Influence of electron-acoustic phonon scattering on off-resonant cavity feeding within a strongly coupled quantum-dot cavity system," *Phys. Rev. B*, vol. 83, p. 165313, Apr 2011.

[247] E. M. Kessler, M. Grochol, and C. Piermarocchi, "Light-mass bragg cavity polaritons in planar quantum dot lattices," *Phys. Rev. B*, vol. 77, p. 085306, Feb 2008.

[248] F. P. Laussy, A. Laucht, E. del Valle, J. J. Finley, and J. M. Villas-Bôas, "Luminescence spectra of quantum dots in microcavities. iii. multiple quantum dots," *Phys. Rev. B*, vol. 84, p. 195313, Nov 2011.

[249] A. Auffèves, D. Gerace, S. Portolan, A. Drezet, and M. F. Santos, "Few emitters in a cavity: from cooperative emission to individualization," *New Journal of Physics*, vol. 13, no. 9, p. 093020, 2011.

[250] G. S. Agarwal and S. DuttaGupta, "Microcavity-induced modification of the dipole-dipole interaction," *Phys. Rev. A*, vol. 57, pp. 667–670, Jan 1998.

[251] C. Piermarocchi, P. Chen, L. J. Sham, and D. G. Steel, "Optical rkky interaction between charged semiconductor quantum dots," *Phys. Rev. Lett.*, vol. 89, p. 167402, Sep 2002.

[252] G. F. Quinteiro, J. Fernández-Rossier, and C. Piermarocchi, "Long-range spin-qubit interaction mediated by microcavity polaritons," *Phys. Rev. Lett.*, vol. 97, p. 097401, Aug 2006.

[253] K. J. Xu and C. Piermarocchi, "Dynamics of elastic and inelastic energy transfer between quantum dots in a microcavity," *Phys. Rev. B*, vol. 84, p. 115316, Sep 2011.

[254] S. Hughes, "Enhanced single-photon emission from quantum dots in photonic crystalwaveguides and nanocavities," *Opt. Lett.*, vol. 29, pp. 2659–2661, Nov 2004.

[255] V. S. C. M. Rao and S. Hughes, "Single quantum dot spontaneous emission in a finite-size photonic crystal waveguide: Proposal for an efficient "on chip" single photon gun," *Phys. Rev. Lett.*, vol. 99, p. 193901, Nov 2007.

[256] G. Lecamp, P. Lalanne, and J. P. Hugonin, "Very large spontaneous-emission β factors in photonic-crystal waveguides," *Phys. Rev. Lett.*, vol. 99, p. 023902, Jul 2007.

[257] P. Yao and S. Hughes, "Macroscopic entanglement and violation of bell's inequalities between two spatially separated quantum dots in a planar photonic crystal system," *Opt. Express*, vol. 17, pp. 11505–11514, Jul 2009.

[258] P. T. Kristensen, J. Mørk, P. Lodahl, and S. Hughes, "Decay dynamics of radiatively coupled quantum dots in photonic crystal slabs," *Phys. Rev. B*, vol. 83, p. 075305, Feb 2011.

[259] R. Kubo, "Statistical-mechanical theory of irreversible processes. i. general theory and simple applications to magnetic and conduction problems," *J. Phys. Soc. Jpn.*, vol. 12, no. 6, pp. 570–586, 1957.

[260] F. Tassone, F. Bassani, and L. Andreani, "Resonant and surface polaritons in quantum wells," *Il Nuovo Cimento D*, vol. 12, pp. 1673–1687, 1990. 10.1007/BF02451267.

[261] L. C. Andreani, *Confined Electrons and Photons*, vol. 340 of *NATO Advanced Study Institute, Series B: Physics.* Plenum Press, New York, 1994.

[262] K. Sakoda, *Optical Properties of Photnoic Crystals.* Springer, Berlin, 2001.

[263] O. J. F. Martin and N. B. Piller, "Electromagnetic scattering in polarizable backgrounds," *Phys. Rev. E*, vol. 58, pp. 3909–3915, Sep 1998.

[264] E. N. Economou, *Green's Functions in Quantum Physics.* Springer, Berlin, 2006.

[265] M. Tavis and F. W. Cummings, "Exact solution for an n-molecule—radiation-field hamiltonian," *Phys. Rev.*, vol. 170, pp. 379–384, Jun 1968.

[266] V. Savona, L. Andreani, P. Schwendimann, and A. Quattropani, "Quantum well excitons in semiconductor microcavities: Unified treatment of weak and strong coupling regimes," *Solid State Communications*, vol. 93, no. 9, pp. 733–739, 1995.

[267] D. Bimberg, M. Grundmann, and N. N. Ledentsov, *Quantum Dot Heterostructures.* John Wiley & Sons, 1999.

[268] B. Gil and A. V. Kavokin, "Giant exciton-light coupling in zno quantum dots," *Applied Physics Letters*, vol. 81, no. 4, pp. 748–750, 2002.

[269] W. Langbein, P. Borri, U. Woggon, V. Stavarache, D. Reuter, and A. D. Wieck, "Radiatively limited dephasing in inas quantum dots," *Phys. Rev. B*, vol. 70, p. 033301, JUL 2004.

[270] L.-W. Wang, J. Kim, and A. Zunger, "Electronic structures of [110]-faceted self-assembled pyramidal inas/gaas quantum dots," *Phys. Rev. B*, vol. 59, pp. 5678–5687, Feb 1999.

[271] O. Stier, M. Grundmann, and D. Bimberg, "Electronic and optical properties of strained quantum dots modeled by 8-band k·p theory," *Phys. Rev. B*, vol. 59, pp. 5688–5701, Feb 1999.

[272] A. Thränhardt, C. Ell, G. Khitrova, and H. M. Gibbs, "Relation between dipole moment and radiative lifetime in interface fluctuation quantum dots," *Phys. Rev. B*, vol. 65, p. 035327, Jan 2002.

[273] J. M. Fink, R. Bianchetti, M. Baur, M. Göppl, L. Steffen, S. Filipp, P. J. Leek, A. Blais, and A. Wallraff, "Dressed collective qubit states and the tavis-cummings model in circuit qed," *Phys. Rev. Lett.*, vol. 103, p. 083601, Aug 2009.

[274] O. Gywat, F. Meier, D. Loss, and D. D. Awschalom, "Dynamics of coupled qubits interacting with an off-resonant cavity," *Phys. Rev. B*, vol. 73, p. 125336, Mar 2006.

[275] Y.-S. Choi, M. T. Rakher, K. Hennessy, S. Strauf, A. Badolato, P. M. Petroff, D. Bouwmeester, and E. L. Hu, "Evolution of the onset of coherence in a family of photonic crystal nanolasers," *Applied Physics Letters*, vol. 91, pp. 031108–031108–3, jul 2007.

[276] A. Surrente, M. Felici, P. Gallo, B. Dwir, A. Rudra, G. Biasiol, L. Sorba, and E. Kapon, "Ordered systems of site-controlled pyramidal quantum dots incorporated in photonic crystal cavities," *Nanotechnology*, vol. 22, no. 46, p. 465203, 2011.

[277] V. S. C. Manga Rao and S. Hughes, "Single quantum-dot purcell factor and β factor in a photonic crystal waveguide," *Phys. Rev. B*, vol. 75, p. 205437, May 2007.

[278] L. O'Faolain, T. P. White, D. O'Brien, X. Yuan, M. D. Settle, and T. F. Krauss, "Dependence of extrinsic loss on group velocity in photonic crystal waveguides," *Opt. Express*, vol. 15, pp. 13129–13138, Oct 2007.

[279] S. R. Huisman, G. Ctistis, S. Stobbe, A. P. Mosk, J. L. Herek, A. Lagendijk, P. Lodahl, W. L. Vos, and P. W. H. Pinkse, "Measurement of a band-edge tail in the density of states of a photonic-crystal waveguide," *Phys. Rev. B*, vol. 86, p. 155154, Oct 2012.

[280] S. Kiravittaya, M. Benyoucef, R. Zapf-Gottwick, A. Rastelli, and O. G. Schmidt, "Ordered gaas quantum dot arrays on gaas(001): Single photon emission and fine structure splitting," *Applied Physics Letters*, vol. 89, no. 23, p. 233102, 2006.

Bibliography

[281] J. Martín-Sánchez, P. Alonso-González, J. Herranz, Y. González, and L. González, "Site-controlled lateral arrangements of inas quantum dots grown on gaas(001) patterned substrates by atomic force microscopy local oxidation nanolithography," *Nanotechnology*, vol. 20, no. 12, p. 125302, 2009.

[282] M. Mehta, D. Reuter, A. Melnikov, A. D. Wieck, and A. Remhof, "Focused ion beam implantation induced site-selective growth of inas quantum dots," *Applied Physics Letters*, vol. 91, no. 12, p. 123108, 2007.

[283] L. O. Mereni, V. Dimastrodonato, R. J. Young, and E. Pelucchi, "A site-controlled quantum dot system offering both high uniformity and spectral purity," *Applied Physics Letters*, vol. 94, no. 22, p. 223121, 2009.

[284] C. Schneider, A. Huggenberger, T. Sünner, T. Heindel, M. Strauß, S. Göpfert, P. Weinmann, S. Reitzenstein, L. Worschech, M. Kamp, S. Höfling, and A. Forchel, "Single site-controlled in(ga)as/gaas quantum dots: growth, properties and device integration," *Nanotechnology*, vol. 20, no. 43, p. 434012, 2009.

[285] M. Z. Hasan and C. L. Kane, "Colloquium: Topological insulators," *Reviews of Modern Physics*, vol. 82, pp. 3045–3067, Nov. 2010.

[286] L. Lu, J. D. Joannopoulos, and M. Soljačić, "Topological photonics," *Nature Publishing Group*, vol. 8, no. 11, pp. 821–829, 2014.

[287] D. R. Yennie, "Integral quantum hall effect for nonspecialists," *Rev. Mod. Phys.*, vol. 59, pp. 781–824, Jul 1987.

[288] F. Haldane and S. Raghu, "Possible Realization of Directional Optical Waveguides in Photonic Crystals with Broken Time-Reversal Symmetry," *Physical Review Letters*, vol. 100, p. 013904, Jan. 2008.

[289] S. Raghu and F. D. M. Haldane, "Analogs of quantum-Hall-effect edge states in photonic crystals," *Physical Review A*, vol. 78, p. 033834, Sept. 2008.

[290] Z. Wang, Y. Chong, J. D. Joannopoulos, and M. Soljacić, "Observation of unidirectional backscattering-immune topological electromagnetic states.," *Nature*, vol. 461, pp. 772–5, Oct. 2009.

[291] M. Hafezi, E. a. Demler, M. D. Lukin, and J. M. Taylor, "Robust optical delay lines with topological protection," *Nature Physics*, vol. 7, pp. 907–912, Aug. 2011.

[292] M. Hafezi, S. Mittal, J. Fan, A. Migdall, and J. M. Taylor, "Imaging topological edge states in silicon photonics," vol. 7, no. October, pp. 1001–1006, 2013.

[293] M. C. Rechtsman, J. M. Zeuner, Y. Plotnik, Y. Lumer, D. Podolsky, F. Dreisow, S. Nolte, M. Segev, and A. Szameit, "Photonic Floquet topological insulators.," *Nature*, vol. 496, pp. 196–200, Apr. 2013.

[294] C. L. Kane and E. J. Mele, "Quantum Spin Hall Effect in Graphene," *Physical Review Letters*, vol. 95, p. 226801, Nov. 2005.

[295] J. Koch, A. a. Houck, K. L. Hur, and S. M. Girvin, "Time-reversal-symmetry breaking in circuit-QED-based photon lattices," *Physical Review A - Atomic, Molecular, and Optical Physics*, vol. 82, no. 4, pp. 1–18, 2010.

[296] R. O. Umucalılar and I. Carusotto, "Artificial gauge field for photons in coupled cavity arrays," *Physical Review A*, vol. 84, p. 043804, Oct. 2011.

[297] R. O. Umucalılar and I. Carusotto, "Fractional Quantum Hall States of Photons in an Array of Dissipative Coupled Cavities," *Physical Review Letters*, vol. 108, p. 206809, May 2012.

[298] K. Fang, Z. Yu, and S. Fan, "Realizing effective magnetic field for photons by controlling the phase of dynamic modulation," *Nature Photonics*, vol. 6, no. October, 2012.

[299] M. Schmidt, S. Kessler, V. Peano, O. Painter, and F. Marquardt, "Optomechanical creation of magnetic fields for photons on a lattice," *Optica*, vol. 2, pp. 635–641, Jul 2015.

[300] V. Peano, C. Brendel, M. Schmidt, and F. Marquardt, "Topological Phases of Sound and Light," vol. 031011, pp. 1–18, 2015.

[301] K. Fang, Z. Yu, and S. Fan, "Photonic Aharonov-Bohm effect based on dynamic modulation," *Physical Review Letters*, vol. 108, no. 153901, pp. 1–5, 2012.

[302] L. D. Tzuang, K. Fang, P. Nussenzveig, S. Fan, and M. Lipson, "Non-reciprocal phase shift induced by an effective magnetic flux for light," *Nature Photonics*, vol. 8, no. August, pp. 2–6, 2014.

[303] F. D. M. Haldane, "Model for a quantum hall effect without landau levels: Condensed-matter realization of the "parity anomaly"," *Physical Review Letters*, vol. 61, no. 18, pp. 2015–2018, 1988.

[304] G. Jotzu, M. Messer, R. Desbuquois, M. Lebrat, T. Uehlinger, D. Greif, and T. Esslinger, "Experimental realisation of the topological Haldane model," *Nature*, vol. 515, no. V, p. 237–240, 2014.

[305] P. Hauke, O. Tieleman, A. Celi, C. Ölschläger, J. Simonet, J. Struck, M. Weinberg, P. Windpassinger, K. Sengstock, M. Lewenstein, and A. Eckardt, "Non-Abelian Gauge Fields and Topological Insulators in Shaken Optical Lattices," *Physical Review Letters*, vol. 109, no. 14, pp. 1–6, 2012.

[306] J. Struck, C. Olschläger, M. Weinberg, P. Hauke, J. Simonet, a. Eckardt, M. Lewenstein, K. Sengstock, and P. Windpassinger, "Tunable gauge potential for neutral

and spinless particles in driven optical lattices," *Physical Review Letters*, vol. 108, no. 22, pp. 1–5, 2012.

[307] N. Goldman and J. Dalibard, "Periodically driven quantum systems: Effective hamiltonians and engineered gauge fields," *Phys. Rev. X*, vol. 4, p. 031027, Aug 2014.

[308] Q. Xu, B. Schmidt, S. Pradhan, and M. Lipson, "Micrometre-scale silicon electro-optic modulator.," *Nature*, vol. 435, no. 7040, pp. 325–327, 2005.

[309] Y.-H. Kuo, Y. K. Lee, Y. Ge, S. Ren, J. E. Roth, T. I. Kamins, D. a. B. Miller, and J. S. Harris, "Strong quantum-confined Stark effect in germanium quantum-well structures on silicon.," *Nature*, vol. 437, no. 7063, pp. 1334–1336, 2005.

[310] E. Yüce, G. Ctistis, J. Claudon, E. Dupuy, R. D. Buijs, B. de Ronde, a. P. Mosk, J. Gérard, and W. L. Vos, "All-optical switching of a microcavity repeated at terahertz rates.," *Optics Letters*, vol. 38, no. 3, pp. 374–376, 2013.

[311] J. H. Shirley, "Solution of the schrödinger equation with a hamiltonian periodic in time," *Phys. Rev.*, vol. 138, pp. B979–B987, May 1965.

[312] A. Eckardt, C. Weiss, and M. Holthaus, "Superfluid-insulator transition in a periodically driven optical lattice," *Physical Review Letters*, vol. 95, no. December, pp. 1–4, 2005.

[313] H. Sambe, "Steady states and quasienergies of a quantum-mechanical system in an oscillating field," *Phys. Rev. A*, vol. 7, pp. 2203–2213, Jun 1973.

[314] K. Ohgushi, S. Murakami, and N. Nagaosa, "Spin anisotropy and quantum hall effect in the *kagomé* lattice: Chiral spin state based on a ferromagnet," *Phys. Rev. B*, vol. 62, pp. R6065–R6068, Sep 2000.

[315] H. M. Guo and M. Franz, "Topological insulator on the kagome lattice," *Physical Review B*, vol. 80, no. 11, pp. 1–4, 2009.

[316] M. V. Berry, "Quantal phase factors accompanying adiabatic changes," *Proceedings of the Royal Society of London A: Mathematical, Physical and Engineering Sciences*, vol. 392, no. 1802, pp. 45–57, 1984.

[317] J. Zak, "Berry ' s Phase for Energy Bands in Solids given the adiabatic form," *Physical Review Letters*, vol. 62, no. 23, pp. 2747–2750, 1989.

[318] R. Resta, "Manifestations of Berry ' s phase in molecules and condensed matter," *Journal of Physics: Condensed Matter*, vol. 12, p. R107, 2000.

[319] A. Soluyanov, *Topological aspects of band theory.* PhD thesis, Rutgers, The State University of New Jersey, 2012.

[320] H. Lira, Z. Yu, S. Fan, and M. Lipson, "Electrically driven nonreciprocity induced by interband photonic transition on a silicon chip," *Physical Review Letters*, vol. 109, no. 3, pp. 1–5, 2012.

[321] A. H. Safavi-Naeini, J. T. Hill, S. Meenehan, J. Chan, S. Gröblacher, and O. Painter, "Two-Dimensional Phononic-Photonic Band Gap Optomechanical Crystal Cavity," *Phys. Rev. Lett.*, vol. 112, p. 153603, Apr. 2014.

[322] F. Intonti, N. Caselli, S. Vignolini, F. Riboli, S. Kumar, A. Rastelli, O. G. Schmidt, M. Francardi, A. Gerardino, L. Balet, L. H. Li, A. Fiore, and M. Gurioli, "Mode tuning of photonic crystal nanocavities by photoinduced non-thermal oxidation," *Applied Physics Letters*, vol. 100, no. 3, 2012.

[323] A. Y. Piggott, K. G. Lagoudakis, T. Sarmiento, M. Bajcsy, G. Shambat, and J. Vučković, "Photo-oxidative tuning of individual and coupled gaas photonic crystal cavities," *Opt. Express*, vol. 22, pp. 15017–15023, Jun 2014.

Momchil Minkov

Curriculum Vitae

EPFL, Station 3, PH H2 434
1015 Lausanne, Switzerland
(+41) 76 237 61 31
momchil.minkov@epfl.ch

Education

2012-Present   **Ph. D. student**, *Ecole Polytechnique Federale de Lausanne*, Lausanne, Switzerland.
Doctoral student in theoretical physics focusing on photonic crystals and their applications, in close collaboration with experimental groups.

2010-2012   **MS in Physics**, *Ecole Polytechnique Federale de Lausanne*, Lausanne, Switzerland.
MS degree in Physics, GPA – 5.71/6, recipient of the EPFL Excellence Scholarship.

2007-2010   **BS in Physics**, *Jacobs University*, Bremen, Germany.
BS degree in Physics, GPA – 1.17/1. Member of the President's List in all three years.

2006-2007   **First year BS in Physics**, *Sofia University*, Sofia, Bulgaria.
Completed the first year of the BS program in Physics.

2001-2006   **High School**, *High School of Mathematics and Natural Sciences*, Veliko Tarnovo, Bulgaria.
Emphasis on Informatics, Mathematics, and English. Graduated with honors, GPA – 6.0/6

Awards and achievements

2015   Laureate of the Chorafas Foundation Award for high-level research by junior scientists

2014   Co-author of the featured articles in two issues of Applied Physics Letters: Issue 24, Vol. 104 and Issue 10, Vol. 105. Results appeared in featured news articles on the EPFL page

2014   Best poster presentation award at the PECS 2014 conference in Shangahi, China

2010-2012   Fellow of the EPFL Excellence Scholarship during the Master's degree studies

2007-2010   Member of the Jacobs University President's List

Experience

2013-Present   **Reviewer**, for peer-reviewed journals.
Paper reviews for the journals Physical Review Letters, Optics Letters, Photonics and Nanostructures: Fundamentals and Applications, Advances in Optics, and Superlattices and Microstructures

2012-Present   **Teaching Assistant**, EPFL, Lausanne, Switzerland.
Teaching in the exercise sessions of the Quantum Physics 3 and 4 courses.

2010-2013   **Online instructor**, VIDEO TUTOR GMBH.
Prepared video tutorials for the IB diploma support platform at www.video-tutor.org. Took part in the project from the beginning and helped develop it into a successful start-up.

06-09/2009   **Summer Student**, CERN, Geneva, Switzerland.
Lectures in a range of topics and practical work at the COLLAPS-ISOLDE collaboration.

2007–2010   **Teaching Assistant**, JACOBS UNIVERSITY, Bremen, Germany.
Teaching duties (tutorials and grading exams/homeworks) for the Engineering and Science Mathematics and the General Physics courses.

Communication Skills

2015	Oral presentation at META, New York, USA
2015	Poster presentation at CLEO-Europe, Munich, Germany
2015	Poster presentation at the QSIT general meeting, Arosa, Switzerland
2014	Poster presentation (best poster award) at PECS, Shanghai, China
2014	Poster presentation at CLEO, San Jose, USA
2013	Oral presentation at OECS, Rome, Italy
2013	Oral presentation at PLMCN, Hersonissos, Greece
2012	Poster presentation at CLEO-Europe, Munich, Germany
2012	Poster presentation at ICPS, Zurich, Switzerland

Computer skills

Professional	MATLAB, LaTeX, Linux, MEEP, Lumerical, Microsoft Windows, Microsoft Office
Advanced	Mathematica, C, FORTRAN, Pascal, OpenOffice, SketchUp, GIMP

Doctoral Thesis

Working Title	*Numerical study and optimization of photonic crystals slabs*
Supervisor	Prof. Vincenzo Savona
Description	We carry out numerical simulations of photonic crystal structures, with a wide variety of applications. Particular focus is given to optimizing designs for better performance, to the effect of fabrication imperfections, and to finding novel applications especially in terms of light-matter coupling and non-linear phenomena.

Languages

Bulgarian	**Mother tongue**	
English	**Fluent**	*Level C2 covered*
French	**Advanced**	*Level B2 covered*
German	**Beginner/Intermediate**	*Level A2 covered*

Interests

- Sports (football, volleyball,...)
- Cooking
- Playing the guitar
- Literature

List of Publications (in chronological order)

[1] H Flayac, **M Minkov**, V Savona, 'Remote macroscopic entanglement on a photonic crystal architecture,' *Phys. Rev. A* (in press) (2015)

[2] **M Minkov**, V Savona, 'Wide-band slow light in compact photonic crystal coupled-cavity waveguides,' *Optica* **2**, 631-634 (2015)

[3] NV Triviño, **M Minkov**, et al., 'Gallium nitride L3 photonic crystal cavities with an average quality factor of 16,900 in the near infrared,' *Appl. Phys. Lett.* **105**, 231119 (2014)

[4] UP Dharanipathy, **M Minkov**, et al., 'High-Q silicon photonic crystal cavity for enhanced optical nonlinearities,' *Appl. Phys. Lett.* **105**, 101101 (2014)

[5] Y Lai, S Pirotta, G Urbinati, D Gerace, **M Minkov**, et al., 'Genetically designed L3 photonic crystal nanocavities with measured quality factor exceeding one million,' *Appl. Phys. Lett.* **104**, 241101 (2014)

[6] **M Minkov**, V Savona, 'Automated optimization of photonic crystal slab cavities,' *Scientific Reports* **4**, 5124 (2014)

[7] **M Minkov**, V Savona, 'Optimizing doubly resonant photonic crystal cavity modes for second harmonic generation,' *Proc. SPIE* **9127**, 91270C (2014)

[8] **M Minkov**, et al., 'Statistics of the disorder- induced losses of high-Q photonic crystal cavities', *Opt. Express* **21**, 28233-28245 (2013)

[9] **M Minkov**, V Savona, 'Long-distance radiative excitation transfer between quantum dots in disordered photonic crystal waveguides,' *Phys. Rev. B (R)* **88**, 081303 (2013)

[10] **M Minkov**, V Savona, 'Radiative coupling of quantum dots in photonic crystal structures,' *Phys. Rev. B* **87**, 125306 (2013)

[11] **M Minkov**, V Savona, 'Effect of hole-shape irregularities on photonic crystal waveguides,' *Optics Letters* **37**, 3108-3110 (2012)

[12] Y Brihaye, **M Minkov**, et al., 'Symmetry breaking in (gravitating) scalar field models describing interacting boson stars and Q-balls,' *Physical Review D* **80**, 064014 (2009)

[13] B Hartmann, **M Minkov**, 'p-q superstrings in anti-de-Sitter spacetime,' *Journal of Physics A* **42**, 035401 (2009)